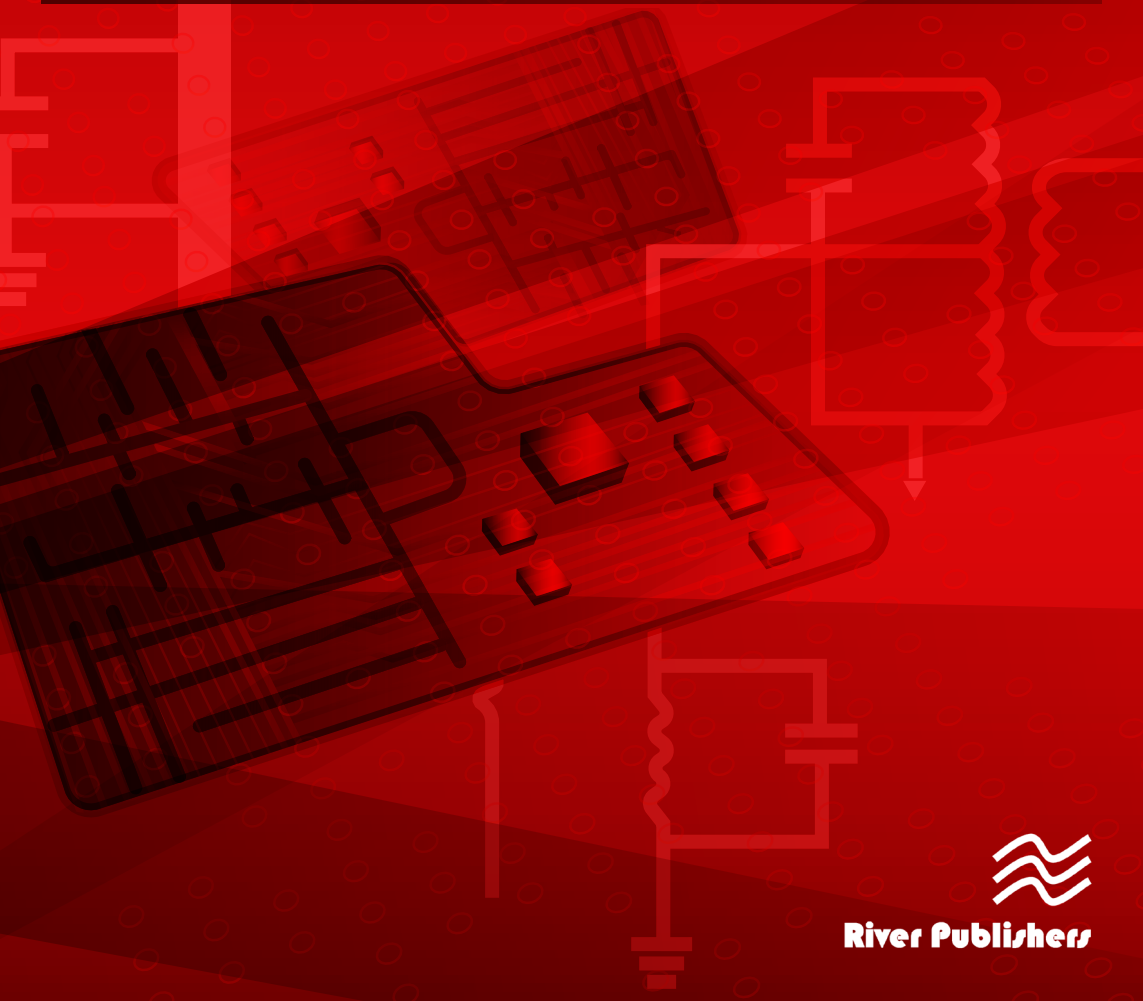


River Publishers Series in Circuits and Systems

New Topics in Simulation and Modeling of RF Circuits

Alexandru Gabriel Gheorghe and
Florin Constantinescu



River Publishers

New Topics in Simulation and Modeling of RF Circuits

RIVER PUBLISHERS SERIES IN CIRCUITS AND SYSTEMS

Series Editors

MASSIMO ALIOTO

*National University of Singapore
Singapore*

KOFI MAKINWA

*Delft University of Technology
The Netherlands*

DENNIS SYLVESTER

*University of Michigan
USA*

The “River Publishers Series in Circuits & Systems” is a series of comprehensive academic and professional books which focus on theory and applications of Circuit and Systems. This includes analog and digital integrated circuits, memory technologies, system-on-chip and processor design. The series also includes books on electronic design automation and design methodology, as well as computer aided design tools.

Books published in the series include research monographs, edited volumes, handbooks and textbooks. The books provide professionals, researchers, educators, and advanced students in the field with an invaluable insight into the latest research and developments.

Topics covered in the series include, but are by no means restricted to the following:

- Analog Integrated Circuits
- Digital Integrated Circuits
- Data Converters
- Processor Architectures
- System-on-Chip
- Memory Design
- Electronic Design Automation

For a list of other books in this series, visit www.riverpublishers.com

New Topics in Simulation and Modeling of RF Circuits

Alexandru Gabriel Gheorghe

University Politehnica of Bucharest
Romania

Florin Constantinescu

University Politehnica of Bucharest
Romania



River Publishers

Published, sold and distributed by:

River Publishers
Alsbjergvej 10
9260 Gistrup
Denmark

River Publishers
Lange Geer 44
2611 PW Delft
The Netherlands

Tel.: +45369953197
www.riverpublishers.com

ISBN: 978-87-93379-46-6 (Hardback)
978-87-93379-45-9 (Ebook)

©2017 River Publishers

All rights reserved. No part of this publication may be reproduced, stored in a retrieval system, or transmitted in any form or by any means, mechanical, photocopying, recording or otherwise, without prior written permission of the publishers.

Contents

| | |
|--|------------|
| Preface | ix |
| List of Figures | xi |
| List of Tables | xix |
| List of Abbreviations | xxi |
| 1 Introduction | 1 |
| 1.1 RF Circuits | 1 |
| 1.2 Customary and Uncustomary Behavior of Non-Autonomous Circuits | 4 |
| 1.2.1 Definitions and Properties | 4 |
| 1.2.2 Customary and Uncustomary Behavior of Linear and Nonlinear Circuits | 6 |
| 1.2.3 Operating Modes | 8 |
| 1.3 Existence and Uniqueness of Dynamic Circuit Solutions . . | 9 |
| References | 16 |
| 2 Analysis of RF Circuits | 17 |
| 2.1 Time Domain Analysis | 17 |
| 2.1.1 Transient Analysis | 17 |
| 2.1.1.1 Time step choice algorithm of SPICE and SPECTRE RF | 17 |
| 2.1.1.2 Brambilla–D’Amore time step choice algorithm | 20 |
| 2.1.1.2.1 <i>Computation of energy errors</i> . . | 20 |
| 2.1.1.2.2 <i>Time step computation</i> | 21 |
| 2.1.1.2.3 <i>Case studies</i> | 23 |
| 2.1.1.3 Time step choice algorithm based on energy balance relative error | 29 |

| | | |
|-----------|--|----|
| 2.1.1.3.1 | <i>Errors used in transient analysis</i> | 29 |
| 2.1.1.3.2 | <i>Time step choice algorithm</i> | 32 |
| 2.1.1.3.3 | <i>Solving the linear circuit with companion models</i> | 33 |
| 2.1.1.3.4 | <i>Examples</i> | 36 |
| 2.1.1.3.5 | <i>Conclusions</i> | 53 |
| 2.1.1.4 | Frequency warping in linear circuits | 54 |
| 2.1.1.4.1 | <i>Parallel RLC autonomous circuit</i> | 55 |
| 2.1.1.4.2 | <i>High quality factor circuit</i> | 56 |
| 2.1.1.4.3 | <i>Linear band-pass BAW filter</i> | 57 |
| 2.1.2 | Envelope Following and the Analysis with Two Time Variables | 59 |
| 2.1.2.1 | Kundert algorithm implemented in SPECTRE RF | 60 |
| 2.1.2.2 | Brambilla-Maffezzoni algorithm implemented in PAN | 62 |
| 2.1.2.3 | Examples | 65 |
| 2.1.2.3.1 | <i>AM demodulator</i> | 65 |
| 2.1.2.3.2 | <i>In-Phase and quadrature modulator (IQ)</i> | 67 |
| 2.1.2.3.3 | <i>Remark</i> | 72 |
| 2.1.2.4 | Exponential approximation of the envelope | 77 |
| 2.1.2.5 | Quadratic approximation of the envelope | 79 |
| 2.1.2.5.1 | <i>Switching between exponential and quadratic envelope approximations</i> | 80 |
| 2.1.2.6 | Examples | 81 |
| 2.1.2.7 | Envelope following analysis of a buck converter with closed loop control | 85 |
| 2.1.2.7.1 | <i>Example</i> | 85 |
| 2.1.2.8 | Transient analysis with two time variables | 90 |
| 2.1.2.8.1 | <i>Remarks</i> | 92 |
| 2.1.3 | Computation of the Periodic Steady State | 92 |
| 2.1.3.1 | The brute force method with the periodicity error control | 92 |

| | | |
|-----------|--|-----|
| 2.1.3.2 | Shooting methods | 93 |
| 2.1.3.2.1 | <i>Shooting with Newton-Raphson</i> | 93 |
| 2.1.3.2.2 | <i>Shooting analysis from PAN</i> . . . | 96 |
| 2.1.3.3 | Shooting with linear extrapolation | 97 |
| 2.1.3.4 | Shooting with exponential extrapolation | 98 |
| 2.1.3.4.1 | <i>Example</i> | 99 |
| 2.1.3.5 | Two time variables method | 100 |
| 2.1.3.5.1 | <i>Finite difference method</i> | 100 |
| 2.1.3.5.2 | <i>Shooting with Newton-Raphson</i> | 102 |
| 2.1.3.6 | Shooting with exponential extrapolation . . . | 102 |
| 2.1.3.6.1 | <i>Example</i> | 104 |
| 2.2 | Frequency Domain Analysis | 105 |
| 2.2.1 | Harmonic Balance Method | 105 |
| 2.2.1.1 | Valtonen harmonic balance method implemented in APLAC | 105 |
| 2.2.1.1.1 | <i>Time domain and frequency domain representations of a periodic signal</i> | 105 |
| 2.2.1.1.2 | <i>Harmonic balance analysis</i> | 106 |
| 2.2.1.1.3 | <i>Remarks</i> | 108 |
| 2.2.1.1.4 | <i>Example</i> | 108 |
| 2.2.1.2 | Mixed frequency – time domain analysis method implemented in SPECTRE RF | 110 |
| 2.2.1.2.1 | <i>Example</i> | 114 |
| 2.2.2 | Source Iteration Method for Circuits with Resistive Nonlinearities | 115 |
| 2.2.2.1 | Equivalent sources | 116 |
| 2.2.2.2 | Periodic solutions of the linear circuit | 117 |
| 2.2.2.3 | Fourier analysis | 118 |
| 2.2.2.4 | Iterative procedure | 118 |
| 2.2.2.5 | Remarks | 119 |
| 2.2.2.6 | Harmonics selection | 119 |
| 2.2.2.7 | Example | 120 |
| 2.2.3 | Circuit Envelope Method | 123 |
| 2.2.3.1 | Example | 128 |
| | References | 130 |

| | | |
|----------|---|------------|
| 3 | Nonlinear Circuit Models for Power Bulk Acoustic Wave Resonators and Filters | 135 |
| 3.1 | Bulk Acoustic Wave Resonators – Structure and Nonlinear Behavior | 135 |
| 3.2 | Linear Parametric Circuit Models | 140 |
| 3.2.1 | Nosek and Albareda Models | 140 |
| 3.2.2 | Identification of the Nosek Model Parameters | 143 |
| 3.2.3 | Discussion on Linear Parametric Circuit Models | 146 |
| 3.3 | Nonlinear Circuit Models | 147 |
| 3.3.1 | Behavioral Circuit Models | 147 |
| 3.3.2 | Parameter Identification for a Behavioral Resonator Model | 156 |
| 3.3.3 | Nonlinear Circuit Model for Anti-Series and Anti-Parallel Connections | 157 |
| 3.3.4 | Example | 160 |
| 3.4 | Physical Model Using Transmission Lines | 162 |
| 3.4.1 | 1D Linear Artificial Transmission Line Model | 164 |
| 3.4.2 | 1D Artificial Transmission Line Model With Mechanical Nonlinearity | 166 |
| 3.4.3 | Example | 167 |
| 3.5 | Behavioral Models for Frequency Domain Analysis of Power BAW Filters Driven by Multi-Tone Excitations | 170 |
| 3.5.1 | Compensation of Connection Wires Influence | 170 |
| 3.5.2 | Example | 173 |
| 3.6 | Conclusions | 175 |
| | References | 177 |
| | Index | 181 |
| | About the Authors | 187 |

Preface

For design purpose, a physical circuit made up of devices is associated to a model (the electrical circuit) by replacing the devices with circuit elements, or circuit models. Each circuit element is an approximation of the real device, so there can be many models for the same device, depending on the effects to be modeled and the analysis to be made. Knowing the interconnection and the constitutive equations of the circuit elements, a system of equations whose solution represents the theoretical results can be written. If the theoretical results obtained from the electric circuit analysis correspond to the practical results obtained from measurements made on the physical circuit, it means that the adopted model is correct. Otherwise either the problem is not well formulated, or the circuit model is not correct, or the analysis method used is not suitable for that circuit. For example, for circuits driven by relatively low frequency signals, the classical transient analysis is suitable. But, this analysis is not suitable for the RF circuits, which are driven by high frequency signals, because, in this case, it uses a lot of CPU time and memory resources. On the other hand, the analysis methods designed for the RF circuits, although faster than the classical transient analysis, can lead to erroneous solutions if they are not carefully set (see Sections 2.1.2 and 2.1.3). The topics addressed in this book are from the scientific areas of interest of the authors, containing their research results together with other approaches from the literature.

Chapter 1 contains a description of the properties of RF circuits, characterization of circuits with customary and uncustomary behavior, and some theorems of solutions existence and uniqueness for dynamic nonlinear circuits. Since many analysis methods are based on the essential properties of non-autonomous circuits with customary behavior (exponential attenuation of transient components, unique periodic steady state solution having the same period with the excitation signal, and spectrum preservation), Section 1.2 presents the properties of these circuits, which are used almost exclusively in technique. Because some of the methods described in Chapter 2 (shooting, finite differences, harmonic balance, envelope following) can be applied only

for circuits with unique solution, in Section 1.3 are presented some theorems of solutions existence and uniqueness for dynamic circuits.

In Chapter 2 are presented the main time domain and frequency domain analysis methods for the RF circuits. The advantages and disadvantages of each method are highlighted. An algorithm for the time step choice in transient analysis based on energy balance errors is also presented.

Chapter 3 contains some nonlinear circuit models of power BAW resonators. The behavioral models for the time domain analysis are simple circuits containing weakly nonlinear elements. The behavioral models for frequency domain analysis are based on the measured values of the frequency dependent S parameters, and on the frequency dependent intermodulation products; these magnitudes are measured for incident powers in a certain range. The physical models contain artificial transmission lines with nonlinear circuit elements corresponding to mechanical and electrical nonlinearities.

List of Figures

| | | |
|--------------------|--|----|
| Figure 1.1 | RF front-end of a coherent super-heterodyne receiver. | 2 |
| Figure 1.2 | Transceiver. | 2 |
| Figure 1.3 | Linear resistive multiport. | 7 |
| Figure 1.4 | Resistive multiport for writing the state equations in normal form. | 10 |
| Figure 1.5 | (a) First order circuit; (b) Characteristic of the nonlinear resistor. | 13 |
| Figure 1.6 | Inductor in Figure 1.5 is replaced with a current source. | 14 |
| Figure 1.7 | Capacitor inserted in parallel with the nonlinear resistor in the circuit in Figure 1.5. | 15 |
| Figure 1.8 | (a) First order circuit; (b) Characteristic of the nonlinear resistor. | 15 |
| Figure 1.9 | Inductor added in series with the resistor in the circuit in Figure 1.8. | 15 |
| Figure 2.1 | Nonlinear RC circuit. | 20 |
| Figure 2.2 | Voltage multiplier schematic. | 23 |
| Figure 2.3 | Class C amplifier. | 23 |
| Figure 2.4 | ne600p mixer. | 24 |
| Figure 2.5 | One diode circuit. | 25 |
| Figure 2.6 | v - i diode characteristic. | 25 |
| Figure 2.7 | Diode voltage. | 26 |
| Figure 2.8 | Diode voltage – detail. | 27 |
| Figure 2.9 | RI voltage. | 27 |
| Figure 2.10 | RI voltage – detail. | 28 |
| Figure 2.11 | RI voltage – detail. | 28 |
| Figure 2.12 | Time step evolution for SPICE and PAN. | 29 |
| Figure 2.13 | Quadratic interpolation. | 31 |
| Figure 2.14 | Evolution of the relative energy balance error – <i>double precision</i> | 34 |

| | | |
|--------------------|--|----|
| Figure 2.15 | Evolution of the absolute energy balance error – <i>double precision</i> | 34 |
| Figure 2.16 | Evolution of the relative energy balance error – <i>long double precision</i> | 35 |
| Figure 2.17 | Evolution of the absolute energy balance error – <i>long double precision</i> | 35 |
| Figure 2.18 | Linear circuit with damped oscillatory response. | 36 |
| Figure 2.19 | Circuit response in the first case. | 37 |
| Figure 2.20 | Circuit response in the first case – detail. | 37 |
| Figure 2.21 | Circuit response in the second case. | 38 |
| Figure 2.22 | Circuit response in the second case – detail. | 39 |
| Figure 2.23 | Diode voltage. | 40 |
| Figure 2.24 | $V(4)$ voltage. | 40 |
| Figure 2.25 | $V(4)$ voltage – detail. | 41 |
| Figure 2.26 | Relative energy balance error for SPICE and the proposed algorithm. | 41 |
| Figure 2.27 | Relative energy balance error for SPICE and the proposed algorithm – detail. | 42 |
| Figure 2.28 | Evolution of the time step for SPICE and the proposed algorithm. | 42 |
| Figure 2.29 | High quality factor circuit. | 43 |
| Figure 2.30 | High quality factor circuit response. | 43 |
| Figure 2.31 | High quality factor circuit response – detail. | 44 |
| Figure 2.32 | High quality factor circuit response computed with SPICE and with the proposed algorithm. | 44 |
| Figure 2.33 | High quality factor circuit response computed with SPICE and with the proposed algorithm – detail. | 45 |
| Figure 2.34 | Bandpass filter (output voltage – node 2 voltage). | 46 |
| Figure 2.35 | $V(2)$ [V] versus time [s]. | 47 |
| Figure 2.36 | I_{Lm1} [A] versus time [s]. | 48 |
| Figure 2.37 | Output voltage of the band-pass filter. | 49 |
| Figure 2.38 | Relative energy balance error for the SPICE solution. | 49 |
| Figure 2.39 | Relative energy balance error for the proposed algorithm solution. | 50 |
| Figure 2.40 | Time step evolution for SPICE and for the proposed algorithm. | 50 |

| | | |
|--------------------|---|----|
| Figure 2.41 | Band pass filter (output voltage – node 2 voltage). . . | 51 |
| Figure 2.42 | Output voltage of the band-pass filter. | 52 |
| Figure 2.43 | Output voltage of the band-pass filter – detail. . . . | 52 |
| Figure 2.44 | Relative energy balance error for SPICE and the proposed algorithm. | 53 |
| Figure 2.45 | Time step evolution for SPICE and for the proposed algorithm. | 53 |
| Figure 2.46 | Parallel RLC circuit. | 55 |
| Figure 2.47 | Voltage of the parallel RLC circuit. | 55 |
| Figure 2.48 | Voltage of the parallel RLC circuit – detail. | 56 |
| Figure 2.49 | Response of the high quality factor circuit. | 56 |
| Figure 2.50 | Response of the high quality factor circuit – detail. | 57 |
| Figure 2.51 | High Q circuit response – detail. | 58 |
| Figure 2.52 | Envelope following: (a) excitation, (b) response. | 60 |
| Figure 2.53 | Kundert’s envelope following algorithm. | 61 |
| Figure 2.54 | AM demodulator. | 65 |
| Figure 2.55 | AM demodulator – the transient analysis response. | 66 |
| Figure 2.56 | AM demodulator – the envelope following analysis response. | 66 |
| Figure 2.57 | In-phase and quadrature modulator. | 67 |
| Figure 2.58 | In-phase and quadrature modulator – input signal. . | 67 |
| Figure 2.59 | In-phase and quadrature modulator – responses. . . | 68 |
| Figure 2.60 | Class C amplifier, SPECTRE RF. | 69 |
| Figure 2.61 | Class C amplifier, PAN. | 70 |
| Figure 2.62 | ne600p mixer – SPECTRE RF solution. | 70 |
| Figure 2.63 | ne600p mixer – SPECTRE RF solution (detail). . . | 70 |
| Figure 2.64 | ne600p mixer – PAN solution. | 71 |
| Figure 2.65 | ne600p mixer – PAN solution (detail). | 71 |
| Figure 2.66 | ne600p mixer – the response corresponding to f_{RF} period jump. | 72 |
| Figure 2.67 | Linear test circuit. | 73 |
| Figure 2.68 | Time step for the transient and for the envelope following analyses from SPECTRE RF. | 74 |
| Figure 2.69 | The time step for the transient and for the envelope following analyses from PAN. | 75 |

| | | |
|--------------------|--|-----|
| Figure 2.70 | Time step for the envelope following analysis from SPECTRE RF and PAN. | 75 |
| Figure 2.71 | Time step for the envelope following analysis for various H_m (PAN). | 76 |
| Figure 2.72 | Time step evolution – detail. | 76 |
| Figure 2.73 | Transient components in the envelope following analysis (SPECTRE RF). | 77 |
| Figure 2.74 | Exponential approximation of the envelope. | 78 |
| Figure 2.75 | Buck converter. | 81 |
| Figure 2.76 | $i_L(t)$ – proposed algorithm. | 82 |
| Figure 2.77 | $i_L(t)$ – proposed algorithm (detail). | 83 |
| Figure 2.78 | Synchronous rectification buck converter. | 83 |
| Figure 2.79 | Output voltage V_0 | 83 |
| Figure 2.80 | Output voltage V_0 – steady state. | 84 |
| Figure 2.81 | Output voltage V_0 – transient solution for the increasing of the load resistance. | 84 |
| Figure 2.82 | Synchronous rectification buck converter with closed-loop control. | 86 |
| Figure 2.83 | Load resistance variation – 1st OC. | 86 |
| Figure 2.84 | Output voltage (proposed algorithm). | 87 |
| Figure 2.85 | Output voltage – detail (proposed algorithm). | 88 |
| Figure 2.86 | Output voltage – detail (SPECTRE RF). | 88 |
| Figure 2.87 | Load resistance variation – 2nd OC. | 89 |
| Figure 2.88 | $b(t)$ represented with one time variable. | 90 |
| Figure 2.89 | $b(t)$ signal represented with two time variables. | 91 |
| Figure 2.90 | Trajectory in the t_1 – t_2 plane. | 92 |
| Figure 2.91 | Shooting. | 94 |
| Figure 2.92 | Steady state of the class C amplifier, PSS analysis of SPECTRE RF. | 95 |
| Figure 2.93 | Steady state of the ne600p mixer, PSS analysis of SPECTRE RF. | 95 |
| Figure 2.94 | Steady state of the class C amplifier, PSS analysis of PAN. | 96 |
| Figure 2.95 | Steady state of the ne600p mixer, PSS analysis of PAN. | 97 |
| Figure 2.96 | DC commutation source. | 100 |
| Figure 2.97 | Two-dimensional x_i table. | 103 |
| Figure 2.98 | AM demodulator: (a) circuit and (b) diode model. | 104 |
| Figure 2.99 | Linear and nonlinear sub-circuits. | 107 |

| | | |
|---------------------|---|-----|
| Figure 2.100 | Port magnitudes for the nonlinear sub-circuit. . . . | 107 |
| Figure 2.101 | First order nonlinear circuit; (a) – circuit, (b) – $V(2)$, (c) – $V(2)$ – detail. | 109 |
| Figure 2.102 | AM demodulator – ADS results (a) transient analysis, (b) HB analysis. | 110 |
| Figure 2.103 | Piecewise linear resistor. | 114 |
| Figure 2.104 | Output voltage – circuit in Figure 2.101(a) with the diode model in Figure 2.103. | 114 |
| Figure 2.105 | Output voltage – circuit in Figure 2.101(a) with the diode model in Figure 2.103 – detail. . . . | 115 |
| Figure 2.106 | Two-port nonlinear resistor. | 116 |
| Figure 2.107 | Equivalent sources for a two port nonlinear resistor. | 117 |
| Figure 2.108 | AM demodulator. | 121 |
| Figure 2.109 | Diode v - i relationship. | 121 |
| Figure 2.110 | Diode voltage. | 122 |
| Figure 2.111 | Capacitor voltage. | 122 |
| Figure 2.112 | Capacitor voltage – detail. | 122 |
| Figure 2.113 | Comparison between various harmonic selections. | 123 |
| Figure 2.114 | u_C given by the proposed method, APLAC, and SPECTRE RF. | 123 |
| Figure 2.115 | Circuit envelope method. | 125 |
| Figure 2.116 | Modulated signal in the time domain. | 126 |
| Figure 2.117 | Spectra in the frequency domain. | 127 |
| Figure 2.118 | Diode characteristic. | 128 |
| Figure 2.119 | $V(2)$ – TRAN analysis. | 128 |
| Figure 2.120 | $V(2)$ – circuit envelope analysis. | 129 |
| Figure 2.121 | $V(2)$ – detail. | 129 |
| Figure 2.122 | $V(2)$ – harmonic balance analysis. | 129 |
| Figure 2.123 | $V(2)$ – harmonic balance analysis (detail). | 130 |
| Figure 3.1 | Crystal resonator. (a) symbol (b) equivalent circuit. | 136 |
| Figure 3.2 | Thin film resonators. (a) FBAR, (b) SMR. | 138 |
| Figure 3.3 | Frequency characteristics of a quartz resonator (I – current through the resonator, U – excitation voltage). | 139 |
| Figure 3.4 | Amplitude-frequency effect of a stack crystal filter with AlN. | 139 |

| | | |
|--------------------|---|-----|
| Figure 3.5 | Linear parametric circuit model for a quartz resonator. | 141 |
| Figure 3.6 | Frequency characteristics of a nonlinear crystal resonator. | 141 |
| Figure 3.7 | Linear parametric circuit model of a resonator. . . | 142 |
| Figure 3.8 | Dependence of the resistance and the reactance on I_1 at different frequencies. | 143 |
| Figure 3.9 | BAW filter. | 146 |
| Figure 3.10 | Controlled source implementation of the first nonlinear circuit model. | 148 |
| Figure 3.11 | Plot of I_a versus frequency for the first model. | 148 |
| Figure 3.12 | Intermodulation products for $V = 1$ V, the first model. | 149 |
| Figure 3.13 | Intermodulation products for $V = 5$ V, the first model. | 149 |
| Figure 3.14 | Plot of I_a versus frequency for the first model with modified capacitor characteristic. . . . | 150 |
| Figure 3.15 | Intermodulation products for the first model with modified capacitor characteristic. | 150 |
| Figure 3.16 | The second nonlinear circuit model. | 151 |
| Figure 3.17 | Implementation with controlled sources of the second nonlinear circuit model. | 151 |
| Figure 3.18 | Plot of I_a versus frequency for the second model. | 152 |
| Figure 3.19 | Intermodulation products for $V = 5$ V, the second model. | 153 |
| Figure 3.20 | Intermodulation products of I_a for the second model with modified inductor characteristic. | 153 |
| Figure 3.21 | Dependence of the series resonance frequency on the incident power. | 157 |
| Figure 3.22 | Connections of two power BAW resonators. . . . | 158 |
| Figure 3.23 | Circuit for the anti-series connection model validation. | 159 |
| Figure 3.24 | Circuit for the anti-parallel connection model validation. | 160 |
| Figure 3.25 | Class D amplifier with a power BAW filter. . . . | 161 |
| Figure 3.26 | Structure of a solidly mounted BAW resonator. . . | 162 |

| | | |
|--------------------|--|-----|
| Figure 3.27 | Mason multi-layer model: (a) physical structure, (b) circuit model. | 163 |
| Figure 3.28 | Part of length Δx of the linear 1D model. | 164 |
| Figure 3.29 | Linear mechanical equivalent circuit. | 165 |
| Figure 3.30 | Linear electrical equivalent circuit. | 165 |
| Figure 3.31 | 1D linear artificial transmission line model with 3 cells. | 166 |
| Figure 3.32 | Amplitude-frequency effect. | 168 |
| Figure 3.33 | Amplitude-frequency effect (detail). | 169 |
| Figure 3.34 | Second harmonic of the reflected power. | 169 |
| Figure 3.35 | T filter with connection wires. | 171 |
| Figure 3.36 | Equivalent circuit of a wired connection. | 171 |
| Figure 3.37 | Behavioral model of $S1$ and $S2$ | 171 |
| Figure 3.38 | Power of the source in $PORT$ 1 so that P_{in} in T filter is 24 dBm. | 172 |
| Figure 3.39 | Comparison between the simulated and extracted data. | 173 |
| Figure 3.40 | T filter transfer characteristic. | 174 |
| Figure 3.41 | $2f$ reflected power at the T filter output. | 174 |

List of Tables

| | | |
|-------------------|---|----|
| Table 2.1 | Simulation results for the voltage multiplier | 23 |
| Table 2.2 | Simulation results for the circuits in Figures 2.2 and 2.3 | 25 |
| Table 2.3 | Simulation results for the circuit in Figure 2.5 | 26 |
| Table 2.4 | Simulation results for the circuit in Figure 2.5 circuit in Figure 2.5 with smaller imposed errors | 28 |
| Table 2.5 | Linear and quadratic interpolation for voltages and currents | 31 |
| Table 2.6 | Simulation results for the ill-conditioned matrix | 34 |
| Table 2.7 | Results obtained using double and long double precision | 36 |
| Table 2.8 | Results obtained for the 1st example | 38 |
| Table 2.9 | Results obtained for the 1st example with smaller imposed errors | 38 |
| Table 2.10 | Results obtained for the 2nd example | 40 |
| Table 2.11 | Results obtained for the 3rd example | 45 |
| Table 2.12 | Results obtained for the 4th example | 46 |
| Table 2.13 | Results obtained for the 5th example | 52 |
| Table 2.14 | Transient analysis results for circuit in Figure 2.34 | 58 |
| Table 2.15 | Results obtained for the AM demodulator with different carrier frequencies | 66 |
| Table 2.16 | Results obtained for in-phase and in-quadrature modulator | 68 |
| Table 2.17 | Results of the envelope following analysis from SPECTRE RF and PAN | 69 |
| Table 2.18 | h_{\min} and H_m influence on the envelope following analysis for a 100 us simulation with PAN | 76 |
| Table 2.19 | $\varepsilon_{r0} = 1e-4$ | 82 |
| Table 2.20 | $\varepsilon_{r0} = 1e-6$ | 82 |
| Table 2.21 | $\varepsilon_{r0} = 1e-2$ | 84 |

| | | |
|-------------------|--|-----|
| Table 2.22 | 1st OC parameters “reitol envlp” = $1e-4$ | 87 |
| Table 2.23 | 1st OC parameters “reitol envlp” = $1e-5$ | 89 |
| Table 2.24 | 1st OC parameters “reitol envlp” = $1e-6$ | 89 |
| Table 2.25 | 2nd OC parameters | 89 |
| Table 2.26 | Steady state of the class C amplifier – SPECTRE RF | 95 |
| Table 2.27 | Steady state of the ne600p mixer – SPECTRE RF | 95 |
| Table 2.28 | Steady state of the class C amplifier – PAN | 96 |
| Table 2.29 | Steady state of the ne600p mixer – PAN | 96 |
| Table 2.30 | Simulation results for the DC commutation source | 100 |
| Table 2.31 | Shooting in the time domain and in the frequency domain – AM demodulator analysis | 115 |
| Table 2.32 | Harmonic selections | 121 |
| Table 3.1 | Coordinates of the resonance points | 146 |
| Table 3.2 | Harmonic components of $I(V)$ for “very weak” nonlinearities | 154 |
| Table 3.3 | Harmonic components of $I(V)$ for “weak” nonlinearities | 154 |
| Table 3.4 | Harmonic components of $I(V)$ for “mild” nonlinearities | 155 |
| Table 3.5 | Harmonic components of $I(V)$ for “strong” nonlinearities | 155 |
| Table 3.6 | Harmonic components of voltage gain of a filter with “mild” nonlinearities | 156 |
| Table 3.7 | PSS analysis results in the frequency domain for the anti-series connection | 160 |
| Table 3.8 | PSS analysis results in the frequency domain for the anti-parallel connection | 160 |
| Table 3.9 | Results obtained for the class D amplifier with a power BAW filter | 161 |
| Table 3.10 | Layers structure of the measured resonator | 167 |
| Table 3.11 | Material parameters | 167 |

List of Abbreviations

| | |
|-------------|---|
| A | Ampere |
| abstol | Best accuracy of currents in SPICE |
| AC | Alternating Current |
| ADS | Advanced Design System |
| AlN | Aluminum Nitride |
| APLAC | Analysis Program for Linear Active Circuits |
| BAW | Bulk Acoustic Wave |
| BE | Backward Euler |
| C | Capacity |
| CdS | Cadmium Sulfide |
| CMOS | Complementary Metal Oxide Semiconductor |
| CPU | Central Processing Unit |
| dBm | Decibel milliwatt |
| DC | Direct Current |
| EER | Relative Energy Error |
| ENVLP | Envelope following method |
| envlteratio | Ratio that multiply the reltol to obtain the relative error for the jump, in SPECTRE RF |
| ereltol | Relative error used by PAN for the jump computation |
| F | Farad |
| f | Frequency |
| FBAR | Thin Film Bulk Acoustic Resonator |
| FE | Forward Euler |
| FORTRAN | Formula Translating System |
| GMRES | Generalized Minimal Residual Method |
| H | The jump used in the envelope following method |
| H | Henry |
| HB | Harmonic Balance |
| Hmax | The maximum jump in the envelope following method |
| Hz | Hertz |
| I | Current |

xxii *List of Abbreviations*

| | |
|------------------|---|
| L_AbsTol | The transient absolute current tolerance in HB analysis of ADS |
| L_RelTol | The transient relative current tolerance in HB analysis of ADS |
| iabstol | Absolute error of currents in SPECTRE RF |
| ITL4 | The maximum number of iterations to adjust the time step in transient analysis from SPICE |
| KrylovLooseIters | The number of iterations allowed in HB analysis of ADS |
| KrylovMaxIters | Maximum number of GMRES iterations in HB analysis of ADS |
| KrylovSS_Tol | Tolerance for the Krylov solver in HB analysis of ADS |
| L | Inductance |
| LTE | Local Truncation Error |
| MAPLE | A symbolic and numeric computing environment developed by Maplesoft |
| MaxOrde | Maximum Order of the intermodulation terms in HB analysis of ADS |
| Order[] | Maximum order of the fundamental in HB analysis of ADS |
| oversample | Increases the number of samples in HB analysis of ADS |
| PAN | Circuit simulator developed by Politecnico di Milano |
| PSS | Periodic Steady State |
| Q | Quality factor |
| R | Resistance |
| reltol | Relative accuracy of V and I in SPICE and SPECTRE RF |
| RF | Radio Frequency |
| SAW | Surface Acoustic Wave |
| SERENADE | Circuit simulator developed by Ansoft |
| SHORE | One of the first versions of PAN program |
| SIP | System In a Package |
| SMR | Solidly Mounted Resonator |
| SoC | System on a Chip |
| SPECTRE RF | SPECTRE with a series of analyses useful for RF circuits |
| SPECTRE | SPICE class circuit simulator |
| SPICE | Simulation Program with Integrated Circuit Emphasis |

| | |
|----------|---|
| T | The period of a signal |
| TMAX | The step to display the results in SPICE |
| TP | Trapezoidal rule |
| trabstol | Absolute error of transient analysis from PAN |
| TRAN | Transient analysis method |
| trreltol | Relative error of transient analysis from PAN |
| V | Voltage/Volt |
| V_AbsTol | The transient absolute voltage tolerance in HB analysis of ADS |
| V_RelTol | The transient relative voltage tolerance in HB analysis of ADS |
| vabstol | Absolute error of voltages in SPECTRE RF |
| W | Watt |
| X | Reactance |
| Z | Impedance |
| ZnO | Zinc Oxide |
| ω | Angular frequency |
| Ω | Ohm |

1

Introduction

1.1 RF Circuits

Wireless transceivers contain baseband and RF circuits. The baseband may be the frequency range of the transmitter input signals or of the receiver output signals. A higher bandwidth of the baseband allows a higher data flow to be processed and transmitted through or received by the communication system. The transmitter RF circuit yields the transmitted signal, modulating the carrier appropriate to the communication channel with the baseband signal. The RF circuit of the receiver extracts the information from the RF signal by converting it to the baseband frequency range [1].

Consider the super-heterodyne receiver shown in Figure 1.1. The filtered antenna signal is amplified by the low noise amplifier (LNA). After that the mixer changes the RF carrier to the intermediate frequency (IF) using the signal of the first local oscillator LO.

Because a receiver has small input signals, its sensitivity is limited by noise. Therefore, one of the starting points in a receiver design is the noise prediction by simulation. The noise components are generated mainly in LNA, and their frequencies are translated similarly to those of the received signal producing the so-called cyclostationary noise [1]. This kind of noise cannot be computed with customary time domain simulators as SPICE.

Transmitters must produce a certain amount of power in a prescribed frequency band, while receivers must recover weak signals in the same frequency range. Both signal transmission and reception are intended to be made using as little amount of power as possible. The useful received signal is forbidden to interfere with signals in the adjacent communication channels.

A transmitter and a receiver using the same antenna form a transceiver. This kind of device is now widely used in the modern communications systems, for example, for the mobile phone and for the base station. As a receiver

2 Introduction

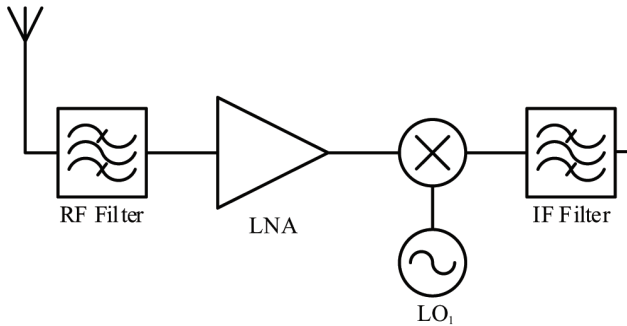


Figure 1.1 RF front-end of a coherent super-heterodyne receiver [1].

must be sensitive to the desired small signal, other signals as those from adjacent channels or intermodulation products resulting from the interference with other signals must not reach the receiver input. To this end, the antenna is connected to the transmitter and to the receiver via the duplexer filter (Figure 1.2).

A new technology that emerged in the last years due to its low price and to its compatibility with CMOS circuitry is the bulk acoustic wave (BAW) filters built with AlN. These filters are working very well in the RF range of frequencies and can be merged with CMOS circuits to build systems on a chip (SoC) and systems in a package (SiP) [2]. In order to reach the nearest base station, a mobile phone transmits a power up to 5 W, which passes through the duplexer filter. While the behavior of BAW filters is linear for the small signal operation, at this power level, some nonlinear effects appear as: the amplitude-frequency effect (the shift of the filter resonance

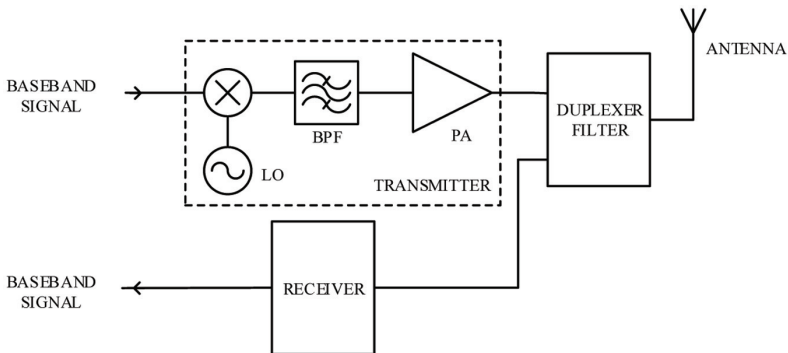


Figure 1.2 Transceiver.

frequencies depending on the transmitter power) and the occurrence of some intermodulation products between transmitted and received signals from adjacent channels [3]. Building of behavioral and physical models that reproduce all these effects remains an open problem [4]. Moreover, the customary time domain simulation (doing the transient analysis for a number of signal periods so that all transients disappear) becomes unpractical due to the fact that the signal period (the least common multiple of the intermodulation component periods) is very large. It follows that more efficient time domain analysis methods of finding the periodic steady state of nonlinear circuits must be used for the RF front-end analysis. Filtering is very important because the large interfering signals can saturate the receiver low noise amplifier, which, in this case, does not sense the small signal in the desired communication channel [1].

The main applications of the RF circuits are wireless communications devices, as those included in a mobile telephony system. In order to ensure the wireless propagation between a mobile phone and a base station, the communication channel is centered at a frequency that is placed between 900 MHz and 2.5 GHz. The channel frequency band is very narrow (10–30 KHz), so that very selective circuits are needed to avoid interferences between the adjacent channels. As some blocks like mixers and demodulators are essentially nonlinear, the computation of the periodic steady state can be done in the time domain by the transient analysis. The high frequency carrier forces a very small time step, while the low frequency modulating signal imposes a very long signal period, and the transient analysis has a poor efficiency. Some special methods such as shooting, envelope following, or two-time variable analysis have been proposed for the fast computation of the periodic steady state in RF circuits.

Modeling of certain passive RF components proves to be a difficult task due to various reasons. The transmission lines being modeled as distributed circuit elements, their lumped circuit models have an intricate structure. The accurate modeling of spiral inductors, connection wires, substrates, and packages, which can influence significantly the RF circuit behavior, is a difficult task.

Sometimes, neglecting certain parasitic elements, which at a first glance seem unimportant, the model of a RF circuit may have an uncustomary behavior or, even worse, no solution. In these cases, the transient analysis may produce strange responses or no solution at all. To avoid this kind of surprises, a designer must build a circuit model having a unique steady state solution which is usually of technical interest. This model belongs to the class of the circuits with customary behavior. On the other hand, industrial applications

4 Introduction

of circuits with uncustomary behavior have been developed in the areas of communications with chaotic carrier [5] and cellular neural networks for image processing [6]. The next paragraph describes the circuits with customary and uncustomary behavior and their properties.

The algorithms used by the commercial time domain simulators as SPICE and SPECTRE fail sometimes to converge. Assuming tacitly that the circuit model has a customary behavior (that in general is not true), some very useful procedures to avoid convergence problems in DC, AC, and transient analyses are described in detail in [7].

1.2 Customary and Uncustomary Behavior of Non-Autonomous Circuits

1.2.1 Definitions and Properties [9–11]

A *non-autonomous* circuit contains at least one independent source whose parameter ($e(t)$ for a voltage source, or $i_s(t)$ for a current source), is a function of time [8, 9]. If the circuit does not contain such type of sources, it is considered as *autonomous*. A natural expectation may be that the response of a non-autonomous circuit to a periodic excitation becomes periodic when the time passed from the connection of the independent sources is large enough. The circuits that have this property prove to have other two remarkable properties, too: spectrum preservation and the exponential decay of the transient components. These three properties characterize *a circuit with a customary behavior* [10].

The rigorous definition of the customary behavior is made using the steady-state response. Consider a nonlinear circuit driven by independent sources of period T , having the state vector $z = (q_C, \varphi_L)$, where q_C contains the capacitor charges and φ_L contains the inductor magnetic fluxes. Suppose that this circuit has the state equations in the normal form $\dot{z} = f(z, t)$. The *steady state response* of this circuit is $z_p(t) = \lim_{t \rightarrow \infty} z(t)$. Obviously, $z(t)$ can be computed only by knowing the initial state $z(0)$ of the circuit. At least in theory, there is a possibility to obtain two different steady-state responses $z_{p1}(t)$ (starting from the initial state $z_1(0)$) and $z_{p2}(t)$ (starting from the initial state $z_2(0)$). Examples with this property can be built [10].

It is considered that a circuit has a unique steady state solution if any pair of solutions $z_1(t)$ and $z_2(t)$ corresponding to the initial states $z_1(0)$ and $z_2(0)$ satisfies the relationship $\lim_{t \rightarrow \infty} \|z_1(t) - z_2(t)\| = 0$, where $\|\cdot\|$ is the Euclidean norm.

Property 1

Obviously, a circuit driven by periodic independent sources with period T has a unique periodic response of the excitation period if it has a unique steady state response $z_p(t)$ with period T .

The magnitude $z_t(t) = z(t) - z_p(t)$ is the transient component of the circuit response. For a circuit that has the property 1, $\lim_{t \rightarrow \infty} z_t(t) = 0$. The following property refers to how $z_t(t)$ tends to zero.

Property 2

A circuit has an exponential decay of the transient components if there are positive real numbers $\tau_{\min}, \tau_{\max}, k_{\min}, k_{\max}$, so that the “distance” between two solutions $z_1(t)$ and $z_2(t)$ corresponding to the initial states $z_1(0)$ and $z_2(0)$ satisfies the relations:

$$k_{\min} \|z_1(0) - z_2(0)\| e^{-\frac{t}{\tau_{\min}}} < \|z_1(t) - z_2(t)\| < k_{\max} \|z_1(0) - z_2(0)\| e^{-\frac{t}{\tau_{\max}}}$$

In other words, for a circuit with property 2, as $t \rightarrow \infty$, the “distance” between the solutions $z_1(t)$ and $z_2(t)$ diminishes being bordered by the “distance” between the initial states weighted with $k_{\min} e^{-\frac{t}{\tau_{\min}}}$ and $k_{\max} e^{-\frac{t}{\tau_{\max}}}$ where τ_{\min} and τ_{\max} are the minimum and the maximum “time constants” of the circuit. Note that there is no algorithm to compute, without knowing the circuit response, the values $\tau_{\min}, \tau_{\max}, k_{\min}, k_{\max}$ for a nonlinear circuit with an arbitrary structure.

The *spectral combination S_s of the sources*, in a circuit driven with DC and sinusoidal sources of angular frequencies $\omega_k (k = 1, 2, \dots)$ only, is the set of angular frequencies $\omega = \sum_k n_k \omega_k$, where n_k are arbitrary integers.

Property 3

A circuit preserves the spectral combination if the spectral combination S_{zp} corresponding to the steady state solution is included in the spectral combination S_s of the sources.

For example, if a circuit is driven by two sinusoidal sources having the angular frequencies ω_1 and ω_2 , the spectral combination S_s of the sources is $n_1 \omega_1 + n_2 \omega_2, n_1, n_2 \in I$, i.e., $\omega_1 + \omega_2, \omega_1 - \omega_2, -\omega_1 + \omega_2, \omega_1 + 2\omega_2, \omega_1 - 2\omega_2, \dots$. If the steady state response is periodic and has only harmonic components that are included in S_s , then this circuit preserves the spectral combination.

1.2.2 Customary and Uncustomary Behavior of Linear and Nonlinear Circuits

An exponentially stable linear circuit, having all natural frequencies s_k with $\text{Re } s_k < 0$, has a customary behavior. Consider such a circuit with a non-zero initial state and being driven by a periodic excitation. Indeed, the response of this circuit can be written as $z(t) = z_0(t) + z_e(t)$ where $z_0(t)$ is the response to null excitation, which depends on the initial state $z(0)$, and $z_e(t)$ is the response to the null initial state, which depends on the excitation [8, 9].

It is known that $z_0(t) = \sum p_k(t)e^{s_k t}$, where s_k are the natural frequencies of the circuit with $\text{Re } s_k < 0$ and $p_k(t)$ are polynomials of t of degree $q = \{\text{the multiplicity order of } s_k\} - 1$. It follows that $\lim_{t \rightarrow \infty} z_0(t) = 0$ (according to Property 2) and $z_p(t) = \lim_{t \rightarrow \infty} z_e(t)$. If $z_e(t)$ is computed with the Laplace transform, $z_e(t) = z_{et}(t) + z_{ep}(t)$ is obtained, where $z_{et}(t)$ is the transient component with $\lim_{t \rightarrow \infty} z_{et}(t) = 0$ and $z_{ep}(t)$ is the steady state response to the periodic excitation. In this case, $z_{ep}(t)$ can be calculated separately for each harmonic component of the excitation, so $z_p(t)$ is periodic of the excitation period (Property 1) and has the same harmonic components as the excitation (Property 3) [8, 9].

There are sufficient conditions that define classes of nonlinear circuits with customary behavior. To formulate them, it is necessary to define the passive characteristic and the strictly local passive characteristic of a circuit element. This characteristic can be $f(v, i) = 0$ for a resistor, $f(\varphi, i) = 0$ for an inductor, or $f(q, v) = 0$ for a capacitor.

The *passive characteristic* $f(x, y) = 0$ is a curve in the xy plane for which $x \cdot y \geq 0$ (the curve passes only through the first and third quadrants).

The *strictly local passive characteristic* $f(x, y) = 0$ has the following property: for any two points with the coordinates (x_0, y_0) , (x_1, y_1) on this characteristic, the magnitudes $\Delta x = x_1 - x_0$ and $\Delta y = y_1 - y_0$ satisfy the relation $\Delta x \cdot \Delta y > 0$. This means that a strictly local passive characteristic has always a strictly positive slope $\frac{\Delta y}{\Delta x}$, so it is *strictly increasing*.

Consider a linear resistive multiport without independent sources, with the voltage ports (a) and the current ports (b) (Figure 1.3).

Considering the port voltages as $v = (v_a, v_b)$ and the port currents as $i = (i_a, i_b)$, this multiport has the hybrid representation [9, 10]:

$$\begin{bmatrix} i_a \\ v_b \end{bmatrix} = \begin{bmatrix} H_{aa} & H_{ab} \\ H_{ba} & H_{bb} \end{bmatrix} \begin{bmatrix} v_a \\ i_b \end{bmatrix}, \text{ where } \begin{bmatrix} H_{aa} & H_{ab} \\ H_{ba} & H_{bb} \end{bmatrix} = \begin{bmatrix} \frac{\partial h_a}{\partial v_a} & \frac{\partial h_a}{\partial i_b} \\ \frac{\partial h_b}{\partial v_a} & \frac{\partial h_b}{\partial i_b} \end{bmatrix}.$$

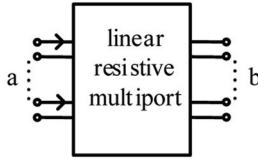


Figure 1.3 Linear resistive multiport.

This multiport resistor is reciprocal if H_{aa} and H_{bb} are symmetrical and $H_{ab} = -H_{ba}^t$. This definition can be generalized for a nonlinear resistive multiport without independent sources described by the equations: $i_a = h_a(v_a, i_b)$ and $v_b = h_b(v_a, i_b)$ considering the incremental (Jacobian) matrix instead of the above H matrix. A dipolar resistor is always reciprocal.

The reciprocity can be similarly defined for the inductive or the capacitive multiports, also. A voltage controlled nonlinear capacitive multiport having the constitutive equation $q = \hat{q}(v)$ is reciprocal if the dynamic capacities matrix (the Jacobian $\frac{\partial \hat{q}}{\partial v}$ of \hat{q}) is symmetrical. A current controlled nonlinear inductive multiport having the constitutive equation $\varphi = \hat{\varphi}(i)$ is reciprocal if the dynamic inductances matrix (the Jacobian of $\hat{\varphi}$) is symmetrical. A dipolar capacitor or a dipolar inductor is always reciprocal.

The sufficient conditions for a customary behavior are as follows [10].

Circuits with Linear Dynamic Elements

A circuit with linear dynamic elements has a customary behavior if the following conditions are fulfilled:

1. There is no loop made of capacitors, inductors, and/or voltage sources, only.
2. There is no cut-set made of capacitors, inductors, and/or current sources, only.
3. All resistors are strictly local passive.
4. The independent sources parameters $(e_k(t), i_{sk}(t))$ are periodic functions of the C^1 class.

RC (RL) Circuits

A RC (RL) circuit has a customary behavior if the following conditions are met:

1. There is no loop (cut-set) made of capacitors (inductors) and/or voltage (current) sources, only.
2. All resistors are linear, passive, and reciprocal.

3. The capacitors (inductors) have strictly increasing characteristics of the C^1 class.
4. The independent sources parameters $(e_k(t), i_{sk}(t))$ are periodic functions of the C^1 class.

RLC Nonlinear Circuits with “Small Signal” Operation

Consider a nonlinear *RLC* circuit with independent sources having DC components and time variable components with period T . Such a circuit has the properties 1 and 3 for any values of the sources DC components if the following conditions are met:

1. There is no loop (cut-set) made of capacitors, inductors, and voltage (current) sources, only.
2. The dynamic elements have strictly local passive characteristics.
3. The resistors have strictly local passive characteristics of C^1 class.
4. The constitutive relations of the capacitors ($q = \hat{q}(v)$ or $v = \hat{v}(q)$) and inductors ($\varphi = \hat{\varphi}(i)$ or $i = \hat{i}(\varphi)$) are of C^1 class.
5. The sources periodic components have “small enough” amplitudes.

Although the necessity of these conditions for the customary behavior is not proved, some examples have been built [9–11], showing that if only one condition is not fulfilled, the circuit has an uncustomary behavior.

The *uncustomary behavior* of the non-autonomous circuits with T – periodic excitation can be characterized by the following:

- the periodic steady state contains sub-harmonics ($f/2, f/3, f/4, \dots$ frequency components, where $f = 1/T$)
- non-periodic responses, as the chaotic ones,
- T' – periodic responses to a T – periodic excitation ($T' \neq T$), T' depending on the circuit initial state.

1.2.3 Operating Modes

An operating mode is defined by certain significant properties of the circuit response [8–11]. These properties are significant both in terms of circuit theory and in terms of technical applications.

Suppose that at $t = t_0$ all independent sources are connected to the circuit. The transient behavior (transient operating mode) of this circuit consists in all circuit responses computed for any $t \geq t_0$. If these responses are considered for $t \rightarrow \infty$, the operating mode of this circuit is the steady state.

The RF circuits with periodic excitation have a special importance. The steady state of a circuit with customary behavior for which the independent sources have DC and T –periodic components is the T –periodic steady state or the non-sinusoidal steady state.

An exponentially stable linear circuit driven by the above sources will have only T –periodic responses in the steady state, so it will operate in the T –periodic steady state. Moreover, any response will have only harmonic components of the excitations, so harmonic components that are not present in the excitations are not generated. The AC circuit is the simplest case of this kind: in the steady state all voltages and currents are sinusoidal having the unique excitation period T and $f = 1/T$ is the AC frequency.

In a customary behavior nonlinear circuit driven by the above independent sources, harmonic components that do not exist in these independent sources can be generated, but their frequencies belong to the spectral combination of these sources. The periodic steady state behavior of the excitation period is of outstanding importance in the power systems and the communications circuits.

The steady state of a circuit with uncustomary behavior driven by independent sources having T –periodic parameters can be the following:

- a periodic steady state of period T ;
- a behavior in which the responses are periodically but the periods are equal to a multiple of the excitation period (sub-harmonic operating mode);
- a behavior in which the responses are not periodically (chaotic operating mode).

A good illustration of these operating modes, using the same circuit with sinusoidal excitations of the same frequencies and various amplitudes, can be found in [12, 13].

The sub-harmonic operating mode and the chaotic operating mode are not commonly used in practice. In the last years, communications circuits [5] and image processing circuits [6] in the chaotic operating mode have been proposed.

1.3 Existence and Uniqueness of Dynamic Circuits Solutions

The existence and uniqueness of the dynamic circuit solutions is linked to the existence of the state equations in the normal form. Consider a dynamic circuit

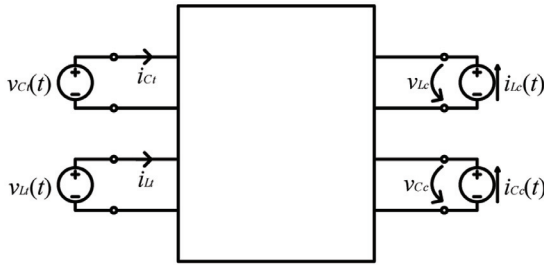


Figure 1.4 Resistive multiport for writing the state equations in normal form.

as a resistive multiport with the dynamic elements connected to its ports. The normal tree, used to determine the independent state variables, contains all voltage sources and as many capacitors as possible. It follows that the normal co-tree (the complementary branch set of the normal tree) contains all current sources and as many inductors as possible. For a linear circuit, the independent state variables are tree capacitor voltages and co-tree inductor currents, while the dependent state variables (excess state variables) are co-tree capacitor voltages and tree inductor currents.

By the substitution theorem, the tree capacitors and inductors are replaced with voltage sources and, the co-tree capacitors and inductors are replaced with current sources. In this way, the resulting circuit is given in Figure 1.4, where, for simplicity, only one source for each category of elements has been represented (tree capacitors, tree inductors, co-tree inductors, co-tree capacitors). The first voltage and current index are C for capacitors and L for inductors. The second index of these magnitudes is t for tree and c for co-tree.

For a linear circuit, we denote:

$$x = \begin{bmatrix} v_{Ct} \\ i_{Lc} \end{bmatrix}, \quad x^* = \begin{bmatrix} v_{Cc} \\ i_{Lt} \end{bmatrix}, \quad y = \begin{bmatrix} i_{Ct} \\ v_{Lc} \end{bmatrix}, \quad y^* = \begin{bmatrix} i_{Cc} \\ v_{Lt} \end{bmatrix}.$$

Where x are the independent state variables, x^* are the excess state variables, v are port voltages, and i are port currents.

Linear Circuits

The independent state variables are tree capacitor voltages v_{Ct} and co-tree inductor currents i_{Lc} , and the excess variables are co-tree capacitor voltages v_{Cc} and tree inductor currents i_{Lt} . The operating equations of the dynamic elements are $y = -\Delta \dot{x}$ and $y^* = -\Delta^* \dot{x}^*$, where $\Delta = \text{diag} [\textit{tree capacities}, \textit{co-tree inductances}]$ and $\Delta^* = \text{diag} [\textit{co-tree capacities}, \textit{tree inductances}]$. In this case, the dynamic elements parameters are constant and have non-zero

values, so Δ^{-1} and Δ^{*-1} exist. If the resistive multiport has one and only one solution for any parameter values of the independent sources connected to the ports, then the superposition theorem gives $y = k_0x + k_1\mu_s + k_2y^*$, where μ_s contains parameters of the independent sources placed inside the multiport in Figure 1.4, and k_0, k_1, k_2 are matrices with constant entries. The excess state variables can be written as $x^* = k_3x + k_4\mu_s$, according to Kirchhoff's laws (k_3 and k_4 are matrices with constant entries). Simple algebra gives the state equation in normal form $\dot{x} = -\Delta^{-1}y = -\Delta^{-1}[k_0x + k_1\mu_s - k_2(\Delta^*k_3 + \Delta^*k_4\mu_s)]$ or $\dot{x} = Ax + B\mu_s + B^*\dot{\mu}_s$ which can be written as $\dot{x} = f(x, t)$.

If the equation $\dot{x} = f(x, t)$ exists, then the mathematical literature shows that: if f is a Lipschitz function (for any x_1 and x_2 and any t , $\|f(x_1, t) - f(x_2, t)\| \leq k \|x_1 - x_2\|$, where $k > 0$ and $\|\cdot\|$ is the Euclidean norm) and if the function $f(0, t)$ is uniformly bounded, then the state equation has a unique solution for any initial state $x_0 = x(t_0)$ [8–10].

It follows that the existence of the normal form of the state equation is related to the following:

- the existence and uniqueness of the resistive multiport solution for any values of the sources parameters (that replace the dynamic elements) connected to the ports,
- the existence of Δ^{-1} and Δ^{*-1} , which can be proved because Δ and Δ^* are diagonal matrices with non zero entries.

It can be shown that in this case, $f(x, t)$ is a Lipschitz function $\|f(x_1, t) - f(x_2, t)\| = \|A(x_1 - x_2)\|$ because there is always a constant k so that $\|A(x_1 - x_2)\| \leq k \|x_1 - x_2\|$. If $f(0, t)$ is uniformly bounded, then the circuit has a unique solution for any initial state $x(t_0)$ [9, 10].

Nonlinear Circuits

If the nonlinear resistive multiport in Figure 1.4 has only one solution for any values of the independent sources parameters connected at its ports, then we can write $y = g(x, y^*, \mu_s)$, where all magnitudes have the same meaning as in the case of a linear circuit presented above.

For the nonlinear dynamic elements, we consider two cases only:

1st Case

- all capacitors are voltage controlled having the operation equations $i_k = C_k \dot{v}_k$, where $C_k = \frac{dq_k}{dv_k} \neq 0$ in any point of the characteristic,
- all inductors are current controlled having the operation equations $v_k = L_k \dot{i}_k$, with $L_k = \frac{d\hat{\varphi}_k}{di_k} \neq 0$ in any point of the characteristic.

12 Introduction

The independent state variables and the excess ones are the same as those of a linear circuit. It can be written $y = -\Delta\dot{x}$ and $y^* = -\Delta^*\dot{x}^*$ where $\Delta = \text{diag} [\textit{tree dynamic capacities, co-tree dynamic inductances}]$ and $\Delta^* = \text{diag} [\textit{co-tree dynamic capacities, tree dynamic inductances}]$.

The state equation follows:

$$\dot{x} = -\Delta^{-1}y = -\Delta^{-1}[g(x, y^*, \mu_s)] = \Delta^{-1}f(x, \mu_s).$$

2nd Case

- all capacitors are charge controlled,
- all inductors are flux controlled.

The state variables are the capacitors charges and the inductors fluxes. With the notation $\bar{x} = [q_{Ca}, \varphi_{Lc}]$, $\bar{x}^* = [q_{Cc}, \varphi_{La}]$, the dynamic elements characteristics are given by $x = g_1(\bar{x})$ and $x^* = g_2(\bar{x}^*)$, and because $y = \dot{\bar{x}}$ and $y^* = \dot{\bar{x}}^*$, the state equations in the normal form are $\dot{\bar{x}} = h(\bar{x}, \mu_s)$. The existence of Δ^{-1} and Δ^{*-1} matrices is obvious because all values of the dynamic capacities and inductances for any values of the control parameters of these elements are non-zero.

The existence and uniqueness conditions are formulated in the case of the circuits without excess state variables, only. When there are excess state variables, the problem is handled in a similar way. If the characteristics of the dynamic elements are strictly increasing and differentiable, a non zero dynamic parameter (C_d or L_d) exists in any operation point, so Δ^{-1} and Δ^{*-1} exist. If the resistors are strictly increasing and the resistive multiport has no loops made of voltage sources only, and cut-sets made of current sources only, then this resistive multiport has a unique solution. It follows that there are state equations in the normal form $\dot{x} = f(x, t)$. In order for the dynamic circuit to have a unique solution for any initial state $x(t_0)$, it is sufficient that f be a Lipschitz function.

So we have justified:

Theorem I

A circuit without excess state variables having the following:

- dynamic elements with strictly increasing and differentiable characteristics,
- resistive elements with strictly increasing characteristics so that $\dot{x} = f(x, t)$, where f is a Lipschitz function, has one and only one solution for any initial state $x(t_0)$.

But the conditions to be fulfilled by f in order to be a Lipschitz function are restrictive enough. For example, if $f(x, t) = x^2 + s(t)$ then $\|f(x_1, t) - f(x_2, t)\| = \|x_1^2 - x_2^2\|$ and there is no k so that $\|x_1^2 - x_2^2\| \leq k \|x_1 - x_2\|$ for any pair x_1, x_2 . It follows that the resistors with polynomial nonlinearities may lead to non-Lipschitz functions f .

The existence and uniqueness conditions for the circuit solutions are usually formulated in terms of elements constitutive equations and their interconnection properties. This feature allows a simple check of those conditions. Unfortunately, the property “ f is a Lipschitz function” cannot be deduced from certain properties of the circuit elements.

It can be proved that a circuit with dynamic and resistive elements having strictly increasing characteristics has a unique solution, although f is not a Lipschitz function.

Theorem II

Consider a circuit with dynamic elements having strictly increasing and differentiable characteristics. If all resistors are strictly increasing and the resistive multiport has one and only one solution, then the dynamic circuit has a one and only one solution for any initial state $x(t_0)$ [10].

It is known that the resistors with non-monotonic characteristics facilitate the appearance of multiple solutions of the resistive circuit containing them. The presence of these resistors can lead to the non-existence of the state equation in normal form.

Consider the first order circuit in Figure 1.5.a, where the nonlinear resistor has the characteristic $i = g(v)$ in Figure 1.5.b. Because $v = -L\dot{i}$, it follows

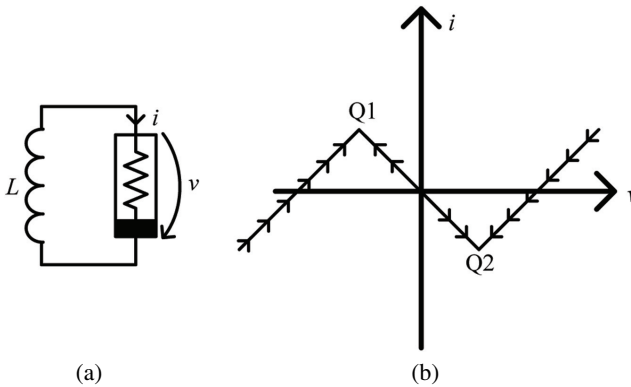


Figure 1.5 (a) First order circuit; (b) Characteristic of the nonlinear resistor.

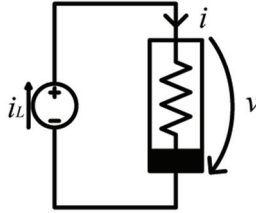


Figure 1.6 Inductor in Figure 1.5 is replaced with a current source.

that for $v > 0$ i decreases and for $v < 0$ i increases, so the possible dynamic routes are shown in Figure 1.5.b.

This circuit has no solution because starting from any initial state an impasse point Q_1 or Q_2 (from which the solution cannot evolve) is reached. This circuit does not have a state equation in the normal form because the function g^{-1} (where $v = g^{-1}(i)$) does not exist, so the state equation in the form $\dot{i} = -\frac{g^{-1}(i)}{L}$ cannot be written.

Indeed, if the inductor is replaced with a current source, the resistive multiport does not have a unique solution for any i because the nonlinear resistor is not current controlled for $i \in (-\infty, +\infty)$.

Consider a *RLC* circuit in which the resistive part forms a multiport to whose ports the dynamic elements are connected. The following theorem is stated and proved in [10].

Theorem III

If in a *RLC* circuit, the following conditions are fulfilled:

- i. no loops (cut-sets), made of capacitors (inductors) and/or independent voltage (current) sources exist,
- ii. any voltage-controlled resistor that is not current-controlled also, is connected in parallel with a capacitor,
- iii. any current-controlled resistor that is not voltage-controlled also, is connected in series with an inductor,
- iv. any resistor that does not meet the conditions *ii* and *iii* is strictly monotone, and its characteristic slope $\frac{dv}{di}$ verifies the relation $0 < \mu_1 < \frac{dv}{di} < \mu_2 < \infty$,
- v. any capacitor has a charge controlled characteristic,
- vi. any inductor has a flux controlled characteristic,

then the state equation $\dot{x} = -f(g(\bar{x}), \mu)$ of the circuit exists, and the circuit has at least one solution.

Remarks

In the previous example, if a capacitor is inserted in parallel with the nonlinear resistor, then the resistive multiport has one and only one solution for any values of i_L and v_C (Figure 1.7).

A circuit made of a linear capacitor in parallel with a nonlinear resistor that is not voltage controlled is treated similarly (Figure 1.8).

In this case, an inductor is added in series with the resistor and the resistive multiport has one and only one solution for any v_C and i_L (Figure 1.9).

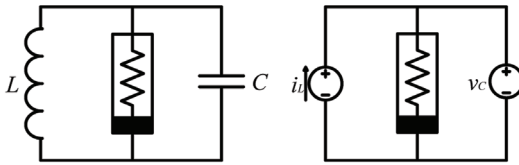


Figure 1.7 Capacitor inserted in parallel with the nonlinear resistor in the circuit in Figure 1.5.

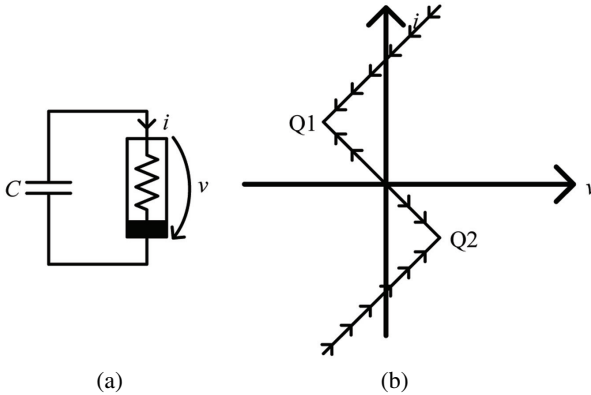


Figure 1.8 (a) First order circuit; (b) Characteristic of the nonlinear resistor.

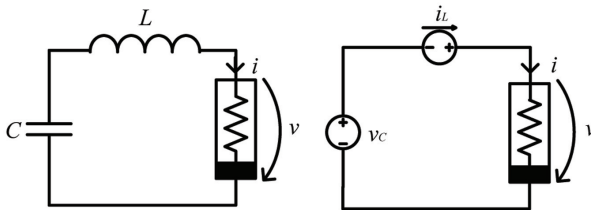


Figure 1.9 Inductor added in series with the resistor in the circuit in Figure 1.8.

References

- [1] Kundert, K. (1999). Introduction to RF simulation and its application. *J. Solid-State Circuits* 34 (9), September, revised version, www.designers-guide.org/Analysis/rf-sim.pdf
- [2] Lakin, K. M. (2005). Thin film resonator technologies. *IEEE Trans. UFFC* 52 (5), 707–716, May.
- [3] Ketcham, R. S., Kline, G. R., and Lakin, K. M. (1988). Performance of TFR filters under elevated power conditions. 42nd Annual Frequency Control Symposium.
- [4] Rocas, E., Collado, C., Orloff, N. D., Mateu, J., Padilla, A., O’Callaghan, J. M., and Booth, J. C. (2011). Passive intermodulation due to self-heating in printed transmission lines. *IEEE Trans. Microw. Theory Tech.* 59 (2), 311–322, Feb.
- [5] Vlădeanu, C., Paleologu, C., and Marghescu, I. (2008). Multilevel chaos-based DS-CDMA system with improved performance. *Rev. Roum. Sci. Techn.—Électrotechn. et Énerg.* 53 (3), 319–328, Bucarest.
- [6] Hanef, H., Venetianer, P. L., Nossek, J. A., Roska, T., and Chua, L. O. (1994) Some Examples of Preprocessing Analog Images Discrete-Time Cellular Neurd Networks. *Third IEEE International Workshop on Cellular Networks and their Applications*, Rome, Italy, December 18–21.
- [7] Kundert, K. S. (1995). The designer’s guide to SPICE and SPECTRE. Kluwer Academic Press.
- [8] Chua, L. O., Desoer, C. A., and Kuh, E. S. (1987). Linear and nonlinear circuits. McGrawHill, New York.
- [9] Constantinescu, F., and Nitescu, M. Fundamentals of Electrical Engineering, Part I-Circuit Theory (in Romanian), <http://ferrari.lce.pub.ro/studenti/>
- [10] Chua, L. O., Green, D. N. (1976). A qualitative analysis of the behavior of dynamic nonlinear networks: steady-state solutions of non-autonomous networks. *IEEE Trans. Circuits Systems* CAS-23 (9), 531–550.
- [11] Hasler, M., Neiryneck, P. (1985). Circuits non lineaires, Presses Polytechniques Romandes, Lausanne, Suisse.
- [12] Azouz, A., Duhr, R., and Hasler, M. (1994). Bifurcation diagram for a piecewise-linear circuit. *IEEE Trans. Circuits Syst.* CAS-31 (6), 587–588, June.
- [13] Constantinescu, F., Gheorghe, A. G., Nitescu, M., Marin, C. V., and Ionescu, A. (2011). Simulation of Electrical Circuits—Laboratory Works (in Romanian), <http://ferrari.lce.pub.ro/studenti>.

2

Analysis of RF Circuits

2.1 Time Domain Analysis

2.1.1 Transient Analysis

The transient analysis computes the transient response of the circuit on a certain time interval [1]. In any simulator you can specify the initial conditions for this analysis. If no initial conditions are specified, the ones corresponding to the DC operating point are considered; these values are determined by a DC analysis.

The circuit simulator formulates nonlinear equations, which are solved numerically. The most used numerical integration algorithms are: backward Euler method, trapezoidal rule and Gear methods. All circuit simulators contain automatic techniques to choose the integration step, based on some errors calculation. A critical analysis of the time step choice methods, together with case studies, is presented in the following.

A major disadvantage of time domain analysis of the RF circuits is that the periodic steady state solution, which is often of interest, requires sweeping of a large number of the excitation periods and consequently a long computation time.

2.1.1.1 Time step choice algorithm of SPICE and SPECTRE RF

The variable order integration algorithms used by SPICE-like simulators, select for each time step the order for which the time step is maximum. A higher order method has a smaller local truncation error, allowing greater integration steps, but may produce unstable solutions for some problems, due to the narrow stability region in the $h\lambda$ plan (h – the time step, λ – test equation eigenvalue) [1].

Consider the integration algorithm based on the trapezoidal rule which chooses the time step according to the local truncation error LTE [2]. This algorithm is used in most SPICE-like programs. At every transient analysis

step, the maximum allowed truncation error is computed for each state variable of the circuit and for its derivative with respect to time. For example the maximum error for the current through a capacitor or for an inductor voltage is estimated as the worst case scenario corresponding to a relative error ε_r and an absolute error ε_a imposed by the user:

$$\varepsilon_{\dot{x}} = \varepsilon_r \cdot \max\left(\left|\dot{x}_{n+1}\right|, \left|\dot{x}_n\right|\right) + \varepsilon_a \quad (2.1)$$

where \dot{x}_{n+1} is the current through the capacitor or the inductor voltage.

SPICE defines a similar error ε_x for charge or magnetic flux using the user defined errors ε_r and ε_a .

For each step of the analysis, the allowed truncation error is given by the greater one of these two errors:

$$E = \max(\varepsilon_x, \varepsilon_{\dot{x}}) \quad (2.2)$$

In the case of the trapezoidal rule (used by SPICE-like simulators when the user does not indicate another method) the truncation errors can be approximated as follows:

$$\varepsilon_x = -\frac{h^3}{12} \frac{d^3x}{dt^3}(\xi) \quad \text{and} \quad \varepsilon_{\dot{x}} = \frac{h^2}{6} \frac{d^3x}{dt^3}(\xi)$$

where $\frac{d^3x}{dt^3}$ is considered at a time value ξ in the interval $[t_n, t_{n+1}]$.

Taking into account that usually the time step, in seconds, is a number less than unity, from (2.2) it follows that $\varepsilon_{\dot{x}} = \max(\varepsilon_x, \varepsilon_{\dot{x}})$. Therefore, if you calculate E using (2.1) and (2.2) based on the values set by the user for ε_r and ε_a , at every step of the transient analysis, the maximum time step h_{n+1} can be computed:

$$h_{n+1} \leq \sqrt{\frac{6E}{\left|\frac{d^3x}{dt^3}(\xi)\right|}} \quad (2.3)$$

In (2.3) the time ξ is not known and the third derivative $\frac{d^3x}{dt^3}$ is approximated by [1]:

$$\frac{d^kx}{dt^k}(\xi) \cong k! \cdot DD_k \quad (2.4)$$

where DD_k is the k -th order finite difference. Finite difference of the k -th order is defined by the recursive expression:

$$DD_k = \frac{DD_{k-1}(t_{n+1}) - DD_{k-1}(t_n)}{\sum_{i=1}^k h_{n+1-i}} \quad (2.5)$$

where $DD_0(t_{n+1}) = x_{n+1}$, $DD_0(t_n) = x_n$, and,

$$\frac{d^3x}{dt^3}(\xi) = 6 \frac{\frac{x_{n+1} - x_n}{h_n} - \frac{x_n - x_{n-1}}{h_{n-1}}}{h_n + h_{n-1}} - \frac{\frac{x_n - x_{n-1}}{h_{n-1}} - \frac{x_{n-1} - x_{n-2}}{h_{n-2}}}{h_{n-1} + h_{n-2}}$$

The Expression (2.4) had been deduced assuming that the solution $x(t)$ is a third degree polynomial for which the third time derivative is a constant.

The integration step choice algorithm can be outlined as follows:

```

 $t_{n+1} = t_n + h_n$ 
solve for  $t_{n+1}$ 
if  $iter\_num < ITLA$ 
compute  $h_{n+1} = f(LTE)$ 
    if  $h_{n+1} < 0.9 \cdot h_n$  then
        reject  $t_{n+1}$ 
         $h_n = h_{n+1}$ 
        compute for the new  $t_{n+1}$ 
    else
        accept  $t_{n+1}$ 
         $h_{n+1} = \min(h_{n+1}, 2 \cdot h_n, TMAX)$ 
        continue with  $t_{n+2}$ 
else
    reject  $t_{n+1}$ 
     $h_n = h_n/8$ 
    reduce integration order to 1 (BE)
    if  $(h_n > h_{min})$  then
        compute for the new  $t_{n+1}$ 
    else
        print TIME STEP TOO SMALL; analysis is aborted.

```

where $f(LTE)$ is given by (2.3), $ITLA$ is the maximum number of iterations to adjust the time step, $TMAX$ is the step to display the results and h_{min} is the minimum allowed step [1]. The values $0.9h_n$, $h_n/8$, $2h_n$ resulted from numerical experiments.

At each time step, SPICE accepts or rejects the solution according to the evaluation of LTE for all state variables and their derivatives with respect to time. As will be explained in the next paragraph, this procedure does not take into account the structure of the circuit.

2.1.1.2 Brambilla-D'Amore time step choice algorithm

2.1.1.2.1 Computation of energy errors

PAN [3] uses a different strategy for choosing the time step, based on some energy errors calculation, which is described below. The circuit shown in Figure 2.1 consists of the nonlinear resistive one-port N_0 and the charge controlled nonlinear capacitor having the constitutive equation $v = \hat{v}(q)$, where q is the electric charge.

Consider the following notations: v_j denotes the voltage $v(t)$ value at the time t_j , and v_{j+1} denotes the voltage $v(t)$ value at the time t_{j+1} . The variation of the energy stored in the capacitor between these time values can be computed exactly [3]:

$$E_{j+1} - E_j = \int_{t_j}^{t_{j+1}} \frac{dq}{dt} v dt = \int_{q_j}^{q_{j+1}} \hat{v}(q) dq \quad (2.6)$$

This energy is transferred to the capacitor by the nonlinear one-port N_0 over the time step $h_{j+1} = t_{j+1} - t_j$. For this capacitor, the energy error can be defined:

$$\Delta E = E_{j+1} - E_j - \int_{t_j}^{t_{j+1}} i(\tau) v(\tau) d\tau \quad (2.7)$$

The stored energy variation in a voltage controlled capacitor characterized by $q = Q(v)$ between the time values t_n and t_{n+1} is:

$$\begin{aligned} E_{n+1} - E_n &= \int_{t_n}^{t_{n+1}} \frac{dQ}{dt} (v(\tau)) v(\tau) d\tau = \\ &= Q(v(\tau)) v(\tau) \Big|_{t_n}^{t_{n+1}} - \int_{t_n}^{t_{n+1}} Q(v(\tau)) \frac{dv}{dt}(\tau) d\tau = \\ &= Q(v(t_{n+1})) v(t_{n+1}) - Q(v(t_n)) v(t_n) - \int_{v(t_n)}^{v(t_{n+1})} Q(v) dv \end{aligned} \quad (2.8)$$

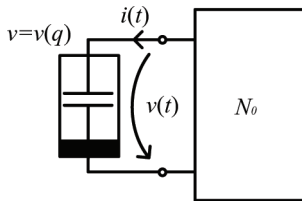


Figure 2.1 Nonlinear RC circuit.

It can be noted that the variation of the stored energy in any type of capacitor depends only on the initial and the final value of the state variable. Obviously the accumulated energy in the capacitor depends on the nonlinear characteristic but not on the voltage or charge waveform versus time. As a numerical method usually gives only the unknown sample values (for the time values t_j and t_{j+1} , for example) and gives not the shape of the functions between these samples, any numerical integration algorithm introduces errors in the solution computation. Similar results were obtained for flux controlled or current controlled linear and nonlinear inductors. In [3] is shown that for simple linear circuits solved with the backward Euler method and the trapezoidal rule $\lim_{h_{j+1} \rightarrow 0} \Delta E = 0$, property that is obvious in the general case.

2.1.1.2.2 Time step computation

The energy error ΔE for a dynamic circuit element is produced by the numerical method used for circuit equations integration. The integration step $h = t_{n+1} - t_n$ is chosen to satisfy, for each dynamic circuit element, the condition:

$$|\Delta E| < \alpha_{rel}|E_{n+1} - E_n| + \alpha_{abs} \quad (2.9)$$

where α_{rel} and α_{abs} are the relative and the absolute errors imposed by the user. For this purpose the PAN software uses an algorithm such as “cut and try”, similar to the SPICE one.

In SHORE, one of the first versions of PAN, another strategy of choosing the integration step has been used, as follows [3].

Consider that the circuit equations are formulated with the modified nodal analysis method and solved with the BE algorithm or the TP rule which are widely used in circuit simulators. The unknowns are the nodes voltages v_{j+1} , currents i_{j+1} through the capacitors, inductors and current controlled devices at t_{j+1} time and the time step h_{j+1} . Each capacitor and each inductor in the circuit generates an inequality type constraint of the form (2.9). The inequality type constraints can be grouped in a penalty scalar function [3], adding the constraint $h_{j+1} > 0$. The penalty function that has been chosen is

$$\begin{aligned} F\left(\Delta E_{j+1}^1, \dots, \Delta E_{j+1}^z, \dots, \Delta E_{j+1}^Z\right) = \\ = \exp\left(-\sum_{z=1}^Z \frac{|\Delta E_{j+1}^z|}{k_0 |E_{j+1}^z - E_j^z| + k_1}\right) : \Re^Z \rightarrow (0, 1] \subset \Re \end{aligned} \quad (2.10)$$

where:

- $|E_{j+1}^z - E_j^z|$ are the energy stored in the z -th generic dynamic circuit device at the time t_{j+1} ;
- ΔE_{j+1}^z is the energy error between the energy stored in the z -th dynamic element and the energy it absorbs from the circuit between the time values t_j and t_{j+1} ;
- k_0 and k_1 are two constants that define the relative and the absolute tolerances allowed for these energies;
- Z is the number of dynamic circuit elements.

The integration step is determined by solving

$$h_{j+1} - (h_{\max} - h_{\min})F(\Delta E_{j+1}^1, \dots, \Delta E_{j+1}^z, \dots, \Delta E_{j+1}^Z) - h_{\min} = 0 \quad (2.11)$$

whose solution h_{j+1} is placed in the positive interval $(h_{\max} - h_{\min}]$. If at least one of the inequalities $\Delta E_{j+1}^z \leq k_0 |E_j^z| + k_1$, $z = 1, \dots, Z$ is not satisfied, the value of F is very close to zero and $h_{j+1} \rightarrow h_{\min}$.

The Equation (2.11) adds a new line to the Jacobian matrix of the modified nodal analysis (MNA) method leading to the system:

$$\begin{cases} \Gamma(v_{j+1}, i_{j+1}, h_{j+1}) = 0 \\ h_{j+1} - (h_{\max} - h_{\min})F(\Delta E_{j+1}^1, \dots, \Delta E_{j+1}^z, \dots, \Delta E_{j+1}^Z) - h_{\min} = 0 \end{cases} \quad (2.12)$$

where $\Gamma(v_{j+1}, i_{j+1}, h_{j+1})$ are implicit nonlinear functions related to the MNA formulation.

At each time value the system of nonlinear algebraic Equations (2.12) is solved, for example by the Newton-Raphson iterative algorithm. Since h_{j+1} is not known at the beginning of these iterations, the solution of the previous iteration is used as the initial estimation.

When the Newton-Raphson iterative algorithm is used, a drawback can occur: the penalty function tends to zero when the energy error is too high, thus reducing the integration step h_{j+1} which tend to zero. This drawback can be avoided by decreasing the h_{\max} value.

Compared to the conventional *LTE* estimation, this algorithm takes into account in part the circuit structure and does not require the computation of the state variables derivatives by the finite differences method, which often introduces numerical errors.

Table 2.1 shows the number of Newton iterations, total step number, along with the number of accepted and rejected steps, and finally the CPU time used to analyze the circuit in Figure 2.2 from $T_{\text{start}} = 0$ to $T_{\text{stop}} = 1$ s.

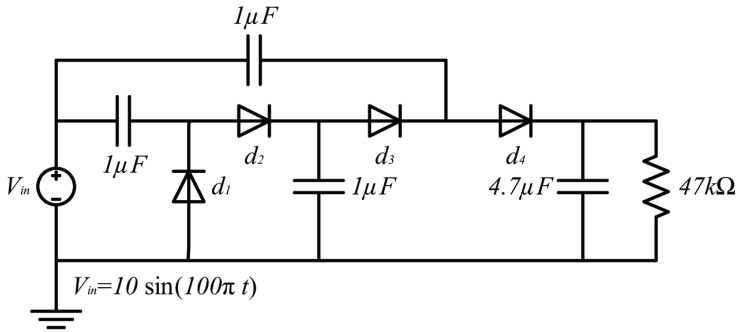


Figure 2.2 Voltage multiplier schematic.

Table 2.1 Simulation results for the voltage multiplier

| | SPICE | SHORE |
|---------------------|-------|-------|
| Newton iterations | 21244 | 15469 |
| Time steps | 4681 | 3434 |
| Accepted time steps | 3351 | 3351 |
| Rejected time steps | 1330 | 83 |
| CPU time (sec) | 38.6 | 21.3 |

2.1.1.2.3 Case studies

Class C amplifier

Numerical experiments made with several test circuits [4, 5], like those shown in Figures 2.3 and 2.4, show that while the CPU time used by SPICE and SPECTRE is almost the same, PAN needs up to 10 times less CPU time. A comparison of SPECTRE RF simulation and PAN is given in Table 2.2.

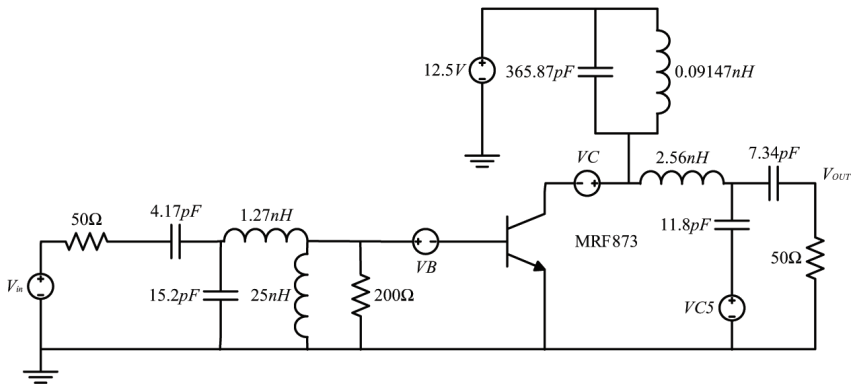


Figure 2.3 Class C amplifier.

The $trreltol$ error from PAN is the relative error in the Expression (2.9) used in transient analysis. $Reltol$ signifies ϵ_r error in (2.1) for SPECTRE and is a relative tolerance that determines when the Newton-Raphson iterations stop in PAN. $Trreltol$ error refers to energies and $reltol$ refers to voltages and currents. In SPECTRE if the user given value for $reltol$ is the maximum tolerance of the time derivative of a state variable, while the tolerance value of this variable is h times smaller or less (because $h \ll 1$). Consequently, it is impossible to set up the error parameters so that SPECTRE and PAN work with the same imposed errors. Therefore we compared the results for which the response waveforms are similar, these results being obtained with maximized values for all error parameters.

ne600p Mixer

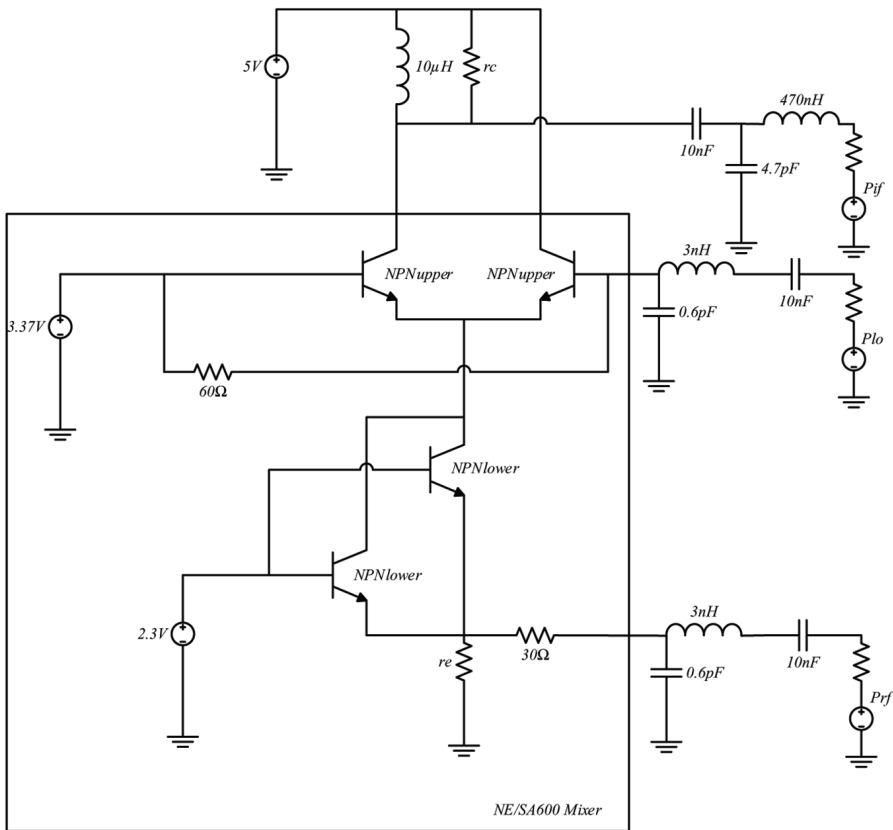


Figure 2.4 ne600p mixer.

Table 2.2 Simulation results for the circuits in Figures 2.2 and 2.3

| Circuit | Reltol | SPECTRE RF | PAN | Remarks (PAN) |
|-------------------|--------|------------|--------|---------------------------|
| Class C amplifier | 1e-5 | 9.68 s | 3.32 s | trreltol = 1e-3 |
| | 1e-6 | 20.1 s | 4.03 s | trreltol = 1e-6 |
| | | | 2.91 s | trreltol = 1e-2 |
| | | | | slightly altered waveform |
| ne600p mixer | 1e-5 | 35.65 s | 7.55 s | trreltol = 1e-3 |
| | 1e-6 | 78.4 s | 8.82 s | trreltol = 1e-3 |

The absolute errors for voltages and currents are set to 10^{-12} in both SPECTRE RF and PAN.

One Diode Circuit

In addition to the diode modeled by a non-linear resistor (Figure 2.6), the circuit (Figure 2.5) also contains a branch having the series resonance frequency of $100f$ where f is the power supply frequency [9, 10]. These properties of the circuit introduce difficulties in obtaining the correct result, as will be explained below.

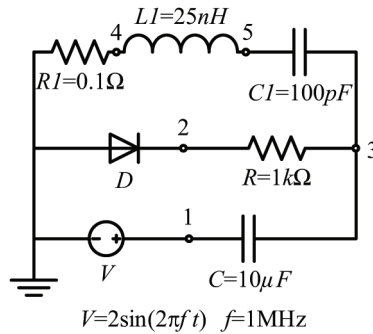


Figure 2.5 One diode circuit.

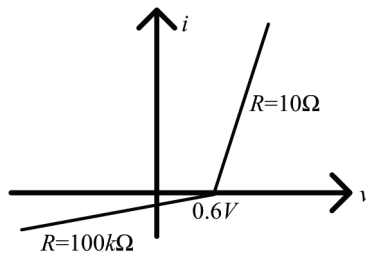


Figure 2.6 v - i diode characteristic.

This circuit has been simulated with SPICE setting $reltol = 0.6e-6$, $abstol = 1e-12$ and with PAN for $trreltol = 1e-13$, $trabstol = 1.5e-18$. With these imposed errors the results shown in Table 2.3 have been obtained.

At the first glance, the rectified voltage obtained with these two simulators is identical (Figure 2.7), but in a detail (Figure 2.8) we can observe a slight difference.

If we consider the voltage of $R1$ (Figure 2.9) and its detail (Figure 2.10) it can be observed that there is a relatively large difference between the solutions obtained with these two simulators.

From the above remarks it can be concluded that in this case at least one obtained solution is not correct. To improve the results the circuit has simulated again with $reltol = 7.5e-11$, $abstol = 1e-12$ for SPICE and $trreltol = 1e-13$, $trabstol = 1.5e-22$ for PAN.

With these imposed errors, the results in Table 2.4 have been obtained.

It is interesting to note that in this case PAN rejects about 11 times more steps than SPICE but the computation time is smaller.

Table 2.3 Simulation results for the circuit in Figure 2.5

| | SPICE | PAN |
|----------------|-------|--------|
| Accepted steps | 16509 | 15486 |
| Rejected steps | 5066 | 3404 |
| CPU time | 0.4 s | 0.23 s |

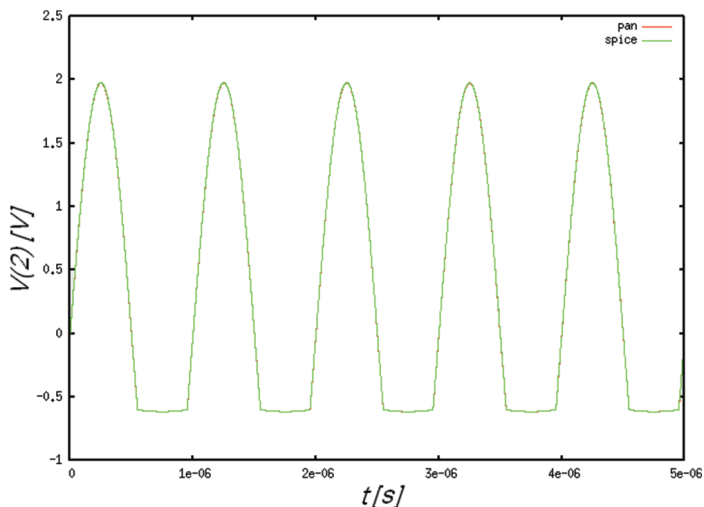


Figure 2.7 Diode voltage.

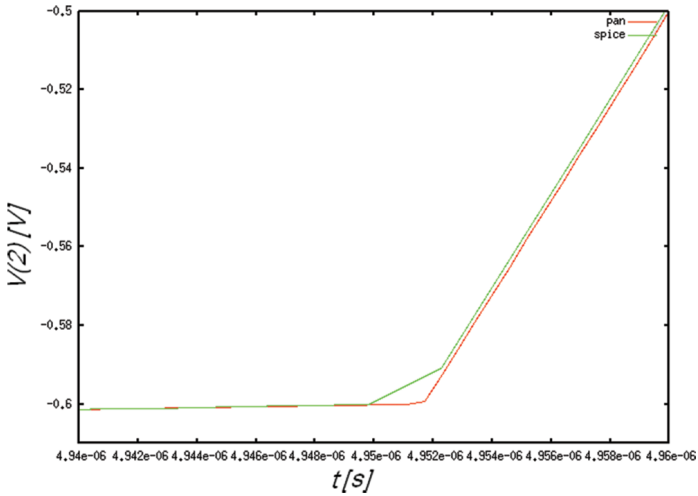


Figure 2.8 Diode voltage – detail.

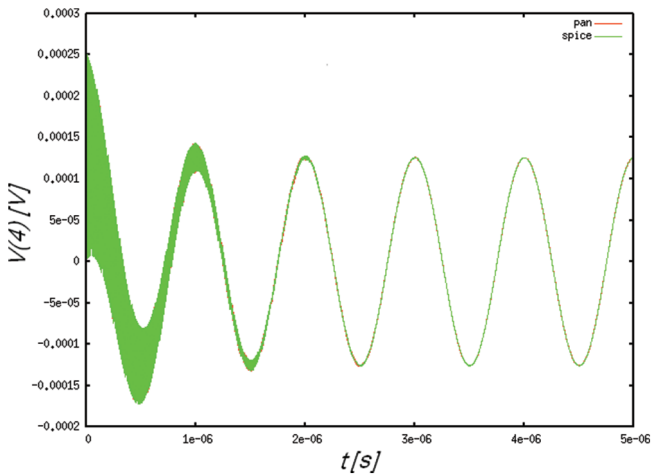


Figure 2.9 RI voltage.

Zooming the same area, a significant improvement of these solutions, which are now similar, is observed (Figure 2.11).

It is interesting to see how the time step evolves in both transient analysis approaches (Figure 2.12).

Since the user cannot impose equivalent errors in these two programs and there are cases where the same waveform is obtained with about the same

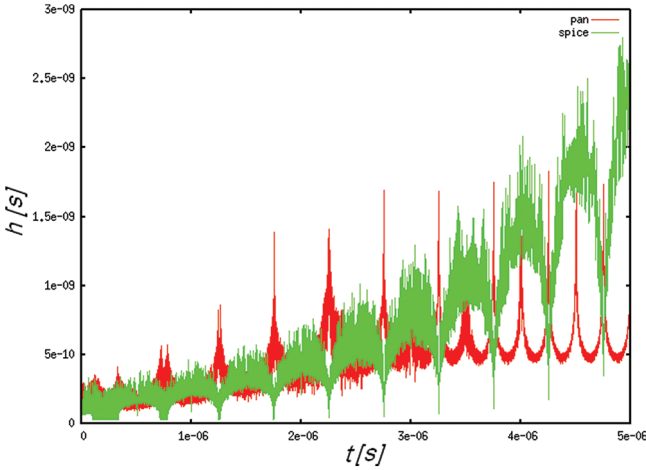


Figure 2.12 Time step evolution for SPICE and PAN.

number of accepted steps, the average time step being about the same, it can be said that the efficiency of transient analysis implemented in SPECTRE and PAN is similar, for this more intricate example.

2.1.1.3 Time step choice algorithm based on energy balance relative error

2.1.1.3.1 Errors used in transient analysis

2.1.1.3.1.1 Local truncation error and energy error

The equations of a nonlinear circuit with the state variables $x(t)$, the inputs $u(t)$ and the outputs $y(t)$ are:

- the state equations $\dot{x}(t) = f(x(t), u(t))$
- the link between inputs and outputs $y(t) = g(x(t), u(t))$.

By imposing certain values for truncation errors related to the relative and the absolute error which are used to compute $x(t)$ and $\dot{x}(t)$, the errors used to check the circuit equations depend on the f and g functions. In other words, to a SPICE user who sets some values for the absolute and relative errors on state variables and their derivatives with respect to time, certain errors values with which are verified the circuit equations are not guaranteed. This is why we say that this method of error parameter setting ignores the circuit structure.

By imposing α_{rel} and α_{abs} in (2.9), PAN limits the error between the accumulated energy and the energy received in an integration step for each dynamic circuit element. It can be said that this way to define the errors takes partially into account the structure of the circuit.

The energy balance errors, which are taking fully into account the circuit structure, are defined in this section. It is expected that using these errors for choosing the time step, a smaller computing time than that of SPICE will be obtained for the computation of a solution having the same overall transient analysis error (computed for the whole time interval).

The energy balance errors are defined in Paragraph 2.1.1.3.1, a time step choice algorithm based on these errors is proposed in Paragraph 2.1.1.3.2, and the analysis of some linear and nonlinear circuits comparing the results of the proposed algorithm with the analytical solution and with the solution given by SPICE is presented in Paragraph 2.1.1.3.3.

2.1.1.3.1.2 The energy balance error [8–12]

For each dynamic element the accumulated energy in a time step $h = t_{n+1} - t_n$ is defined. For capacitors we have:

- charge controlled linear capacitor

$$\Delta E_C = E_{j+1} - E_j = \int_{t_j}^{t_{j+1}} \frac{dq}{dt} v dt = \int_{q_j}^{q_{j+1}} \hat{v}(q) dq \quad (2.13)$$

- voltage controlled linear capacitor

$$\begin{aligned} \Delta E_C &= E_{n+1} - E_n = \int_{t_n}^{t_{n+1}} \frac{dQ}{dt} (v(\tau)) v(\tau) d\tau = \\ &= Q(v(\tau)) v(\tau) \Big|_{t_n}^{t_{n+1}} - \int_{t_n}^{t_{n+1}} Q(v(\tau)) \frac{dv}{dt}(\tau) d\tau = \\ &= Q(v(t_{n+1})) v(t_{n+1}) - Q(v(t_n)) v(t_n) - \int_{v(t_n)}^{v(t_{n+1})} Q(v) dv \end{aligned} \quad (2.13')$$

and for inductors:

- flux controlled linear inductor

$$\Delta E_L = E_{j+1} - E_j = \int_{t_j}^{t_{j+1}} \frac{d\phi}{dt} i dt = \int_{\phi_j}^{\phi_{j+1}} \hat{i}(\phi) d\phi \quad (2.14)$$

- current controlled linear inductor

$$\begin{aligned} \Delta E_L &= E_{n+1} - E_n = \int_{t_n}^{t_{n+1}} \frac{d\phi}{dt} (i(\tau)) i(\tau) d\tau = \\ &= \phi(i(\tau)) i(\tau) \Big|_{t_n}^{t_{n+1}} - \int_{t_n}^{t_{n+1}} \phi(i(\tau)) \frac{di}{dt}(\tau) d\tau = \\ &= \phi(i(t_{n+1})) i(t_{n+1}) - \phi(i(t_n)) i(t_n) - \int_{i(t_n)}^{i(t_{n+1})} \phi(i) di \end{aligned} \quad (2.14')$$

The energy absorbed by the resistors and sources between t_n and t_{n+1} is:

$$E_k = \int_{t_n}^{t_{n+1}} u(t) \cdot i(t) dt \quad (2.15)$$

where, starting from the samples computed with a numerical integration method, $v(t)$ and $i(t)$ are approximated by a linear or a quadratic interpolation (Table 2.5).

Table 2.5 Linear and quadratic interpolation for voltages and currents

| Linear Interpolation | Quadratic Interpolation |
|----------------------------|--|
| $v(t) = a_1 \cdot t + a_0$ | $v(t) = a_2 \cdot t^2 + a_1 \cdot t + a_0$ |
| $i(t) = b_1 \cdot t + b_0$ | $i(t) = b_2 \cdot t^2 + b_1 \cdot t + b_0$ |

With linear interpolation between samples [9] it is obvious that higher errors are obtained in energy calculation than using quadratic interpolation for voltages and currents. To simplify the formulas that calculate the coefficients of these polynomials we use a “local” coordinate system $0, h_1, h_1+h_2$ instead of “global” one t_{n-1}, t_n, t_{n+1} (Figure 2.13). Significant interpolation errors can occur if the denominator of these coefficients is too small. These errors can be avoided by using linear interpolation between h_1 and h_1+h_2 if $h_1 h_2 (h_1 + h_2) \leq \Delta$, where $h_1 h_2 (h_1 + h_2)$ is the denominator of the coefficient and Δ is a limit set by the user.

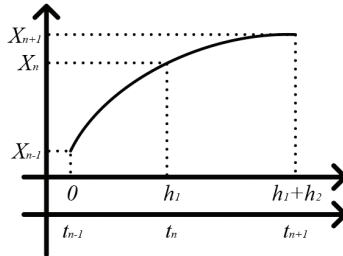


Figure 2.13 Quadratic interpolation.

Certainly, this approximation of the waveform introduces errors in the voltage and current energy calculation. So, these errors affect also the calculation of energy balance. To ensure a smooth waveform between t_n and t_{n+1} a condition that halves the time step if the interpolation parabola peak is in this range, is added.

The absolute energy balance error is defined as:

$$\Delta E_a = \sum_{k=1}^N E_k \quad (2.16)$$

and the relative energy balance relative error [10] as:

$$\Delta E_r = \Delta E_a / \sqrt{\sum_{k=1}^N E_k^2} \quad (2.17)$$

where N is the number of all elements in the circuit. These errors are computed at each time point and if ΔE_r is greater than an imposed threshold, the time step is rejected.

2.1.1.3.2 *Time step choice algorithm*

The time step choice algorithm based on energy balance error is given below [8, 10, 11]. In the following EER is the imposed relative energy error and $TMAX$ is the step to display the results.

EER = the imposed relative energy error

$$t_{n+1} = t_n + h_n$$

solve for t_{n+1}

compute ΔE_r

if $\Delta E_r < EER/10$

 accept t_{n+1}

$$h_{n+1} = 1.5 \cdot h_n$$

$$h_{n+1} = \min(h_{n+1}, TMAX)$$

 continue

else if $EER/10 < \Delta E_r < EER$

 accept t_{n+1}

$$h_{n+1} = h_n$$

 continue

else if $\Delta E_r > EER$

 reject t_{n+1}

$$h_{n+1} = h_n/1.5$$

 if $h_{n+1} < H \min$ print TIME STEP TOO SMALL;

 the analysis is aborted

The total error can be computed as $\Delta E_{total} = \sum \Delta E_a$, where ΔE_a is given by (2.16), and the sum is considered for all accepted steps. This error is a global estimation of the transient analysis accuracy, for the entire circuit and for the entire time interval considered of the transient analysis accuracy. A truncation error [2], or an energy error [3] does not allow this kind of global estimation.

Computing both ΔE_a and ΔE_{total} the compensation of some different signs errors can lead to a wrong estimation of the solution accuracy. Since the accumulated energy variation in the dynamic elements depends only on

the values of the state variables at the boundaries of the interval $[t_n, t_{n+1}]$, a special attention in solving the resistive circuit containing companion models (see Section 2.1.1.3.3) has been paid, this procedure being performed in *long double* precision. In addition, the powers balance test that verifies the accuracy of solving this circuit has been introduced.

This algorithm has been implemented in C and tested for linear circuits with damped oscillating transient response, circuits with piecewise linear resistors and circuits with polynomial nonlinearities. For the tested examples that contain a relatively small number of circuit elements, the proposed algorithm rejects a smaller number of steps than SPICE, the number of accepted steps being about the same.

2.1.1.3.3 Solving the linear circuit with companion models

In transient analysis, at each time step, a system of equations $Ax = b$ is solved. This system results from the node voltage equations of the resistive circuit obtained by replacing the dynamic elements with their equivalent companion models [42]. If the integration step is very small, a common case in the analysis of the oscillating circuits with high quality factor, the numerical values of this matrix differ by several orders of magnitude and the matrix of the system can become ill-conditioned. This introduces errors in computing the system solution. Therefore, iterative methods were developed to improve the solution, the most known and used being GMRES (generalized minimal residual method) [14]. Briefly, the algorithm of this method is as follows:

```

{
  calculate the residue  $r = b - A \cdot x$ 
  solve  $A \cdot d = r$ 
  update the solution  $x = x + d$ 
} until  $r$  or  $d$  is small enough or the maximum number of iterations is
reached

```

This algorithm works well up to a certain point. If the condition number ($\|A\| \cdot \|A^{-1}\|$) is very high the residue is not worsen, but the solution x (although it is usually improved by this process) is often worsen [13]. It seems that using a greater precision in computations, a better solution can be obtained even without GMRES.

For example, consider a 23×23 matrix similar to those occurring in circuit analysis. This ill conditioned matrix has the condition number $2.1e+5$ and the determinant value $3.08e-61$. The results obtained using the GMRES algorithm are given in Table 2.6 [42].

Now consider the nonlinear circuit in Figure 2.5 [9, 10] the power balance at each time step being computed using *double* and *long double* precision.

Table 2.6 Simulation results for the ill-conditioned matrix

| | GMRES | Full Pivoting | Maximum Residue | CPU Time |
|-------------|-------|---------------|-----------------|----------|
| Double | YES | YES | 1.27E-18 | 152.4 us |
| Long double | NO | YES | 4.41E-22 | 104.4 us |
| Long double | NO | NO | 3.04E-22 | 58.8 us |

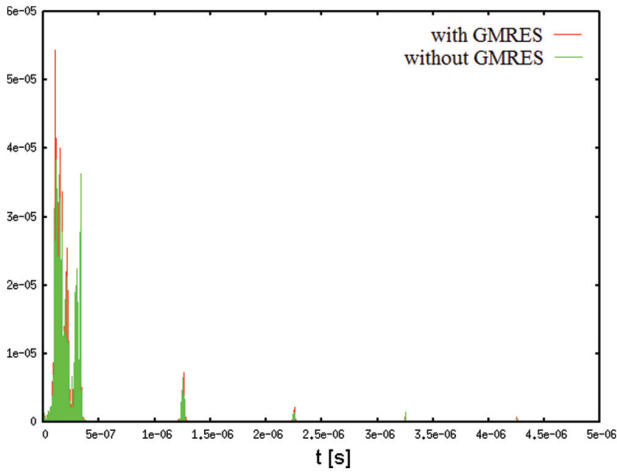


Figure 2.14 Evolution of the relative energy balance error – *double precision*.

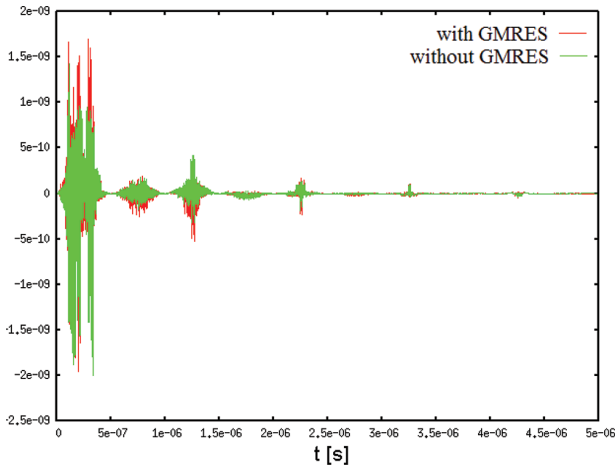


Figure 2.15 Evolution of the absolute energy balance error – *double precision*.

When for solving the linear system of the circuit with companion models the *double* precision is used, with or without GMRES iterations, the evolution of the power balance relative error is similar (Figure 2.14).

A similar evolution of the absolute power balance error can be observed (Figure 2.15).

If the *long double* precision is used, both the relative power balance error (Figure 2.16) and the absolute power balance error (Figure 2.17) are much improved even without GMRES iterations compared to the errors computed with *double* precision (Figure 2.14, Figure 2.15).

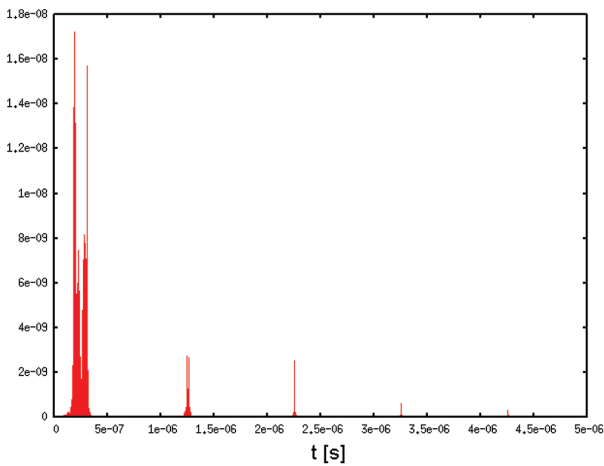


Figure 2.16 Evolution of the relative energy balance error – *long double* precision.

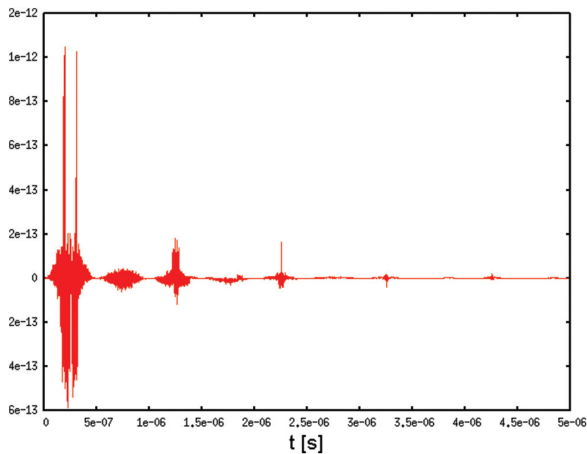


Figure 2.17 Evolution of the absolute energy balance error – *long double* precision.

Table 2.7 Results obtained using double and long double precision

| Precision | GMRES | P_{rel} max | P_{abs} max | CPU Time | Accepted Steps | Rejected Steps |
|-------------|-------|---------------|---------------|----------|----------------|----------------|
| Double | YES | 5.5E-5 | 2E-9 | 0.54 s | 18911 | 981 |
| Long double | NO | 1.7E-8 | 1.05E-12 | 0.43 s | 13974 | 842 |

A summary of the results is presented in Table 2.7:

Where:

$$P_{abs} = \sum_{k=1}^n P_k$$

and

$$P_{rel} = \frac{P_{abs}}{\sqrt{\sum_{k=1}^n (P_k)^2}}$$

Remarks [42]

In the computations performed with the *double* precision the *long double* errors cannot be achieved no matter how many GMRES iterations are performed.

At least in these cases, using *long double* precision, the solution obtained using LU factorization with full pivoting is the same as that obtained using LU factorization without pivoting.

Using the *long double* precision the correct solution is obtained in less CPU time than using *double* precision with GMRES iterations.

2.1.1.3.4 Examples

Using the opportunity of having the sources of SPICE+ (a variant of SPICE3F5), a comparison of the proposed algorithm with SPICE for a set of examples has been made.

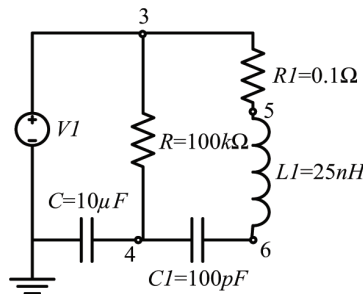


Figure 2.18 Linear circuit with damped oscillatory response.

2.1.1.3.4.1 1st Example

The circuit in Figure 2.18 [11, 12] has been analyzed starting from an initial condition selected such as it generates a damped oscillatory response. This circuit is powered by a 1 MHz sinusoidal voltage of 1 V amplitude. To compare the results obtained with the proposed algorithm and with SPICE, two cases have been considered. The first case has a higher level of the errors than the second case.

For the first case, the voltage on the capacitor C is given in Figure 2.19 and Figure 2.20, the initial conditions being $v_C = 1\text{V}$, $v_{C1} = 1\text{V}$ and $i_{L1} = 0\text{A}$.

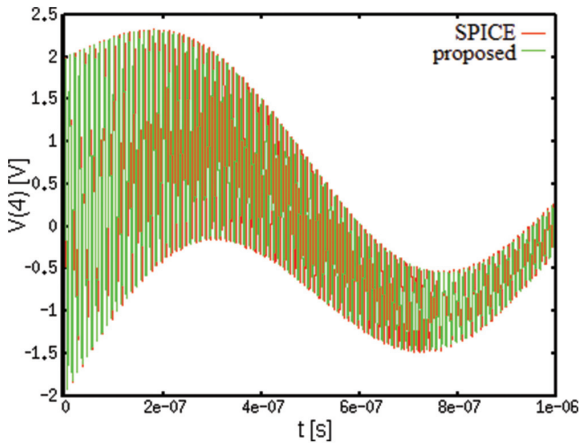


Figure 2.19 Circuit response in the first case.

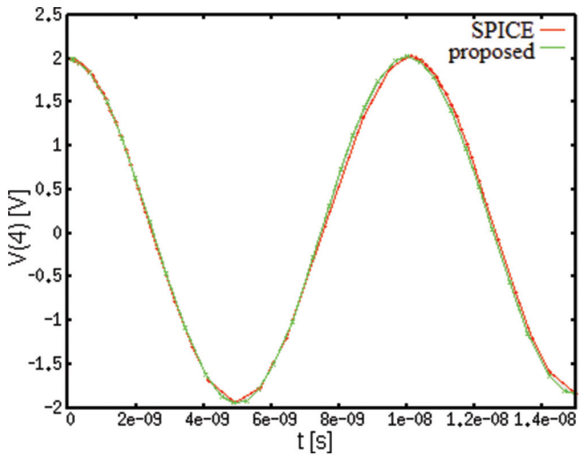


Figure 2.20 Circuit response in the first case – detail.

The analysis parameters have been set so that the high frequency detail obtained by SPICE is almost identical with that resulting using the proposed algorithm (Figure 2.20). The main parameters of the SPICE analysis and those of the analysis with the proposed algorithm are described in Table 2.8.

In the second case smaller imposed errors are used. The circuit response is shown in Figure 2.21 and Figure 2.22, while the parameters of the analyses are given in Table 2.9.

It may be noted that in both cases the proposed algorithm rejects fewer steps than the SPICE one, the number of accepted steps being similar. The similar

Table 2.8 Results obtained for the 1st example

| Algorithm | Imposed Errors | Accepted Steps | Rejected Steps |
|-----------|-------------------------------------|----------------|----------------|
| SPICE | reltol = $1e-4$ abstol = $1e-15$ | 2117 | 814 |
| Proposed | ERR = $0.6e-4$ | 2087 | 304 |

Table 2.9 Results obtained for the 1st example with smaller imposed errors

| Algorithm | Imposed Errors | Accepted Steps | Rejected Steps |
|-----------|-------------------------------------|----------------|----------------|
| SPICE | reltol = $2e-6$ abstol = $1e-15$ | 8507 | 2924 |
| Proposed | ERR = $0.6e-5$ | 8641 | 885 |

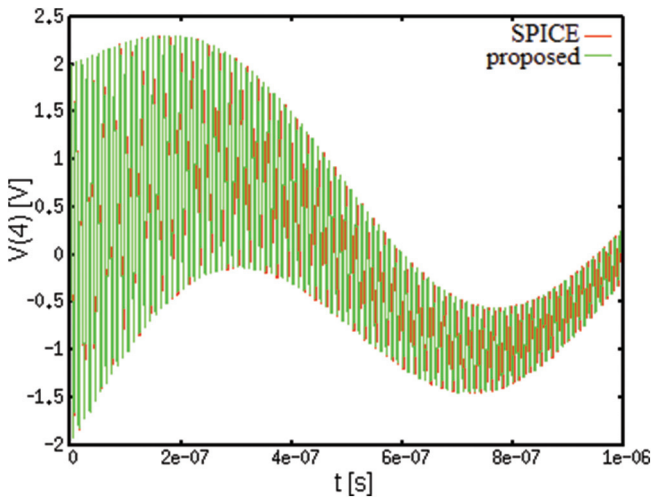


Figure 2.21 Circuit response in the second case.

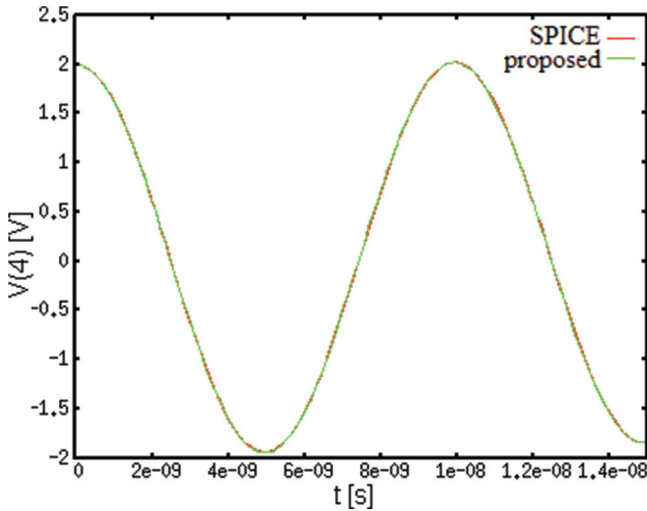


Figure 2.22 Circuit response in the second case – detail.

number of accepted steps results from the similar accuracy conditions imposed, in order to ensure a set of valid comparison between these algorithms.

2.1.1.3.4.2 2nd Example

The second example is the circuit in Figure 2.5 which contains a nonlinear element and a resonant branch. This circuit is driven by a signal of 1 MHz, the natural frequency of the transient component generated by the RLC resonance branch being 100 MHz. The nonlinear element is a diode modeled by a piecewise linear resistor in series with a voltage source (Figure 2.6).

The diode voltage $V(2)$ computed with the proposed algorithm and with SPICE is given in Figure 2.23.

Using the error limits $reltol = 7.5e-11$, $abstol = 1e-12$ for SPICE and $EER = 7e-7$ for the proposed algorithm, we have obtained the results in Table 2.10.

The errors imposed in the two algorithms have been chosen so that the total error ΔE_{total} produced by the proposed algorithm is almost the same as the value ΔE_{total} obtained with SPICE. It follows that for about the same total error ΔE_{total} , the proposed algorithm is better from the point of view of rejected steps and computation time.

Using the trapezoidal rule for the circuit equations integration with both algorithms, similar waveforms have been obtained, as expected (Figures 2.23, 2.24, and 2.25). It is interesting to observe the evolution of the energy balance

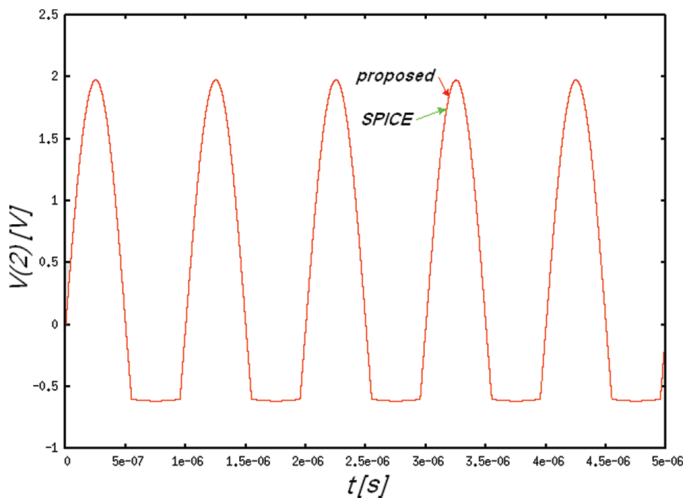


Figure 2.23 Diode voltage.

Table 2.10 Results obtained for the 2nd example

| | Proposed | SPICE |
|---------------------------|-------------|-------------|
| Accepted steps | 303705 | 306215 |
| Rejected steps | 2921 | 6883 |
| ΔE_{total} | $7.769e-17$ | $9.396e-17$ |
| CPU time | 7.38 s | 7.56 s |

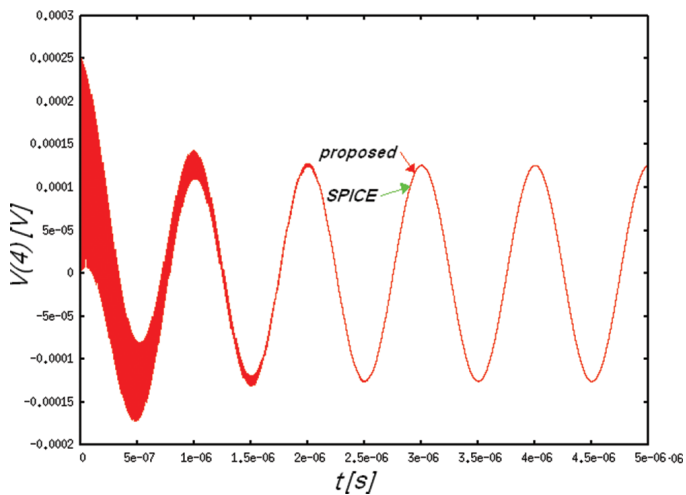


Figure 2.24 $V(4)$ voltage.

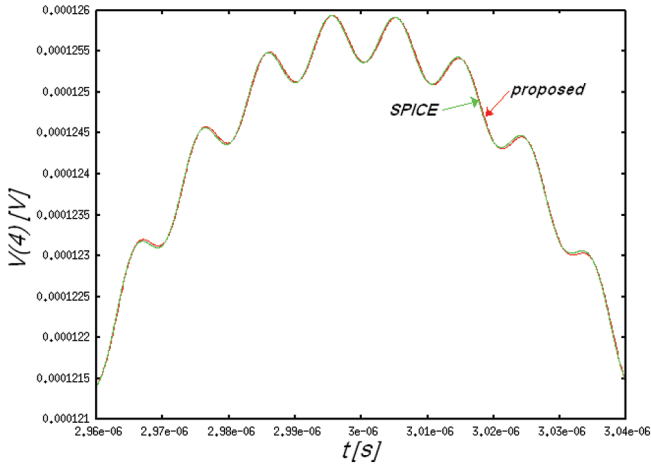


Figure 2.25 $V(4)$ voltage – detail.

relative error computed for the SPICE solution and for the proposed algorithm (Figure 2.26, Figure 2.27).

The evolution of the time step both for SPICE and for the proposed algorithm is shown in Figure 2.28.

It follows that using the same limit for the relative energy balance relative error for all time steps, the proposed algorithm makes an average step greater

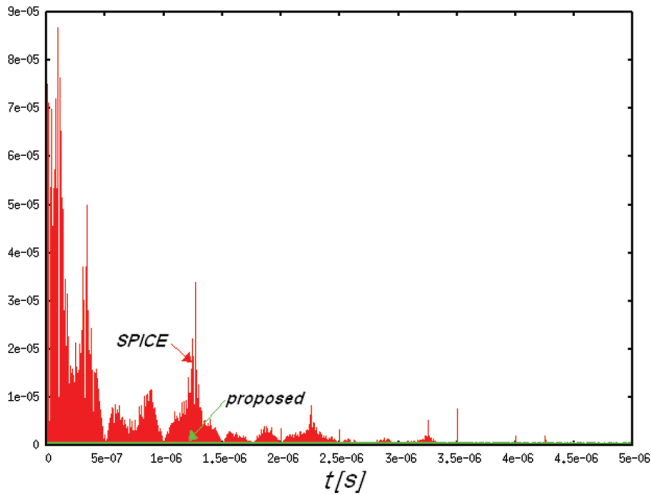


Figure 2.26 Relative energy balance error for SPICE and the proposed algorithm.

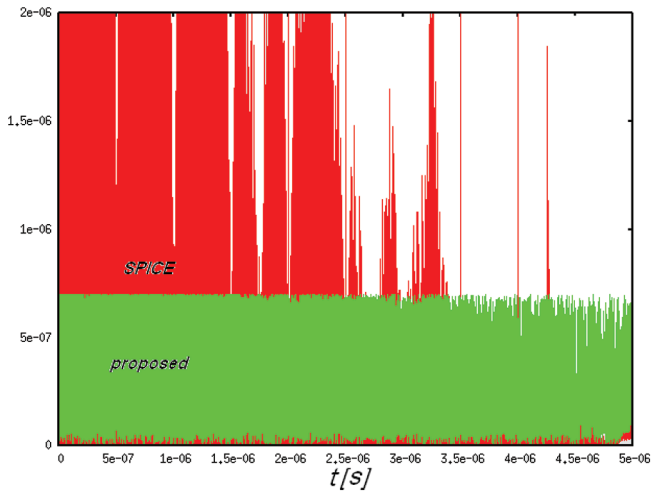


Figure 2.27 Relative energy balance error for SPICE and the proposed algorithm – detail.

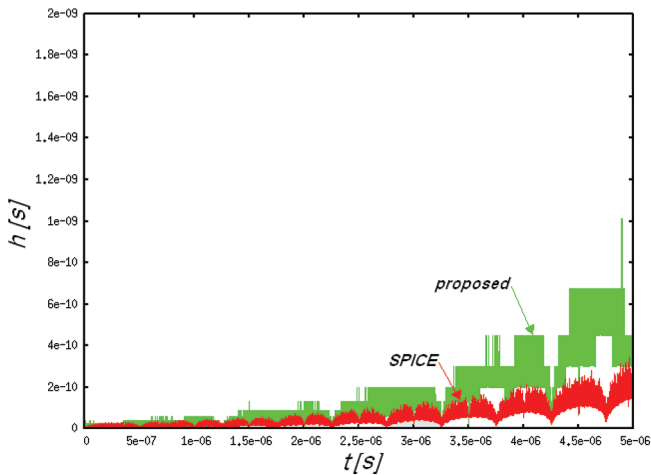


Figure 2.28 Evolution of the time step for SPICE and the proposed algorithm.

than the SPICE algorithm that uses the same local truncation error limit for all time steps.

2.1.1.3.4.3 3rd Example

The equivalent circuit of the quartz crystal resonator (Figure 2.29) from the amplifier given in [8] has been considered. This circuit has a quality factor

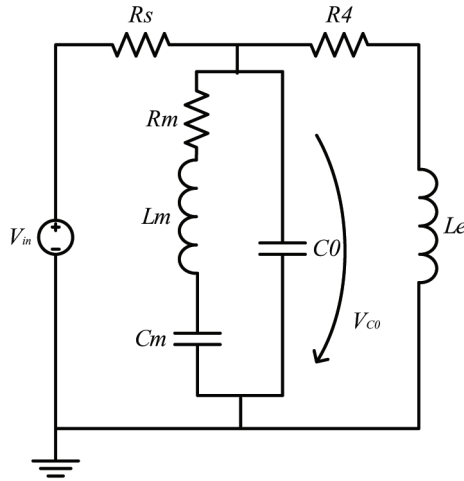


Figure 2.29 High quality factor circuit.

$Q = 1.6 \times 10^6$ at the series resonance frequency of 5 MHz and it has been analyzed starting from the null initial state, being driven by a 5 MHz signal.

2.1.1.3.4.3.1 Comparison with the analytical solution

The $V_{C0}(t)$ response after sweeping 497 periods is presented in Figure 2.30. A detail is given in Figure 2.31.

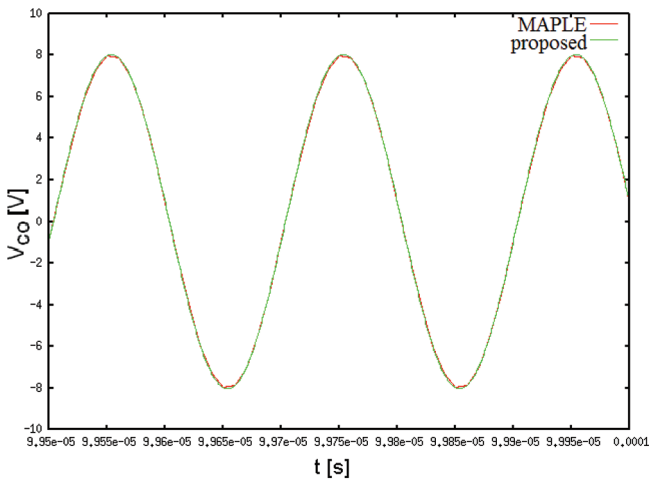


Figure 2.30 High quality factor circuit response.

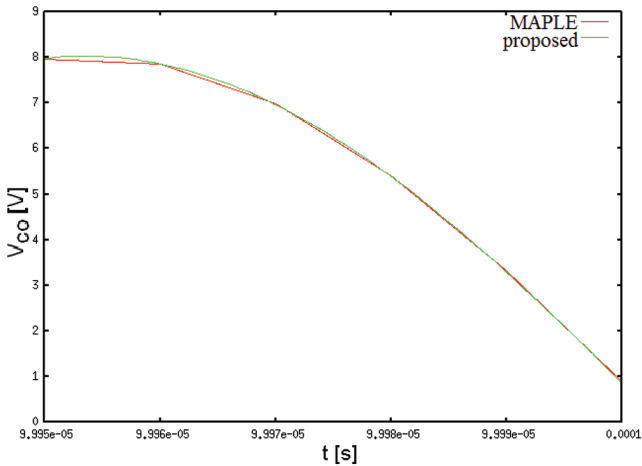


Figure 2.31 High quality factor circuit response – detail.

2.1.1.3.4.3.2 Comparison with the SPICE solution

The response computed with the proposed algorithm is virtually identical with the SPICE response (Figure 2.32) for $reltol = 1e-7$. The detail given in Figure 2.33, considered in the last period of the analysis, shows a very small the difference between these results.

The analysis parameters performed with SPICE and the proposed algorithm for choosing the time step are given in Table 2.11.

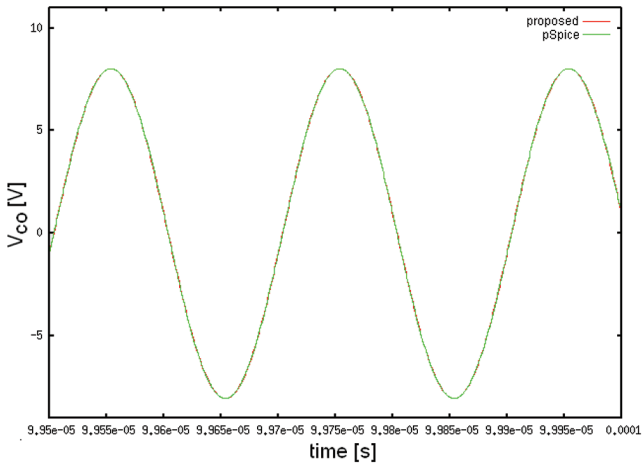


Figure 2.32 High quality factor circuit response computed with SPICE and with the proposed algorithm.

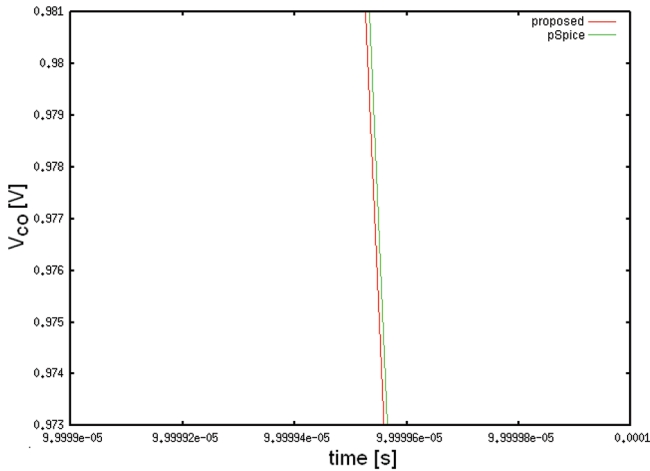


Figure 2.33 High quality factor circuit response computed with SPICE and with the proposed algorithm – detail.

Table 2.11 Results obtained for the 3rd example

| Algorithm | Imposed Errors | Accepted Steps | Rejected Steps | CPU Time (s) |
|-----------|---------------------------------------|----------------|----------------|--------------|
| SPICE | reltol = $0.7e-7$ abstol = $1e-15$ | 163028 | 15245 | 2.01 |
| Proposed | ERR = $5.5e-3$ | 163207 | 3884 | 1.96 |

It follows that the number of rejected steps for the proposed algorithm is almost four times smaller than the number of SPICE rejected steps, the number of the accepted steps being similar.

2.1.1.3.4.4 4th Example

A bandpass filter built with two BAW (bulk acoustic wave) resonators has been analyzed with SPICE, MAPLE and the proposed algorithm [9, 10]. The Butterworth-Van Dyke equivalent circuit is used for each resonator (Figure 2.34). This circuit is driven by a sinusoidal signal of 2.025 GHz (the series resonance frequency of the first resonator).

2.1.1.3.4.4.1 Comparison with the analytical solution

After sweeping 10 periods of the signal source, the output voltage $V(2)$ computed with the proposed algorithm is basically the same with the analytical solution computed with the MAPLE software (a).

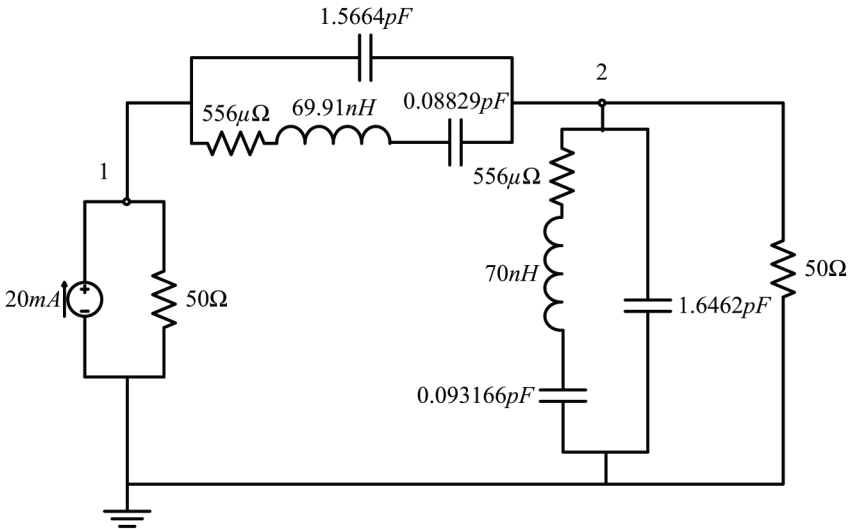


Figure 2.34 Bandpass filter (output voltage – node 2 voltage).

At the beginning of the simulation there is a small difference between the numerical and the analytical solution for $V(2)$ and $I_{L,m1}$ (the current through the motional branch of the first resonator) Figures 2.35 (b) and 2.36 (b).

2.1.1.3.4.4.2 Comparison with the SPICE solution

After sweeping 100 periods of the signal source, the output voltage $V(2)$ computed with the proposed algorithm and with SPICE is given in Figure 2.37.

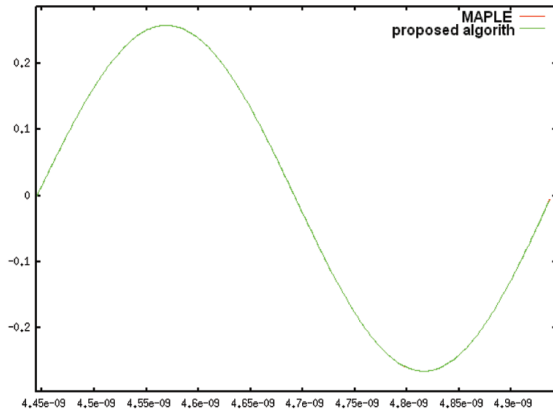
Considering the imposed errors $reltol = 3.2e-6$ and $EER = 1e-5$ the results obtained with these two algorithms have the properties in Table 2.12.

It can be observed that for a similar ΔE_{total} value, the number of steps computed with the proposed algorithm is about 80% of the number of steps computed with SPICE.

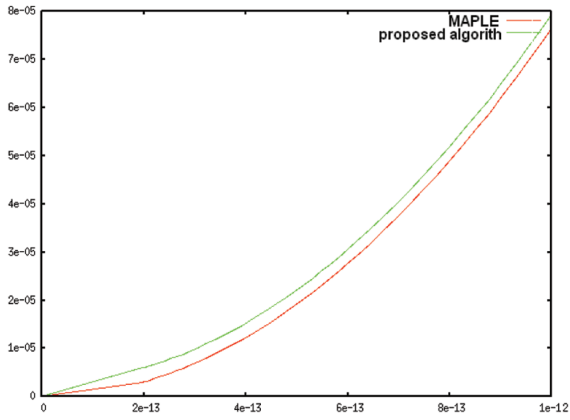
It is interesting to observe the evolution of the relative energy balance relative error for the SPICE solution (Figure 2.38) and to compare it with the

Table 2.12 Results obtained for the 4th example

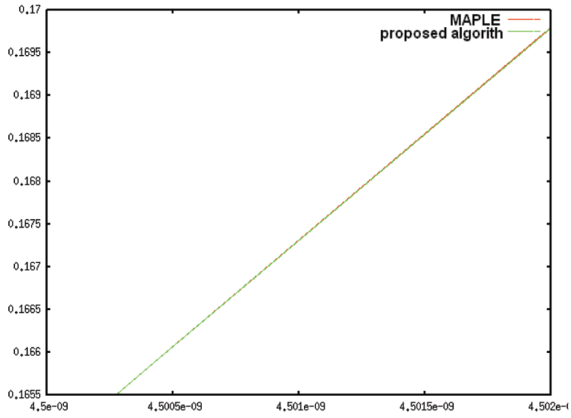
| | Proposed | SPICE |
|--------------------|-------------|-------------|
| Accepted steps | 9270 | 9238 |
| Rejected steps | 1161 | 3532 |
| ΔE_{total} | $6.124e-16$ | $2.417e-15$ |
| $\Delta E_r, \max$ | $1e-5$ | $6.559e-3$ |
| CPU time | 0.18 s | 0.25 s |



(a) global



(b) initial



(c) final

Figure 2.35 $V(2)$ [V] versus time [s].

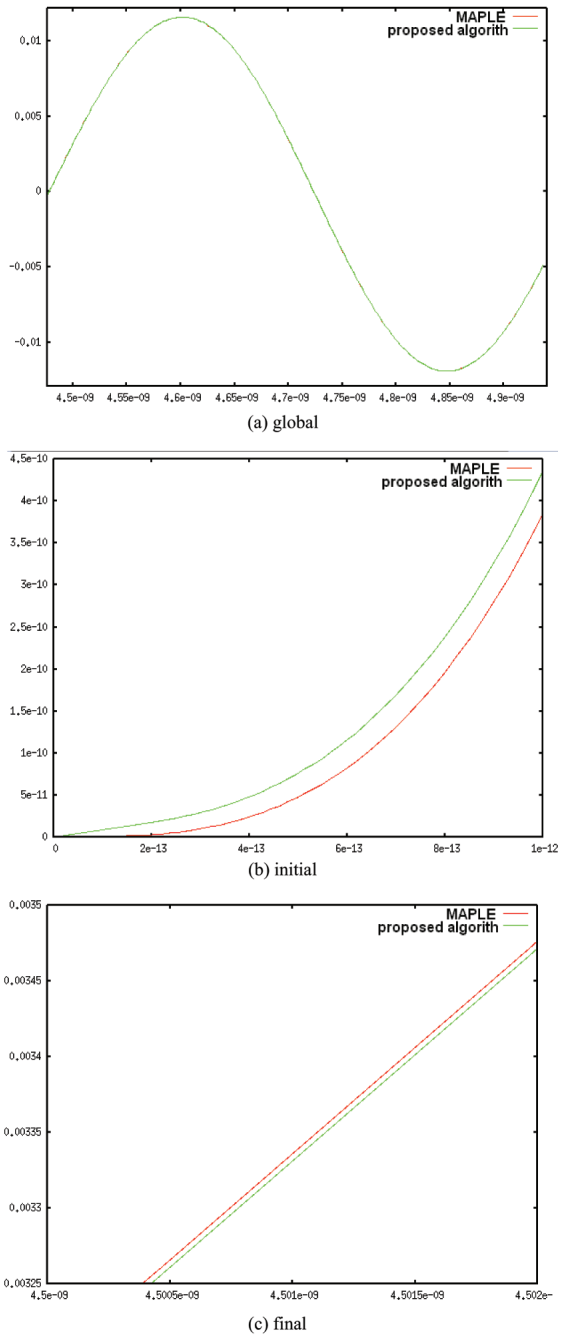


Figure 2.36 I_{Lm1} [A] versus time [s].

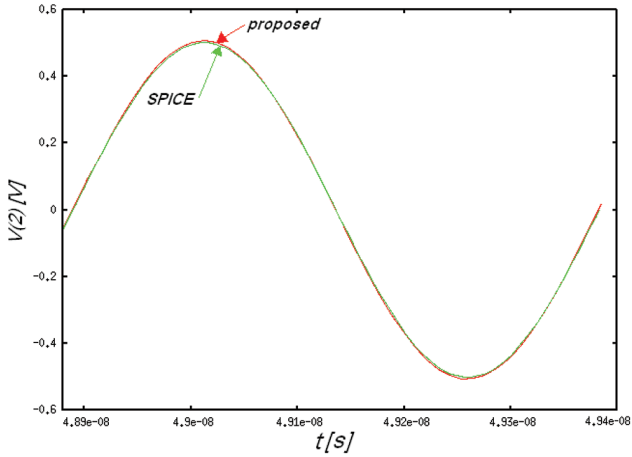


Figure 2.37 Output voltage of the band-pass filter.

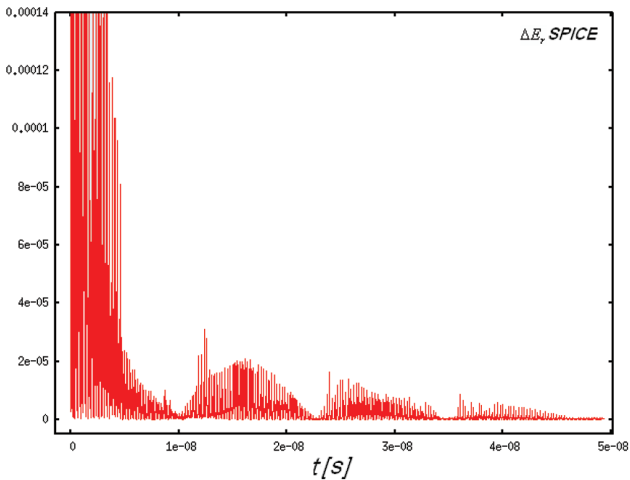


Figure 2.38 Relative energy balance error for the SPICE solution.

relative energy balance relative error computed for the proposed algorithm (Figure 2.39).

The evolution of the time step for SPICE and for the proposed algorithm is given in Figure 2.40.

2.1.1.3.4.5 5th Example

The band-pass filter from the previous example where both linear BAW resonators were replaced with nonlinear resonators has been analyzed with

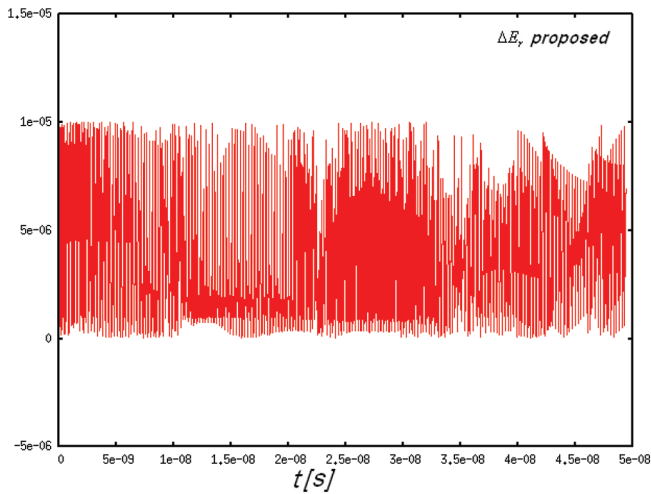


Figure 2.39 Relative energy balance error for the proposed algorithm solution.

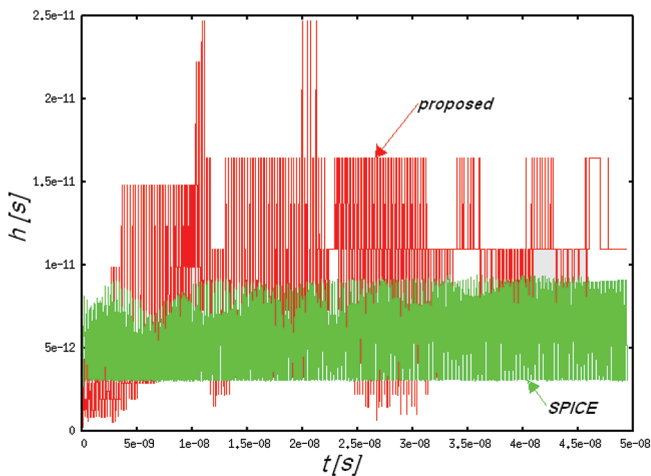


Figure 2.40 Time step evolution for SPICE and for the proposed algorithm.

SPICE and the proposed algorithm. The nonlinear equivalent circuit proposed in Chapter 3 is used for each resonator (Figure 2.41). This circuit is driven with a sinusoidal signal of 2.025 GHz (the series resonance frequency of the first resonator).

For the motional branch of the first resonator the following nonlinear circuit elements were used:

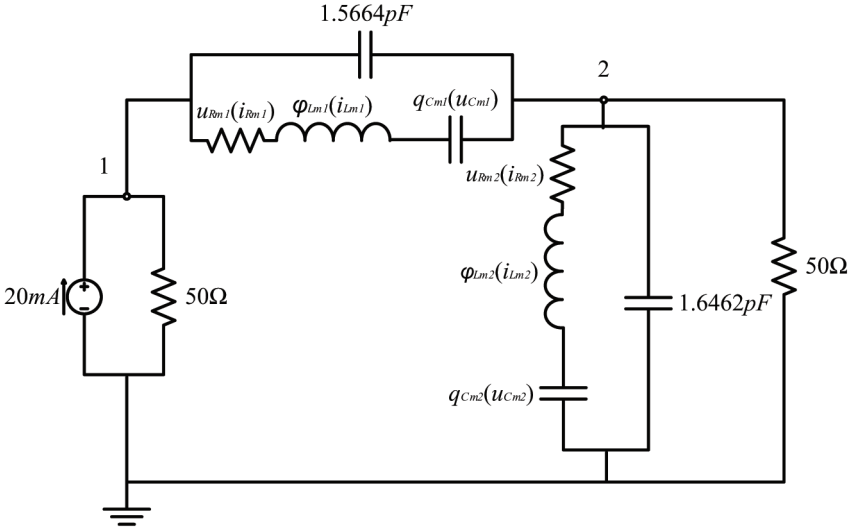


Figure 2.41 Band pass filter (output voltage – node 2 voltage).

$$\begin{aligned}
 u_{Rm1}(i_{Rm1}) &= 4.56 \cdot (i_{Rm1} + 0.5e - 5 \cdot i_{Rm1}^2 + 0.5e - 6 \cdot i_{Rm1}^3) \\
 \varphi_{Lm1}(i_{Lm1}) &= 69.91e - 9 \cdot (i_{Lm1} + 5e - 3 \cdot i_{Lm1}^2 + 1e - 5 \cdot i_{Lm1}^3) \\
 q_{Cm1}(u_{Cm1}) &= 88.29e - 15 \cdot (u_{Cm1} + 6e - 8 \cdot u_{Cm1}^2 + 6e - 10 \cdot u_{Cm1}^3)
 \end{aligned}$$

and for the motional branch of the second resonator we have:

$$\begin{aligned}
 u_{Rm2}(i_{Rm2}) &= 4.56 \cdot (i_{Rm2} + 0.5e - 5 \cdot i_{Rm2}^2 + 0.5e - 6 \cdot i_{Rm2}^3) \\
 \varphi_{Lm2}(i_{Lm2}) &= 70e - 9 \cdot (i_{Lm2} + 5e - 3 \cdot i_{Lm2}^2 + 1e - 5 \cdot i_{Lm2}^3) \\
 q_{Cm2}(u_{Cm2}) &= 93.166e - 15 \cdot (u_{Cm2} + 6e - 8 \cdot u_{Cm2}^2 + 6e - 10 \cdot u_{Cm2}^3)
 \end{aligned}$$

2.1.1.3.4.5.1 Comparison with the SPICE solution

After sweeping 100 periods of the voltage source, the output voltage $V(2)$ computed with the proposed algorithm is identical with the SPICE solution (Figure 2.42). A detail is shown in Figure 2.43.

Considering the absolute error required for SPICE $abstol = 1e-12$, the results obtained with these two algorithms have the properties in Table 2.13.

It is noted that for similar values of the total error ΔE_{total} , the total number of steps computed with the proposed algorithm is about 75% of the total number of steps computed with SPICE.

Is interesting to observe the relative energy balance error evolution of the SPICE solution compared with the energy balance relative error computed for

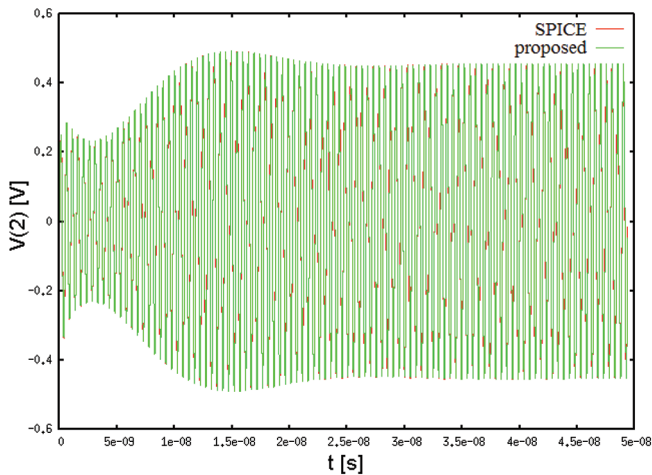


Figure 2.42 Output voltage of the band-pass filter.

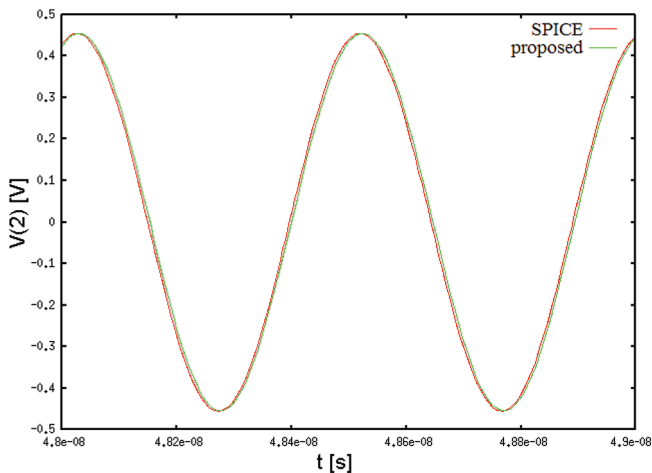


Figure 2.43 Output voltage of the band-pass filter – detail.

Table 2.13 Results obtained for the 5th example

| | Proposed | SPICE |
|--------------------|--------------|-------------------|
| Imposed error | $EER = 9e-5$ | $reltol = 5.5e-6$ |
| Accepted steps | 7863 | 7816 |
| Rejected steps | 448 | 3031 |
| ΔE_{total} | $3.906e-15$ | $1.04e-14$ |
| CPU time | 0.25 s | 0.32 s |

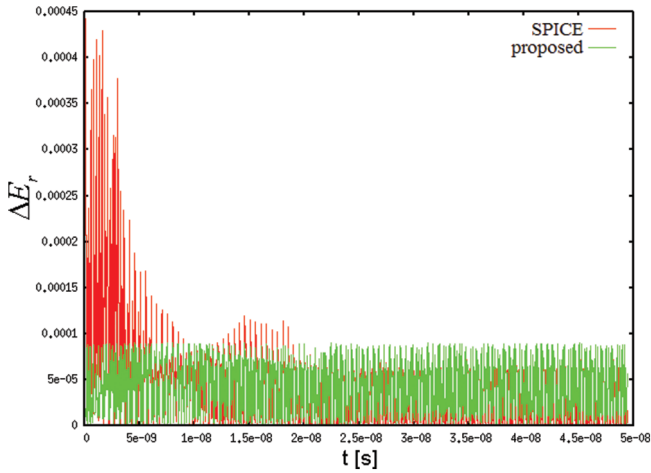


Figure 2.44 Relative energy balance error for SPICE and the proposed algorithm.

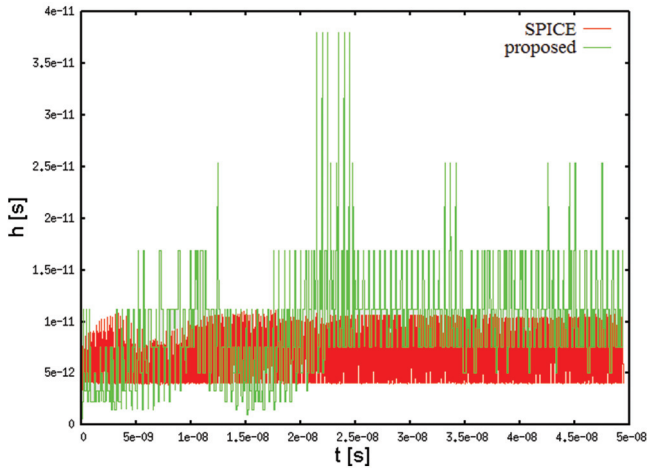


Figure 2.45 Time step evolution for SPICE and for the proposed algorithm.

the proposed algorithm (Figure 2.44). Time step evolution for SPICE and for the proposed algorithm is given in Figure 2.45.

2.1.1.3.5 Conclusions

A new error for transient analysis of electrical circuits has been proposed. Using this approach, if the maximum relative energy balance error is small

enough and the circuit doesn't have too many branches, it is possible to estimate the overall correctness of the transient analysis for the entire circuit and for the entire time interval, unlike the LTE type errors and those used in PAN.

A new algorithm for the time step choice, using this error has been developed. Preliminary tests, carried out on linear and nonlinear circuits with a relatively small number of elements, show that for a similar global error, the proposed algorithm makes fewer steps, particularly the number of rejected steps being reduced compared with the SPICE algorithm. Moreover, the proposed algorithm is better than the algorithm of SPICE in terms of computing time.

If the energy balance errors are not correctly enough computed, the solution accuracy can be wrongly estimated. In comparison with the SPICE family programs, the resistive circuit solution containing companion models is more accurate because it is computed in *long double* precision and a test to check its power balance is made. It follows that the change in accumulated energy of dynamic elements is correctly computed. Although the quadratic interpolation used to avoid peak voltages and currents in the range of interest seems more natural than a interpolation polynomial of third degree used in the truncation errors calculation, an estimation of error produced by this interpolation in the computation of the energy absorbed by the resistors and sources was not made. This topic will be a priority for further research.

The computation of all state variables and their derivatives with the same relative error is too restrictive. The proposed approach, imposing the same relative energy balance error for each time step, seems more natural although errors compensation may occur.

Beside the above mentioned topics, future research will be carried out to test this new algorithm on larger nonlinear circuits driven by signals with steep variations and to develop adaptive strategies for choosing the time step.

2.1.1.4 Frequency warping in linear circuits

The computation errors in the transient analysis can be interpreted as a change of frequency in autonomous circuits [6] or a response of a different period than the excitation one for the non-autonomous circuits with customary behavior and high quality factor [7]. Such errors are called in the literature "frequency warping" and are explained as an intrinsic property of the first or second order numerical integration methods. To eliminate this type of errors the use of higher order numerical integration methods is proposed, which leads to

more complicated computations. In [8] is shown that simply by appropriate choosing of the relative error $reltol$, the trapezoidal method can give a solution very close to the exact one.

2.1.1.4.1 Parallel RLC autonomous circuit

Consider the RLC parallel circuit mentioned in [6] (Figure 2.46) with the initial state $V_C = 10V$, $I_L = 0$ mA.

The analytical solution $V_C(t)$, computed with MAPLE is shown in Figure 2.47 together with the SPICE solutions for the $reltol = 1e-3$ and $reltol = 1e-6$.

While the solution given by SPICE for $reltol = 1e-3$ can be seen as a result of alteration of its own frequency value phenomenon, the solution given by SPICE for $reltol = 1e-6$ is virtually indistinguishable by the analytical solution (at this time scale).

A detail of $V_C(t)$ is given in Figure 2.48.

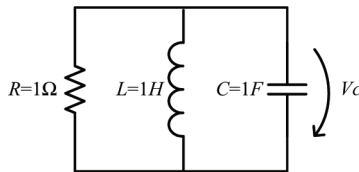


Figure 2.46 Parallel RLC circuit.

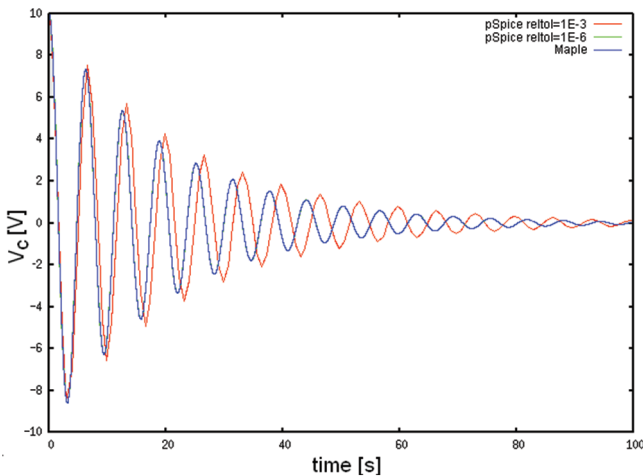


Figure 2.47 Voltage of the parallel RLC circuit.

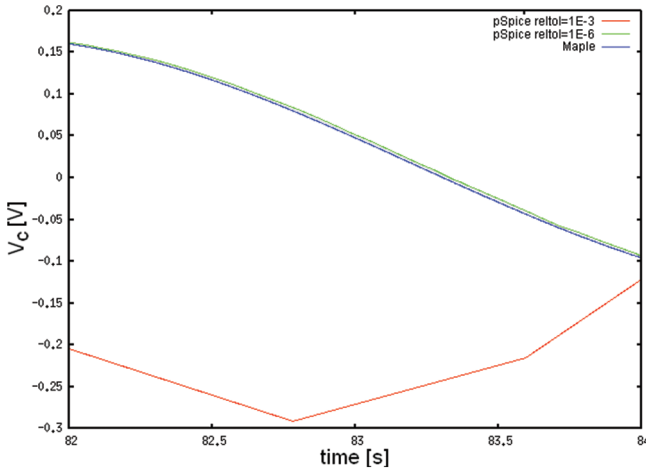


Figure 2.48 Voltage of the parallel RLC circuit – detail.

At least in this case, it seems that the errors introduced by the trapezoidal method are the result of LTE accumulation rather than a change in the natural frequency of the circuit [8].

2.1.1.4.2 High quality factor circuit

To calculate the analytical solution, only the reaction circuit from the transistor emitter of the amplifier studied in [7] has been considered (Figure 2.34). This

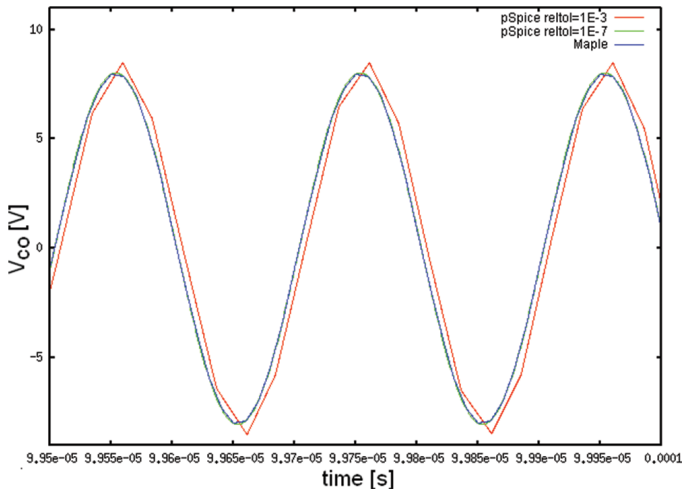


Figure 2.49 Response of the high quality factor circuit.

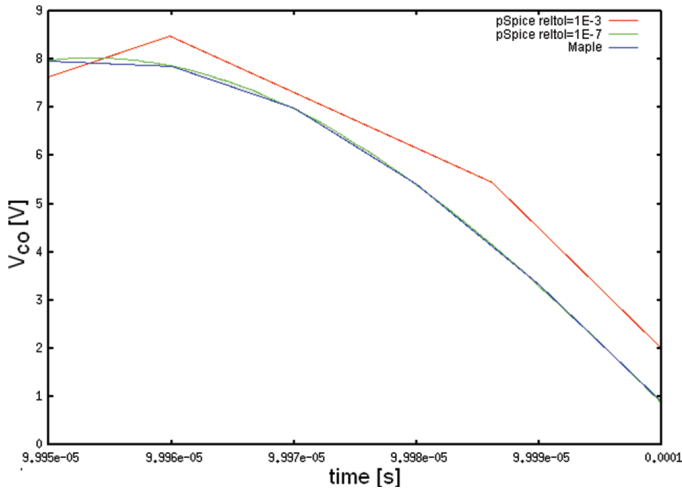


Figure 2.50 Response of the high quality factor circuit – detail.

circuit contains a quartz crystal having the quality factor $Q = 1.6e+6$ (at the series resonance frequency of 5 MHz) and it was analyzed from the null initial state and driven by a sinusoidal signal of 5 MHz.

The analytical solution $V_{C0}(t)$ after sweeping 487 periods of the source signal, computed with MAPLE, is shown in Figure 2.49 together with the SPICE solutions for $reitol = 1e-3$ and $reitol = 1e-7$. A detail of this solution is given in Figure 2.50.

A similar interpretation (the errors introduced by the trapezoidal rule are the result of LTE accumulation, not a change of the response period for a customary behavior circuit) can be given for the results obtained analyzing this circuit. Moreover, the response for $reitol = 1e-7$ is practically identical to the analytical solution.

2.1.1.4.3 Linear band-pass BAW filter

In the following we present a case study aimed to estimate the efficiency of using the trapezoidal method and the Gear methods (from the second order to the sixth one) [43].

Consider the pass-band filter in Figure 2.34 built with two BAW resonators and driven by a sinusoidal source having $f_0 = 2.025$ GHz.

The numerical solution obtained with each of the above mentioned methods implemented in SPICE is compared to the exact (analytical) solution, computed by MAPLE. This circuit has quality factor $Q = 1.57e+6$ at $f_s = f_0$ frequency and was analyzed starting from the null initial state.

The response $V(z)$ is roughly the same with the analytical solution using $reltol = 1e-10$ for all methods. A detail of this response is given in Figure 2.51. In order to estimate the error with respect to the exact solution we compute

$$\varepsilon = \max_k \frac{\sqrt{\int_0^T \Delta x_k^2(\tau) d\tau}}{N}$$
 where $T = tstop$, $k = 1, \dots, p$ is the index of the state variable, $\Delta x_k = x_k - x_{ek}$, (x_k -numerical solution, x_{ek} -exact solution) and N is the number of accepted time steps [43].

The main characteristics of the transient analyses with $T = 30/f_0$ are given in Table 2.14 [43].

The most accurate result is given by the trapezoidal method, while the most efficient method is Gear 5. Gear 6 is less efficient than Gear 5 because of the time spent with the computation of the coefficients in Gear's formula, which must be done for each time step. For a circuit with 100 elements or

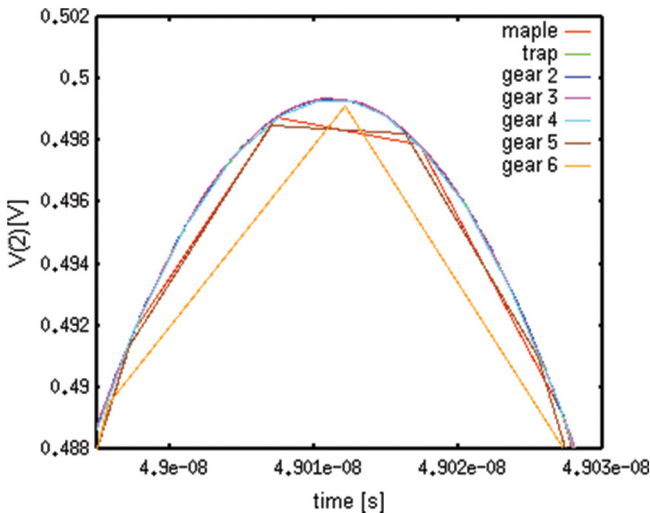


Figure 2.51 High Q circuit response – detail [43].

Table 2.14 Transient analysis results for circuit in Figure 2.34

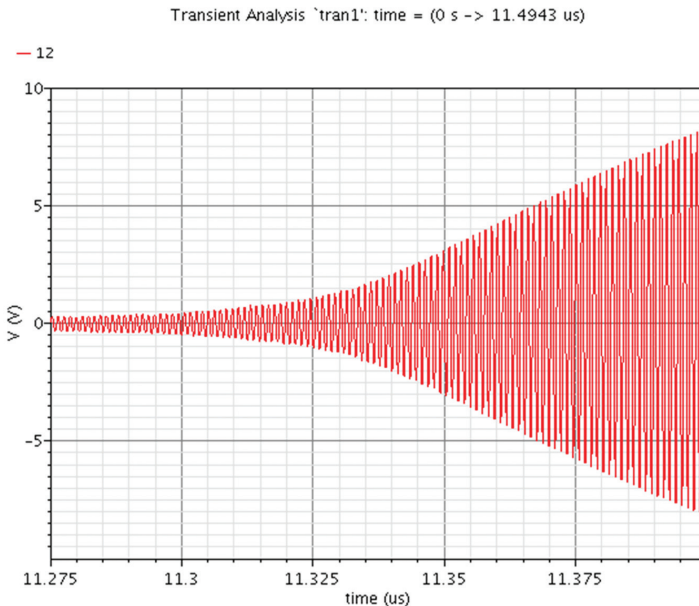
| Method | Accepted Steps | Rejected Steps | CPU Time | ε |
|--------|----------------|----------------|----------|---------------|
| Trap | 103118 | 522 | 6.64 s | $5.01e-8$ |
| Gear 2 | 143175 | 537 | 9.51 s | $1.28e-7$ |
| Gear 3 | 11090 | 86 | 0.80 s | $3.29e-7$ |
| Gear 4 | 4302 | 170 | 0.38 s | $1.54e-7$ |
| Gear 5 | 1568 | 17 | 0.21 s | $4.80e-6$ |
| Gear 6 | 1197 | 55 | 0.34 s | $5.72e-6$ |

more, this computation requires a negligible CPU time and Gear 6 should be the most efficient. So that the recommendation to use Gear 5 (or Gear 6) given in [14] in order to avoid the “frequency warping” effect remains valid, but for efficiency reasons [43].

2.1.2 Envelope Following and the Analysis with Two Time Variables

Consider a circuit driven by an amplitude modulated signal (Figure 2.52 (a)). If the carrier period is T_c and the modulation signal period is T_m , and $T_c \ll T_m$ the circuit response to two carrier periods which are close each other but are placed at a certain non-zero distance in time may be considered as similar. It follows that, performing a transient analysis, it is not always mandatory to sweep all carrier periods of the excitation. So, jumping over some carrier periods the transient analysis duration may be shortened. An *envelope following method* makes this kind of jumps, computing a correct transient response (Figure 2.52 (b)).

If the error for the jump computation is small enough, the envelope following algorithm doesn’t make any jump and this analysis uses the same



(a)

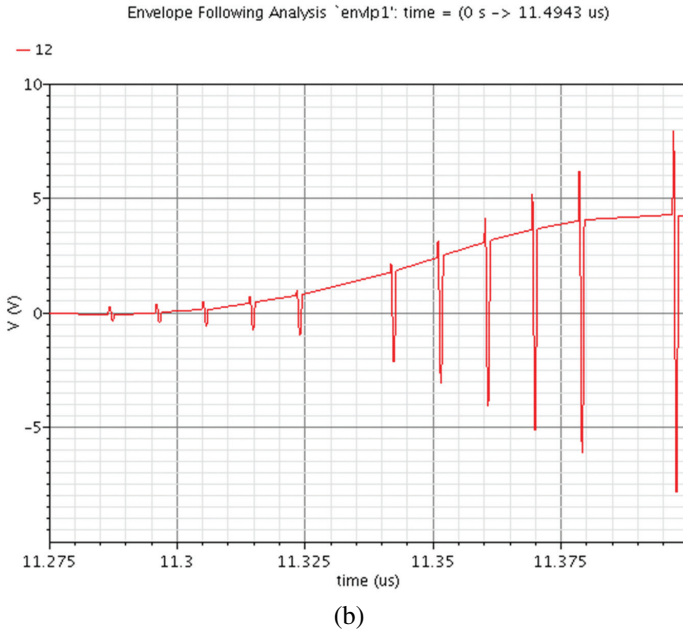


Figure 2.52 Envelope following: (a) excitation, (b) response.

time steps as the transient analysis. In this case the computation time is larger than that of the transient analysis, because it includes the calculations made for the unsuccessful jump attempts.

2.1.2.1 Kundert algorithm implemented in SPECTRE RF

Figure 2.53 shows how the envelope following algorithm works [15]. In this algorithm two previous values are used to compute a new one. It is assumed that the values are known at the beginning of the carrier period for the time values $t_{(n-1)}$ and t_n which are separated by an integer number of carrier periods T . The state variable values $v(t_{(n-1)} + T)$ at $t_{(n-1)} + T$ are obtained from those at $t_{(n-1)}$ integrating over a time period, i.e.

$$v(t_{(n-1)} + T) = \Phi(v(t_{(n-1)}), t_{(n-1)}, t_{(n-1)} + T) \quad (2.18)$$

where Φ is the transition function. The state variables values at t_n and $t_n + T$ are related by $v(t_n + T) = \Phi(v(t_n), t_n, t_n + T)$, also.

The goal of the algorithm is to find the state variable value at a new time value $t_{(n+1)}$ several periods away from t_n so that the point with coordinates $(v(t_{(n+1)}), t_{(n+1)})$ lies with a certain error on the parabola passing through three points whose coordinates are: $(v(t_{(n-1)}), t_{(n-1)})$,

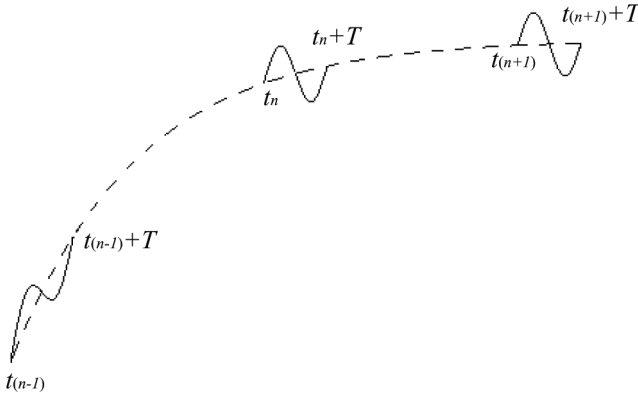


Figure 2.53 Kundert's envelope following algorithm.

$(v(t_{(n)}), t_{(n)})$, and $(v(t_{(n+1)} + T), t_{(n+1)} + T)$. The value $v(t_{(n+1)} + T)$ is given by

$$v(t_{(n+1)} + T) = \Phi(v(t_{(n+1)}), t_{(n+1)}, t_{(n+1)} + T) \quad (2.19)$$

On the other hand, from the interpolation condition, $v(t_{(n+1)} + T)$ can be written as a linear combination of $v(t_{(n-1)})$, $v(t_n)$, $v(t_{(n+1)})$, meaning that there exist real constants $\alpha_1, \alpha_2, \alpha_3$ so that [15].

$$\alpha_1 v(t_{(n-1)}) + \alpha_2 v(t_n) + \alpha_3 v(t_{(n+1)}). \quad (2.20)$$

The real constants $\alpha_1, \alpha_2, \alpha_3$ may be obtained by standard techniques [15]. Combining these two equations it follows:

$$\alpha_1 v(t_{(n-1)}) + \alpha_2 v(t_n) + \alpha_3 v(t_{(n+1)}) - \Phi(v(t_{(n+1)}), t_{(n+1)}, t_{(n+1)} + T) = 0 \quad (2.21)$$

which can be used to determine $v(t_{(n+1)})$ with the Newton-Raphson method. At each iteration, from the Newton-Raphson equation,

$$\left[\alpha_3 I - \frac{\partial \Phi}{\partial v(t_{(n+1)})} \right] \Delta v(t_{(n+1)}) = RHS \quad (2.22)$$

is computed a correction $\Delta v(t_{(n+1)})$ of $v(t_{(n+1)})$, where the right hand side (*RHS*) value results from (2.21).

This process is repeated until the interpolation equation is satisfied with the imposed relative error. If this error cannot be satisfied, t_{n+1} is chosen

closer to t_n and the process is repeated. These three steps are repeated until the desired stop time is reached.

If the algorithm cannot make any jump, the analysis is reduced to the transient one. As it is shown in the examples, this method cannot always be more efficient than transient analysis due to the jumps recalculation.

2.1.2.2 Brambilla-Maffezzoni algorithm implemented in PAN

Consider the state equation

$$\frac{dy(t)}{dt} = f(y, t) \quad (2.23)$$

where $y(t): \mathbb{R}^1 \rightarrow \mathbb{R}^N$, $f(y, t): \mathbb{R}^{N+1} \rightarrow \mathbb{R}^N$ which models a customary behavior non-autonomous circuit having a T-periodic excitation and an unique T-periodic response.

The nonlinear transition function,

$$\Phi(y(t), t) = y(t) + \int_{\tau=t}^{\tau=t+T} f(y(\tau), \tau) d\tau \quad (2.24)$$

computes the state equation solution at the time value $t + T$, starting from the value $y(t)$.

Assume that we have solved (2.24) up to the period m defined as $[t_m = mT, t_{m+1} = (m + 1)T]$, where m is a positive integer. At a subsequent time value $t_n = t_{m+1} + H$, where $H = (n - m) \cdot T$, $n > m$ is a multiple of T , the state variables $y_n = y(t_n)$ can be estimated as follows. A modified variant of a numerical integration methods such as Forward Euler (FE), Backward Euler (BE) or Trapezoidal rule (TP) is used for the envelope following methods described by the relations 2.25'–2.27' [16], where y_m and y_n represents samples of the envelope, and H is the jump over $n-m$ periods of the carrier.

The numerical integration methods are:

$$\text{FE: } y_n = y_m + H \left. \frac{dy}{dt} \right|_{t=t_m} \quad (2.25)$$

$$\text{BE: } y_n = y_m + H \left. \frac{dy}{dt} \right|_{t=t_n} \quad (2.26)$$

$$\text{TP: } y_n = y_m + \frac{H}{2} \left(\left. \frac{dy}{dt} \right|_{t=t_m} + \left. \frac{dy}{dt} \right|_{t=t_n} \right) \quad (2.27)$$

Their corresponding envelope following methods are defined by:

$$\text{FE: } y_n = y_m + \frac{H}{T}(y_{m+1} - y_m) \quad (2.25')$$

$$\text{BE: } y_n = y_m + \frac{H}{T}(y_{n+1} - y_n) \quad (2.26')$$

$$\text{TP: } y_n = y_m + \frac{H}{2T}(y_{n+1} - y_n + y_{m+1} - y_m) \quad (2.27')$$

It can be observed that (2.26) and (2.27) are implicit integration formulas because the unknown term y_{n+1} is in the right-hand of the expression. The term y_{n+1} can be obtained by integrating (2.23) on the interval $[t_n, t_{n+1}]$ starting from the initial state $y(t_n)$. However, the value y_{n+1} depends on y_n through the unknown transition function (2.24): $y_{n+1} = \Phi(y_n, t_n)$. Substituting $\Phi(y_n, t_n)$ in (2.26') and (2.27') the following nonlinear algebraic equations are obtained.

$$\Gamma^{BE}(y_n) = y_n - \Phi(y_n, t_n) + \frac{T}{H}(y_n - y_m) = 0 \quad (2.28)$$

$$\Gamma^{TP}(y_n) = y_n - \Phi(y_n, t_n) + y_m - \Phi(y_m, t_m) + \frac{2T}{H}(y_n - y_m) = 0 \quad (2.29)$$

It can be noted that if $H \rightarrow \infty$, $\Gamma^{BE}(y_n)$ no longer depends on y_m and becomes the equation that represents the shooting method

$$\lim_{H \rightarrow +\infty} \Gamma^{BE}(y_n) = \overbrace{y_n - \Phi(y_n, t_n)}^{\text{shooting method}} = 0 \quad (2.30)$$

where, in this case, y_n is the periodic steady state of the circuit. Considering $\Gamma^{TP}(y_n)$, a similar result is obtained

$$\lim_{H \rightarrow +\infty} \Gamma^{TP}(y_n) = \overbrace{y_n - \Phi(y_n, t_n)}^{\text{shooting formulation in the } n - \text{th period}} + \overbrace{y_m - \Phi(y_m, t_m)}^{\text{shooting formulation in the } m - \text{th period}} = 0. \quad (2.31)$$

Because any variant of the periodic steady state correct calculation leads to the same result, the circuit having a unique periodic solution, the terms for m and n periods of (2.31) have the same solution, $y_n = y_m$. Therefore, the envelope following method can be considered as a modified shooting method.

The main difficulty when applying the BE and TP integration methods modified for the envelope following is that these are implicit formulas, requiring the transition function $\Phi(y, t)$ evaluation, which can be done only numerically. If we assume that (2.28) and (2.29) are solved with the Newton iterative method, a transient analysis is required at each iteration of the Newton algorithm. Two significant remarks follow [16]:

- the number of Newton iterations required to converge to a solution for the time instant t_n , should not be greater than $(n - m) = H/T$, or else the envelope following method is less efficient than a conventional transient analysis performed on the entire time interval H ,
- it is mandatory to give a good initial approximation to Newton method so that it can converge in few iterations.

To obtain this estimation, $\Phi(y, t)$ is expanded in Taylor series with respect to $y(t)$ and only the first order term is kept.

$$\Phi(y_n, t) = \Phi(y_m, t) + \left. \frac{d\Phi}{dy} \right|_{y=y_m} (y_n - y_m) \quad (2.32)$$

where $\left. \frac{d\Phi}{dy} \right|_{y=y_m} \in \mathfrak{R}^{N \times N}$ is the sensitivities matrix. Substituting (2.32) in (2.28) yields

$$y_n^{p-BE} - \left[\Phi(y_m, t_m) + \left. \frac{d\Phi}{dy} \right|_{y=y_m} (y_n^{p-BE} - y_m) \right] + \frac{T}{H} (y_n^{p-BE} - y_m) = 0 \quad (2.33)$$

which can be rewritten as

$$y_n^{p-BE} = \left[\left(1 + \frac{T}{H} \right) I - \left. \frac{d\Phi}{dy} \right|_{y=y_m} \right]^{-1} \cdot \left[y_{m+1} + \left(\frac{T}{H} I - \left. \frac{d\Phi}{dy} \right|_{y=y_m} \right) y_m \right] \quad (2.34)$$

where $I \in \mathfrak{R}^{N \times N}$ is the unity matrix and $\left. \frac{d\Phi}{dy} \right|_{y=y_m}$ is the sensitivities matrix of y_{m+1} with respect to y_m . Since Newton-Raphson method is used to solve (2.28), the $d\Phi/dy$ term is available at each iteration, as part of the Jacobian matrix. Expression (2.34) is the predictor, and, used with BE corrector it estimates $y(t_n)$ with y_n^{p-BE} starting from the known values of y_{m+1} and y_m .

The analysis algorithm based on BE has the following steps

1. Do the numerical integration of the equations for the $[t_m, t_{m+1}]$ time interval starting from y_m initial condition y_m .

2. During the transient analysis compute $\frac{d\Phi}{dy}$.
3. Apply (2.34) and estimate y_n^{p-BE} .
4. Do the numerical integration of the equations for the $[t_n, t_{n+1}]$ starting from y_n^{p-BE} .
5. Compute $\Phi(y_n^{p-BE}, t_n)$ and $\frac{d\Phi}{dy}\Big|_{y=y_n^{p-BE}}$.
6. Apply the Newton method to (2.28) and do only one iteration:

$$y_n^1 = y_n^p - \left[\left(1 + \frac{T}{H} \right) I - \frac{d\Phi}{dy}\Big|_{y=y_n} \right]^{-1} \cdot \left[y_n^p - \Phi(y_n^p, t_m) + \frac{T}{H}(y_n^p - y_m) \right].$$

7. If t_n is after the final time of the analysis stop the computation, otherwise continue with step 3.

Similar to the BE, a predictor for the TP can be determined:

$$y_n^{p-TP} = \left[\left(\frac{2T}{H} + 1 \right) I - \frac{d\Phi}{dy}\Big|_{y=y_m} \right]^{-1} \cdot \left[2y_{m+1} - \left(\frac{d\Phi}{dy}\Big|_{y=y_m} + \left(1 - \frac{2T}{H} \right) I \right) y_m \right] \quad (2.35)$$

2.1.2.3 Examples

To illustrate the concepts presented above, some circuits used in radio communications are considered:

2.1.2.3.1 AM demodulator

This circuit in Figure 2.54 is driven by the amplitude modulated signal:

$$e(t) = 2 \sin(2\pi f_p t)(1 + \sin(2\pi f_m t))$$

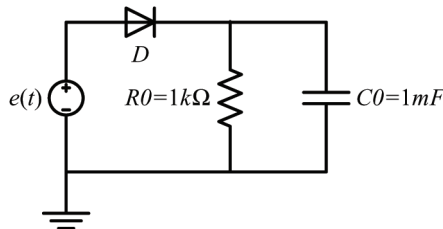


Figure 2.54 AM demodulator.

Consider $f_m=1$ KHz and $f_p=1$ MHz, 10 MHz, 100 MHz.

The algorithm of SPECTRE RF gives the correct circuit response but the envelope following analysis computation time is 2-3 times smaller than the time used by the transient analysis even if the ratio between the carrier frequency and modulation frequency is only 10^3 (Figures 2.55 and 2.56). A better efficiency is obtained if this ratio increases (Table 2.15).

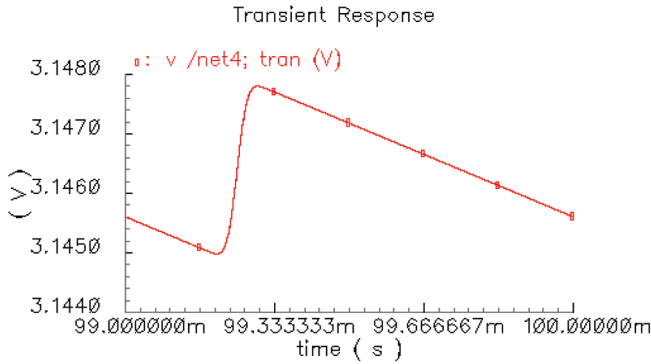


Figure 2.55 AM demodulator – the transient analysis response.

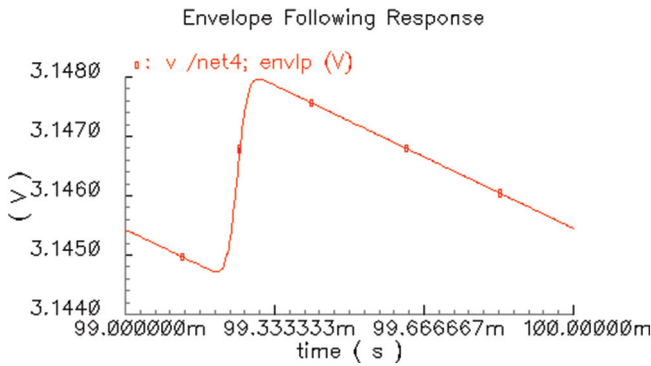


Figure 2.56 AM demodulator – the envelope following analysis response.

Table 2.15 Results obtained for the AM demodulator with different carrier frequencies

| $\log_{10}\left(\frac{f_p}{f_m}\right)$ | Transient Analysis (Tran) | Envelope Following Analysis (Envlp) |
|---|---------------------------|-------------------------------------|
| 3 | 80.08 s | 29.7 s |
| 4 | 800.8 s | 138.7 s |
| 5 | 8008 s | 314.8 s |

2.1.2.3.2 In-Phase and quadrature modulator (IQ)

The circuit is composed of a modulator and an amplifier (Figure 2.57).

The modulator consists of two multipliers and an adder, each multiplier having a rectangular input signal of low frequency (1 MHz) and a sinusoidal signal of a higher frequency (1 GHz). The two output signals from each multiplier are inputs to the adder. The selective amplifier is designed to filter and amplify the input signals around 1 GHz.

At one entry of each multiplier the signal in Figure 2.58 has been applied simulating a digital signal. Due to the envelope following method operating mode which involve relatively large jumps on the time axis, the same input signal is represented as in the following figure.

The local oscillator is considered as a sine wave of 1V magnitude and is applied in-phase and in-quadrature to the inputs of the two ideal multipliers.

This circuit has been simulated in SPECTRE RF with two methods: the envelope following method (ENVLV) and the transient analysis method

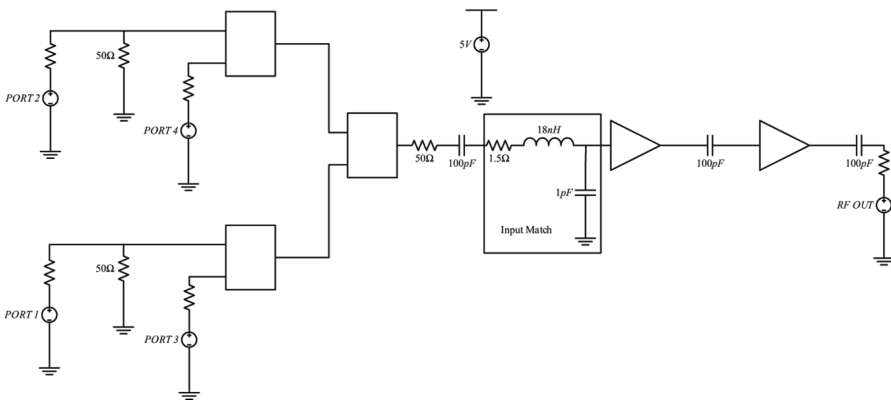


Figure 2.57 In-phase and quadrature modulator.

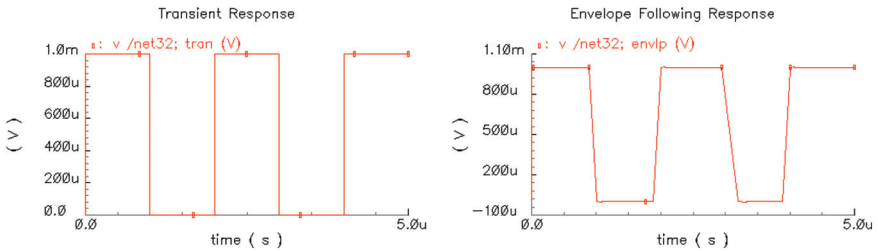


Figure 2.58 In-phase and quadrature modulator – input signal.

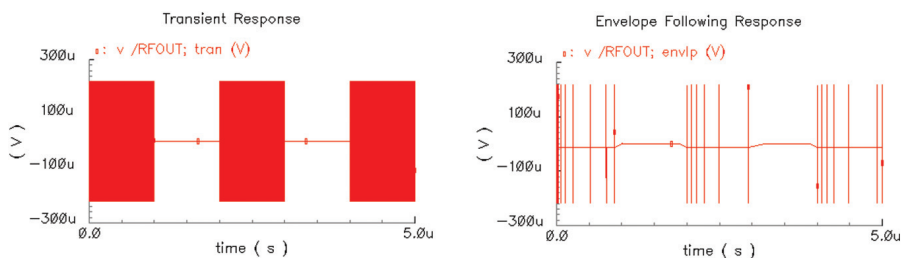


Figure 2.59 In-phase and quadrature modulator – responses.

Table 2.16 Results obtained for in-phase and in-quadrature modulator

| | Transient Analysis (Tran) | Envelope Following Analysis (Envlp) |
|--------------------------|------------------------------|--|
| errpreset = moderate | 35.25 s | 5.6 s |
| errpreset = conservative | 6.63 s | 790 ms |

(TRAN). In the following, a comparison of the results obtained with these two methods is made.

The response obtained with these two methods is shown in Figure 2.59.

Comparing the results obtained with these two methods it can be observed that relative to the transient analysis method, the simulation time is smaller in the case of ENVLP method due to the jumps. This explains the different waveforms obtained for the two methods. However, if the algorithm cannot make any jump, ENVLP analysis is reduced to the transient one. Not always this analysis can be more efficient than the transient analysis due to jump failed attempts and/or recalculation.

To illustrate the problems that arise in simulating the RF circuits with different envelope following algorithms, a class C amplifier (Figure 2.3) and a commercial down-converter mixer ne600p (Figure 2.4) have been simulated.

Table 2.17 shows the results of the envelope following analysis from SPECTRE RF, and PAN [4, 5]. The circuits and the absolute error values are the same as those mentioned in the transient analysis. Some additional settings are made to simulate with the envelope following method. The relative error for the jump calculation is *reltol* multiplied by *envlteratio* in SPECTRE RF, while *ereltol* is the relative error used by PAN for the jump computation.

The waveforms obtained simulating these two circuits are shown in Figures 2.60–2.65. The effect of changing *envlteratio* can be seen in Figure 2.60.

Table 2.17 Results of the envelope following analysis from SPECTRE RF and PAN

| Circuit | Reltol | SPECTRE RF | PAN | Comments |
|-------------------|--------|-------------------|----------|---------------------------------------|
| | | | | SPECTRE: Envlteratio PAN: Ereltol |
| Class C amplifier | | 11.9 s | 115 s | envlteratio = 10 ereltol = 1e-4 |
| | 1e-5 | 8.57 s | 62.36 s | envlteratio = 100 ereltol = 1e-3 |
| | | 6.72 s | 30.44 s | envlteratio = 1000 ereltol = 1e-2 |
| | | 2.8 s | 12.58 s | envlteratio = 10000 ereltol = 1e-1 |
| | 1e-6 | 25.15 s | 108.75 s | envlteratio = 100 ereltol = 1e-4 |
| | | 22.11 s | 65.44 s | envlteratio = 1000 ereltol = 1e-3 |
| | | 13 s | 31.02 s | envlteratio = 10000 ereltol = 1e-2 |
| ne600p mixer | | no jumps | 288.92 s | envlteratio = 10 ereltol = 1e-4 |
| | 1e-5 | no jumps | 295.08 s | envlteratio = 100 ereltol = 1e-3 |
| | | erroneous results | 138.7 s | envlteratio = 1000 ereltol = 1e-2 |
| | | no jumps | 288.40 s | envlteratio = 100 ereltol = 1e-4 |
| | 1e-6 | no jumps | 292.77 s | envlteratio = 1000 ereltol = 1e-3 |
| | | erroneous results | 141.9 s | envlteratio = 10000 ereltol = 1e-2 |

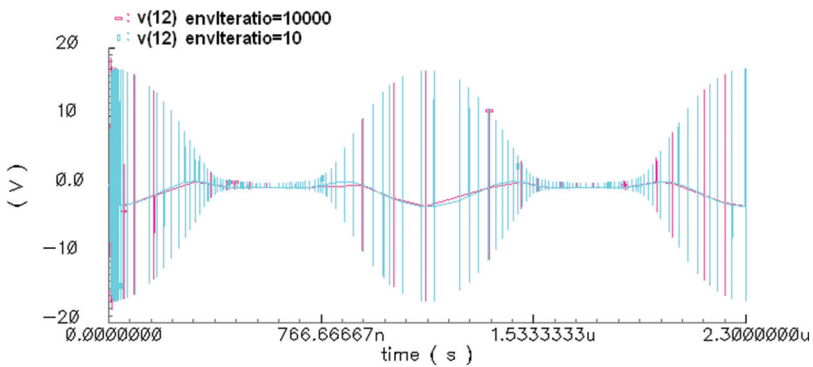


Figure 2.60 Class C amplifier, SPECTRE RF.

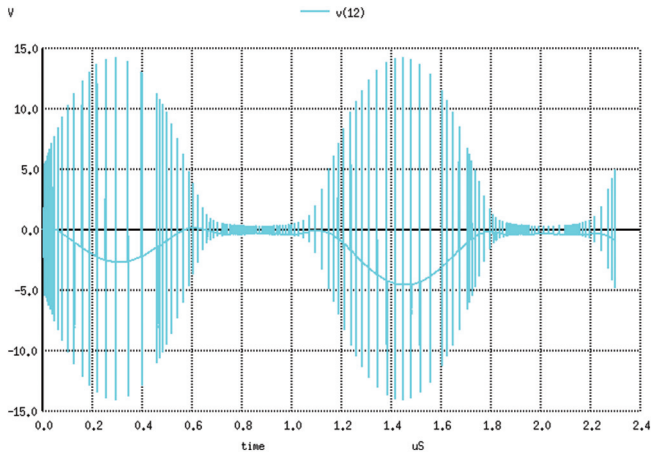


Figure 2.61 Class C amplifier, PAN.

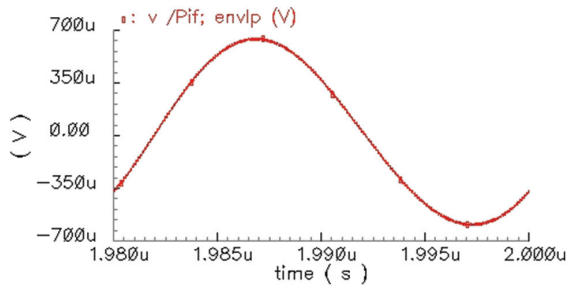


Figure 2.62 ne600p mixer – SPECTRE RF solution.

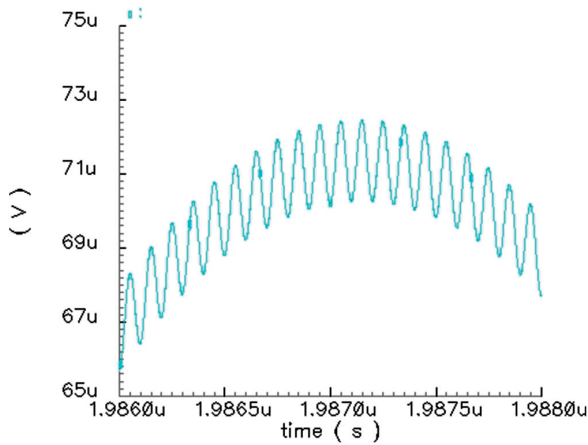


Figure 2.63 ne600p mixer – SPECTRE RF solution (detail).

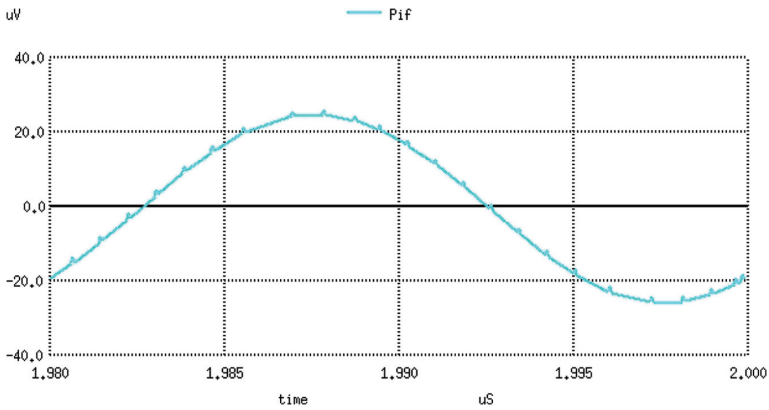


Figure 2.64 ne600p mixer – PAN solution.

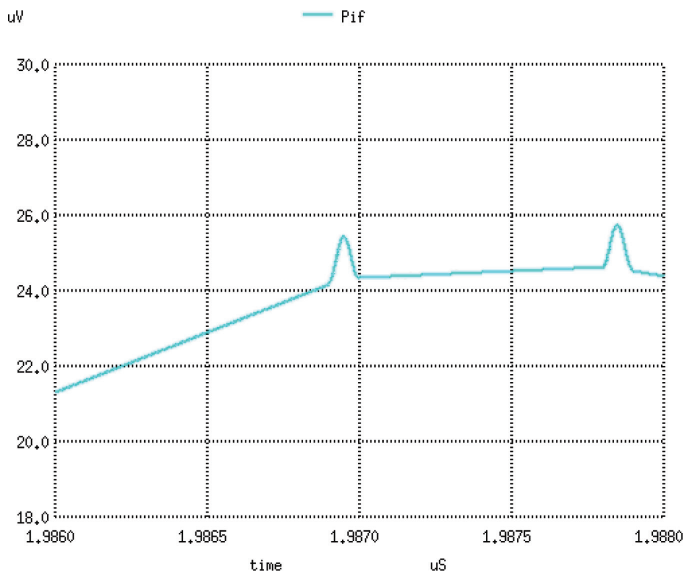


Figure 2.65 ne600p mixer – PAN solution (detail).

Although designed to reduce the computation time, many test circuits show that the envelope following implementations are not competitive with the classical transient analysis.

An example showing that Brambilla's jump algorithm is better than Kundert's algorithm is the ne600p down-converter mixer. From the detailed figure it can be seen that SPECTRE RF cannot make any jump. In this case

the time used by the envelope following analysis is greater than that used for transient analysis.

The result presented in the following figures is obtained by simulating the same circuit with the envelope following algorithm implemented in PAN.

In this case the algorithm works better but the computation time of the envelope following analysis is still greater than the time used by the transient analysis. The simulation time of the envelope following analysis in PAN is close to that of transient analysis if the time interval is very big because the algorithm can make higher jumps when the solution is close to the periodic steady state. In conclusion, for many applications, contrary to expectations, no envelope following algorithm is more efficient than the transient analysis.

2.1.2.3.3 Remark

The envelope following analysis from PAN allows you to choose any value for the jump, not only a multiple of the largest frequency period (the local oscillator period for the mixer case). If you choose to jump exactly the intermediate frequency period ($f_{IF} = f_{LO} - f_{RF}$) the analysis looks like a shooting method which not only displays the periodic steady state solution but the whole analysis period. This is the only way that gives good results faster than the transient analysis, but due to the large jump, the transient response at the beginning of the analysis is lost (Figure 2.66).

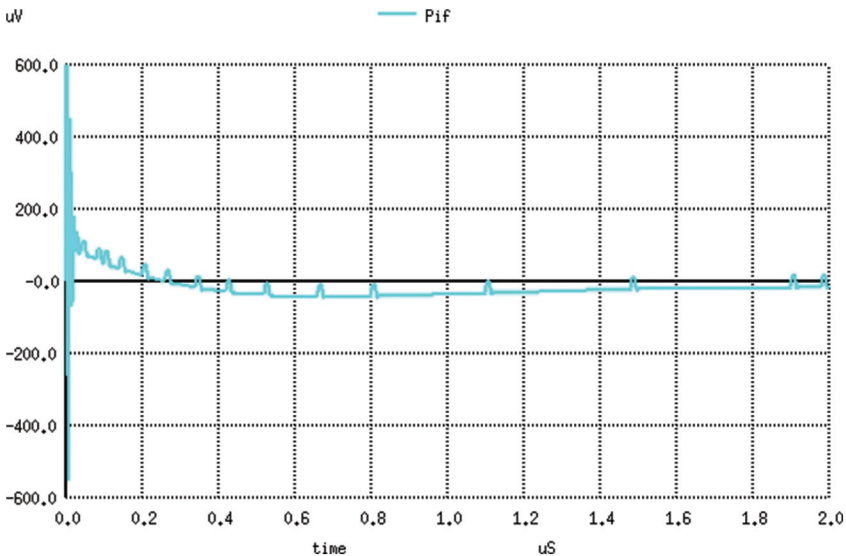


Figure 2.66 ne600p mixer – the response corresponding to f_{RF} period jump.

Considering the absolute error of 10^{-12} and the relative errors of 10^{-5} and 10^{-6} the envelope following method analysis has been done with SPECTRE RF and PAN. Different values for the relative error were considered in the jump calculation, so that a correct result be obtained. When no jump attempt is made, simulation time is much greater than for a simple transient analysis. Even if some jumps are made, the classical transient analysis is much more efficient than the envelope following method [5].

In Figure 2.67 is presented a linear test circuit used to illustrate the low efficiency of the envelope following method [5]. The independent sources describe an amplitude modulated signal with the carrier frequency $f_c = 1 \text{ MHz}$ and the modulation frequency $f_m = 1 \text{ KHz}$. The RI , LI , CI series branch produces a transient component of 100 MHz.

The response is the voltage on the C capacitor (V [4]).

The same errors values for all envelope following method simulations in PAN and SPECTRE RF have been used: $reltol = 1e-6$, $iabstol = 1e-12$, and $vabstol = 1e-12$.

All the above computations lead to the same circuit solution, independently of the analysis (transient or envelope following) and software (SPECTRE RF or PAN).

In order to compare the time step evolution for the transient analysis or envelope following, the errors have been set so that the envelope following makes no jump. In this case, the waveform obtained with the envelope following analysis is the same as that computed by the transient analysis, and therefore a comparison of the simulations is relevant. In Figure 2.68 are given the time step values obtained by SPECTRE RF considering the maximum

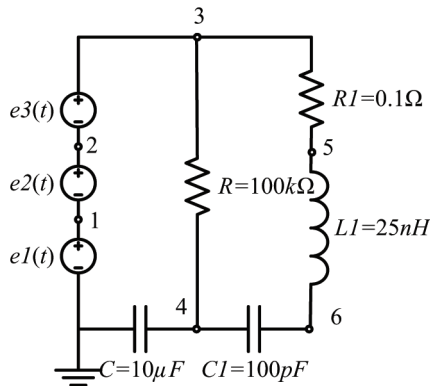


Figure 2.67 Linear test circuit.

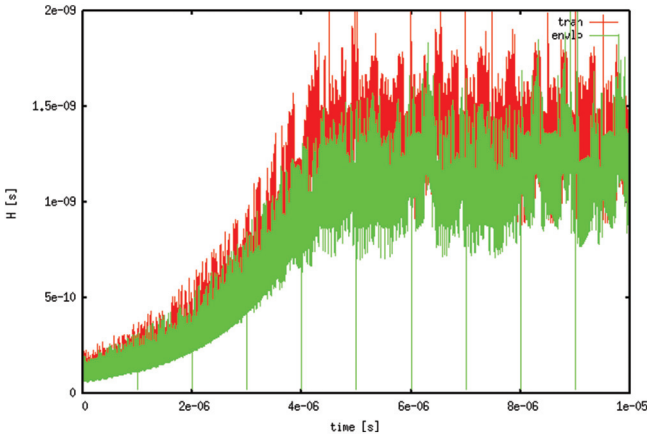


Figure 2.68 Time step for the transient and for the envelope following analyses from SPECTRE RF.

relative error for the jump computation (corresponding to $envlteratio = 1000$) for which no jump has been made.

It follows that even if the average time step for the transient analysis is only about 50% higher than the envelope following one, the simulation time for the envelope method is about nine times greater. This result can be explained both by unsuccessful jump attempts, as well as due to the drastic reduction of the time step after each jump. In Figure 2.68 has been used $errpreset = conservative$ option which implies that the maximum time step is $carrierperiod/100$. With $errpreset = moderate$ corresponding to a maximum time step of $carrierperiod/50$ a similar average time step to that obtained with the transient analysis has been achieved.

Using a similar setup for the envelope analysis in PAN ($ereltol = 1e-6$) the results in Figure 2.69 are obtained. Even if PAN allows it, the minimum time step in this analysis is not set by the user. The minimum and the maximum time step are computed by PAN in this example. In this case, the simulation time for the envelope analysis is two times higher than that for the transient analysis.

In these circumstances the simulation time for the envelope analysis with SPECTRE RF is about 17 times greater than that for PAN, while the simulation time for the transient analysis with SPECTRE RF is about 4 times greater than that for PAN (Figure 2.70). The maximum time step in the envelope analysis from PAN is computed according to the minimum jump time H_m . The minimum time step h_{min} can be chosen by the user, but it is better to

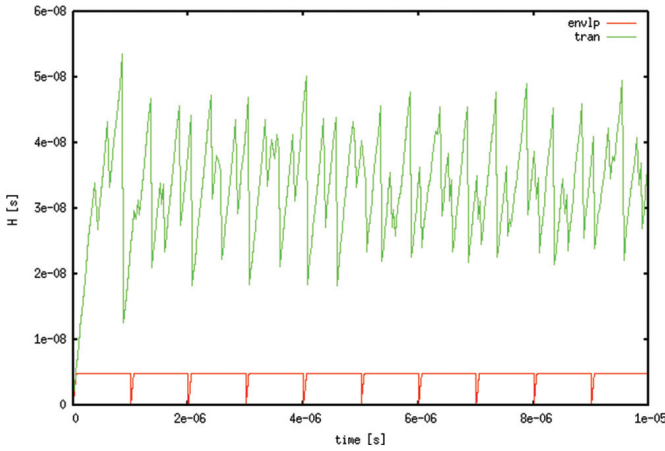


Figure 2.69 The time step for the transient and for the envelope following analyses from PAN.

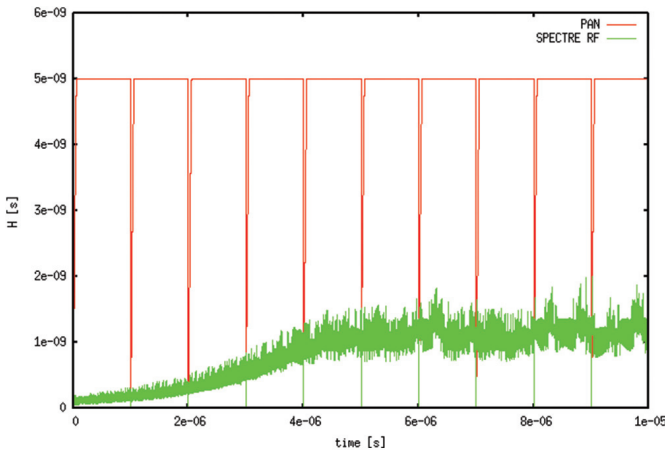


Figure 2.70 Time step for the envelope following analysis from SPECTRE RF and PAN.

let the program to compute it. These aspects are illustrated in Table 2.18 and Figure 2.71.

The dependence of h_{\max} on H_m for the envelope analysis with PAN is illustrated in Figure 2.71. A detail of the time step evolution at the beginning of a carrier period is given in Figure 2.72.

Transient components higher than the carrier frequency lead to a time step reduction. A detail given in Figure 2.73 illustrates this for the circuit in

Table 2.18 h_{\min} and H_m influence on the envelope following analysis for a 100 us simulation with PAN

| h_{\min} | $H_m = 1\mu\text{s}$ | | $H_m = 2\mu\text{s}$ | |
|------------|----------------------|---------------------|----------------------|---------------------|
| | CPU time (s) | Max Jump (x H_m) | CPU time (s) | Max Jump (x H_m) |
| $4.00e-09$ | 0.41 | 1 | 0.25 | 1 |
| $2.00e-09$ | 0.62 | 0 | 0.21 | 1 |
| $1.00e-11$ | 0.12 | 7 | 0.09 | 13 |
| $1.00e-12$ | 0.09 | 24 | 0.10 | 10 |
| PAN choice | 0.10 | 21 | 0.11 | 10 |

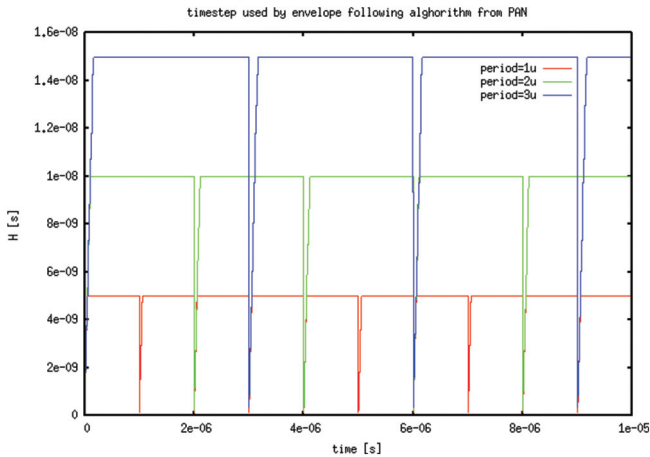


Figure 2.71 Time step for the envelope following analysis for various H_m (PAN).

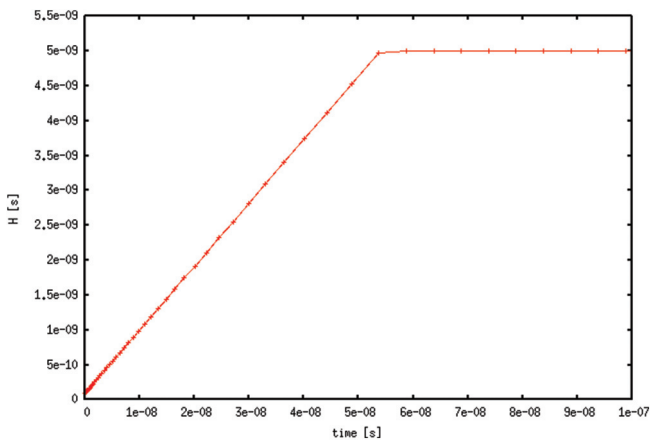


Figure 2.72 Time step evolution – detail.

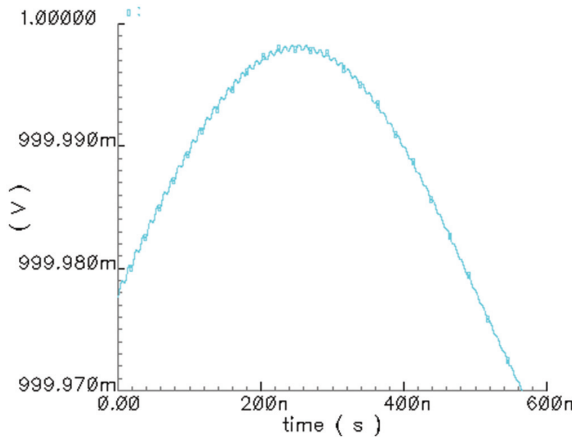


Figure 2.73 Transient components in the envelope following analysis (SPECTRE RF).

Figure 2.67. The time value $t = 0$ in this figure corresponds to $t = 3e-6$ in Figure 2.68, where the time step is relatively small. This type of behavior can occur after an erroneous jump, too.

Computing the jump by integrating the circuit equations, the Brambilla-Maffezzoni method is conceptual superior to Kundert method that fits some points on a parabola. This conclusion is confirmed also by case studies. However, due to the unsuccessful jump attempts computations and reduction of the time step after each jump, in many cases a simulation time shorter than the one corresponding to the classical transient analysis cannot be obtained, as expected. It follows that the development of an efficient envelope following method remains an open problem.

2.1.2.4 Exponential approximation of the envelope

The envelope of the transient response in certain linear circuits evolves like an exponential or like a combination of exponentials, one of them being dominant.

We consider that the value of the state variable v after the jump (at t_{n+1}) interpolates an exponential defined by three state variable values $v(t_{n-1})$, $v(t_n)$, $v(t_{n+1} + T)$ at the corresponding time values (Figure 2.74) [44].

Considering the “local coordinate” system shown in Figure 2.13, it follows:

$$v(t_{(n+1)} + T) = A + B \cdot e^{-\frac{h_1+h_2+T}{\tau}} \tag{2.36}$$

The value $v(t_{(n+1)} + T)$ is obtained from $v(t_{(n+1)})$ integrating the circuit equations over a carrier period, i.e.

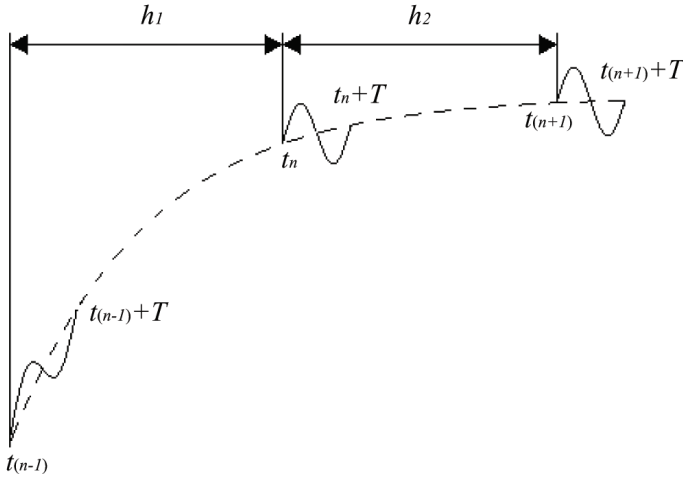


Figure 2.74 Exponential approximation of the envelope.

$$v(t_{(n+1)} + T) = \Phi(v(t_{(n+1)}), t_{(n+1)}, t_{(n+1)} + T) \quad (2.37)$$

where Φ is the transition function. We define [44]:

$$f(v(t_{(n+1)})) = \Phi(v(t_{(n+1)}), t_{(n+1)}, t_{(n+1)} + T) - A - B \cdot e^{-\frac{h_1+h_2+T}{\tau}} \quad (2.38)$$

The equation $f(v(t_{(n+1)})) = 0$ is solved for $v(t_{(n+1)})$ with the Newton-Raphson algorithm:

$$\left[\frac{\partial f}{\partial v(t_{(n+1)})} \right] \Big|_{v(t_{(n+1)})^{(j)}} \cdot (v(t_{(n+1)})^{(j+1)} - v(t_{(n+1)})^{(j)}) = -f(v(t_{(n+1)})^{(j)}) \quad (2.39)$$

where j is the iteration index. The sensitivity matrix is computed as follows:

$$\frac{\partial f}{\partial v(t_{(n+1)})} = \frac{\partial \Phi}{\partial v(t_{(n+1)})} - \frac{\partial A}{\partial v(t_{(n+1)})} - \frac{\partial B}{\partial v(t_{(n+1)})} \cdot e^{-\frac{h_1+h_2+T}{\tau}} - \frac{B(h_1 + h_2 + T)}{\tau^2} \cdot \frac{\partial \tau}{\partial v(t_{(n+1)})} \cdot e^{-\frac{h_1+h_2+T}{\tau}} \quad (2.40)$$

and $\frac{\partial A}{\partial v(t_{(n+1)})}$, $\frac{\partial B}{\partial v(t_{(n+1)})}$, $\frac{\partial \tau}{\partial v(t_{(n+1)})}$ are computed from

$$\begin{cases} v(t_{(n-1)}) = A + B \\ v(t_{(n)}) = A + B \cdot e^{-\frac{h_1}{\tau}} \\ v(t_{(n+1)}) = A + B \cdot e^{-\frac{h_1+h_2}{\tau}} \end{cases} \quad (2.41)$$

replacing $v(t_{(n+1)})$ with $v(t_{(n+1)}) + \Delta v(t_{(n+1)})$ and approximating

$$\frac{\partial A}{\partial v(t_{(n+1)})} \cong \frac{\Delta A}{\Delta v(t_{(n+1)})}.$$

$$\text{Similarly: } \frac{\partial B}{\partial v(t_{(n+1)})} \cong \frac{\Delta B}{\Delta v(t_{(n+1)})}, \quad \frac{\partial \tau}{\partial v(t_{(n+1)})} \cong \frac{\Delta \tau}{\Delta v(t_{(n+1)})}.$$

To obtain a quicker convergence, the algorithm starts with an exponential predictor $v(t_{(n+1)})^{(0)}$ (defined by $v(t_{(n-1)})$, $v(t_{(n)})$, $v(t_{(n)} + T)$), whose coefficients A , B , and τ are obtained by solving a system similar to (2.41) [44]. The iterations (2.39) are repeated until the imposed relative error limit ε_{r0} for $v(t_{(n+1)})$ is satisfied:

$$\varepsilon_r = \frac{\left\| v(t_{(n+1)})^{(j)} - v(t_{(n+1)})^{(j+1)} \right\|}{\max\left(v(t_{(n+1)})^{(j)}, v(t_{(n+1)})^{(j+1)}\right)} \leq \varepsilon_{r0} \quad (2.42)$$

The solving of the system (2.41) for A , B , and τ needs a good initial guess in order to avoid a great number of Newton-Raphson iterations. The most sensitive initial value is that of τ [44]. Its initial guess can be chosen as follows:

$$\tau = \frac{h_1}{\ln\left(\frac{(v(t_n) - v(t_{n-1}))h_2}{(v(t_{n+1}) - v(t_n))h_1}\right)} \quad (2.43)$$

2.1.2.5 Quadratic approximation of the envelope

While the idea in Kundert's algorithm (i.e. the value of a state variable at $t_{(n+1)}$ interpolates with an imposed error a quadratic polynomial defined by the state variable values at $t_{(n-1)}$, $t_{(n)}$ and $t_{(n+1)} + T$) remains unchanged, its implementation is not the same.

The implemented algorithm is similar to the exponential approximation of envelope, using the Newton-Raphson method to solve

$$\Phi(v(t_{(n+1)}), t_{(n+1)}, t_{(n+1)} + T) - p(h_1 + h_2 + T) = 0 \quad (2.44)$$

for $v(t_{(n+1)})$, where $p(t) = a_2 t^2 + a_1 t + a_0$, with a_0 , a_1 , a_2 computed so that the quadratic polynomial passes through the values corresponding to $(t_{(n-1)}, t_{(n)})$ and $t_{(n+1)} + T$. The formulas giving a_0 , a_1 , a_2 are computed in "local time coordinates" 0 , h_1 and h_2 , (Figure 2.74) for the sake of simplicity [44].

2.1.2.5.1 **Switching between exponential and quadratic envelope approximations**

Obviously, the coefficients in (2.36) can be identified only if the slopes of the unknown computed on the time intervals h_1 and h_2 have the same sign and $|\text{slope}(h_1)| > |\text{slope}(h_2)|$. These two conditions are used to check if the exponential approximation of the envelope can be built [44].

The proposed algorithm, outlined in the following, is used for each state variable [44].

```

while  $t < t_{\text{stop}}$ 
  if  $t = 0$ 
    solve for  $t = 0, T$  and for  $2T$ 
  end
  compute the predictors using  $v(t_{n-1}), v(t_n)$  and  $v(t_n + T)$ 
  compute the correctors using  $v(t_{n-1}), v(t_n)$  and  $v(t_{n+1})$ 
  if corrector method is exponential
    verify if exponential can be built
    if NO
      reject H and use quadratic for next jump
    if YES
      continue
    end
  end
end
end
estimate the method for next jump H
if  $\text{slope}(h_1) \cdot \text{slope}(h_2) > 0$  and  $|\text{slope}(h_1)| > |\text{slope}(h_2)|$ 
  exponential
else
  quadratic
end
end
if  $\varepsilon_r \leq 1e - 2 \cdot \varepsilon_{r0}$ 
  accept the solution for H and next jump  $H_{\text{new}} = 2H$ 
else if  $\varepsilon_r \leq \varepsilon_{r0}$ 
  accept the solution for H and next jump  $H_{\text{new}} = H$ 
else if  $\varepsilon_r > \varepsilon_{r0}$ 
  reject the solution for H and next jump  $H_{\text{new}} = H - 1$ 
end
end
end

```

2.1.2.6 Examples

The simulation of the buck converter in Figure 2.75 has been performed both with the transient analysis and with the envelope following algorithm which uses the quadratic and the exponential approximation of the envelope. Its parameters are: $V_i = 10$ V, $L = 420$ μ H, $C = 38$ μ F, $R = 140$ Ω , and the diode is modeled as a piecewise-linear resistor with $R_d = 1e-3$ Ω and $R_i = 1e+15$ Ω . The switch parameters are $R_{on} = 0.01$ Ω , $R_{off} = 1$ K Ω , $f = 100$ KHz [44]. The results given by the proposed envelope algorithm have been compared with those obtained with similar algorithms implemented in SPECTRE RF and PAN.

The minimum jump size is the switch signal period T . The efficiency η of an envelope following algorithm is defined as follows:

$$\eta = \frac{\sum_k H_k}{t_{stop}} \quad (2.45)$$

H_k being the accepted jumps magnitudes, and t_{stop} being the total simulation time.

SPECTRE RF analyses consider that each node has a capacity of 10^{-17} F connected to the ground, unlike the proposed algorithm and PAN that analyze the circuit in Figure 2.75.

In all analysis algorithms (transient and envelope) the absolute errors have been set as $iabstol = 1e-12$ A, $vabstol = 1e-12$ V. The relative error in transient analyses has been set to $reltol = 1e-9$. Two relative error limits for the jump computation (ε_{r0} in the case of the proposed algorithm) have been considered. The results for $\varepsilon_{r0} = 1e-4$ are given in Table 2.19, and the results for $\varepsilon_{r0} = 1e-6$ are given in Table 2.20.

In these tables the maximum jump H_{max} is given in switch periods. The transient analysis with the program using the proposed algorithm needs 7.82s, so that only the proposed envelope analysis for $\varepsilon_{r0} = 1e-4$ leads to a significant CPU time saving.

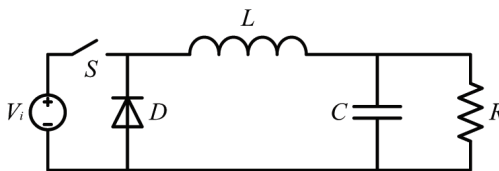


Figure 2.75 Buck converter.

Table 2.19 $\epsilon_{r0} = 1e-4$

| Algorithm | η | H_{max} | CPU Time [s] |
|------------|--------|-----------|--------------|
| Proposed | 0.9298 | 30 | 1.86 |
| Spectre RF | 0.8105 | 19 | 7.58 |
| PAN | 0.2620 | 8 | irrelevant |

Table 2.20 $\epsilon_{r0} = 1e-6$

| Algorithm | η | H_{max} | CPU Time [s] |
|------------|--------|-----------|--------------|
| Proposed | 0.4860 | 10 | 13.15 |
| Spectre RF | 0.2935 | 19 | 42.09 |
| PAN | 0.0010 | 1 | irrelevant |

The waveforms in Figure 2.76 and Figure 2.77 show that the proposed method gives the same results as the transient analysis.

The second example [44] is a synchronous rectification buck converter (Figure 2.78) with a sampling frequency $f_s = 1/T = 530$ KHz. A transient analysis with $t_{stop} = 700T$ has been performed starting from a null initial state. For $t_s = 500T$ the load resistance increases from 0.137Ω to 1.37Ω . The output voltage waveform is given in Figure 2.79. A steady state detail after $497T$ is given in Figure 2.80, and the transient response produced after the increase of the load resistance is given in Figure 2.81. The results are given in Table 2.21.

In this case, the transient analysis in the program using the proposed algorithm requires 1.74 s [44].

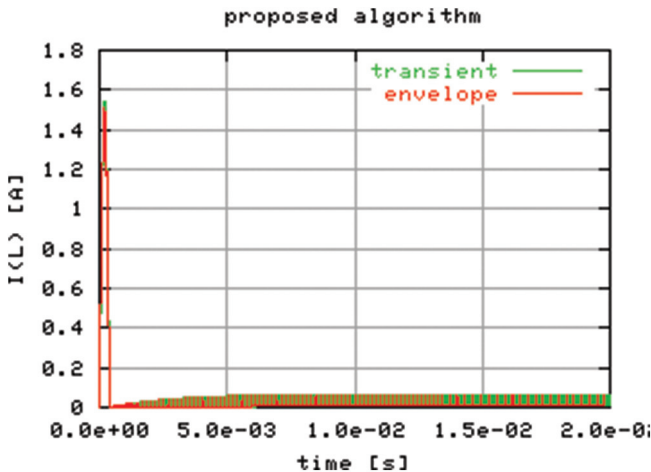


Figure 2.76 $i_L(t)$ – proposed algorithm.

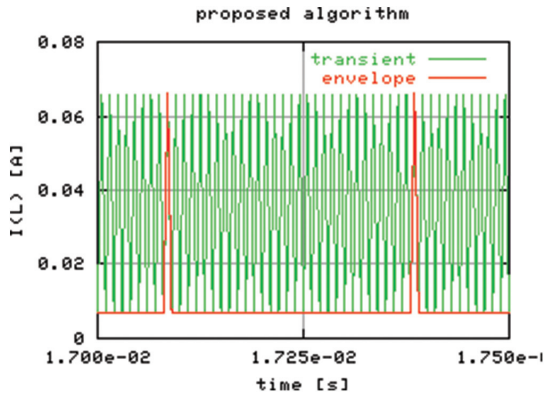


Figure 2.77 $i_L(t)$ – proposed algorithm (detail).

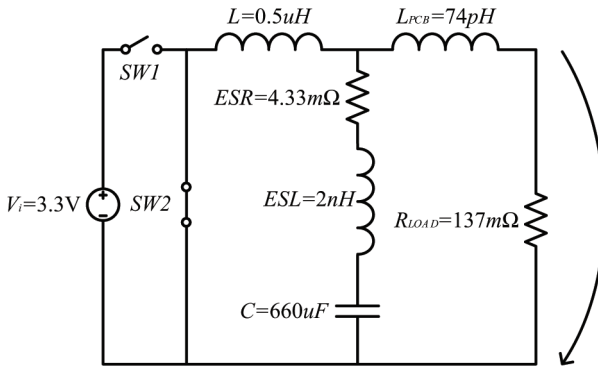


Figure 2.78 Synchronous rectification buck converter.

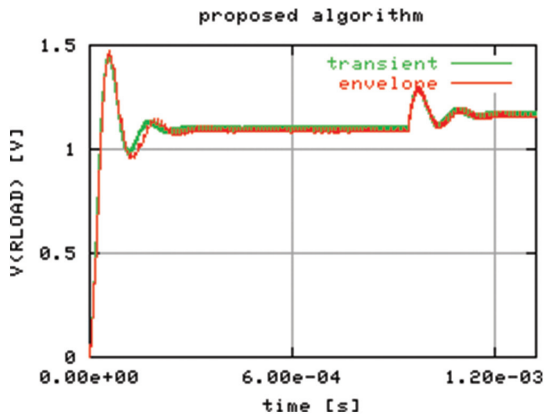


Figure 2.79 Output voltage V_O .

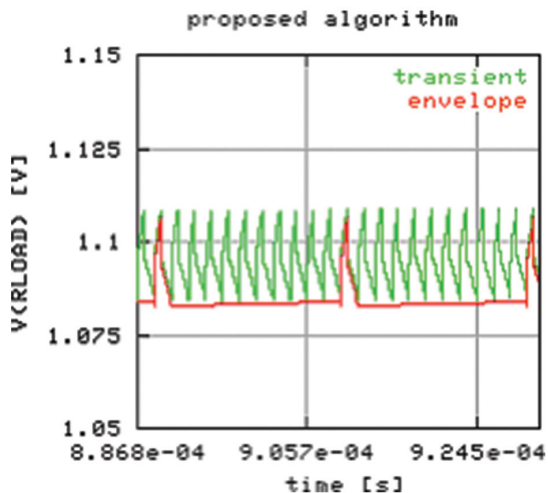


Figure 2.80 Output voltage V_0 – steady state.

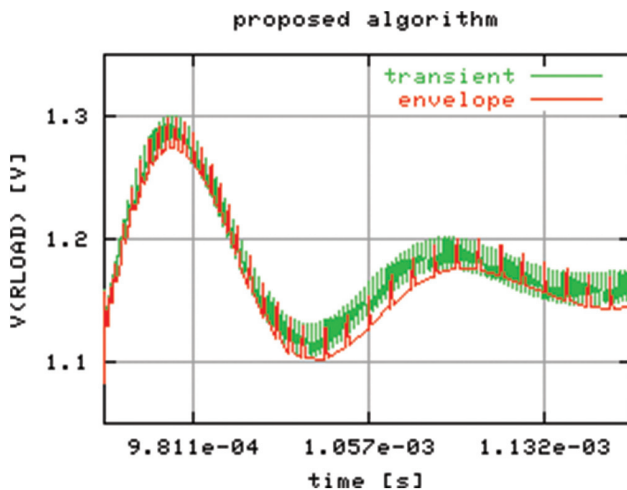


Figure 2.81 Output voltage V_0 – transient solution for the increasing of the load resistance.

Table 2.21 $\epsilon_{r0} = 1e-2$

| Algorithm | η | CPU Time |
|--------------------|--------|------------|
| Proposed algorithm | 0.802 | 0.99 s |
| Spectre RF | 0.768 | 4.28 s |
| PAN | 0.678 | irrelevant |

2.1.2.7 Envelope following analysis of a buck converter with closed loop control

Due to the variations in the pulse widths (especially when the load is varying or the input voltage is changing), the neighboring clock periods are not as similar as, for example, in switched capacitor circuits driven by the same clock. The poor efficiency of all envelope following algorithms presented above for buck converters with closed loop control is explained in [45] through the existence of some state variables in the control loop which vary very fast, their values at t_{n+1} having a weak dependence on their own history. This is because, in these conditions, the algorithm implementation reported in [44] reduces drastically its time step leading to a poor efficiency of the envelope following. Various intricate algorithms have been proposed to overcome this difficulty [46].

In order to avoid useless jump attempts of the algorithm in [44] in these circumstances, the minimum time step for the jump computation is set 10 times greater than the minimum time step for the transient analysis [46]. For example, if the maximum time step for the transient analysis is $T/100$, then the minimum time step for the transient analysis is $1e-14$ times smaller ($4e-20s$) and the minimum time step for the jump computation is $4e-19s$. In order to obtain a better efficiency of the envelope following analysis the maximum Newton-Raphson iteration number is set to 5 for the transient analysis and to 10 for the jump computation [46].

For the comparison between various settings of the proposed algorithm as well as between our algorithm and that implemented in SPECTRE RF, the efficiency of an envelope algorithm is defined as in relation (2.45).

2.1.2.7.1 Example

The synchronous rectification buck converter with closed-loop control in Figure 2.82 has been analyzed [46]. The parameters of this circuit are: $V_{in} = 10V$, $R_s = 1 \text{ m}\Omega$, $L = 3.4 \text{ }\mu\text{H}$, $ESR = 2 \text{ m}\Omega$, $C = 10 \text{ mF}$, $R_{f1} = 1.2 \text{ K}\Omega$, $R_{f2} = 0.8 \text{ K}\Omega$, $C_1 = 1 \text{ nF}$, $C_2 = 8.5 \text{ pF}$, $R_1 = 150 \text{ K}\Omega$, $V_{ref} = 1.2 \text{ V}$, and $f = 250 \text{ KHz}$ (switch frequency).

In order to ensure a precise derivative computation both operational amplifiers are modeled as nonlinear VCVS described by [46]:

$$V_{out} = \frac{5}{2} \cdot (1 + \tanh(1.25e + 4 \cdot (V_{in} + 1.25e - 4))). \quad (2.46)$$

Switches are modeled by voltage controlled resistors [46]:

$$R_{SW} = \frac{1e + 5}{\pi} \cdot \left(\frac{\pi}{2} + \arctan(1e + 5 \cdot (U_{ctrl} - 4.999)) \right) \quad (2.47)$$

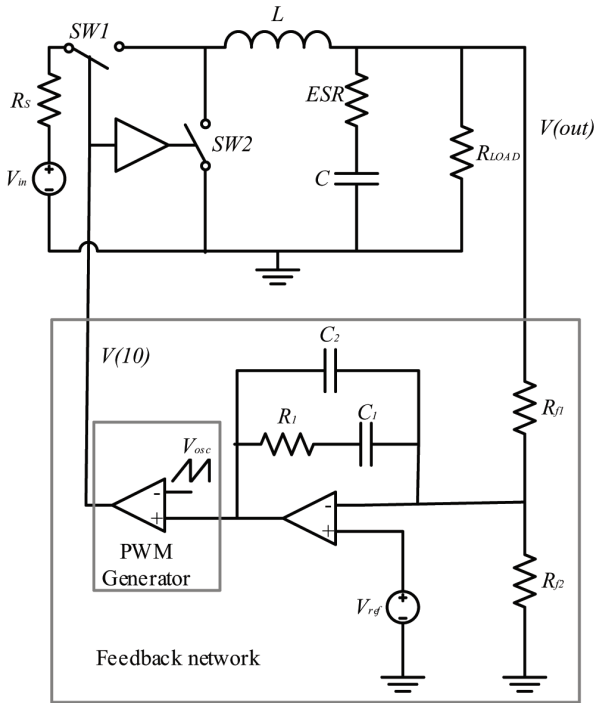


Figure 2.82 Synchronous rectification buck converter with closed-loop control.

where $U_{ctrl} = 5 - V(10)$ for SW1 and $U_{ctrl} = V(10)$ for SW2, and U_{ctrl} is the output voltage of the PWM generator.

Two sets of operating conditions, defined by the load resistance variation, have been simulated for this converter. The load resistance variation for the first set of operating conditions (1st OC) is given in Figure 2.83 [46].

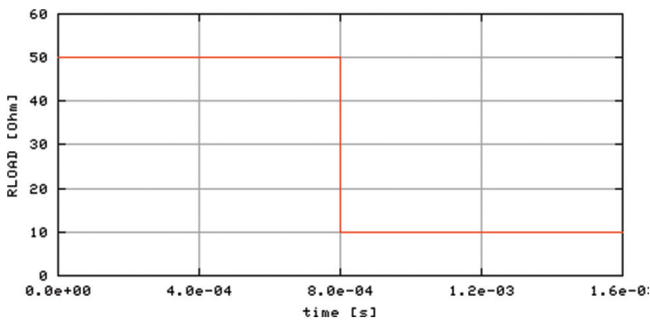
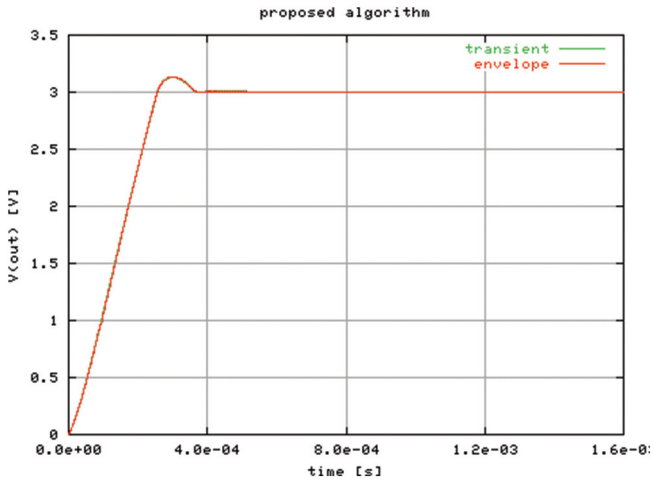


Figure 2.83 Load resistance variation – 1st OC.

Table 2.22 1st OC parameters “reitol envlp” = $1e-4$

| | Proposed | Spectre |
|--------------|----------|---------|
| T stop | 400T | 400T |
| H total | 250T | 244T |
| η | 0.625 | 0.61 |
| reitol tran | $1e-9$ | $1e-8$ |
| reitol envlp | $1e-4$ | $1e-4$ |
| abstol | $1e-12$ | $1e-12$ |

**Figure 2.84** Output voltage (proposed algorithm) [46].

The relative error reitol has different values for the transient analysis and for the jump computation (reitol envlp). The absolute error is the same for both types of computation [46].

The simulation results are given in Table 2.22 and are illustrated in Figures 2.84–2.86.

The proposed algorithm has a slightly better efficiency than SPECTRE RF [46]. This feature can be observed also in Figure 2.85 and Figure 2.86, representing the waveforms around the moment of the load resistance commutation.

The results for smaller jump computation errors are given in Tables 2.23 and 2.24. As this error decreases, the efficiency difference between the proposed algorithm and that implemented in SPECTRE RF increases [46].

The relative error for the transient analysis (reitol tran) has been chosen as $1e-9$ so that the proposed algorithm performs the largest jumps. The corresponding error for SPECTRE RF is $1e-8$ because this is the smallest value

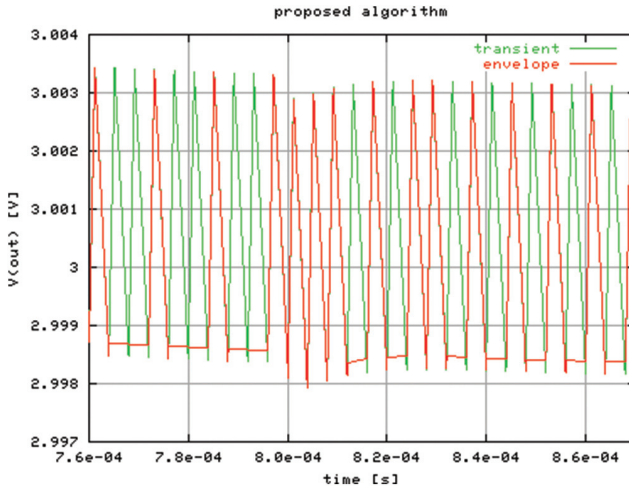


Figure 2.85 Output voltage – detail (proposed algorithm) [46].

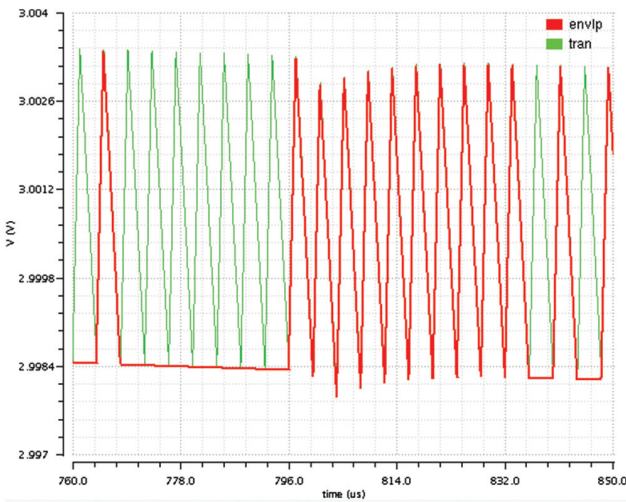


Figure 2.86 Output voltage – detail (SPECTRE RF) [46].

for which this algorithm can operate (for $1e-9$ the chosen time step oscillates between the values $4.35e-19$ and $8.7e-19$ leading to a huge simulation time) [46].

The load resistance variation for the second set of operating conditions (2nd OC) is given in Figure 2.87 [46].

Table 2.23 1st OC parameters “reitol envlp” = $1e-5$

| | Proposed | Spectre |
|--------------|----------|---------|
| T stop | 400T | 400T |
| H total | 206T | 192T |
| η | 0.515 | 0.48 |
| reitol tran | $1e-9$ | $1e-8$ |
| reitol envlp | $1e-5$ | $1e-5$ |
| abstol | $1e-12$ | $1e-12$ |

Table 2.24 1st OC parameters “reitol envlp” = $1e-6$

| | Proposed | Spectre |
|--------------|----------|---------|
| T stop | 400T | 400T |
| H total | 149T | 70T |
| η | 0.3725 | 0.175 |
| reitol tran | $1e-9$ | $1e-8$ |
| reitol envlp | $1e-6$ | $1e-6$ |
| abstol | $1e-12$ | $1e-12$ |

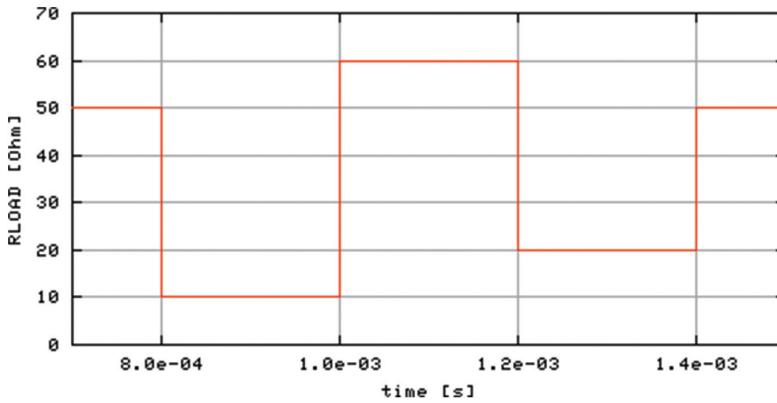


Figure 2.87 Load resistance variation – 2nd OC.

The simulation results are given in Table 2.25.

It can be observed that the proposed algorithm is more or less better than that implemented in SPECTRE in all cases [46].

Table 2.25 2nd OC parameters

| reitol envlp | Proposed | η . Proposed | SPECTRE | η SPECTRE |
|--------------|----------|-------------------|---------|----------------|
| $1e-4$ | 218 | 0.545 | 189 | 0.4725 |
| $1e-5$ | 160 | 0.4 | 122 | 0.305 |
| $1e-6$ | 133 | 0.3325 | 53 | 0.1325 |

2.1.2.8 Transient analysis with two time variables

Consider a two-tone signal [17], given by the following expression:

$$b(t) = \sin\left(\frac{2\pi}{T_1}t\right) \sin\left(\frac{2\pi}{T_2}t\right) \quad (2.48)$$

The two tones are at very distant frequencies, for example $f_1 = 1/T_1 = 1 \text{ kHz}$, and $f_2 = 1/T_2 = 1000 \text{ kHz}$. In other words, every modulating period $T_1 = 1 \text{ ms}$ (the slow signal) contains 1,000 periods of the carrier $T_2 = 0.001 \text{ ms}$ (the fast signal).

In the time domain analysis of a circuit driven by such a signal, the time step must be small enough to compute the correct response to rapid variation in the $b(t)$ signal. For example, if 50 points are used for a carrier period 50,000 points are needed to sweep a modulation period. Please note that this is computed for $T_1/T_2 = 10^3$, but this ratio can reach 10^6 or more. Taking into account that the steady state is reached after sweeping at least several signal periods, a huge computation effort may be needed.

Now consider the two variables representation of $b(t)$ obtained as follows: For the slow variations of the $b(t)$ expression, t is replaced with t_1 and for the rapid variations of the $b(t)$ expression, t is replaced with t_2 . The resulting function is as follows:

$$\hat{b}(t_1, t_2) = \sin\left(\frac{2\pi}{T_1}t_1\right) \sin\left(\frac{2\pi}{T_2}t_2\right) \quad (2.49)$$

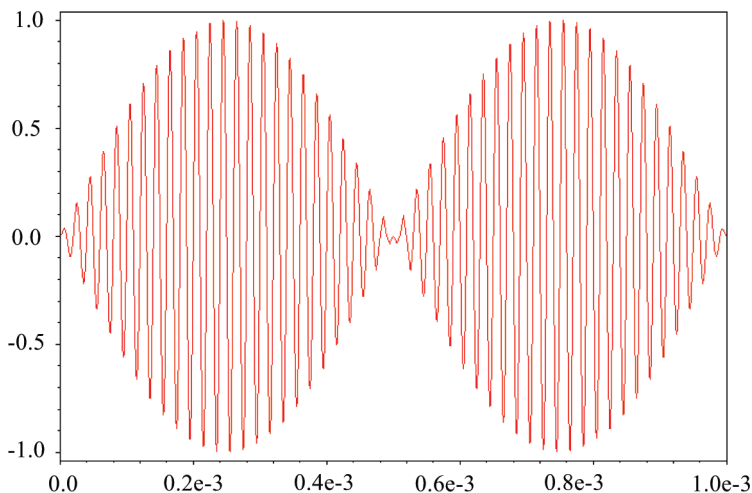


Figure 2.88 $b(t)$ represented with one time variable [18, 19].

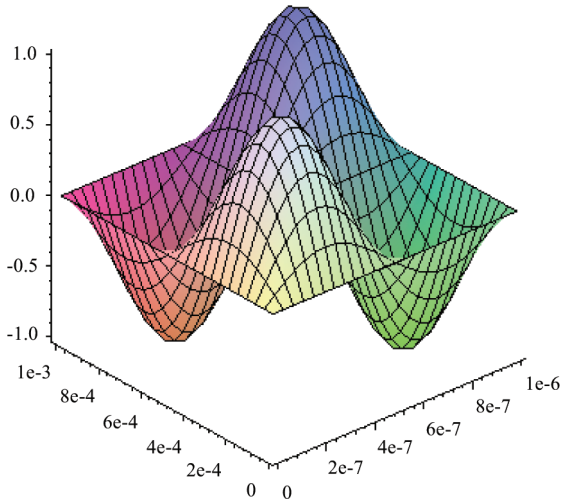


Figure 2.89 $b(t)$ signal represented with two time variables.

The function $\hat{b}(t_1, t_2)$ is bi-periodic, that is periodic with respect to both t_1 and t_2 : $\hat{b}(t_1 + T_1, t_2 + T_2) = \hat{b}(t_1, t_2)$.

The function $\hat{b}(t_1, t_2)$ for $0 \leq t_1 \leq T_1$, $0 \leq t_2 \leq T_2$ is shown in Figure 2.89. Considering that for plotting the function all the computed points of the circuit response are used, a mesh with 50×50 nodes i.e. 2500 samples, it results a much smaller number than those 50,000 samples used for the single time variable calculations.

Note that it is easy to reconstruct $b(t)$ from the $\hat{b}(t_1, t_2)$ setting $t_1 = t_2 = t$ and taking into account that \hat{b} is bi-periodic. Giving any value for t , the \hat{b} arguments are given by $t_i = t \bmod T_i$. For example:

$$\begin{aligned}
 b(1.952ms) &= \hat{b}(1.952ms, 1.952ms) \\
 &= \hat{b}(T_1 + 0.952ms, 195T_2 + 0.002ms) \\
 &= \hat{b}(0.952ms, 0.002ms)
 \end{aligned} \tag{2.50}$$

Giving the $\hat{b}(t_1, t_2)$ is easy to see how $b(t)$ looks. When t increases from 0, the trajectory given by $\{t_i = t \bmod T_i\}$ draws the trajectory in the saw teeth form as it is shown in Figure 2.90.

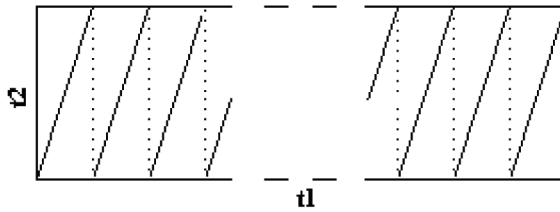


Figure 2.90 Trajectory in the t_1 - t_2 plane [40].

Writing the circuit equations for this method is presented in the Section 2.1.3.3. The transient analysis of the circuit starts from the specified initial conditions $x(t_1, 0)$ and $x(0, t_2)$.

2.1.2.8.1 *Remarks*

Due to the wide spectrum of the RF signals, the classical transient analysis is very time consuming.

Although designed to shorten the computation time, the envelope following method implemented in SPECTRE RF cannot be used efficiently to compute the transient response for a large class of RF circuits.

Recently, continuing the ideas in [20], several two-time variables analysis methods have been developed but are not yet implemented in any commercial software. It follows that the efficient transient analysis of the RF circuits remains an open problem.

2.1.3 Computation of the Periodic Steady State

In the RF circuit design and simulation, the periodic steady state response is of great interest. Some of these circuits are characterized by a very long transient response and their simulation with the traditional transient analysis from SPICE is not efficient. For this reason, some methods that compute directly the periodic steady state response have been developed.

2.1.3.1 *The brute force method with the periodicity error control*

The classical transient analysis, also called “the brute force method”, computes the transient response of a circuit until all transient components decay. All time domain circuit simulators can perform this analysis on a specified interval (from 0 to T_{stop}) without computing the periodicity error. A more efficient and accurate analysis can be easily obtained by calling a user-defined procedure to compute the periodicity error after each excitation period. For example the periodic steady state can be considered reached if the state vector x satisfies

$$\varepsilon^{(j)} \leq \varepsilon_0, \quad j = 1, \dots, M \quad (2.51)$$

where ε is the global relative periodicity error between the $(m+1)$ -th and the m -th periods for all state variables $x^{(j)}$ $k = 1, \dots, n$, and ε_0 is the imposed relative error [21]:

$$\varepsilon^{(j)} = \frac{1}{n} \cdot \sqrt{\sum_{k=1}^n \frac{1}{T} \cdot \int_0^T \frac{\Delta x_k^{(j)2}}{x_k^{(j)2}} d\tau} \quad (2.52)$$

with $\Delta x_k^{(j)}(\tau) = x_k^{(j)}[(m+1)T + \tau] - x_k^{(j)}(mT + \tau)$.

By this way the transient analysis is stopped if the imposed periodicity error is satisfied.

2.1.3.2 Shooting methods

2.1.3.2.1 Shooting with Newton-Raphson

The PSS (periodic steady state) analysis [22] implemented in SPECTRE RF computes directly the permanent response of the circuit in the time domain. This simulation technique is known in the literature as shooting with Newton-Raphson. It uses a shooting method to compute the steady state response and can handle circuits having strong nonlinearities.

If the circuit has strongly nonlinear elements, the advantage of a shooting method over early implementations of the harmonic balance method (Section 2.2.1.1) is considerable. For this kind of circuits the last method is slow and has convergence difficulties, requiring a huge memory space, while the shooting methods are not affected by the strong nonlinear behavior of some circuit elements.

How a shooting method works is illustrated in Figure 2.91, showing the evolution of the state variable V_k .

For a circuit with customary behavior driven by T-periodic sources, the T-periodic steady state solution [23] satisfies the following condition:

$$v(T) - v(0) = 0. \quad (2.53)$$

The transition function $\Phi_T(v_0, t_0)$ is defined, as a solution of the following equation at the time value $t_0 + T$

$$f(v(t), t) = i(v(t)) + \frac{dq(v(t))}{dt} + u(t) = 0 \quad (2.54)$$

which has the initial condition v_0 at the time value t_0 .

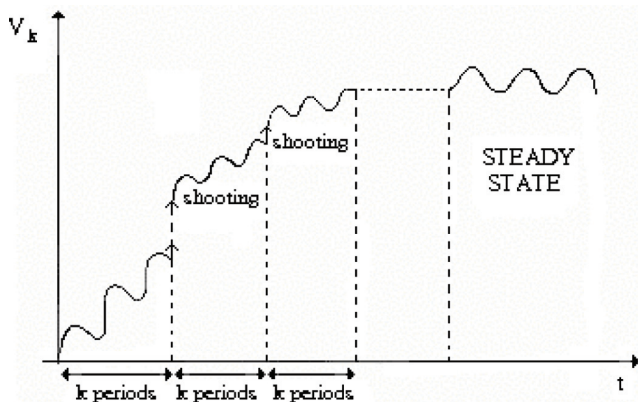


Figure 2.91 Shooting.

This can be written as follows:

$$v_0(t_0 + T) = \Phi_T(v_0(t_0), t_0) \quad (2.55)$$

In (2.54) $v(t)$ is the voltages vector, $i(t)$ is the currents vector of the voltage controlled nonlinear resistors, $q(t)$ is the charges vector of the voltage controlled nonlinear capacitors, and $u(t)$ is the vector of the independent sources.

The shooting methods combines (2.53) and (2.55) in

$$\Phi_T(v(0), 0) = v(0) \quad (2.56)$$

which is a nonlinear algebra problem, so the Newton-Raphson method can be used to solve it for $v(0)$ [24]. The combination of shooting and Newton-Raphson method is known as the shooting algorithm with Newton-Raphson.

In order to apply the shooting with Newton-Raphson, it is necessary to compute both the circuit response over a period and the sensitivities of the final state $v(T)$ with respect to changes in the initial state $v(0)$. The Jacobian J is the sensitivity matrix of (2.56) and is used to determine how to correct the initial state to reduce the difference between the initial and the final states:

$$v(0)^{j+1} = v(0)^j - J^{-1}(v(0)^j)(\Phi_T(v(0)^j) - v(0)^j) \quad (2.57)$$

Two test circuits that have been presented in the Section 2.1.2.3, the class C amplifier and the ne600p mixer, have been simulated with the PSS analysis of SPECTRE RF. The waveforms together with the iterations number needed to obtain the periodic steady state response and the simulation time are listed in the Tables 2.26 and 2.27 [25].

Table 2.26 Steady state of the class C amplifier – SPECTRE RF

| | |
|------------------|---------|
| Iteration number | 5 |
| Simulation time | 30.22 s |

Table 2.27 Steady state of the ne600p mixer – SPECTRE RF

| | |
|------------------|--------|
| Iteration number | 5 |
| Simulation time | 52.4 s |

For the class C amplifier, the following results have been obtained:

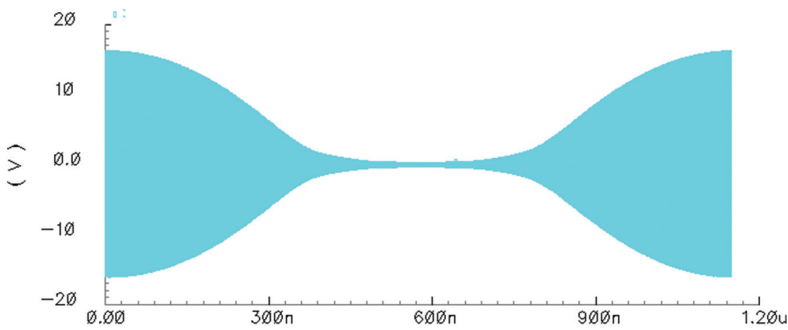


Figure 2.92 Steady state of the class C amplifier, PSS analysis of SPECTRE RF.

For the ne600p mixer, the following results have been obtained:

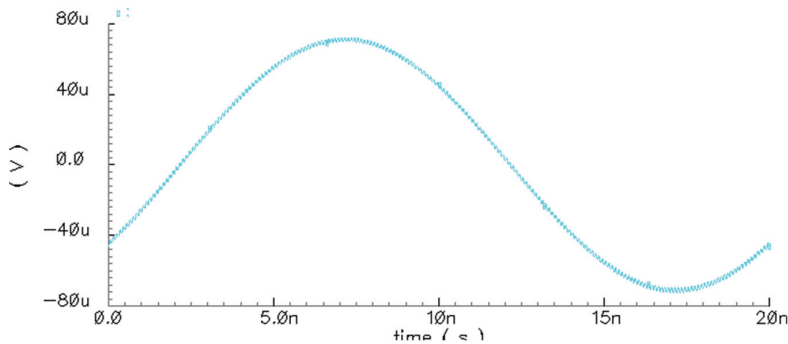


Figure 2.93 Steady state of the ne600p mixer, PSS analysis of SPECTRE RF.

For both simulations a relative error $reltol = 1e-3$ and an absolute error: $vabstol = 1e-6$ for voltage and $iabstol = 1e-12$ for current have been used.

2.1.3.2.2 Shooting analysis from PAN

Although the shooting analysis of PAN is based on the same algorithm as the PSS analysis of SPECTRE RF, different performances are obtained. One explanation could be that the transient analysis underlying the shooting analysis is controlled by a set of errors which is not the same as that of SPECTRE RF. Moreover, it is not clear how the periodicity error is defined in PAN.

For the class C amplifier, the following results have been obtained:

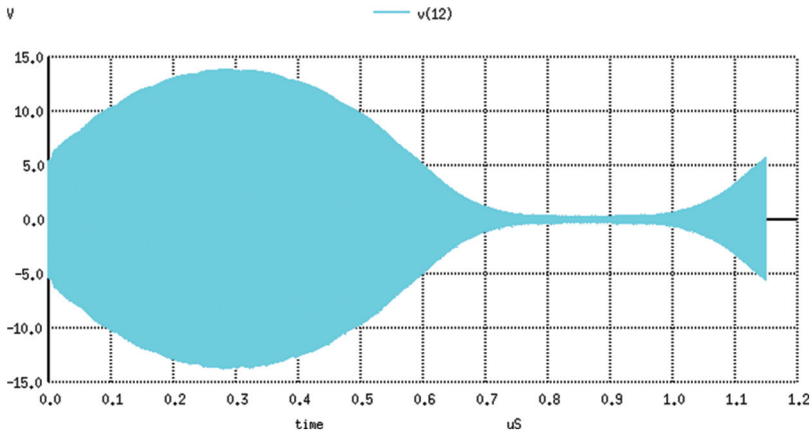


Figure 2.94 Steady state of the class C amplifier, PSS analysis of PAN.

Table 2.28 Steady state of the class C amplifier – PAN

| | |
|------------------|--------|
| Iteration number | 2 |
| Simulation time | 8.98 s |

For the ne600p mixer, the following results have been obtained (Figure 2.95, Table 2.29):

Table 2.29 Steady state of the ne600p mixer – PAN

| | |
|------------------|-------|
| Iteration number | 2 |
| Simulation time | 1.8 s |

2.1.3.2.2.1 Remarks

The difference of the response amplitudes obtained with SPECTRE and PAN is mainly due to the different transistors models implemented in these two programs [25].

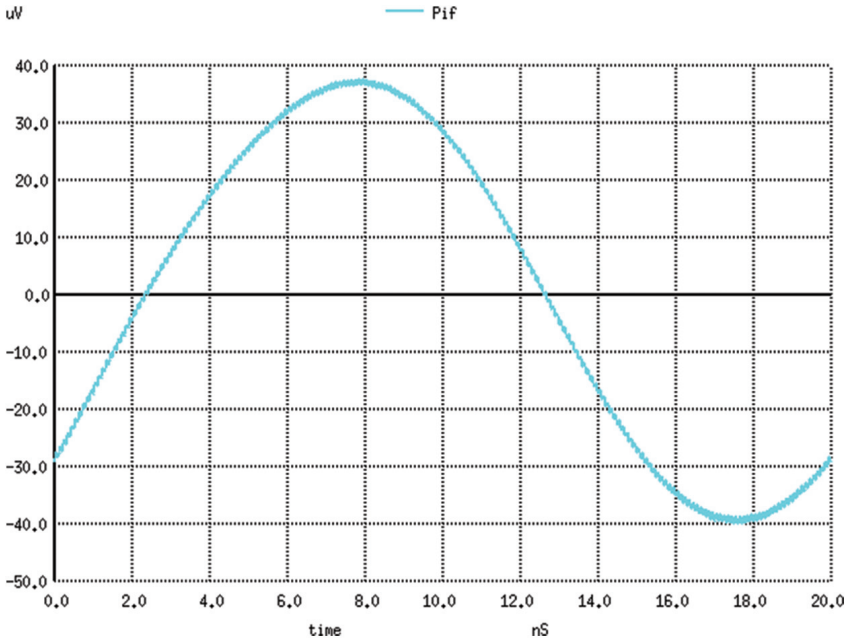


Figure 2.95 Steady state of the ne600p mixer, PSS analysis of PAN.

At the first glance, in terms of the implementation of the same shooting method, PAN seems more efficient than SPECTRE RF. But, PAN documentation does not explain clearly in which conditions the shooting iterations are stopped.

2.1.3.3 Shooting with linear extrapolation

The linear extrapolation method assumes that the states vector v_{j+1} at the beginning of $(j+1)$ -th period is an affine function of the states vector v_j at the beginning of the j -th period: $v_{j+1} = A \cdot v_j + b$ where A and b are unknown [26]. When the steady state is reached it follows:

$$x^* = Ax^* + b \Rightarrow x^*(1 - A) = b. \quad (2.58)$$

Supposing that the steady state x^* can be obtained solving (2.58), it follows that the components of x^* are linear independent. If N is the number of the state variables, it follows that p values

$$\Delta x^0, \Delta x^1, \dots, \Delta x^{p-1} \quad (2.59)$$

where $\Delta x^{(i)} = x^{(i+1)} - x^{(i)}$ are linearly independent and Δx^p is a linear combination of $\Delta x^0, \Delta x^1, \dots, \Delta x^{p-1}$:

$$V \cdot c = \Delta x^p \Leftrightarrow [[\Delta x^0][\Delta x^1] \dots [\Delta x^{p-1}]] \begin{bmatrix} c_1 \\ c_2 \\ \dots \\ c_{p-1} \end{bmatrix} = [\Delta x^p] \quad (2.60)$$

where V is a square $p \times p$ matrix whose columns are $\Delta x^0, \Delta x^1, \dots, \Delta x^{p-1}$ considered at the beginning of the periods 0 (initial state), 1, . . . , $p-1$ in the transient analysis [26].

The matrix V columns are computed by sweeping p periods of the excitation and solving the problem of minimizing the value:

$$\varepsilon = \|V \cdot c - \Delta x_0^p\|^2. \quad (2.61)$$

The solution of this minimization problem using the least squares method is as follows:

$$x^* = \sum_{i=0}^p c_i x^{(i)} / \sum_{i=0}^p c_i \quad (2.62)$$

where x^* is the fixed point of (2.58).

The computation of x^* is an iteration of this extrapolation procedure. These iterations include sweeping of p excitation periods by a transient analysis algorithm. The values in x^* converge to the initial state corresponding to the periodic steady state. The value of p is practically equal to the number of the independent state variables that change slowly with time. The linear extrapolation method is efficient if p is not a large number.

2.1.3.4 Shooting with exponential extrapolation

Consider a linear exponentially stable circuit driven by a sinusoidal signal with period T . Having a customary behavior, this circuit has a T -periodic sinusoidal steady state. Assume that this circuit has a real natural frequency $s_1 = -\alpha_1$ corresponding to the maximum time constant of this circuit $\tau_1 = 1/\alpha_1$ with $\tau_1 \gg T$. Moreover, this circuit has no complex natural frequencies $s_k = -\alpha_k + j\omega_k$, with $T_k = 2\pi/\omega_k$ of the same order of magnitude as T and $\tau_k = 1/\alpha_k \gg T$. The brute force method can reach the steady state of this circuit after sweeping a number of $5 \tau_1/T$ periods. It can be easily shown that the average value $\tilde{x}_{j(k)}$ on the period k for any response x_j having a significant term depending on s_1 can be written as:

$$\tilde{x}_{j(k)} = a_j + A_j e^{-kT/\tau_1} \quad (2.63)$$

Computing the average values $\tilde{x}_{j(1)}$, $\tilde{x}_{j(2)}$, and $\tilde{x}_{j(3)}$ for three consecutive periods 1, 2, and 3 it follows that the steady state average value a_j is as follows:

$$a_j = \frac{\tilde{x}_j(1)\tilde{x}_j(3) - \tilde{x}_j^2(2)}{\tilde{x}_j(1) + \tilde{x}_j(3) - 2\tilde{x}_j^2(2)}, \quad (2.64)$$

The shooting algorithm with exponential extrapolation has the following steps [21]:

1. Three excitation periods are swept using a stiff stable method and the average values $\tilde{x}_j(1)$, $\tilde{x}_j(2)$, $\tilde{x}_j(3)$ corresponding to each period are computed for all state variables;
2. The asymptotic values a_j are computed with the relation (2.64) for all state variables (for $j = 1, \dots, n$),
3. The initial states corresponding to the periodic response x_{j0}^* are computed for all state variables as $x_{j0}^* = x_{j0}^{(3)} - \tilde{x}_j^{(3)} + a_j$ for $j = 1, \dots, n$, where $x_{j0}^{(3)}$ are the initial states for the 3-rd period;
4. Two periods 4 and 5 are swept starting from x_{j0}^* , $j = 1, \dots, n$;
5. If the steady state error (2.52) between the responses in the 4th and the 5th periods satisfies the imposed error, the periodic response is obtained; if not, the computation continues with the first step.

2.1.3.4.1 Example

The test circuit (Figure 2.96) is a DC commutation source. The circuit parameters are: $EI = 200$ V, $RI = 3$ K Ω , $Rb = 1$ Ω , $R3 = 1.5$ K Ω , $Rptx = 0.1$ Ω , $Rpri = 10$ Ω , $Resr = 3.75$ m Ω , $Rl = 0.25$ m Ω , $CI = 0.1$ μ F, $C2 = 16000$ μ F, $C3 = 1360$ pF, $L1 = 2034$ μ H, $L2 = 358.5$ μ H, $k = 0.99$. All diodes included those in the Ebers-Moll transistor model are considered as piecewise-linear resistors with two linear regions, having the break point in $i = 0$ A and $v = 0.4$ V and dynamic conductances $g1 = 3.7$ S and $g2 = 5.56 \cdot 10^{-12}$ S. The filter capacitor $C2$ generates a huge time constant, this being the reason why this circuit is used for testing the fast method for steady state computation [47].

The simulation results are given in Table 2.30, where b.f. is the brute force method, e.e. is the exponential extrapolation method, swp/shp is the swept period number/shootings number, h is the time step used in simulations, and t is the simulation time in seconds.

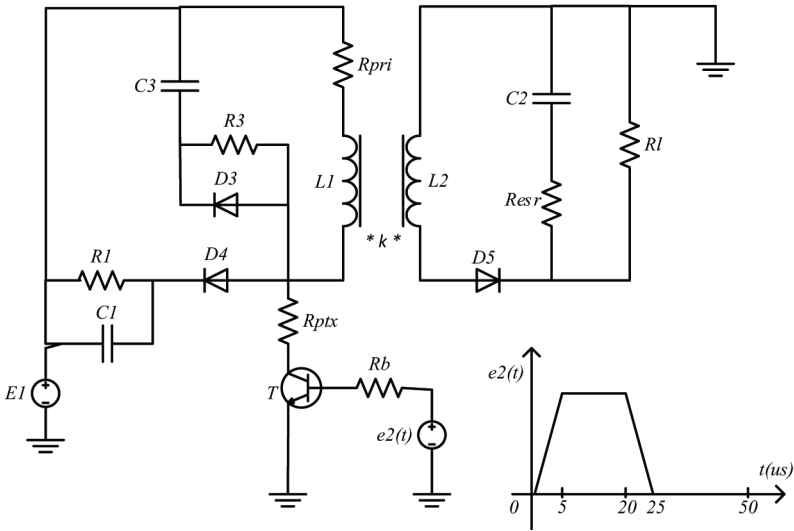


Figure 2.96 DC commutation source.

Table 2.30 Simulation results for the DC commutation source

| | h = T/50 | | h = T/100 | | h = T/300 | |
|-------|----------|-------|-----------|-------|-----------|-------|
| Meth. | swp/shp | t (s) | swp./sh | t (s) | swp./shp. | t (s) |
| b. f. | 193 | 66.2 | 192 | 94.5 | 188 | 220.2 |
| e. e. | 22/5 | 7.4 | 41/10 | 21 | 22/5 | 29.5 |

2.1.3.5 Two time variables method

2.1.3.5.1 Finite difference method

In this method [38], the multiple partial differential equation (MPDE)

$$\frac{\partial q(\hat{x})}{\partial t_1} + \dots + \frac{\partial q(\hat{x})}{\partial t_m} = f(\hat{x}) + \hat{b}(t_1, \dots, t_m) \quad (2.65)$$

is solved on a grid in the t_1, \dots, t_m space, where m is the number of time variables [18]. Let this grid consists of $\{\bar{t}_1, \dots, \bar{t}_n\}$ points where each $\bar{t}_i = (t_{1i}, \dots, t_{mi})$. The partial differential operators of the MPDE are discretized and the MPDE is associated with this grid. This results in a set of nonlinear algebraic equations having the unknowns $\{\hat{x}(\bar{t}_1), \dots, \hat{x}(\bar{t}_n)\}$. The nonlinear equations are numerically solved using the Newton-Raphson method.

In practice, only the two time variables case is considered. The MPDE equation corresponding to the relation (2.65) is as follows:

$$\frac{\partial q(\hat{x})}{\partial t_1} + \frac{\partial q(\hat{x})}{\partial t_2} = f(\hat{x}) + \hat{b}(t_1, t_2) \quad (2.66)$$

with boundary conditions $\hat{x}(t_1 + T_1, t_2 + T_2) = \hat{x}(t_1, t_2)$. Consider a uniform grid $\{\bar{t}_{i,j}\}$ of $n_1 \times n_2$ size on $[0, T_1] \times [0, T_2]$ area. Here $\bar{t}_{i,j} = (t_{1i}, t_{2j})$, $t_{1i} = (i - 1)h_1$ and $t_{2j} = (j - 1)h_2$, $1 \leq i \leq n_1$, $1 \leq j \leq n_2$. The distances between the grid nodes are: $h_1 = \frac{T_1}{n_1}$ and $h_2 = \frac{T_2}{n_2}$ on the directions t_1 and t_2 .

Discretizing the partial differential operators using the Backward Euler method, the following relations are obtained:

$$\begin{aligned} \frac{\partial q(\hat{x})}{\partial t_1}(\bar{t}_{i,j}) &= \frac{q(\hat{x}(\bar{t}_{i,j})) - q(\hat{x}(\bar{t}_{i-1,j}))}{h_1} \\ \frac{\partial q(\hat{x})}{\partial t_2}(\bar{t}_{i,j}) &= \frac{q(\hat{x}(\bar{t}_{i,j})) - q(\hat{x}(\bar{t}_{i,j-1}))}{h_2} \end{aligned} \quad (2.67)$$

Writing in each grid node $\{\bar{t}_{i,j}\}$ the equation of the method, $n = n_1 \times n_2$ equations are obtained:

$$F_{i,j} = \frac{\hat{q}_{i,j} - \hat{q}_{i-1,j}}{h_1} + \frac{\hat{q}_{i,j} - \hat{q}_{i,j-1}}{h_2} - \hat{f}_{i,j} - \hat{b}_{i,j} = 0, \quad (2.68)$$

$$\begin{aligned} \forall i \in \{1, \dots, n_1\}, \forall j \in \{1, \dots, n_2\}, \hat{q}_{i,j} &= q(\hat{x}(\bar{t}_{i,j})), \hat{f}_{i,j} = f(\hat{x}(\bar{t}_{i,j})), \\ \hat{b}_{i,j} &= b(\hat{x}(\bar{t}_{i,j})). \end{aligned}$$

These n equations have a large number of unknowns; $n_1 + n_2$ additional unknowns are resulting from discretization of the differential operators for $t_1 = 0$ and $t_2 = 0$. These unknowns are eliminated using bi-periodic boundary conditions.

The following system of equations is obtained:

$$F(X) = 0 \quad (2.69)$$

where $F = [F_{1,1}, \dots, F_{1,n_2}, F_{2,1}, \dots, \dots, F_{n_1,1}, \dots, F_{n_1,n_2}]^T$,
and $X = [\hat{x}(\bar{t}_{1,1}), \dots, \hat{x}(\bar{t}_{1,n_2}), \hat{x}(\bar{t}_{2,1}), \dots, \dots, \hat{x}(\bar{t}_{n_1,n_2})]^T$.
This system can be solved by Newton-Raphson method [18].

2.1.3.5.2 Shooting with Newton-Raphson

The key of extending the shooting method to more than one time variable is to view MPDE as ordinary differential equations with variables that are functions of other variables. Consider again the case of the MPDE having two time variables:

$$\frac{\partial q(\hat{x})}{\partial t_1} + \frac{\partial q(\hat{x})}{\partial t_2} = f(\hat{x}) + \hat{b}(t_1, t_2) \quad (2.70)$$

In this equation the variables \hat{x} , q , f , and \hat{b} are vectors of two arguments t_1 and t_2 . Let $Q(t_1)$, $X(t_1)$, $F(t_1)$, and $B(t_1)$ be functions of t_1 whose values are functions of t_2 . In other words, the value of $Q(t_1)$, for example, for a fixed t_1 is the whole $q(t_1, \cdot)$ function.

The MPDE equation can be formally written as a differential-algebraic equation (DAE) having a function as an independent variable:

$$\frac{dQ(X)}{dt_1} = F(X) + B(t_1) - D_{t_2}[Q(X)] \quad (2.71)$$

where D_{t_2} is an operator that differentiates the function (of t_2) on which it operates.

The shooting method can be applied now on (2.71). Let $\Phi(X_0, t)$ be the transition function of the differential-algebraic equation. The shooting method consists in solving the equation:

$$\Phi(X, T_1) - X = 0 \quad (2.72)$$

using the Newton-Raphson method.

2.1.3.6 Shooting with exponential extrapolation

For circuits having a customary behavior (including the property to attenuate exponentially the transient components) and a unique T-periodic response to a T-periodic excitation, exponential extrapolation method can be applied with two time variables [30].

Let $dx/dt = f(x, s(t))$ be the state equations of the circuit in which $f(x)$ is nonlinear and $s(t)$ corresponds to a periodic excitation. Consider that the slow component of $s(t)$ and $x(t)$ depends on $\alpha_1 = t/T_1$ (T_1 – the modulating signal period) and the fast components of $s(t)$ and $x(t)$ depends on $\alpha_2 = t/T_2$ (T_2 – the carrier period). It follows

$$\frac{dx}{dt} = \frac{\partial x}{\partial \alpha_1} \cdot \frac{\partial \alpha_1}{\partial t} + \frac{\partial x}{\partial \alpha_2} \cdot \frac{\partial \alpha_2}{\partial t} \quad (2.73)$$

and the state equations become:

$$\frac{1}{T_1} \frac{\partial x}{\partial \alpha_1} + \frac{1}{T_2} \frac{\partial x}{\partial \alpha_2} = f[x(\alpha_1, \alpha_2), s(\alpha_1, \alpha_2)] \quad (2.74)$$

in which $s(\alpha_1, \alpha_2)$ has the unity period with respect to both variables α_1 and α_2 .

The Equations (2.74) can be discretized, for example, with the backward Euler method, with respect to both α_1 and α_2 . For the presentation simplicity, the step of the mesh can be considered for both variables α_1 and α_2 equal to $h = 1/N$ where N is the number of intervals in a period for both variables α_1 and α_2 ; in this case each unknown x_j can be described by a table of $N+1$ by $N+1$ samples. For $\alpha_1 = ph$ and $\alpha_2 = qh$ ($p, q \leq N + 1$), the Equation (2.74) for x_j is written as:

$$\begin{aligned} \frac{1}{T_1} \frac{x_j[ph, qh] - x_j[(p-1)h, qh]}{h} + \frac{1}{T_2} \frac{x_j[ph, qh] - x_j[ph, (q-1)h]}{h} = \\ = f_j(x(ph, qh), s(ph, qh)) \end{aligned} \quad (2.75)$$

If $x_j[(p-1)h, qh]$ and $x_j[ph, (q-1)h]$ are known for $j = 1, \dots, n$, then (2.75) can be solved with the Newton-Raphson method to compute $x_j[ph, qh]$ for $j = 1, \dots, n$, applying the same algorithm as the exponential extrapolation method for one time variable. The relatively small size of the system ($n \times n$) is one of the advantages of the shooting method compared to the finite difference method.

For $n = 1$, sweeping one period by backward Euler method requires to know the values on the line 0 and on the column 0 of the two-dimensional array x_1 . Integrating with respect to α_2 for $\alpha_1 = h$ leads to the calculation of the values in the first line of the two-dimensional array and so on.

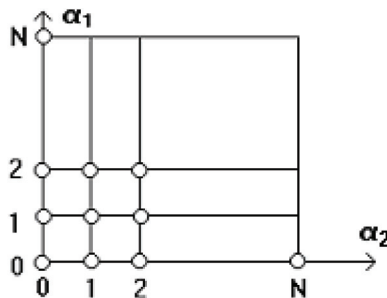


Figure 2.97 Two dimensional x_1 table.

In the periodic steady state the line n is identical to the line 0 and the column n is identical to the column 0. The average value of each line is initialized by the exponential extrapolation method followed by iterations of the values on this line until an imposed periodicity error is reached on this line, which represents a carrier period. These iterations, performed on all lines, lead to differences between elements of the column 0 and of the column n that are within the imposed limits for the line periodicity error.

To get the slow variable periodicity (error between the values imposed on the line 0 and on the line n), the unknowns arrays sweeping is restarted from the line 0 containing the “initial condition” given by the values obtained on the previous line n .

2.1.3.6.1 Example

Consider the circuit in Figure 2.98(a) driven by an AM signal $e(t) = \sin 2\pi(t/T_1) \sin 2\pi(t/T_2)$, the diode being modeled as the piecewise linear resistor in Figure 2.98(b).

The following cases have been analyzed [48] for $T_1 = 1 \text{ ms}$:

- case 0 ($T_2 = 1 \mu\text{s}$);
- case 1 ($T_2 = 0.1 \mu\text{s}$);
- case 2 ($T_2 = 10 \text{ ns}$);
- case 3 ($T_2 = 1 \text{ ns}$).

The exponential extrapolation is used for an average value prediction which may be computed for the entire array, each line, each column. For this example, the best results have been obtained using the entire array average as an initial value for the row average.

Considering the relative periodicity error $\varepsilon_d = 10^{-9}$ per line and a maximum of 40 cycles of the state variable array $u_c(\alpha_1, \alpha_2)$ an envelope with the maximum relative error of $5e-2$ is obtained compared with the result

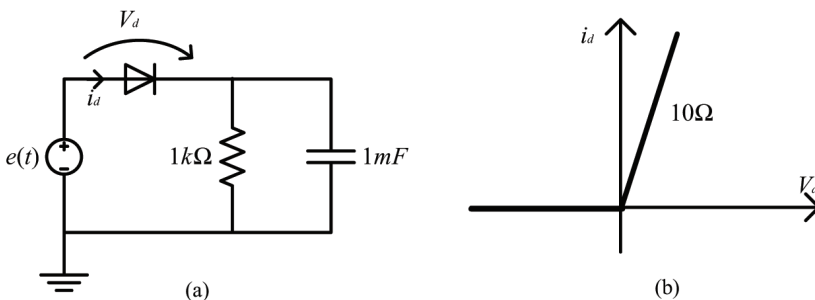


Figure 2.98 AM demodulator: (a) circuit and (b) diode model.

of the classical time domain analysis (1D). The computation time with the 2D analysis using exponential extrapolation is lower than that with 1D analysis using the same shooting method only if $T_1/T_2 > 10^5$. Considering 100 samples for the fast variable and the same number for the slow variable, the results for $T_1/T_2 > 10^7$ are not correct. By increasing the number of samples at 800 for the slow variable, correct results are obtained for $T_1/T_2 = 10^8$.

If the time steps h_1 and h_2 are constant, the two-time variables analysis is very fast, but the lack of errors estimation cannot guarantee the accuracy of the solution. In [37], the computation time is considerably reduced using a much lower carrier frequency than the real one for the initial approximation computations. In [39], companion models are proposed for 2D analysis for the case where the fast variable analysis is performed with SPICE (with the appropriate absolute and relative imposed errors) coupled with a program in FORTRAN performing the slow variable analysis. The elimination of some state variables may be useful to improve the 2D analysis [27].

By doing basically the same type of calculations as the envelope following method, the 2D time domain analysis is not always better than the 1D analysis. The problem of developing efficient methods to obtain the periodic steady state response of the RF circuits by the time domain analysis remains open.

2.2 Frequency Domain Analysis

2.2.1 Harmonic Balance Method

2.2.1.1 Valtonen harmonic balance method implemented in APLAC

2.2.1.1.1 *Time domain and frequency domain representations of a periodic signal*

A T-periodic signal can be written as a complex Fourier series

$$x(t) = \sum_{k=-\infty}^{+\infty} C_k e^{jk\omega t} \quad (2.76)$$

It is obvious that $C_{-k} = C_k^*$. Usually a finite number of spectral components are considered:

$$x(t) = \sum_{k=-K}^K C_k e^{jk\omega t} \quad (2.77)$$

These spectral components can be computed taking into account N samples of $x(t)$, namely $x(0), \dots, x((N-1)\Delta t)$, where $\Delta t = T/N$. It follows:

$$C_k = \frac{1}{T} \sum_{n=0}^{N-1} x(n\Delta t) e^{-jk\omega n\Delta t} \Delta t = \frac{1}{N} \sum_{n=0}^{N-1} x(n\Delta t) e^{-jk\frac{2\pi}{N}n} \quad (2.78)$$

where

$$X_k = \sum_{n=0}^{N-1} x(n\Delta t) e^{-jk\frac{2\pi}{N}n}, k = 0, 1, \dots, N-1 \quad (2.79)$$

are the direct discrete Fourier transform of the set of samples $x(0), \dots, x((N-1)\Delta t)$.

The relations

$$x(n\Delta t) = \frac{1}{N} \sum_{k=0}^{N-1} X_k e^{jk\frac{2\pi}{N}n} \quad (2.80)$$

define the inverse discrete Fourier transform of the spectral components X_k , $k = 0, \dots, N-1$.

The signal $x(t)$ has both the time domain representation $x(0), \dots, x((N-1)\Delta t)$ and the frequency domain representation X_k , $k = 0, \dots, N-1$. Using the direct and the inverse discrete Fourier transforms one can easily pass from a signal representation to the other one.

2.2.1.1.2 Harmonic balance analysis

In the harmonic balance method [28], the non-linear circuit is partitioned into a linear sub-circuit and a nonlinear sub-circuit. The linear sub-circuit can be described by the admittance matrix Y , the scattering matrix S , or any other parameters. The nonlinear elements are modeled by their constitutive equations and their operation equations.

The harmonic balance formulates the circuit equations having the harmonic components of the voltages and currents as unknowns. Computing the periodic steady state only, the solution can be written as a Fourier series.

Consider, for the sake of simplicity, a circuit having as nonlinear elements only voltage controlled resistors and voltage controlled capacitors. For such a circuit one can write the nodal equations having as unknowns only the nodes voltages.

Suppose that the steady state is characterized by N_h harmonic components. It follows that each voltage has $2N_h + 1$ harmonic components (one DC component, N_h components with positive frequencies and N_h components with negative frequencies), whose complex amplitudes X_k have to be computed. The circuit to be solved can be partitioned into a linear sub-circuit which contains the independent sources, too, and a nonlinear sub-circuit. These two sub-circuits are connected through $n + 1$ nodes (Figures 2.99 and 2.100).

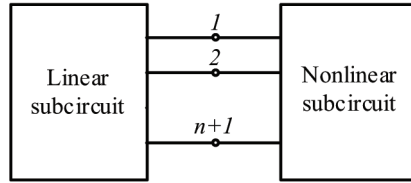


Figure 2.99 Linear and nonlinear sub-circuits.

Suppose that the linear sub-circuit has a voltage controlled representation at the ports $(1, n + 1), (2, n + 1), \dots, (n, n + 1)$ described by $I = YV + J$ where I and V are the vectors of port currents and voltages, and J is the vector of the independent equivalent current sources. The size of the vectors is n and the Y matrix size is $n \times n$. For each harmonic component k , the currents entering the first n linear multiport terminals are $I_k = Y_k V_k + J_k$ where J_k and V_k are the complex magnitudes and Y_k is the port complex admittance matrix computed for the k -th harmonic component.

Let $x(t)$ be the time domain node voltages vector of the nonlinear sub-circuit. These voltages are represented in the frequency domain by the vector X which has $N_x(2N_h + 1)$ components (complex amplitudes) where $N_x + 1$ is the number of nodes in the nonlinear sub-circuit.

The iterative procedure starts from an initial estimation of X which allows the computation of $x(t)$ at certain time points kh ($k = 1, \dots, 2N_h$) using the inverse discrete Fourier transform. Knowing the constitutive equations of the nonlinear elements ($i = i(u)$ for resistors and $q = q(u)$ for capacitors), the current values at the same time points can be computed. The direct discrete Fourier transform computes the complex amplitudes of the nonlinear resistors currents, and the nonlinear capacitors charges. The complex amplitudes of the nonlinear capacitors currents are found from $i = dq/dt$ deriving with respect to time, term by term, the Fourier series of each charge. Knowing the complex amplitudes of all nonlinear sub-circuit currents, the complex amplitudes I_k can be computed using Kirchoff's current law.

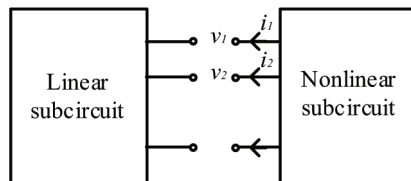


Figure 2.100 Port magnitudes for the nonlinear sub-circuit.

Obviously, the complex amplitudes I_k and V_k depend on X . In the periodic steady state, the currents entering the linear sub-circuit terminals must be equal to those leaving the terminals of the nonlinear sub-circuit. Both due to the arbitrary choice of X and due to the finite number of considered harmonics, this currents equality is verified up to a certain error. For the k -th harmonic component this error is:

$$E_k(X) = Y_k V_k(X) + J_k + I_k(X) \quad (2.81)$$

The aim of this method is to minimize this error up to an imposed limit by using the Newton-Raphson method for solving the equation $E(X) = 0$.

It follows $X^{(n+1)} = X^{(n)} - J^{(-1)}(X^{(n)})E(X^{(n)})$, where J is the Jacobian of the equation $E(X) = 0$. The algorithm of the harmonic balance method is:

1. Initialize X .
2. Analyzing the nonlinear sub-circuit in the time domain, $V_k(X)$ and $I_k(X)$ are computed.
3. Knowing Y_k for each harmonic component, $E_k(X)$ is computed.
4. If $\|E\| \leq \varepsilon$ the solution is obtained, if $\|E\| > \varepsilon$ compute the new X using the Newton-Raphson method and restart from step 2.

2.2.1.1.3 Remarks

The computation becomes very intricate even for simple circuits; for example, if we consider $N_h = 4$ and we have $N_x = 10$ state variables in the nonlinear circuit then the dimension of E is $10 \times (2 \times 4 + 1) = 90$ components and J has 90×90 components.

The convergence of the Newton-Raphson iterations is not guaranteed. To overcome this difficulty, the sub-relaxation may be used: $X^{(n+1)} = X^{(n)} - \alpha J^{-1}(X^{(n)})E(X^{(n)})$ where $\alpha < 1$.

Harmonic balance is implemented in ADS, SERENADE, and APLAC simulators.

It is well known that harmonic balance works very well when the periodic steady state has relatively few harmonics but it has convergence problems for waveforms with steep transitions and for circuits with strongly nonlinear elements. These issues are illustrated by the following example – a first order nonlinear circuit [29].

2.2.1.1.4 Example

The periodic steady state response is computed both in the time domain by the brute force method from PSPICE (OrCad 9.0) and in the frequency domain with the harmonic balance from APLAC Student version 7.70.

For the diode, a piecewise linear characteristic consisting of two segments was considered. Two waveforms have been tested: a sine one and one AM ($\sin(2\pi f_1 t) \sin(2\pi f_2 t)$, $f_1 = 1 \text{ KHz}$, $f_2 = 10 \text{ MHz}$). The harmonic balance result is compared with the one obtained with PSPICE. The slope of the linear segment from the diode characteristic is adjusted in order to observe the influence of the weak or strong nonlinearity.

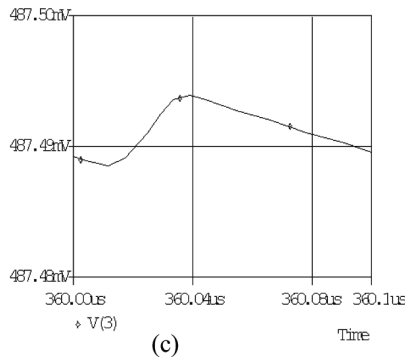
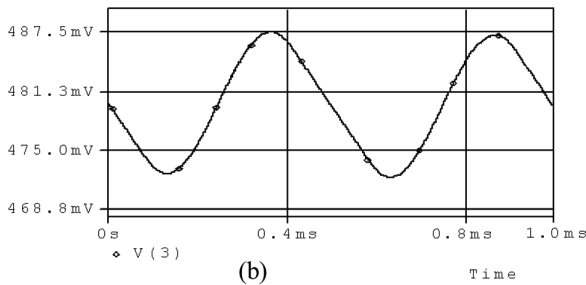
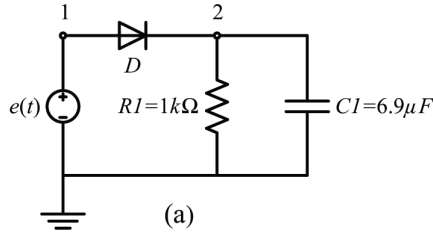


Figure 2.101 First order nonlinear circuit; (a) – circuit, (b) – $V(2)$, (c) – $V(2)$ – detail.

For a sinusoidal input signal there is a good agreement between these two approaches for direct resistance $R_d \in (0.1 \Omega, 10 \Omega)$ and inverse resistance $R_i \in (10 \text{ K}\Omega, 10 \text{ M}\Omega)$. For the amplitude modulated input signal APLAC fails to display the high frequency details of the capacitor voltage. As the ratio

R_i/R_d increases (the nonlinearity becomes strong), the envelope computed by APLAC becomes less accurate. For example, if $R_d = 1 \Omega$, $R_i = 1 M\Omega$, the envelope amplitude computed by APLAC is less than 50% of the one computed with PSPICE. The high frequency detail from Figure 2.99(c) corresponds to $R_d = 0.01 \Omega$ and $R_i = 1 M\Omega$.

A more efficient implementation of the harmonic balance algorithm seems to be that from Advanced Design System (ADS). A simple test has been performed with the AM demodulator in Figure 2.101(a) with $R_d = 1 \Omega$, $R_i = 1 M\Omega$. The envelope amplitude is similar with that obtained by the transient analysis (Figure 2.102).

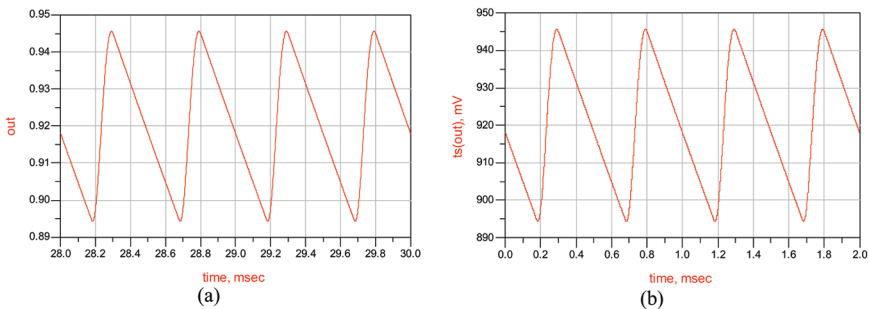


Figure 2.102 AM demodulator – ADS results (a) transient analysis, (b) HB analysis.

Some other tests have shown that the harmonic balance algorithm implemented in ADS gives better results than that implemented in APLAC.

2.2.1.2 Mixed frequency – time domain analysis method implemented in SPECTRE RF

Consider a circuit containing switches, controlled by a relatively high frequency periodic signal compared to the frequency range of the node voltages. For such a circuit the response corresponding to a clock period is similar, but not exactly the same, with the response to the next or previous cycles. Based on this remark, a very efficient algorithm that computes the periodic response of a nonlinear circuit has been developed [36].

Consider the sequence of the initial points of each clock cycle for the circuit node n , noted with $v_n(\tau_1), v_n(\tau_2), \dots, v_n(\tau_n)$ where S is the number of clock cycles in an input period. Suppose that this sequence can be accurately approximated by a truncated Fourier series,

$$V_0 + \sum (V_k^C \cos k\omega\tau_S + V_k^S \sin k\omega\tau_S) = v_n(\tau_S) \quad (2.82)$$

where ω is the fundamental frequency of the input signal, K is the number of the harmonics, and $J = 2K + 1$ is the number of unknown coefficients. Given (2.82), there is a linear relation between any set of J initial points and any other set of J initial points. We are interested in the linear operator that converts a set $v_n(\tau_{\eta_1}), \dots, v_n(\tau_{\eta_J})$ into $v_n(\tau_{\eta_1} + T), \dots, v_n(\tau_{\eta_J} + T)$ where T is the clock period and $\{\eta_1, \dots, \eta_J\}$ is a subset of $\{1, \dots, S\}$. This linear operator is called the delay matrix.

The delay matrix computation is a two-stage process. First, the J points $v_n(\tau_{\eta_1}), \dots, v_n(\tau_{\eta_J})$ are used to calculate the Fourier coefficients. Then the Fourier series (using these coefficients) is evaluated at the J times, $\tau_{\eta_1} + T, \dots, \tau_{\eta_J} + T$. The Fourier coefficients are then eliminated obtaining the desired relation. To compute the Fourier coefficients, (2.82) is written as a system of J linear equations in J unknowns [36]:

$$\Gamma^{-1} \begin{bmatrix} V_0 \\ V_1^R \\ \vdots \\ V_K^R \\ V_K^S \end{bmatrix} = \begin{bmatrix} v_n(\tau_{\eta_1}) \\ v_n(\tau_{\eta_2}) \\ v_n(\tau_{\eta_3}) \\ \vdots \\ v_n(\tau_{\eta_J}) \end{bmatrix} \quad (2.83)$$

where $\Gamma^{-1} \in \Re^{J \times J}$ is given by

$$\begin{bmatrix} 1 & \cos \omega \tau_{\eta_1} & \sin \omega \tau_{\eta_1} & \cdots & \cos K \omega \tau_{\eta_1} & \sin K \omega \tau_{\eta_1} \\ 1 & \cos \omega \tau_{\eta_2} & \sin \omega \tau_{\eta_2} & \cdots & \cos K \omega \tau_{\eta_2} & \sin K \omega \tau_{\eta_2} \\ 1 & \cos \omega \tau_{\eta_3} & \sin \omega \tau_{\eta_3} & \cdots & \cos K \omega \tau_{\eta_3} & \sin K \omega \tau_{\eta_3} \\ \vdots & \vdots & \vdots & & \vdots & \vdots \\ 1 & \cos \omega \tau_{\eta_J} & \sin \omega \tau_{\eta_J} & \cdots & \cos K \omega \tau_{\eta_J} & \sin K \omega \tau_{\eta_J} \end{bmatrix} \quad (2.84)$$

The Γ^{-1} matrix is known as the inverse discrete Fourier transform. If the $\tau_{\eta_1}, \dots, \tau_{\eta_J}$ times are reasonably evenly distributed over one period of the input signal, then Γ^{-1} is invertible. Its inverse, the forward discrete Fourier transform, is denoted by Γ . We can also write

$$\Gamma^{-1} \begin{bmatrix} V_0 \\ V_1^R \\ \vdots \\ V_K^R \\ V_K^S \end{bmatrix} = \begin{bmatrix} v_n(\tau_{\eta_1} + T) \\ v_n(\tau_{\eta_2} + T) \\ v_n(\tau_{\eta_3} + T) \\ \vdots \\ v_n(\tau_{\eta_J} + T) \end{bmatrix} \quad (2.85)$$

where $\Gamma^{-1}(T) \in \mathfrak{R}^{J \times J}$ is given by

$$\begin{bmatrix} 1 & \cos \omega(\tau_{\eta_1} + T) & \sin \omega(\tau_{\eta_1} + T) & \cdots & \cos K\omega(\tau_{\eta_1} + T) & \sin K\omega(\tau_{\eta_1} + T) \\ 1 & \cos \omega(\tau_{\eta_2} + T) & \sin \omega(\tau_{\eta_2} + T) & \cdots & \cos K\omega(\tau_{\eta_2} + T) & \sin K\omega(\tau_{\eta_2} + T) \\ 1 & \cos \omega(\tau_{\eta_3} + T) & \sin \omega(\tau_{\eta_3} + T) & \cdots & \cos K\omega(\tau_{\eta_3} + T) & \sin K\omega(\tau_{\eta_3} + T) \\ \vdots & \vdots & \vdots & & \vdots & \vdots \\ 1 & \cos \omega(\tau_{\eta_J} + T) & \sin \omega(\tau_{\eta_J} + T) & \cdots & \cos K\omega(\tau_{\eta_J} + T) & \sin K\omega(\tau_{\eta_J} + T) \end{bmatrix} \quad (2.86)$$

Given a sequence of samples, a delayed version is computed by applying Γ to the sequence to compute the Fourier coefficients, and then multiplying the vector of coefficients by $\Gamma^{-1}(T)$:

$$\begin{bmatrix} v_n(\tau_{\eta_1} + T) \\ v_n(\tau_{\eta_2} + T) \\ \vdots \\ v_n(\tau_{\eta_J} + T) \end{bmatrix} = \Gamma^{-1}(T)\Gamma \begin{bmatrix} v_n(\tau_{\eta_1}) \\ v_n(\tau_{\eta_2}) \\ \vdots \\ v_n(\tau_{\eta_J}) \end{bmatrix} \quad (2.87)$$

Thus, the delay matrix $D(T) \in \mathfrak{R}^{J \times J}$ is defined as

$$D(T) = \Gamma^{-1}(T)\Gamma \quad (2.88)$$

As the delay matrix is a function only of ω , K , $\{\tau_{\eta_1}, \dots, \tau_{\eta_J}\}$, and T , it can be computed once and used for every node.

Assumed that any analog circuit can be described by a system of differential equations of the form

$$\frac{d}{dt}q(v(t), u(t)) + i(v(t), u(t)) = 0 \quad (2.89)$$

where $v(t) \in \mathfrak{R}^N$ is the vector of node voltages, $u(t) \in \mathfrak{R}^M$ is the vector of independent sources, $q(v(t), u(t)) \in \mathfrak{R}^N$ is the vector of the charges sums at each node, and $i(v(t), u(t)) \in \mathfrak{R}^N$ is the vector of the currents sums entering each node. If the node voltages are known at t_0 time, it is possible to solve (2.89) and compute the node voltages at some later time t_1 . In general, one can write

$$v(t_1) = \phi(v(t_0), t_0, t_1) \quad (2.90)$$

where ϕ is the state transition function and can be written as

$$\phi(v(t_0), t_0, t_1) = \begin{bmatrix} \phi_1(v(t_0), t_0, t_1) \\ \vdots \\ \phi_N(v(t_0), t_0, t_1) \end{bmatrix} \quad (2.91)$$

where $\phi_n : \mathfrak{R}^{N \times 1 \times 1} \rightarrow \mathfrak{R}$ for all nodes $n \in \{1, \dots, N\}$.

For each $j \in \{1, \dots, J\}$ and for each node $n \in \{1, \dots, N\}$ one can write

$$v_n(\tau_{\eta_j} + T) = \phi_n(v(\tau_{\eta_j}), \tau_{\eta_j}, \tau_{\eta_j} + T) \quad (2.92)$$

where T is the clock period. $v_n(\tau_{\eta_j} + T)$ is the initial point of the cycle immediately following the cycle beginning at τ_{η_j} . Also, the node voltages at τ_{η_j} can be related to the node voltages at $\tau_{\eta_j} + T$ by the delay matrix $D(T)$, i.e.

$$D(T) \begin{bmatrix} v_n(\tau_{\eta_1}) \\ \vdots \\ v_n(\tau_{\eta_J}) \end{bmatrix} = \begin{bmatrix} v_n(\tau_{\eta_1} + T) \\ \vdots \\ v_n(\tau_{\eta_J} + T) \end{bmatrix} \quad (2.93)$$

It is possible to use (2.92) to eliminate the $v_n(\tau_{\eta_j} + T)$ terms from (2.93)

$$D(T) \begin{bmatrix} v_n(\tau_{\eta_1}) \\ \vdots \\ v_n(\tau_{\eta_J}) \end{bmatrix} = \begin{bmatrix} \phi_n(v(\tau_{\eta_1}), \tau_{\eta_1}, \tau_{\eta_1} + T) \\ \vdots \\ \phi_n(v(\tau_{\eta_J}), \tau_{\eta_J}, \tau_{\eta_J} + T) \end{bmatrix} \quad (2.94)$$

for each $n \in \{1, \dots, N\}$.

The relations (2.94) can be written as a system whose unknowns are the N vectors of the node voltages at the beginning of the J periods of the clock:

$$F \begin{pmatrix} v(\tau_{\eta_1}) \\ \vdots \\ v(\tau_{\eta_J}) \end{pmatrix} = D(T) \begin{bmatrix} v_1(\tau_{\eta_1}) \\ \vdots \\ v_N(\tau_{\eta_1}) \\ \vdots \\ v_1(\tau_{\eta_J}) \\ \vdots \\ v_N(\tau_{\eta_J}) \end{bmatrix} - \begin{bmatrix} \phi_1(v(\tau_{\eta_1}), \tau_{\eta_1}, \tau_{\eta_1} + T) \\ \vdots \\ \phi_N(v(\tau_{\eta_1}), \tau_{\eta_1}, \tau_{\eta_1} + T) \\ \vdots \\ \phi_1(v(\tau_{\eta_J}), \tau_{\eta_J}, \tau_{\eta_J} + T) \\ \vdots \\ \phi_N(v(\tau_{\eta_J}), \tau_{\eta_J}, \tau_{\eta_J} + T) \end{bmatrix} \quad (2.95)$$

and

$$F \begin{pmatrix} v(\tau_{\eta_1}) \\ \vdots \\ v(\tau_{\eta_J}) \end{pmatrix} = 0 \quad (2.96)$$

where $F : \mathfrak{R}^{NJ} \rightarrow \mathfrak{R}^{NJ}$, and $D_N \in \mathfrak{R}^{NJ \times NJ}$ is given by

$$D_N(T) = \begin{bmatrix} d_{11}I_N & \cdots & d_{1J}I_N \\ \vdots & & \vdots \\ d_{J1}I_N & \cdots & d_{JJ}I_N \end{bmatrix} \quad (2.97)$$

where $d_{ij} \in \mathfrak{R}$ is the ij -th element of the delay matrix $D(T)$, and $I_N \in \mathfrak{R}^{N \times N}$ is the identity matrix.

The system (2.95) can be solved by the Newton-Raphson.

2.2.1.2.1 Example

The circuit is the same with that tested with the APLAC program (Figure 2.101(a)). The excitation is $e(t) = 2 \sin(2\pi f_p t)(1 + \sin(2\pi f_m t))$ with $f_p = 1$ KHz and $f_m = 1$ MHz and the diode is modeled by a piecewise linear resistor (Figure 2.103).

As it is shown in the following figure, the result obtained with shooting in the time domain is the same with the result obtained with shooting in the frequency domain, a slight difference being observed in the high frequency detail.

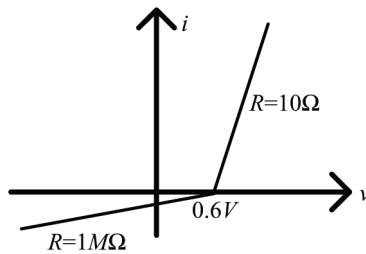


Figure 2.103 Piecewise linear resistor.

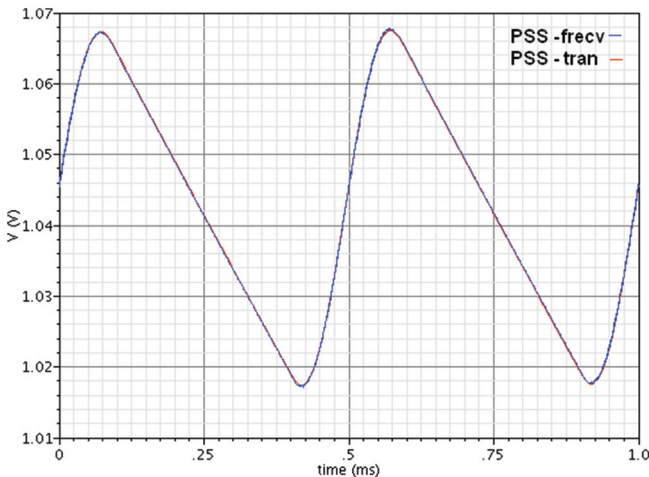


Figure 2.104 Output voltage – circuit in Figure 2.101(a) with the diode model in Figure 2.103.

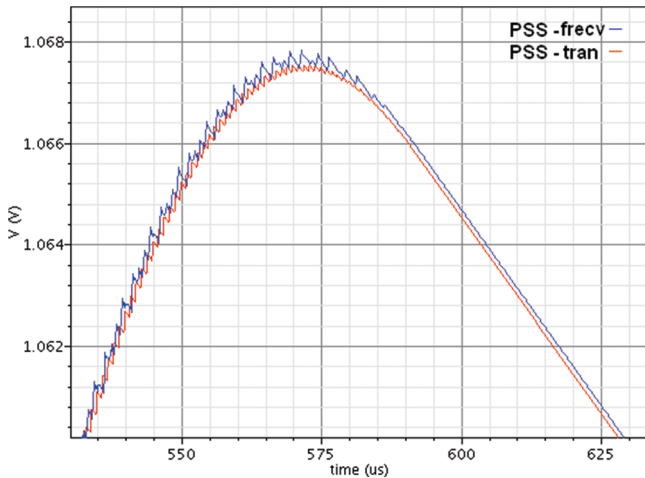


Figure 2.105 Output voltage – circuit in Figure 2.101(a) with the diode model in Figure 2.103 – detail.

In order to obtain this detail many harmonics are needed, increasing substantially the computation time as it is shown in the Table 2.31. This algorithm is implemented in SPECTRE RF as the periodic steady state (PSS) frequency domain analysis, while shooting with Newton-Raphson is implemented as time domain PSS Analysis.

Table 2.31 Shooting in the time domain and in the frequency domain – AM demodulator analysis

| | PSS Time Domain | PSS Frequency Domain |
|------------|-----------------|----------------------|
| Harmonics | 30 | 2800 |
| Iterations | 5 | 11 |
| CPU time | 3.88 s | 24.42 s |

2.2.2 Sources Iteration Method for Circuits with Resistive Nonlinearities

This is a frequency domain method for circuits having linear dynamic elements and resistive nonlinearities. The nonlinearity is treated iteratively using a fixed point method employed successfully in solving nonlinear electromagnetic field problems [31]. The nonlinear resistor is replaced with an equivalent controlled voltage or current source having a linear internal resistance. In this way the nonlinearities are “transferred” to the sources so that the circuit

impedances become linear. Using a Fourier decomposition of the sources, each value of a control voltage (current) is computed by solving a linear circuit. These values are used for sources correction and so on. It can be demonstrated that this iterative process is convergent. The number of the linear equation systems to be solved within an iteration is given by the number of the considered harmonics. The iterations may begin with a small number of harmonics, to improve the calculation efficiency [31].

2.2.2.1 Equivalent sources

Consider that constitutive relationship $i = F(u)$, of the p -port resistor, where $F : R^p \rightarrow R^p$ is Lipschitzian, i.e.

$$\|F(u') - F(u'')\|_{R^p} \leq \Lambda \|u' - u''\|_{R^p}, \forall u', u'' \in R^p \tag{2.98}$$

and monotonic, i. e.

$$\langle F(u') - F(u''), u' - u'' \rangle_{R^p} \geq \lambda \|u' - u''\|_{R^p}^2, \forall u', u'' \in R^p \tag{2.99}$$

with $\lambda > 0$, where the inner product is $\langle x, y \rangle_{R^p} = x^T y$

The resistor may be replaced at any port, by the sources:

$$u_k = r_k i_k + e_k \tag{2.100}$$

where e_k has a nonlinear dependence on u_k [31]:

$$e_k = u_k - r_k F_k(u) \equiv G_k(u). \tag{2.101}$$

If $r_k = \alpha$ with $\alpha \in (0, \frac{2\lambda}{\Lambda^2})$, then the function G is a contraction, i.e.

$$\|G(u') - G(u'')\|_{R^p} \leq \theta \|u' - u''\|_{R^p} \tag{2.102}$$

where the contraction factor is $\theta = \sqrt{1 - 2\alpha\lambda + \alpha^2\Lambda^2} < 1$ [31].

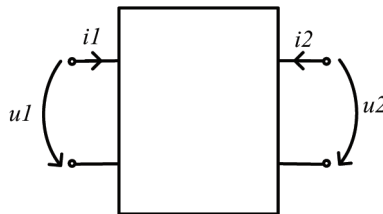


Figure 2.106 Two-port nonlinear resistor.

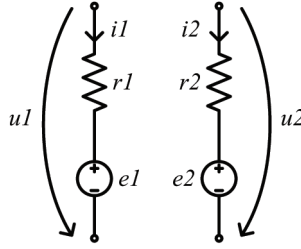


Figure 2.107 Equivalent sources for a two port nonlinear resistor [31].

The smallest value $\theta = \sqrt{1 - \frac{\lambda^2}{\Lambda^2}}$ of the contraction factor is obtained for $\alpha = \frac{\lambda}{\Lambda^2}$.

In the case of the one-port nonlinear resistor, Equations (2.98) and (2.99) lead to a positive bounded increasing u - i relationship and

$$\theta = \text{Max}(1 - \alpha \cdot g_{\min}, \alpha \cdot g_{\max} - 1),$$

with $g_{\min} = \text{Inf}_{u', u''} \frac{F(u') - F(u'')}{u' - u''}$, $g_{\max} = \text{Sup}_{u', u''} \frac{F(u') - F(u'')}{u' - u''}$.

The circuit may contain many nonlinear resistors whose equivalent circuits are similarly built. For the sake of simplicity, in the following is considered a circuit containing only one p -port nonlinear resistor [31].

2.2.2.2 Periodic solutions of the linear circuit

Replacing the nonlinear resistors with voltage (current) dependent sources, we obtain a linear circuit with “linear” relationships (2.88) for resistors. Let u'_β, u''_β and i'_β, i''_β be the branch voltages and currents, corresponding to e', e'' respectively, and $\Delta u_\beta = u'_\beta - u''_\beta$, $\Delta i_\beta = i'_\beta - i''_\beta$, corresponding to $\Delta e = e' - e''$ sources. Tellegen’s theorem gives:

$$\begin{aligned} \langle \Delta u_\beta, \Delta i_\beta \rangle_{R^b} &= \langle \Delta u_\rho, g \Delta u_\rho - g \Delta e \rangle_{R^r} + \left\langle \Delta u_\gamma, C \frac{d \Delta u_\gamma}{dt} \right\rangle_{R^c} + \\ &+ \left\langle L \frac{d \Delta i_\eta}{dt}, \Delta i_\eta \right\rangle_{R^l} = 0 \end{aligned} \tag{2.103}$$

where u_ρ, u_γ are the vectors of the resistors and the capacitors voltages and i_η is the vector of the inductors currents; r, c, l, b are the numbers of the resistors,

capacitors, inductors and of all branches respectively; C and L are positively defined matrices of the capacitances and inductances respectively, and $g = r^{-1}$ is the symmetric and positively defined matrix of all conductances.

The vector Δe has nonzero entries only for the nonlinear resistor ports. Therefore, for the periodic solution we have [31]:

$$\int_0^T \langle \Delta u_\rho, g \Delta u_\rho \rangle_{R^r} dt \leq \int_0^T \langle \Delta u_\rho, g \Delta e \rangle_{R^r} dt \quad (2.104)$$

$$\int_0^T \langle \Delta u_\rho, g \Delta u_\rho \rangle_{R^r} dt \leq \int_0^T \langle \Delta e, g \Delta e \rangle_{R^p} dt \quad (2.105)$$

It follows that the function $e \xrightarrow{W} u$, giving the periodic solution of the linear circuit, is non-expansive in the Hilbert space of the periodic functions [31].

2.2.2.3 Fourier analysis

Any periodic source e_k has a Fourier series expansion in the form

$$e_k(t) = \sum_n ((e'_k)_n \sin(n\omega t) + (e''_k)_n \cos(n\omega t)) \quad (2.106)$$

For the numerical computation, we retain only a finite number N of harmonics, namely $e \cong e_a \equiv Y(e)$, the approximation Y being non-expansive. For each harmonic of e_a the corresponding complex voltage is considered [31].

2.2.2.4 Iterative procedure

Starting from arbitrary initial values for the sources in (2.106) the port voltages of the nonlinear resistor are computed. If the null initial value is chosen, we obtain [31]:

$$u(t) = u^{(0)} = W(0) \quad (2.107)$$

These voltages are produced by the independent sources in the circuit. It follows the sources correction using the relation (2.101):

$$e(t) = e^{(1)} = G(u^{(0)}) \quad (2.108)$$

The harmonic components of these sources are computed and some of them are used for further computation. The harmonic components of the resistor port voltages are computed as:

$$\begin{pmatrix} (u'_k)_n \\ (u''_k)_n \end{pmatrix} = \begin{pmatrix} (a_{k11})_n & (a_{k12})_n \\ (a_{k21})_n & (a_{k22})_n \end{pmatrix} \begin{pmatrix} (e'_k)_n \\ (e''_k)_n \end{pmatrix} \quad (2.109)$$

Using the superposition theorem in the linear equivalent circuit, the time domain port voltages $u_k^{(1)}$ of the nonlinear resistor are computed. These values are obtained as a sum of the voltages $u^{(0)}$ produced by the independent sources and the time domain waveforms corresponding to the result in (2.109). The above steps are repeated until the difference between the last two values of the resistor port voltages is small enough. Each step may be outlined as:

$$e^{(m)} \xrightarrow{Y} e_a^{(m)} \xrightarrow{W} u^{(m)} \xrightarrow{G} e^{(m+1)} \quad (2.110)$$

Because the functions W and Y are non-expansive, and G is a contraction, the composition of these three functions is a contraction having the contraction factor θ . It follows that the above iterative procedure generates a Picard-Banach sequence which converges to the fixed point of the composed function [31].

2.2.2.5 Remarks

1. The initial value $u^{(0)} = W(0)$ and the matrices $((a_k)_n)$ in (2.109) are computed only once, before starting the iterations [31].
2. In most circuits the number of the nonlinear resistor ports is smaller than the resistor branch number, because the most resistors are linear. Using (2.105) it follows:

$$\int_0^T \langle \Delta u, g\Delta u \rangle_{R^p} dt < \int_0^T \langle \Delta u_\rho, g\Delta u_\rho \rangle_{R^r} dt \leq \int_0^T \langle \Delta e, g\Delta e \rangle_{R^p} dt \quad (2.111)$$

The inequality defining the non-expansive nature of the mapping L is stronger in this case, and the convergence speed of the iterative procedure is increased.

3. As the harmonics number taken into account in the Fourier series is smaller, the inequality $\int_0^T (Y(e_k))^2 dt \leq \int_0^T e_k^2 dt$, defining the non-expansive nature of the approximation functions Y is stronger and the speed of the iterative procedure is increased [31].

2.2.2.6 Harmonics selection

The third remark suggests a method for the convergence speed improvement through the selection of the most important weight harmonics. In the first iteration all harmonic components of $e^{(1)}$ up to a certain range N are computed. Starting with the second iteration only those harmonic components having a weight greater than an imposed value are selected [31]:

$$\frac{\sqrt{(e'_k)^2 + (e''_k)^2}}{E} \geq q_1 \quad (2.112)$$

where E is a reference value, for example:

$$E = \sqrt{\frac{2}{T} \int_0^T \|u^{(0)}\|_{R^p}^2 dt} \quad (2.113)$$

The iterative procedure is started using the selected harmonic components only. The Fourier analysis is much faster than the case where all harmonic components are taken into account and the contractive nature of the function chain is stronger. Therefore the convergence speed is increased compared with the case when all N harmonics are used. The iterations are stopped if the error is smaller than an imposed value ε_1 :

$$err = \frac{1}{E} \sqrt{\frac{1}{T} \int_0^T \|\Delta u^{(m+1)}\|_{R^p}^2 dt} \leq \varepsilon_1 \quad (2.114)$$

The Fourier analysis with N harmonic components can be made again, selecting only those components having a weight $q_2 < q_1$. Using these harmonics the iterations are stopped if the error ε_2 is reached. Considering more harmonics and having a weaker contractive nature of the function chain, the convergence speed decreases. The harmonics selection algorithm can be stopped if the iteration number for the new selection is small (for example eight iterations), therefore the improvement obtained by increasing the harmonics number is insignificant [31].

2.2.2.7 Example

Consider the AM demodulator in Figure 2.108 with $e(t) = 2 \sin(2\pi f_1) \sin(2\pi f_2)$, $f_1 = 1 \text{ kHz}$, $f_2 = 1 \text{ MHz}$ and the diode v - i relationship given in Figure 2.109.

The nonlinear element is replaced by a 10Ω resistor in series with a voltage source, whose dependence on the diode branch voltage u is:

$$e = G(u) = \begin{cases} 0, & \text{for } u \geq 0 \\ 0.99999u, & \text{for } u < 0 \end{cases} \quad (2.115)$$

The value $E = 2$ is considered in the relations (2.112) and (2.114). The data describing a set of harmonics selection are given in Table 2.32.

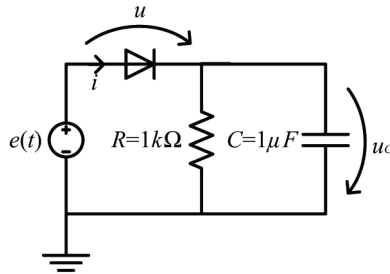


Figure 2.108 AM demodulator.

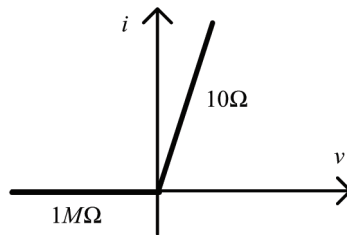
Figure 2.109 Diode v - i relationship.

Table 2.32 Harmonic selections

| Selection | Weight | Harmonic Number | Iteration | Selection |
|-----------|--------|-----------------|-----------|-----------|
| 1 | 0.01 | 16 | 78 | 0.890E-07 |
| 2 | 0.005 | 19 | 27 | 0.841E-05 |
| 3 | 0.002 | 32 | 11 | 0.882E-05 |
| 4 | 0.001 | 41 | 31 | 0.945E-05 |
| 5 | 0.0005 | 85 | 55 | 0.984E-07 |

A part of the diode voltage plot is given in Figure 2.110 [31, 32]. The capacitor voltage is shown in Figure 2.111 and Figure 2.112 shows a high frequency detail.

If 16, 41, 85 or 10,000 harmonic components are used, the plots in Figures 2.108 and 2.109 remain the same. Zooming an area of Figure 2.112, the detail in Figure 2.113 is obtained, illustrating the small differences between various harmonic selections. A 0.7‰ error can be observed between the results obtained with 85 and 10,000 harmonics.

The result obtained with this algorithm is compared with the result of the harmonic balance method and of the shooting with Newton-Raphson method [31]. The capacitor voltage waveforms given by these methods are shown in Figure 2.114.

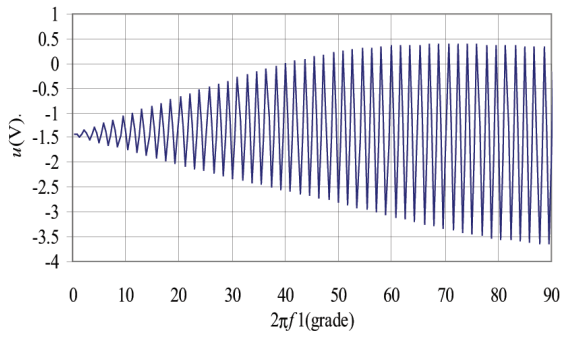


Figure 2.110 Diode voltage.

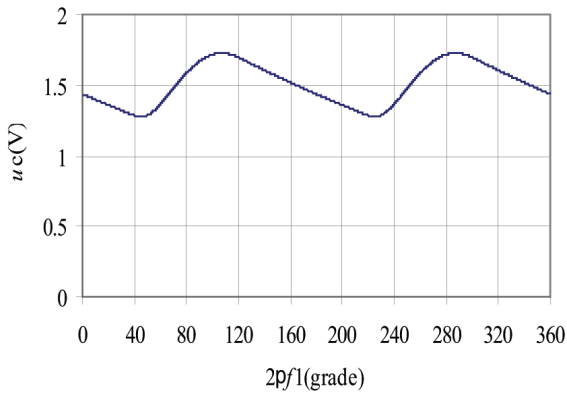


Figure 2.111 Capacitor voltage.

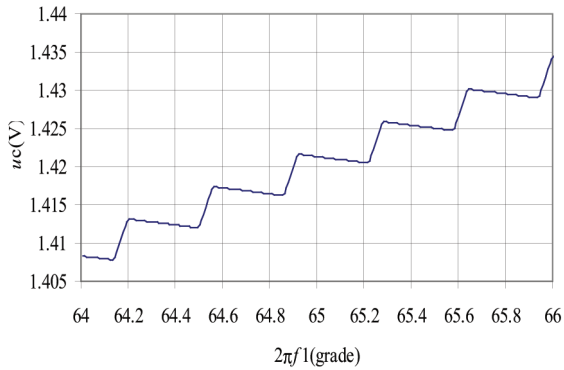


Figure 2.112 Capacitor voltage – detail.

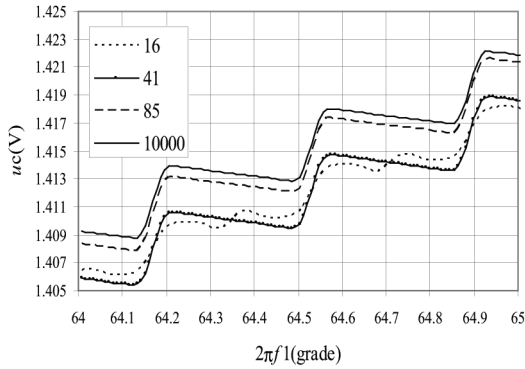


Figure 2.113 Comparison between various harmonics selections.

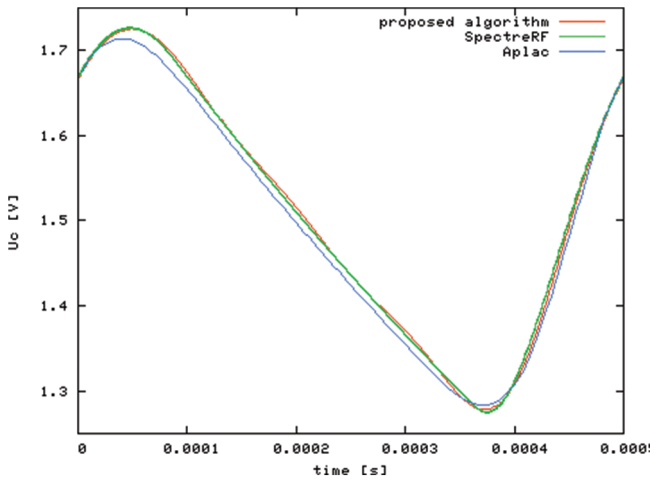


Figure 2.114 u_c given by the proposed method, APLAC, and SPECTRE RF.

The harmonic balance response is obtained with APLAC, while the shooting response is computed with the PSS analysis of SPECTRE RF. A very good agreement between the proposed algorithm and the shooting method can be observed. The differences between these two waveforms and the APLAC harmonic balance response can be explained by the convergence problems of this last method in the case of strong nonlinearities [31].

2.2.3 Circuit Envelope Method

For the efficient and accurate computation of the envelope, a new method of the “Fourier envelope” type, known as the *circuit envelope* method has

been developed. This method uses the time domain techniques combined with the solution computed with the harmonic balance in the frequency domain [33]. The differential equation of the envelope is solved in an outer loop in which the time step is not limited by the signal with rapid changes, while at each time step of the transient analysis, in an inner loop is solved a steady state problem with the harmonic balance method [34]. Unlike the classical method of harmonic balance where the Fourier coefficients are constants representing the value of the periodic steady state [23], in the circuit envelope method, these coefficients are complex time functions $\bar{X}_k(t)$, but are not necessarily periodic. The Fourier coefficients $\bar{X}_k(t)$ are slowly varying transient waveforms. The signals have the form

$$v(t) = \sum_{k=-\infty}^{\infty} \bar{X}_k(t) e^{j2\pi kft} \quad (2.116)$$

where f is the fundamental frequency of the base Fourier series. $\bar{X}_k(t)$ represents the complex modulation of the k -th harmonic. $\bar{X}_k(t)$ must vary slowly relative to f because if the bandwidth of \bar{X}_k becomes greater than $f/2$ then the sidebands of the adjacent harmonics begin to overlap and the representation is not unique.

Rewriting (2.54) and assuming that v and f take the form of (2.116), it results

$$\sum_{k=-\infty}^{\infty} \bar{F}_k(\bar{V}(t), t) e^{j2\pi kft} = 0 \quad (2.117)$$

where

$$F_k(\bar{V}(t), t) = \frac{d\bar{Q}_k(\bar{V}(t))}{dt} + j2\pi kf\bar{Q}_k(\bar{V}(t)) + \bar{I}_k(\bar{V}(t)) + \bar{U}_k \quad (2.118)$$

Assuming that the bandwidth of each term in (2.118) is much less than $f/2$, the terms associated with each harmonic k will sum to zero individually. Then, $F_k(\bar{V}(t), t) = 0$ for each k , or in vector form

$$\bar{F}_k(\bar{V}(t), t) = \frac{d\bar{Q}_k(\bar{V}(t))}{dt} + \Omega\bar{Q}_k(\bar{V}(t)) + \bar{I}_k(\bar{V}(t)) + \bar{U}_k = 0 \quad (2.119)$$

where Ω is a diagonal matrix with $j2\pi kf$ on the k -th diagonal. As with transient analysis, discretization methods such as trapezoidal rule or the backward difference formulae replace dQ/dt with a finite-difference approximation,

converting (2.119) to a system of nonlinear algebraic equations that are solved with Newton's method. For example, applying backward Euler converts (2.119) to

$$\frac{\bar{Q}(\bar{V}(t_m)) - \bar{Q}(\bar{V}(t_{m-1}))}{t_m - t_{m-1}} + \Omega \bar{Q}(\bar{V}(t_m)) + \bar{I}(\bar{V}(t_m)) + \bar{U}(t_m) = 0 \quad (2.120)$$

$\bar{I}(\bar{V}(t_m))$ and $\bar{Q}(\bar{V}(t_m))$ are evaluated at t_s by converting $\bar{V}(t_m)$ into the time domain using the inverse discrete Fourier transform, passing the time-domain voltage waveform through $i(\cdot)$ and $q(\cdot)$, and converting the resulting current and charge waveforms back into the frequency domain using the forward discrete Fourier transform. This procedure relies on the property stating that the envelope is practically constant over the length of a cycle of the carrier.

Circuit envelope has the fundamental advantage over time domain simulators by the fact that the time step must be small enough just to cover the envelope bandwidth instead that of the RF carrier. Figure 2.115 presents the input and the output data of the Circuit Envelope method [33].

It is obvious that the modulated data are completely represented in the time domain as a complex envelope of the RF carrier. The modulation frequency information is not represented by adding signals in the spectrum, but by the time-varying behavior of the spectrum. Hence, even though circuit envelope uses harmonic balance, the matrix size remains reasonable even for the simulation on a personal computer.

Circuit envelope simulates RF circuits with transient or digital signals more efficiently than the existing time and frequency domain simulators exploiting the benefits of both techniques. It does this by processing modulated signal information in the time domain [35] and the RF carrier in the frequency domain (Figure 2.116).

The following five concepts present a basic overview of the circuit envelope simulation process [35].

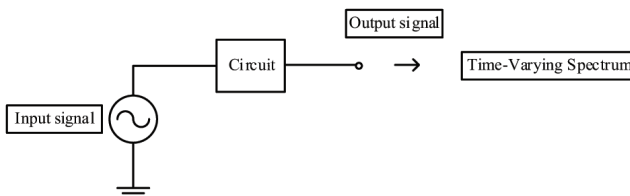


Figure 2.115 Circuit envelope method.

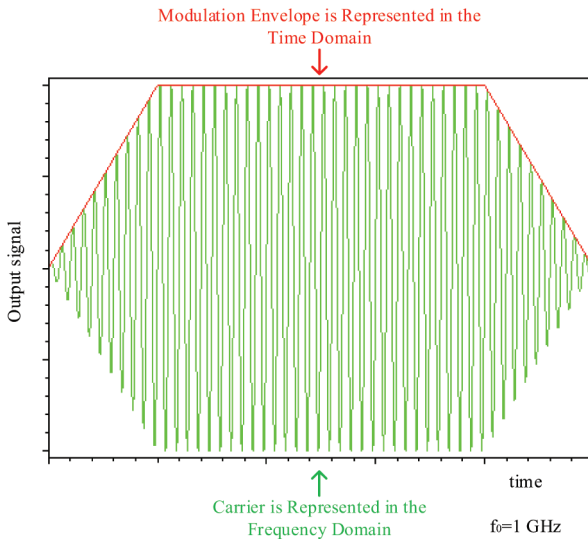


Figure 2.116 Modulated signal in the time domain.

- *Transform input signal*

Each modulated signal can be represented as a carrier modulated by an envelope – $A(t) \cdot e^{jf(t)}$. The values of the amplitude and phase of the sampled envelope are used as input signals for the harmonic balance analyses.

- *Time domain analysis*

Circuit envelope provides a complete non-steady state solution of the circuit through a Fourier series with time-varying coefficients.

- *Frequency domain analysis*

Harmonic balance analysis is performed at each time step, which includes both the basic HB equations as well as the effects due to time-varying envelopes. This process creates a succession of spectra that characterize the response of the circuit at the different time steps.

- *Extract data from time domain*

Selecting the desired harmonic spectral line, it is possible to analyze:

- Amplitude versus time
- Phase versus time
- Amplitude and phase versus time

- *Extract data from frequency domain*

By applying FFT to the selected time-varying spectral line it is possible to analyze:

- Adjacent channel power ratio
- Noise power ratio
- Power added efficiency
- Higher order intermodulation products (3rd, 5th, 7th, 9th)

The set of spectral frequencies is user-defined; the amplitude and phase at each spectral frequency can vary with time, so the signal representing the harmonic is no longer limited to a constant, as it is with harmonic balance. Each spectral frequency can be thought of as the center frequency of a spectrum; the width of each spectrum is $\pm 0.5/\text{Time step}$ [35]. Figure 2.117 illustrates this, where the minimum envelope bandwidth is equal to the bandwidth of the modulation signal. In most cases the bandwidth of the modulation signal is much smaller than the lowest user-defined spectral frequency set by the user.

The band-limited signal within each spectrum can contain periodic, transient, or random tones. The actual time-domain waveform is represented as a sum of carriers (with harmonics and intermodulation products), where each envelope can vary with time [35]:

$$v(t) = \text{real} \left[\sum_{k=0}^N V_k(t) e^{j2\pi f_k t} \right] \quad (2.121)$$

Here, $v(t)$ is a voltage at any node in the circuit, including the input. The Fourier coefficients $V_k(t)$ are allowed to vary with time and may represent an

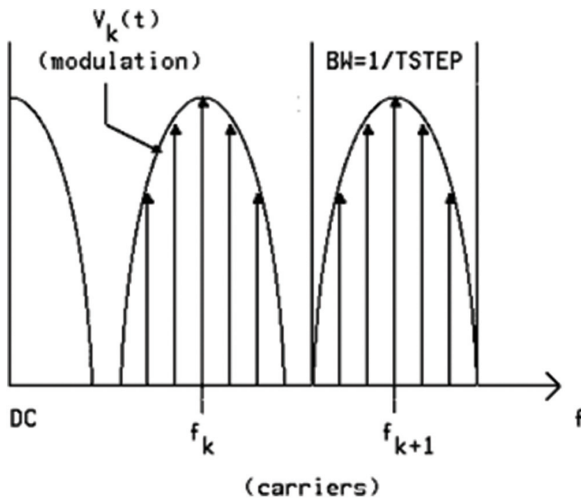


Figure 2.117 Spectra in the frequency domain [35].

arbitrary modulation of each carrier. Since each time-varying spectrum $V_k(t)$ can be thought of as a modulation waveform with a center frequency f_k , these are often referred to as “envelopes”. This spectrum may represent transient signals with continuous spectra, or periodic signals with discrete spectral lines [35].

2.2.3.1 Example

Consider the AM demodulator in Figure 2.101(a), with the diode having the characteristic in Figure 2.118.

This circuit is driven by $e(t) = \sin(2\pi f_m t) \sin(2\pi f_c t)$, $f_m = 1\text{ KHz}$, $f_c = 1\text{ MHz}$, and the response $V(2)$ computed with the transient analysis (TRAN) and with the circuit envelope is given in Figures 2.119 and 2.120.

The two high-frequency details are overlapping (Figure 2.121).

The harmonic balance method from ADS calculates an envelope very close to those computed with the TRAN and ENVLP analyses (Figure 2.122), but the high frequency detail is distorted (Figure 2.123).

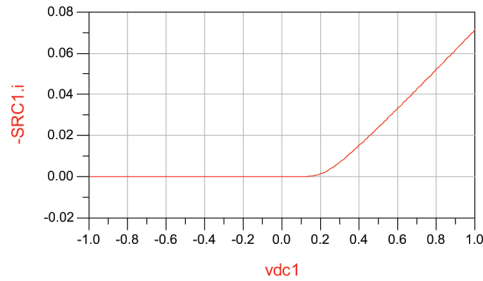


Figure 2.118 Diode characteristic.

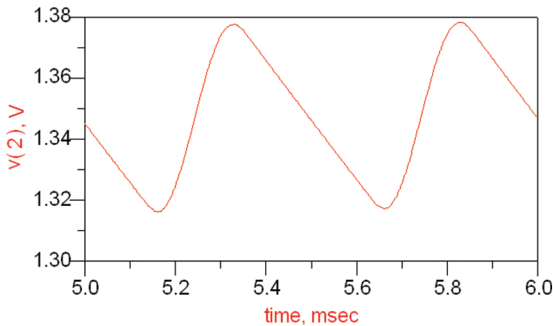


Figure 2.119 V(2) – TRAN analysis.

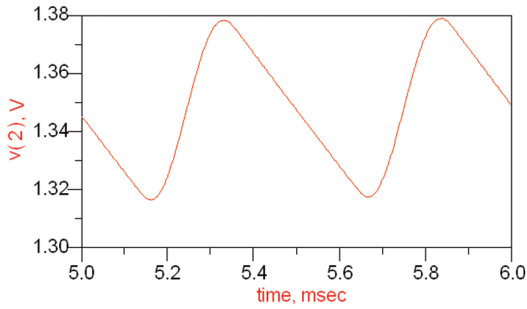


Figure 2.120 V(2) – circuit envelope analysis.

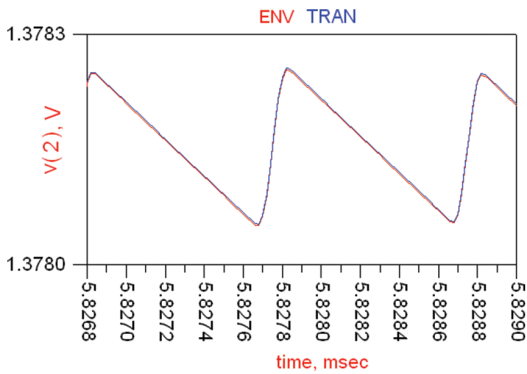


Figure 2.121 V(2) – detail.

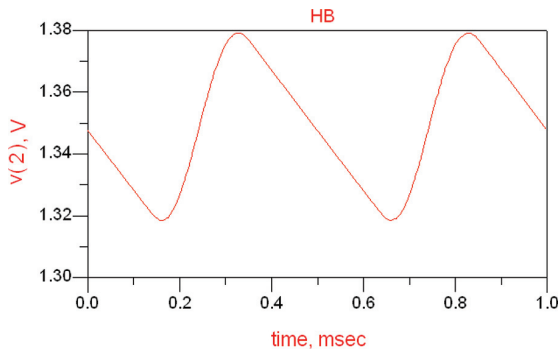


Figure 2.122 V(2) – harmonic balance analysis.

The Fourier envelope method implemented in ADS converge for circuits having strong nonlinearities, while the harmonic balance method from ADS gives better results than the APLAC but the high frequency detail is distorted.

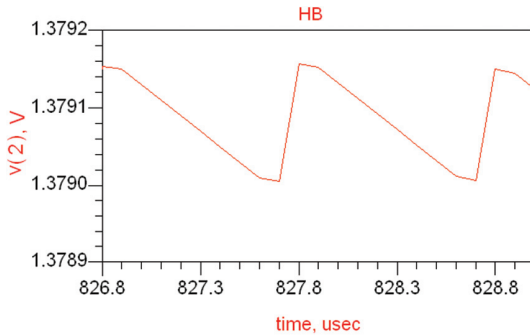


Figure 2.123 $V(2)$ – harmonic balance analysis (detail).

As it can be seen from the above examples the harmonic balance method implemented in ADS works better than the harmonic balance method implemented in APLAC. Both implementations work well if the analyzed circuit has weak nonlinearities and the circuit response has few harmonics. If the circuit contains strong nonlinearities a harmonic balance solution may be affected by errors and if the circuit response contains many harmonics its convergence is slow and the computation time may become high. To speed up the convergence one can use a relatively small number of harmonics in which case the high frequency detail cannot be computed. The sources iteration method is not affected by the strong nonlinearities and can compute the high frequency detail, but its convergence speed is low. Moreover, it can be used only for circuits with nonlinear resistors, the dynamic elements in these circuits being linear. The mixed frequency – time analysis implemented in SPECTRE RF can solve circuits with strong nonlinearities in a relatively small number of iterations but the solution is very sensitive to the choice of the analysis parameters. To obtain the high frequency detail, many harmonics are needed which greatly increases the computation time. The circuit envelope method is designed for circuits having signals with spectrum of the type shown in Figure 2.117 and converges for circuits with strong nonlinearities.

A general mathematical framework for the fast methods aimed to compute the steady state of the RF circuits is given in [49].

References

- [1] Nagel, L. W. (1975). SPICE2: A computer program to simulate semiconductor circuits, Memorandum No. UCB/ERL M520, Electronics Research Laboratory, University of California, Berkeley.

- [2] Vladimirescu, A. (1994). *The SPICE Book*. John Wiley & Sons, Inc.
- [3] Brambilla, A., and A'Amore, D. (2001). Energy-based control of numerical errors in time-domain simulation of dynamic circuits. *IEEE Trans. Circuits Syst. I: Fundamental Theor. Appl.* 48(5) May.
- [4] Constantinescu, F., Gheorghe, A.-G., and Nitescu, M. (2006). Large signal analysis of RF circuits—an overview, *Proceedings of the Conference on Advanced Topics in Electrical Engineering (ATEE 2006)*, Politehnica University, Bucharest, Romania, November 24–25.
- [5] Gheorghe, A. G., Constantinescu, F., and Nitescu, M. (2007). Efficiency of the Envelope Following Analyses. *Proceedings of IEEE International Symposium on Signals, Circuits and Systems (ISSCS 2007)*, 12–13 Iulie, Iasi, Romania, pp. 517–520.
- [6] Brambilla, A., and D'Amore, D. (1993). The simulation errors introduced by the Spice transient analysis, *IEEE Trans. Circuits Syst.–I: Fundamental Theor. Appl.* 40 (1), 57–60, (January).
- [7] Brambilla, A., Storti-Gajani, G. (2003). *Frequency warping in time domain circuit simulation*. *IEEE Trans. Circuits Syst. I: Fundamental Theor. Appl.* 50 (7), 904–913 (July).
- [8] Gheorghe, A. G., Constantinescu, F., Nitescu, M. (2009). Error control in circuit transient analysis, *2009 IEEE International Conference on Electronics, Circuits, and Systems, Medina Hammamet, Tunisia*, December 13–16.
- [9] Constantinescu, F., Gheorghe, A. G., Nitescu, M. (2009). A time step choice algorithm for transient analysis of circuits, *AFRICON 2009*, Nairobi, Kenya, September 23–26.
- [10] Constantinescu, F., Gheorghe, A. G., and Nitescu, M. (2009). An energy balance error based algorithm for time step choice, *JAPMED'6*, Politehnica University Bucharest, July 27–29 2009, Bucharest Romania, extended summary pp. 91–92.
- [11] Constantinescu, F., Gheorghe, A. G., Nitescu, M. (2008). The energy balance error for circuit transient analysis, *Advanced Topics in Electrical Engineering, ATEE'08*, November 20–21, 2008, Bucharest, Romania.
- [12] Constantinescu, F., Gheorghe, A. G., and Nitescu, M. (2010). The energy balance error for circuit transient analysis, *Rev. Roum. Sci. Techn, serie electrotechn. et Energ.* 3.
- [13] Li, X. S., Demmel, J. W., Bailey, D. H., Henry, G., et.al. (2000). Design, implementation and testing of extended and mixed precision BLAS, October 20, 2000, <http://repositories.cdlib.org/lbnl/LBNL-45991>

- [14] Saad, Y., Schultz, M. H. (1986). GMRES: A Generalized Minimal Residual Algorithm for Solving Non-symmetric Linear Systems. *SIAM J. Sci. Stat. Comput.* 7(3), July
- [15] Kundert, K. (2002). A User's Guide to Envelope Following Analysis. CADENCE document, 2002.
- [16] Brambilla, A., Maffezzoni, P. (2003). Envelope—following method to compute steady-state solutions of electrical circuits. *IEEE Trans. Circuits Syst. I: Fundamental Theor. Appl.* 50 (3), March.
- [17] Roychowdhury, J. (1999). Analyzing circuits with widely separated time scales using numerical pde methods. *IEEE Trans. Circuits Syst. I: Fundamental Theor. Appl.* May.
- [18] Roychowdhury, J. (1997). Efficient methods for simulating highly nonlinear multi—rate circuits. *Proceedings of Design Automation Conference.*
- [19] Dunlop, A., Demir, A., Feldmann, P., Kapur, S., Long, D., Melville, R., and Roychowdhury, J. (1998). Tools and Methodology for RF-IC Design. *Proceedings of Design Automation Conference*, June 15–19, San Francisco, CA, pp. 414–420.
- [20] Brachtendorf, H. G., Welsch, G., Laur, R., and Bunse-Gerstner, A. (1996). Numerical steady state analysis of electronic circuits driven by multi-tone signals. *Electrical Engineering*, Springer, Berlin, 79 pp. 103–112.
- [21] Constantinescu, F., Ionescu, A., Nitescu, M. (1998). A new extrapolation method for fast finding of the periodic steady state in nonlinear circuits. *Simposium on nonlinear theory and application (NOLTA'98)*, Crans—Montana, Switzerland, Sept. 14–17, 1998.
- [22] Kundert, K.—“Spectre RF Theory”; July 2002.
- [23] Kundert, K. (1999). Introduction to RF Simulation and its Application. *J. Solid State Circuits*, updated on 23 April 2003.
- [24] Aprille, Jr., T. J., and Trick, T. N. (1972). Steady state analysis of nonlinear circuits with periodic inputs. *Proc. IEEE* 60, 108–114 (Jan).
- [25] Gheorghe, A. G. Efficient Methods for the analysis of nonlinear RF circuits. 3-rd Report of the Ph.D. program (in Romanian).
- [26] Skelboe, S. (1980). “Computation of the periodic steady state response of nonlinear networks by extrapolation methods”, *IEEE Trans. Circuits Syst.*, CAS-27, pp. 161–175.
- [27] Iordache, M., and Dumitriu, L. (2007). “Multi-Time Method Based On State Equations For RF Circuit Analysis”, ISCAS 2007.
- [28] Heikkila, P., Valtonen, M., and Veijola, T. (1991). Harmonic balance of nonlinear circuits with multitone excitation. *Proceedings of ECCTD-91.*

- [29] Constantinescu, F., Nitescu, M., and Marin, C. V. (2006). A glimpse into some aspects of nonlinear circuit analysis. *Rev. Roum. Sci. Techn., Ser. Electrotechn. et Energ.*
- [30] Constantinescu, F., and Nitescu, M. (1999). A multi-rate method for finding the periodic steady-state of nonlinear high speed circuits. *Proceedings of European Conference on Circuit Theory and Design (ECCTD'99)*, vol. 2, pp. 767–770.
- [31] Hantila, I. F., Constantinescu, F., Gheorghe, A. G., and Nitescu, M. (2008). A frequency domain method for analysis of dynamic circuits with resistive nonlinearities. *European Conference on Circuits and Systems for Communications (ECCSC)*, July 10–11, 2008, Politehnica University, Bucharest, Romania.
- [32] Hantila, I. F., Constantinescu, F., Maricar, M., Nitescu, M., and Gheorghe, A. G. (2008). A new method for solving steady-state nonlinear circuits. *Simpozionul Național de Electrotehnică Teoretică (SNET)*, 5–7 iunie 2008, Bucuresti.
- [33] Yap, H.-S. (1998) Designing to digital wireless specifications using circuit envelope simulation. *Applied Microwave & Wireless*, June, pp. 84–89.
- [34] Maryaram, K., Lee, D. C., Moinian, S., Rich, D. A., and Roychowdhury, J. (2000). Computer-aided circuit analysis tools for RFIC simulation: algorithms, features, and limitations. *IEEE Trans. Circuits and Syst. II: Analog and Digital Signal Proces.* 47 (4), April.
- [35] Agilent Technologies, “Circuit Envelope Simulation”, September 2004.
- [36] Kundert, K. S., and White, J. K., and Sangiovanni-Vincentelli, A. (1989). A mixed frequency-time approach for distortion analysis of switching filter circuits. *IEEE Journal of Solid-State Circuits*, April.
- [37] Constantinescu, F., Nitescu, M., and Enache, F. (2004). 2D time domain analysis of nonlinear circuits using pseudo-envelope initialization, *ICCSC'04*, Moscow.
- [38] Kundert, K. S., Sangiovanni-Vincentelli, A., and Tsugawara, T. (1988). Techniques for finding the periodic steady-state response of non-linear circuits, in *Analog Methods for Computer-aided Circuit Analysis and Diagnosis*, edited by T. Ozawa, Marcel Dekker, New York.
- [39] Constantinescu, F., Nitescu, M., Marin, C.V. (2000). SPICE models for two-rate computation of the periodic steady state in nonlinear RF circuits. *Proceedings of NOLTA 2000*, pp. 213–216.

- [40] Gheorghe, A. G. (2009). New methods for the analysis of nonlinear RF circuits, Ph.D. thesis, Department of Electrical Engineering, University Politehnica of Bucharest, November 2009 (in Romanian).
- [41] Gheorghe, A. G., and Constantinescu, F. (2010). Solution computation for resistive circuits containing companion models. University Politehnica of Bucharest, *Sci. Bull. Series C Electr. Eng.* 72 (4), 2010.
- [42] Constantinescu, F., and Nitescu, M. Fundamentals of Electrical Engineering, Part I- Circuit Theory (in Romanian), <http://ferrari.lce.pub.ro/studenti/>
- [43] Constantinescu, F., Nitescu, M., Gheorghe, Al. G., Florea, A., and Llopis, O. (2012). “Behavioral circuit models of power BAW resonators and filters. *Analog Circuit Design and Signal Processing* 73 (1), 57–64.
- [44] Gheorghe, A. G., Constantinescu, F., and Nitescu, M. (2012). Transient computation of DC-DC converters using a new envelope following method. *International Conference on Synthesis, Modeling, Analysis and Simulation Methods and Applications to Circuit Design*, Seville, Spain, September 19–21.
- [45] White, J., and Leeb, S. B. (1991). A envelope following approach to switching power converter simulation. *IEEE Trans. Power Elect.* 6 (2) pp. 303–307 (March 1991).
- [46] Gheorghe, Al. G., Constantinescu, F., Marin, M. E., and Nitescu, M. (2013). The envelope following analysis of a buck converter with closed loop control. *4-th International Symposium on Electrical and Electronics Engineering*, 11–13 Oct. 2013, DOI: 10.1109/ISEEE.2013.6674359, pp. 1–5, ISBN 978-1-4799-2442-4, INSPEC Accession Number: 13936673, Galati ROMANIA.
- [47] Rumin, N. C. (1988). Evidence for the existence of a useful periodic steady-state algorithm for nonlinear circuits. *IEEE Trans. Circuits Syst.* 35 1444–1447.
- [48] Constantinescu, F., and Nitescu, M. (2000). Two-rate computation of the periodic steady-state in RF-IC circuits, *International Symposium on Circuits and Systems*, May 28–31, 2000, Geneva Switzerland, pp. 121–124.
- [49] Nastov, O., Telichevsky, R., Kundert, K., and White, J. (2007). Fundamentals of fast simulation algorithms for RF circuits. *Proceedings IEEE*, 95 (3) (March 2007), pp. 600–621.

3

Nonlinear Circuit Models for Power Bulk Acoustic Wave Resonators and Filters

3.1 Bulk Acoustic Wave Resonators – Structure and Nonlinear Behavior

The thin film piezoelectric resonators technology has emerged about 40 years ago. Since the series resonance frequency is inversely proportional to the thickness of the piezoelectric material layer, the film became thinner in order to obtain resonance frequencies increasingly larger. Modern thin films deposition technology of piezoelectric materials allows fabrication of resonators and filters in the 500 MHz–20 GHz range [1].

Because in the near future, the production of high power CMOS transistors is not expected, the front end of the mobile phones will remain analogic. In order to miniaturize the mobile phones, the numerical and the analogical part can be integrated together to form a SIP/SoC system (System In a Package/System On a Chip). To this end, the bulk acoustic wave (BAW) resonators having AlN as piezoelectric layer is one of the best solutions. BAW technology is compatible with the silicon substrate and with the CMOS integrated circuits and is significantly cheaper than the surface acoustic wave (SAW) resonators technology [2].

As a BAW resonator is incorporated into an electronic system, its equivalent circuit is very useful for its design. Further, the relations between the equivalent circuit parameters and the physical phenomena in the resonator are of outstanding interest in the design of these devices [1].

The electromechanical devices, just like the ones with quartz crystal, are of interest in electronic systems because they can have a large Q at resonance. The quality factor of the mechanical system can be retrieved at the electronic system terminals. An AC signal applied to a crystal having a frequency close

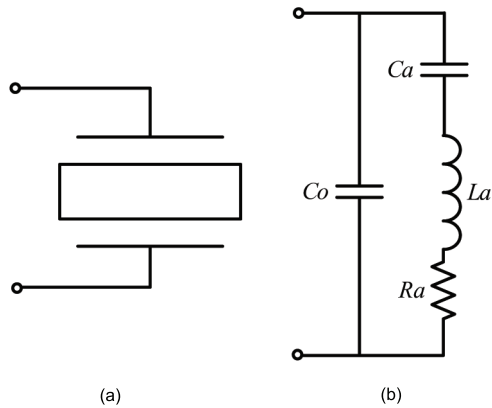


Figure 3.1 Crystal resonator. (a) symbol (b) equivalent circuit.

to the mechanical resonance will result in mechanical vibrations that will produce a current at the electrical terminals (Figure 3.1).

From the geometric point of view, the resonator has the form of a capacitor having a piezoelectric material as dielectric, and metal electrodes. The symbol for the crystal resonator in Figure 3.1 is associated with a simple equivalent circuit. This symbol dates back to the time when the piezoelectric material was ‘glued’ to the metal electrodes that do not touch the vibration surface. Given that the mechanical motion is measured in fractions of a nanometer, practically there is no movement and the thin electrodes can be deposited directly on the resonator. Most resonators have the main propagation direction of the acoustic wave perpendicular to the electrodes, which means that the bulk acoustic wave (BAW) is reflected between the surface of the electrodes. The boundary conditions correspond to small border losses, leading to a high Q at resonance. The Butterworth-Van Dyke equivalent circuit of the piezoelectric resonator (Figure 3.1(b)) illustrates the transducer mechanism and the resonance response. C_o is the geometric capacity of the structure, close to the resonance, and the $C_a L_a R_a$ series circuit (called the motional branch) represents the mechanical resonance. The ratio C_o/C_a is fixed by the topology and by the piezoelectric material of the resonator. C_a and L_a , resonate at a frequency determined by the thickness of the resonator, and R_a is determined by losses. Starting from a lower frequency, the first resonance is a series resonance of the motional branch, and increasing the frequency, the inductive reactance becomes greater and the parallel resonance with C_o occurs. Between the series and the

parallel resonance, the circuit behavior is inductive. In addition, the equivalent inductance has a very high quality factor Q , for acoustics reasons. This is the explanation why the crystal resonators are used in so many applications requiring frequency control. A second reason could be that the crystal resonators have very small sizes, because in the crystal the wavelength of sound is four times smaller than that of the electromagnetic waves. This small wavelength, translated from the technological point of view in a very thin structure, was the source of difficulties in obtaining microwave crystal resonators [3].

Since the resonant frequency is inversely proportional to the thickness of the piezoelectric layer, for the microwave frequencies a very thin layer is needed. In the 1960s, because of the existing technologies, CdS and ZnO have been used as piezoelectric layers. Since the thin layers of piezoelectric material must be deposited on a substrate about which no one knew how will support these thin films, the first applications were for radar transducers. With the current technologies (micro and nano), the crystal resonators can be used for the synthesis of microwave filters.

The achievement of a high Q can be provided by the treatment of appropriate layers and by obtaining the needed thickness (in the micrometers range). At frequencies below 500 MHz, the crystal layer can be processed to the desired thickness, but the microwave frequency range is necessary to deposit a film on a suitable substrate. For example, a resonator with aluminum nitride (AlN) at 1,600 MHz has a thickness of 3 μm , aluminum electrodes of 0.3 μm thickness, and an area of 0.25×0.25 mm, and its ratio between the lateral dimension and the thickness is greater than 50: 1.

In Figure 3.2 (a) is shown a resonator with air gap, which is provided in order to prevent the mechanical waves to reach the substrate; this phenomenon is responsible for the substrate heating and its consequence – the decrease in the Q value. For the fabrication, initially the substrate is deposited, followed by the introduction of a temporary support; next the lower electrode, a piezoelectric film, and then the upper electrode are deposited. Finally, the support is removed and remains a film resonator having adjacent air borders and certain mechanical peripheral supports. This technology is known as FBAR.

In Figure 3.2 (b), the structure of a SMR resonator (solidly mounted resonator) is presented. This device is obtained by isolating the resonator from the substrate through a reflector (Bragg mirror) made from layers of a quarter thickness of the nominal wavelength. The number of deposits depends on the required reflection coefficient and on the ratio of the characteristic impedance

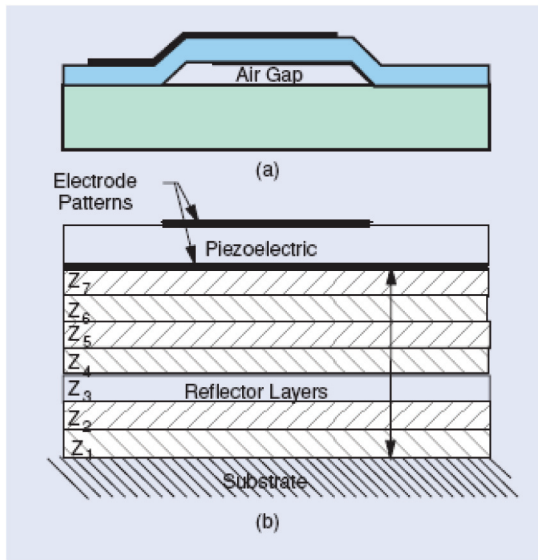


Figure 3.2 Thin film resonators [3]. (a) FBAR, (b) SMR.

of two successive layers. For example, a nine-layer reflector for a 1.575 MHz GPS will have 5 layers of silicon dioxide ($0.93 \mu\text{m}$) and 4 layers of AlN ($1.7 \mu\text{m}$) [3].

The BAW resonators have a linear behavior if they are driven by a low power excitation. In this case, a linear Butterworth-Van Dyke equivalent circuit (Figure 3.1.(b)) may be used to simulate their behavior.

Some measurements highlight the nonlinear behavior of these devices while they are driven by a high power excitation. Such devices are called power BAW resonators. The nonlinear behavior of the piezoelectric materials is a problem that goes back about 40 years [4]. There have been many attempts to explain it using the perturbation theory that led to the identification of the “nonlinear constants” associated with different material properties (elastic, electrical, electromechanical coupling) [3, 4].

By measuring the periodic steady state response at the resonator terminals, three effects can be evidenced:

- **the amplitude-frequency effect**

The amplitude-frequency effect of a quartz resonator represents the increase of the resonance frequency when the input power increases

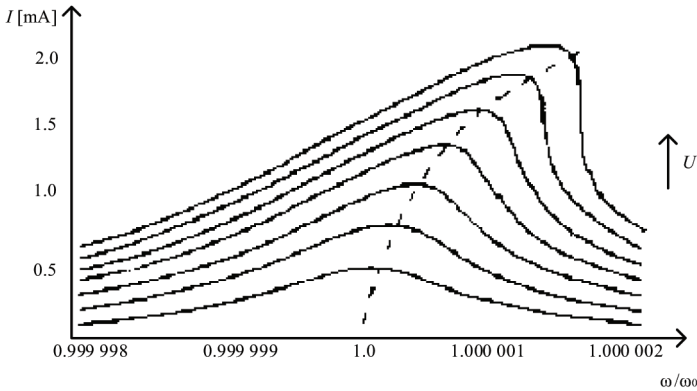


Figure 3.3 Frequency characteristics of a quartz resonator (I – current through the resonator, U – excitation voltage).

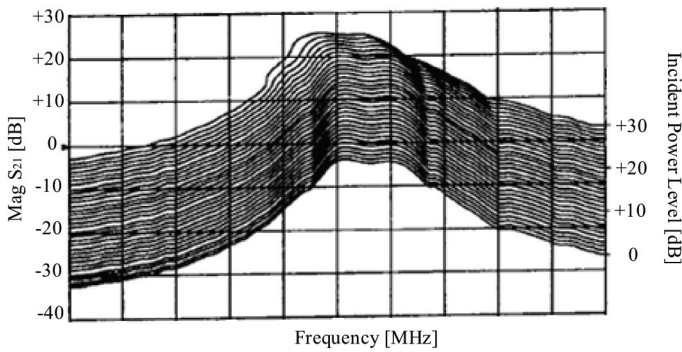


Figure 3.4 Amplitude-frequency effect of a stack crystal filter with AlN.

(Figure 3.3.). For the AlN resonators, the series resonance frequency decreases (Figure 3.4) if the input power increases.

- **the intermodulation effect**

The intermodulation effect of a power BAW resonator driven by a sinusoidal signal of frequency f consists in the appearance of the $2f$ and $3f$ harmonics in the resonator response.

- **the bias-frequency effect**

The bias-frequency effect refers to the change in the resonance frequency by introducing a direct current component of tens of volts in the excitation signal.

3.2 Linear Parametric Circuit Models

Some physical models of the power BAW resonators have been proposed in the literature. These models are based on the assumption that at least one of the constitutive equations of the electromechanical field (electrical, mechanical, or electromechanical) is nonlinear. For the nonlinear approximation of these equations Taylor series expansion is used taking into account terms up to the 3rd or 4th order. In [4], it is shown that the results obtained by different authors who are using these types of models differ from each other. The reason for this mismatch is related to systematic measurement errors, errors in judging the crystal orientation, mathematical calculation errors, the computation with improper chosen coefficient, etc. However, very good concordances between the simulation results of these models and the measurements made by their authors are reported [4]. What bothers most is that these models cannot be implemented in any type of circuit analysis program.

A solution for modeling a power BAW resonator could be a circuit whose parameters are identified from the measurements made under real conditions. This circuit is a behavioral model, which apparently seems to ignore the physical phenomena in a BAW resonator. Nevertheless, these phenomena are used to choose which elements are nonlinear and what is the nature of their nonlinearities.

In the first stage of the modeling, the material parameters changes with the temperature are not taken into account. These models illustrate correctly the amplitude-frequency effect and the intermodulation effect for a practical interest range of frequencies and excitation amplitudes. In the second stage of the modeling, the effects of temperature variation on material parameters and heat exchange between the resonator and its environment must be considered.

3.2.1 Nosek and Albareda Models

In [5], a linear parametric circuit model for a quartz resonator is proposed (Figure 3.5).

Starting from the measured quadratic dependence of the resonance frequency with the r.m.s. value of the current, this model contains a constant inductance and a capacity which depend on the r.m.s. value of the current:

$$\frac{1}{C(I)} = \frac{1}{C}(1 + \alpha I^2) \quad (3.1)$$

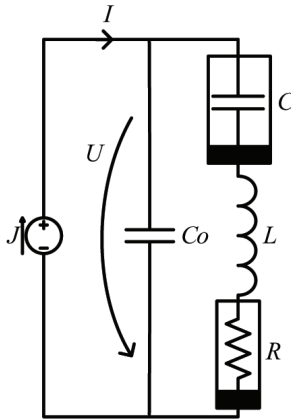


Figure 3.5 Linear parametric circuit model for a quartz resonator [5].

The resistance value is given by (3.2):

$$R(I) = R(1 + \beta I^2) \quad (3.2)$$

This model leads to a correct dependence of the current value on frequency, for a set of the input voltages U . Obviously, a correct dependence of the series resonance frequency on the input voltage is obtained [5]. The set of graphs in Figure 3.6 is given for $U = U_0 = 0.1 \text{ V}$ and $U = U_0 + k\Delta U$ where $\Delta U = 0.0533 \text{ V}$ and $k = 0, 1, \dots, 6$.

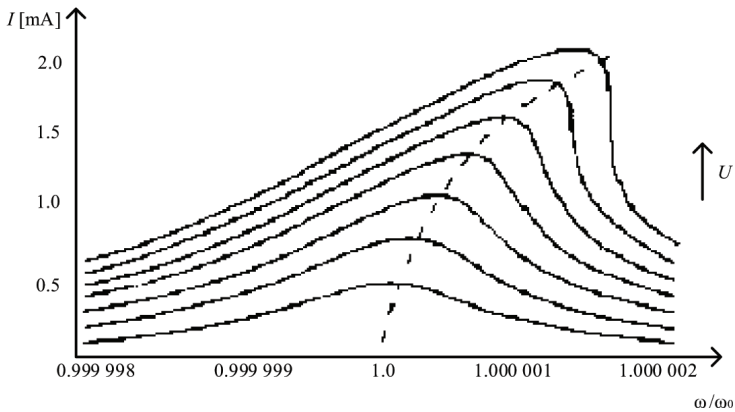


Figure 3.6 Frequency characteristics of a nonlinear crystal resonator [5].

The analysis of this circuit is made in the complex domain neglecting the current through C_0 [5]. It is not clear how this analysis is made, given that it is considered a dependency of C on $i = I \sin \omega t$ instead of the proposed $C(I)$ [7].

In [6] is proposed a similar parametric linear model (Figure 3.7) containing a series reactance $X_1 = X_{10} + \alpha_2 I_1^2 + \alpha_4 I_1^4$ and a series resistance $R = R_{10} + \beta_2 I_1^2 + \beta_4 I_1^4$, where I_1 is the r.m.s. value of the series branch current. This model considers a 4th order nonlinear mechanical constitutive equation.

The measured dependences of the reactance and resistance on current through the resonator motional branch are given in Figure 3.8.

This model reproduces the measured reactance and resistance of a resonator with a ceramic piezoelectric.

These two models can reproduce the amplitude-frequency effect for frequency and amplitude values of practical interest, but cannot reproduce the intermodulation effect.

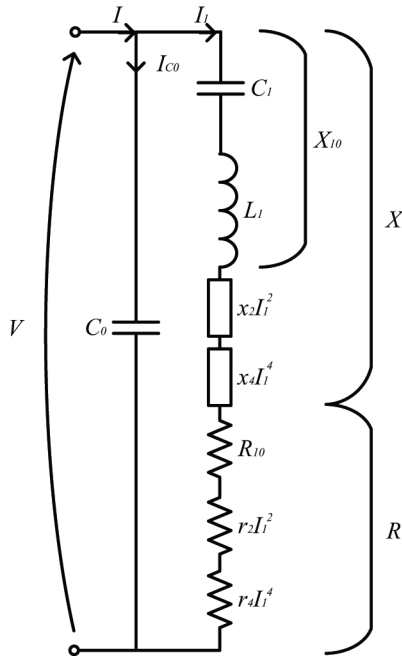


Figure 3.7 Linear parametric circuit model of a resonator [6].

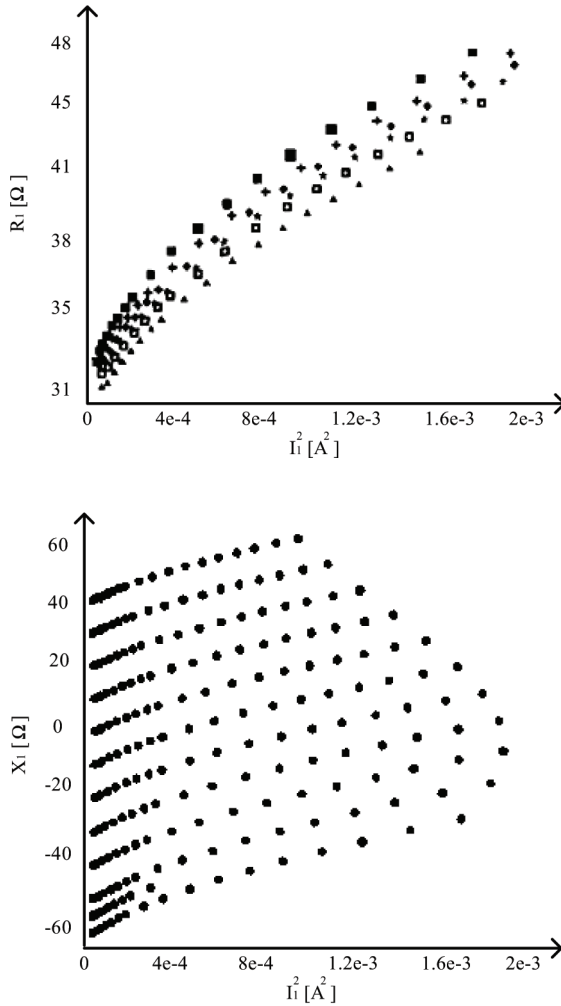


Figure 3.8 Dependence of the resistance and the reactance on I_1 at different frequencies.

3.2.2 Identification of the Nosek Model Parameters

The model parameters identification can be made based on the approximate formulas for resonance frequencies, the expression of the voltage across the model and the measured frequency characteristics (Figure 3.6) [7]. The parameter identification method is presented in the following.

The admittance of this model is computed as follows:

$$Y(s) = C_0 \frac{s(s - z_1)(z - s_2)}{(s - p_1)(s - p_2)}$$

where

$$p_{1,2} = -\frac{R}{2L} \pm \frac{1}{2} \sqrt{\frac{R^2}{L^2} - \frac{4}{LC}}$$

and

$$z_{1,2} = -\frac{R}{2L} \pm \frac{1}{2} \sqrt{\frac{R^2}{L^2} - \frac{4}{L} \left(\frac{1}{C} + \frac{1}{C_0} \right)}.$$

Setting $s = j\omega$ the admittance module is as follows:

$$|Y(j\omega)|^2 = \frac{\omega^2 R^2 / L^2 + (1/(LC) + 1/(LC_0) - \omega^2)^2}{\omega^2 R^2 / L^2 + (1/(LC) - \omega^2)^2} \cdot C_0^2 \omega^2$$

The resonance frequencies are defined as corresponding to the maximum and minimum values of $|Y(j\omega)|$. Considering $\frac{\partial |Y(j\omega)|}{\partial \omega} = 0$, no analytical solution has been found. Even though the algorithm in [8] could be used to compute the approximate symbolic expressions of poles and zeros, the known relations

$$\omega_s^2 = \frac{1}{LC}, \quad \omega_p^2 = \omega_s^2 + \frac{1}{LC_0}$$

are preferred for the approximate solutions of $\frac{\partial |Y(j\omega)|}{\partial \omega} = 0$.

Consider a given family of n frequency characteristics as in Figure 3.6. The series resonance frequency on the curve k satisfies the relation

$$\omega_{sk}^2 = \frac{1}{LC} (1 + \alpha I_k^2) \quad (3.3)$$

for $k = 1, \dots, n$.

Considering the expressions (3.3) of two frequencies ω_{sk} and ω_{sj} , by their division one can compute the value of α :

$$\alpha = \frac{\omega_{sk}^2 - \omega_{sj}^2}{\omega_{sk}^2 I_k^2 - \omega_{sj}^2 I_j^2} \quad (3.4)$$

where I_k is the r.m.s. value corresponding to ω_{sk} .

Taking into account that the values ω_{sk} and I_k are measured with certain errors, the following algorithm will give the best value for α . The

Equation (3.3) can be written as $a_k = LC\omega_{sk}^2 = 1 + \alpha I_k^2$ ($k = 1, \dots, n$). If the measured pairs (a_k, I_k^2) are represented with respect to the coordinates a and I^2 , a straight line corresponding to the least squares approximation will give the best value for α .

For each ω_{sk} , it follows:

$$U_k^2 = \frac{I_k^2}{\frac{1}{R^2(1 + \beta I_k^2)} + \omega_{sk}^2 C_0^2}$$

$k = 1, \dots, n$, which can be written as

$$A_k = 1 + \beta I_k^2 \quad (3.5)$$

$k = 1, \dots, n$, where A_k are some constants.

The best value for β can be determined from (3.5) in a similar manner to the above mentioned best value for α .

The frequency characteristic for the small signal excitation being given, the value of the quality factor at ω_s in this case is known and satisfies

$$Q = \frac{\omega_s L}{R} \quad (3.6)$$

The series and parallel resonance frequencies for the small signal input are as follows:

$$\omega_s^2 = \frac{1}{LC}, \quad \omega_p^2 = \omega_s^2 + \frac{1}{LC_0}. \quad (3.7)$$

The input voltage at ω_s for the small signal excitation satisfies the following relationship where U and I are small signal values

$$U^2 = \frac{I^2}{\frac{1}{R^2} + \omega_s^2 C_0^2} \quad (3.8)$$

The algorithm for parameter identification of the Nosek AC model is as follows:

- 1) The values L , C , C_0 , and R are computed using (3.6–3.8).
- 2) The best values for α and β are computed using the above mentioned algorithm for α .

Example

The resonator data are: $\omega_s = 2\pi \cdot 5 \cdot 10^6 \text{ s}^{-1}$, $\omega_p = 2\pi \cdot 5.06 \cdot 10^6 \text{ s}^{-1}$, $Q = 0.8 \cdot 10^6$, and the coordinates of the resonance points are given in Table 3.1 corresponding to the family of the frequency characteristics in Figure 3.6.

Table 3.1 Coordinates of the resonance points

| ω_{sk}/ω_s | $I(mA)$ | $U(V)$ |
|------------------------|---------|--------|
| 1.00000015 | 0.70 | 0.1000 |
| 1.00000025 | 0.80 | 0.1533 |
| 1.00000040 | 1.25 | 0.2066 |
| 1.00000060 | 1.45 | 0.2599 |
| 1.00000085 | 1.70 | 0.3132 |
| 1.00000120 | 1.90 | 0.3665 |
| 1.00000145 | 2.10 | 0.4198 |

From the Equations (3.6–3.8), it follows: $R = 165 \Omega$, $L = 4.2 \text{ H}$, $C = 2.412 \cdot 10^{-16} \text{ F}$, $C_0 = 1.116 \cdot 10^{-10} \text{ F}$.

The least squares approximation algorithm led to the following results: $\alpha = 1.14 \text{ A}^{-2}$, $\beta = 3.405 \cdot 10^5 \text{ A}^{-2}$.

Taking into account these values, $\frac{\partial|Y(j\omega)|}{\partial\omega}$ is evaluated in ω_s and ω_p . The obtained figures ($0.9 \cdot 10^{-6}$, $0.3 \cdot 10^{-11}$) using a computation with 50 digits in MAPLE 9 may be considered as satisfactory approximations of 0.

3.2.3 Discussion on Linear Parametric Circuit Models

Development of some circuit models for BAW resonators is very useful in design of mobile phone filters which are made of multiple resonators (Figure 3.9).

Linear behavior of the resonators in the vicinity of the fundamental frequency is modeled by the Butterworth-Van Dyke circuit. The nonlinear effects occurring in power BAW resonators are modeled using several types of circuits that attempt to explain these phenomena using the theory of nonlinear perturbations to identify the constants associated with various material properties (elastic, electric, electromechanical).

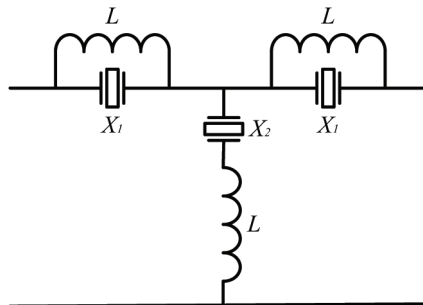


Figure 3.9 BAW filter.

Physical models like those described in [5, 6] assume that at least one of the constitutive equations of the electromechanical field in resonator is nonlinear. In [4] is shown that the results obtained by various authors are not consistent with each other. The reason that these models do not match each other is related to the fact that so-called “nonlinear constants” that appear in Taylor series expansion of nonlinear constitutive equations cannot be measured directly.

To avoid these difficulties, behavioral models based on measured data taken under similar conditions to the real operation of the resonators have been developed.

In [9, 12] a process for identifying the parameters based on a set of frequency characteristics is proposed.

Parametric linear models can reproduce only amplitude-frequency effect, but not the intermodulation effect. Since the frequency domain analysis programs APLAC, Serenade, and ADS do not allow the using of r.m.s. values as a control variable, linear parametric models cannot be implemented in this kind of programs. Implementation of these models is not possible either in time domain analysis programs like SPICE or SPECTRE RF because the r.m.s. value depends on the instantaneous values of the current for a period. The utility of these models is that they can illustrate through equivalent circuits the nonlinear amplitude–frequency effect for the power BAW resonators.

Simulation of resonators and filters using linear parametric circuit models can be made using special methods such as AC iterative analysis [7] or a symbolic method [13]. But these methods can be used only for simple circuits with few resonators.

3.3 Nonlinear Circuit Models

3.3.1 Behavioral Circuit Models

The most promising model is a nonlinear circuit model suggested in [14] without mentioning the values of circuit parameters or simulations results and comparison with measured values. Starting from this idea and taking into account the shortcomings of linear parametric circuit models, some models that can be implemented in a time domain analysis program like SPICE or SPECTRE RF (Cadence) and in a frequency domain simulator as APLAC or ADS have been proposed [15–18].

The first proposed model is based on the BVD circuit whose schematic is given in Figure 3.1. (b). The resistor, inductor, and capacitor in the motional branch are nonlinear and are implemented as nonlinear controlled sources with polynomial nonlinearities as in Figure 3.10.

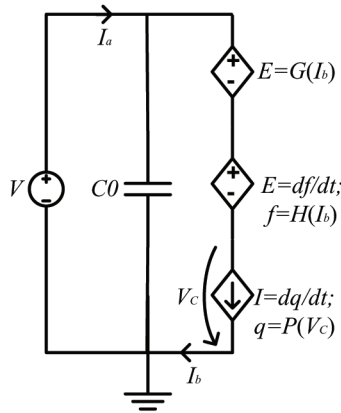


Figure 3.10 Controlled source implementation of the first nonlinear circuit model.

To implement this circuit in APLAC is considered the following parameter values:

```

C0 = 1.566e-12
CCVS R1 1 2 1 b [4.7 *(CI(0)+0.5*CI(0)^2+0.5*CI(0)^3)] R
CCVS L1 2 3 1 b [3.5e-9*(CI(0)-5e-2*CI(0)^2+1e-2*CI(0)^3)] L
VCCS C1 3 5 1 3 5 [.177e-12*(CV(0)+1e-2*CV(0)^2+1e-4*CV(0)^3)] C
    
```

The amplitude-frequency effect of this model is shown in Figure 3.11, where the frequency characteristics are given for amplitude excitation of 1 V, 3 V, and 5 V.

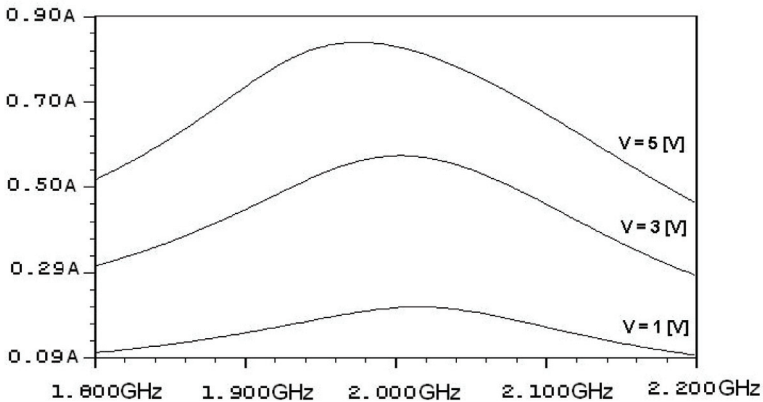


Figure 3.11 Plot of I_a versus frequency for the first model.

Amplitudes of the second and third harmonics obtained with the first model are given in Figure 3.12 and Figure 3.13 for three excitation frequencies.

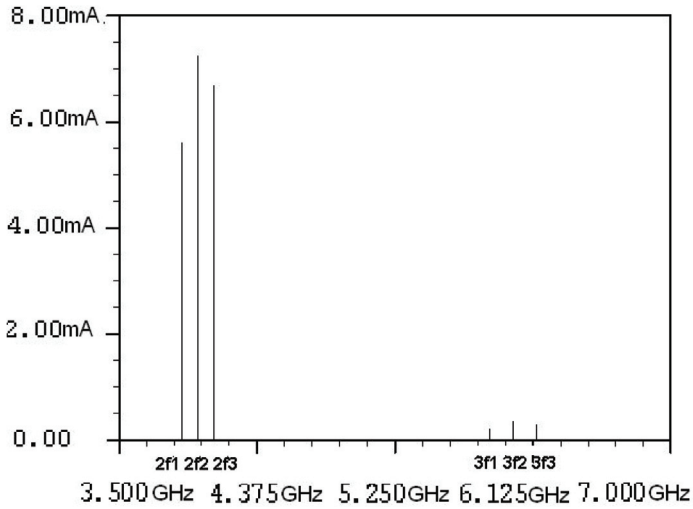


Figure 3.12 Intermodulation products for $V = 1$ V, the first model.

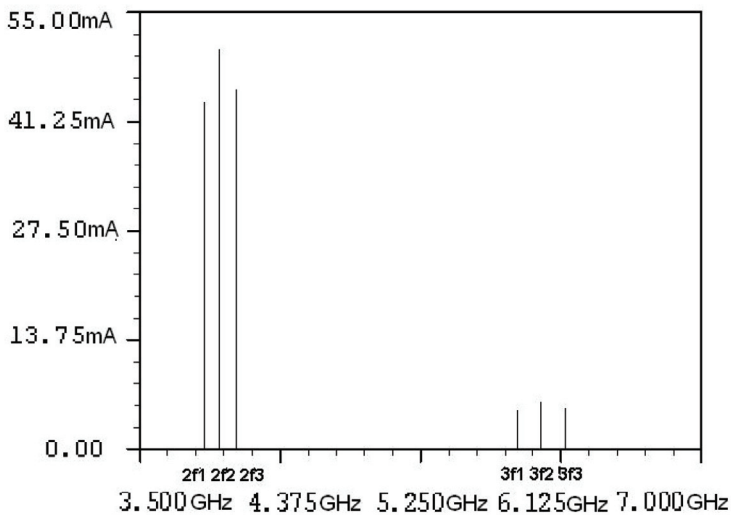


Figure 3.13 Intermodulation products for $V = 5$ V, the first model.

Changing the capacitor parameters as:

$$VCCS\ C1\ 3\ 5\ 1\ 3\ 5\ [0.177e-12*(CV(0)+1e-4*CV(0)^2+1e-5*CV(0)^3)]\ C$$

the resonance frequency shift is diminished (Figure 3.14) and all amplitudes of the intermodulation products are about four times smaller (Figure 3.15).

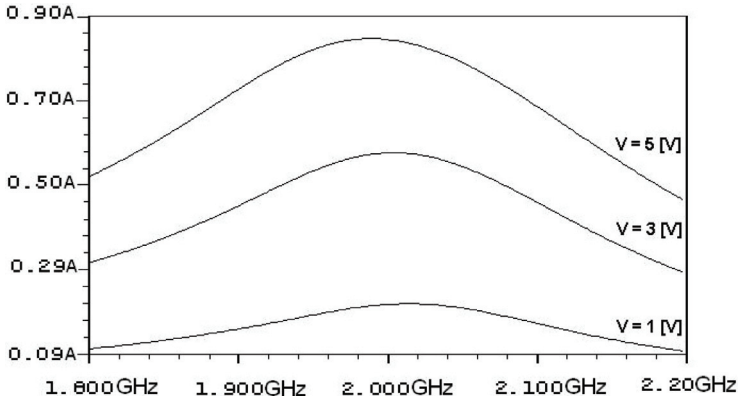


Figure 3.14 Plot of I_a versus frequency for the first model with modified capacitor characteristic.

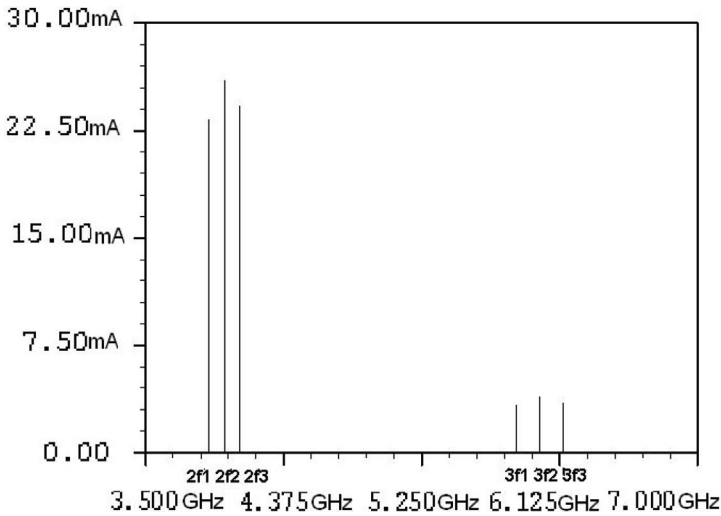


Figure 3.15 Intermodulation products for the first model with modified capacitor characteristic.

Forcing the current value of the mechanical branch by the voltage controlled current source, the capacitor has a dominant role in this model. In this way, the value of series resonance frequency and the intermodulation products amplitudes will depend directly on the polynomial coefficients defining nonlinear characteristic of the capacitor.

To avoid this disadvantage, a second nonlinear circuit model was proposed (Figure 3.16).

Its implementation with nonlinear controlled sources is given in Figure 3.17.

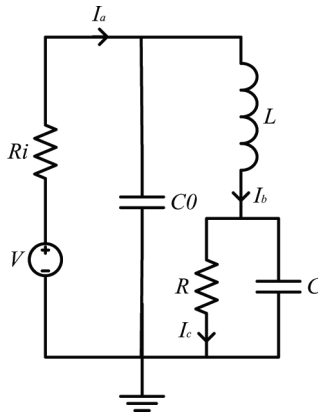


Figure 3.16 The second nonlinear circuit model.

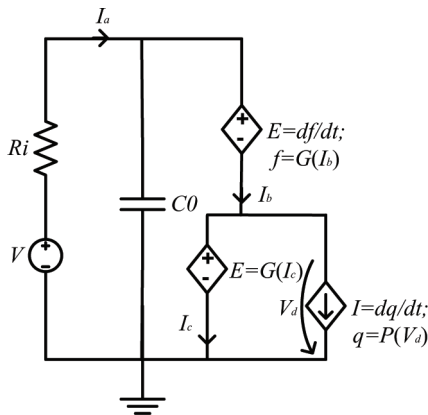


Figure 3.17 Implementation with controlled sources of the second nonlinear circuit model.

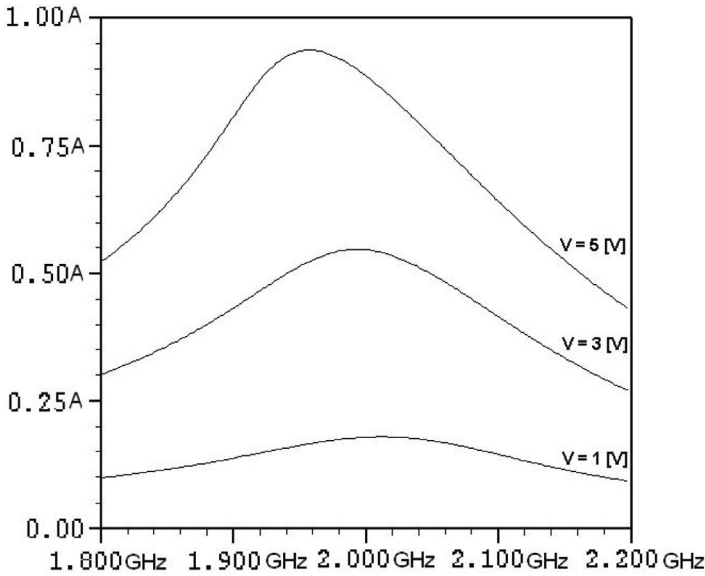


Figure 3.18 Plot of I_a versus frequency for the second model.

To implement this circuit in APLAC, the following parameter values have been used:

```

C0 = 1.566e-12
Res Ri 4 6 1
CCVS L1 1 2 1 b [3.5e-9*(CI(0)+1e-1*CI(0)^2+1e-2*CI(0)^3)] L
CCVS R1 3 5 1 c [430*(CI(0)+2e-2*CI(0)^2+2e-2*CI(0)^3)] R
VCCS C1 3 GND 1 3 GND [.177e-12*(CV(0)+5e-5*CV(0)^2+
5e-5*CV(0)^3)] C
    
```

The amplitude-frequency effect of this model is given in Figure 3.18 with frequency characteristics corresponding to the 1 V, 3 V, and 5 V amplitude excitation. The intermodulation products for $V = 5V$ are given in Figure 3.19.

By changing the nonlinear characteristic of the inductor as follows:

```

CCVS L1 1 2 1 b [3.5e-9*(CI(0)+1e-3*CI(0)^2+1e-3*CI(0)^3)] L
    
```

the amplitude-frequency effect remains unchanged, while the second harmonic current is negligible (Figure 3.20).

This example illustrates the superiority of the second nonlinear model, which allows adjusting the amplitude of the second harmonic of the current without influencing the change in the series resonance frequency produced by the excitation amplitude variation. Using some simple relations of AC

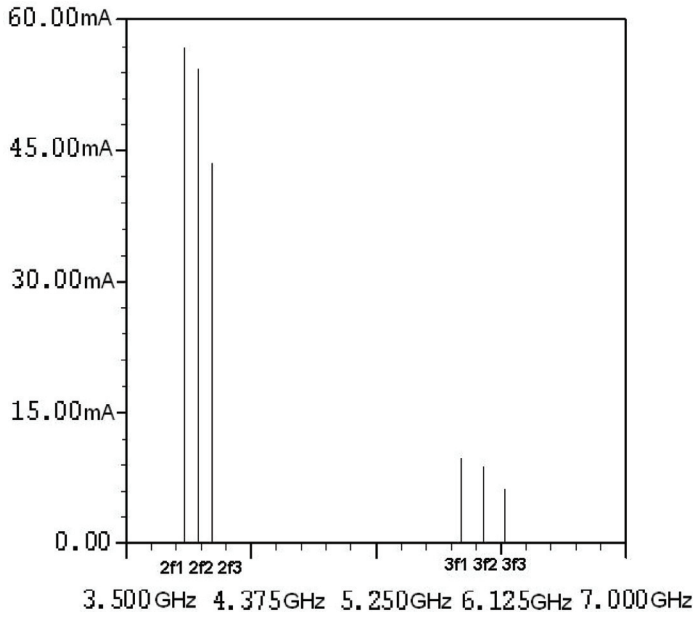


Figure 3.19 Intermodulation products for $V = 5$ V, the second model.

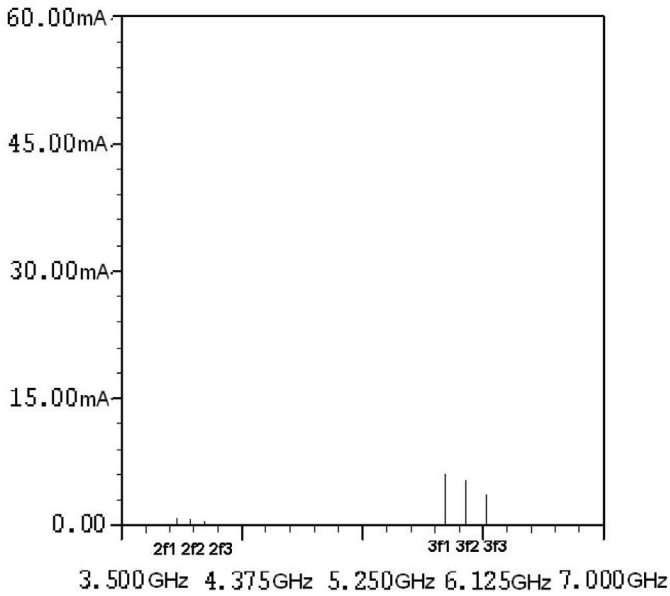


Figure 3.20 Intermodulation products of I_a for the second model with modified inductor characteristic.

impedance equivalence, other models, more complex, with more circuit elements which allow the adjustment of the various parameters of the response can be obtained.

The correctness of the nonlinear circuit model is verified by the fact that the amplitude-frequency effect and the intermodulation effect are reduced decreasing the nonlinear coefficients values of the circuit elements' constitutive equations.

Examples

The nonlinear circuit models presented before have been implemented in the APLAC simulator, working in the frequency domain, and in the SPICE simulator, working in the time domain. In order to verify the computation accuracy and the agreement between time domain and frequency domain results, four circuits of the same type (first model) have been analyzed. The results obtained by doing these simulations are given in the following. The frequency of the excitation signal was $f = 2.025$ GHz, close to the series resonance frequency. In order to reach the sinusoidal steady state, a transient analysis with $T_{stop} = 400$ T has been used [17].

Simulation of the circuit having “very weak” nonlinearities, defined by:

```
CCVS R1 1 2 1 b [4.56*(CI(0)+0.5e-6*CI(0)^2+0.5e-7*CI(0)^3)] R
CCVS L1 2 3 1 b [69.91e-9*(CI(0)+5e-4*CI(0)^2+1e-6*CI(0)^3)] L
VCCS C1 3 5 1 3 5 [88.29e-15*(CV(0)+6e-9*CV(0)^2+6e-11*CV(0)^3)] C
```

led to the following results:

Table 3.2 Harmonic components of $I(V)$ for “very weak” nonlinearities

| Software | f | $2f$ | $3f$ |
|----------|----------|---------------|--------------|
| APLAC | 882.9 mA | 251.1 μ A | 2.85 μ A |
| PSPICE | 881.2 mA | 127.6 μ A | 3 μ A |

Simulation of the circuit having “weak” nonlinearities, defined by:

```
CCVS R1 1 2 1 b [4.56*(CI(0)+0.5e-5*CI(0)^2+0.5e-6*CI(0)^3)] R
CCVS L1 2 3 1 b [69.91e-9*(CI(0)+5e-3*CI(0)^2+1e-5*CI(0)^3)] L
VCCS C1 3 5 1 3 5 [88.29e-15*(CV(0)+6e-8*CV(0)^2+6e-10*CV(0)^3)] C
```

led to the following results:

Table 3.3 Harmonic components of $I(V)$ for “weak” nonlinearities

| Software | f | $2f$ | $3f$ |
|----------|----------|--------|------------|
| APLAC | 884.2 mA | 2.5 mA | 40 μ A |
| PSPICE | 882.7 mA | 1.5 mA | 23 μ A |

Simulation of the circuit having “mild” nonlinearities, defined by:

```
CCVS R1 1 2 1 b [4.56*(CI(0)+0.5e-5*CI(0)^2+0.5e-6*CI(0)^3)] R
CCVS L1 2 3 1 b [69.91e-9*(CI(0)+5e-3*CI(0)^2+1e-5*CI(0)^3)] L
VCCS C1 3 5 1 3 5 [88.29e-15*(CV(0)+6e-8*CV(0)^2+6e-10*CV(0)^3)] C
```

led to the following results:

Table 3.4 Harmonic components of $I(V)$ for “mild” nonlinearities

| Software | f | $2f$ | $3f$ |
|----------|----------|---------|-------------|
| APLAC | 861.9 mA | 25.2 mA | 1.5 mA |
| PSPICE | 881.6 mA | 13.3 mA | 384 μ A |

Simulation of the circuit having “strong” nonlinearities, defined by:

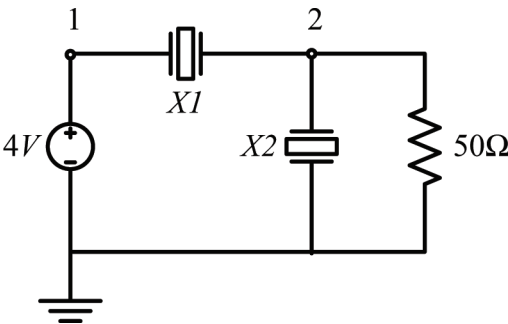
```
CCVS R1 1 2 1 b [4.56*(CI(0)+1e-3*CI(0)^2+1e-3*CI(0)^3)] R
CCVS L1 2 3 1 b [69.91e-9*(CI(0)+1e-1*CI(0)^2+1e-2*CI(0)^3)] L
VCCS C1 3 5 1 3 5 [88.29e-15*(CV(0)+1e-5*CV(0)^2+1e-6*CV(0)^3)] C
```

led to the following results:

Table 3.5 Harmonic components of $I(V)$ for “strong” nonlinearities

| Software | f | $2f$ | $3f$ |
|----------|----------|---------|-------------|
| APLAC | 125.8 mA | 2.69 mA | 579 μ A |
| PSPICE | 213 mA | 2.53 mA | 585 μ A |

A two resonators filter has been simulated with APLAC and SPICE, the results being given in Table 3.6.



$$f_{p2} = f_{s1}$$

$$K^2 = \frac{f_p^2 - f_s^2}{f_p^2}$$

$$K_1^2 = K_2^2$$

Simulation of the circuit having “mild” nonlinearities, defined by:

X1: $C_0 = 1.5664$ pF; $R = 4.56$ Ω ; $L = 69.91$ nH; $C = 88.29$ fF

X2: $C_0 = 1.6462$ pF; $R = 4.56$ Ω ; $L = 70$ nH; $C = 93.166$ fF

led to the following results:

Table 3.6 Harmonic components of voltage gain of a filter with “mild” nonlinearities

| Software | f | $2f$ | $3f$ |
|----------|---------|-------------|--------|
| APLAC | 3.646 V | 477 μ V | 388 nV |
| PSPICE | 3.646 V | 239 μ V | 772 nV |

As it is known, the harmonic balance used by APLAC gives no accurate results for mild and strong nonlinearities. Increasing by two orders of magnitude the coefficients of the polynomial describing the characteristic of the LI element, a strong nonlinearity is obtained and the results given by APLAC are incorrect.

By implementing a power balance verification procedure both in PSPICE and APLAC was found that both implementations lead to results with errors. SPICE solution is affected by local truncation errors and the APLAC solution is obtained according to a local minimum, which is not the global minimum.

3.3.2 Parameter Identification for a Behavioral Resonator Model

The second and third harmonic components measurements and the interpretation of the results are made with difficulty because the components of the third harmonic are located below the noise level, and the results for the second harmonic components must be corrected taking into account the errors introduced by the lack of adaptation between various components of the measurement chain at this frequency. For these reasons, in the first stage were identified the parameters of the first nonlinear circuit model, which replicate the measured variation of the series resonance frequency depending on the incident power. These measurements have been made in the framework of the European project MOBILIS at the XLIM laboratory (University of Limoges, France).

For obtaining the simulation results in Figure 3.21, the following parameters of the first nonlinear model have been chosen:

```
Cap C0 1 GND 1.56p
CCVS R1 1 2 b [4.56*(CI(0)+0.5e-4*CI(0)^2+0.5e-5*CI(0)^3)] R
CCVS L1 2 3 1 b [69.91e-9*(CI(0)+5e-2*CI(0)^2+1e-4*CI(0)^3)] L
VCCS C1 3 5 1 3 5 [88.29e-15*(CV(0)+6e-7*CV(0)^2+6e-9*CV(0)^3)] C
```

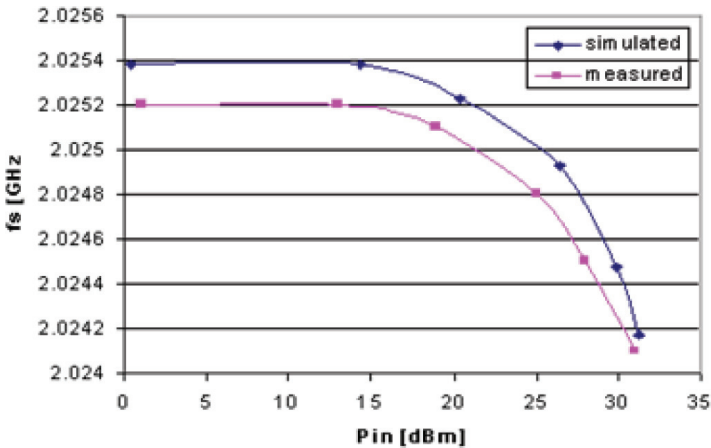


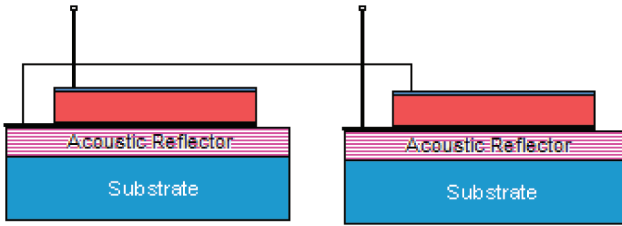
Figure 3.21 Dependence of the series resonance frequency on the incident power.

in order to correspond to the measured values of the series resonance frequency (the amplitude-frequency effect):

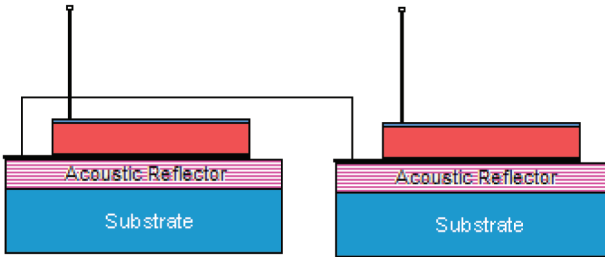
3.3.3 Nonlinear Circuit Model for Anti-Series and Anti-Parallel Connections

Figure 3.22 shows the series and the parallel connections of two power BAW resonators together with their anti-series and anti-parallel connections. The anti-series and anti-parallel connections have been patented [19] and are used in the power BAW filters design by Infineon and EPCOS AG companies.

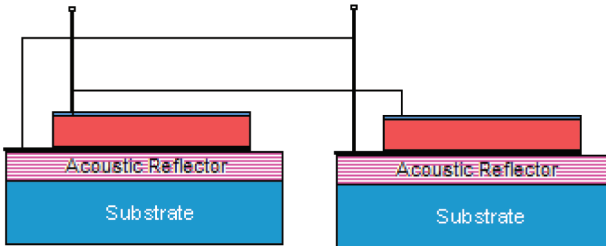
Using the anti-series connection, a significant reduction in second harmonic amplitude relative to the series connection has been experimentally observed. A similar effect was found for the anti-parallel connection compared to the parallel connection. Even though some measurements results for two anti-series and anti-parallel resonators have not been published by the patents authors, these design solutions have been used for power BAW filters, a significant reduction in the distortions at the filter output being measured. This reduction of the $2f$ frequency components has been explained by the bias-frequency effect. This effect means the series resonance frequency modification by introducing a DC component of tens of volts in the excitation signal. This explanation can only suggest that a DC component voltage could stress the piezoelectric material and change its behavior, but probably has no real connection with the phenomenon underlying the reduction in certain harmonic amplitudes for anti-series and anti-parallel connections. This phenomenon has not been identified, yet.



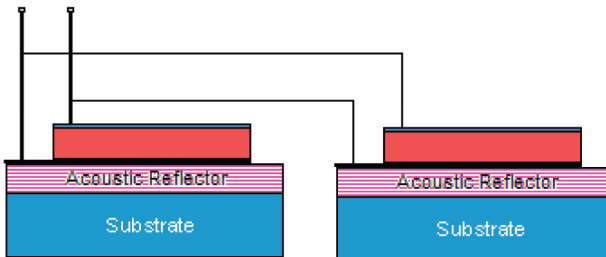
a) Series connection of two BAW resonators.



b) Anti-series connection of two BAW resonators.



c) Parallel connection of two BAW resonators.



d) Anti-parallel connection of two BAW resonators.

Figure 3.22 Connections of two power BAW resonators.

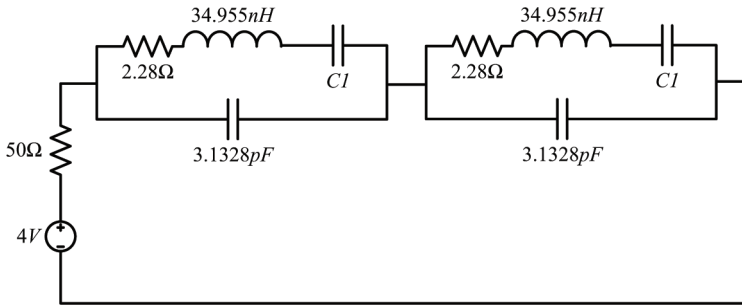


Figure 3.23 Circuit for the anti-series connection model validation.

A simple circuit model that reproduces this effect has been proposed. This model contains only one nonlinear element (the capacitor of the motional branch) described by a $q-u$ polynomial characteristic of the second degree. For the anti-series or anti-parallel connection the second-degree coefficients have different signs for those two resonators, while for the series and parallel connections these coefficients have the same sign.

The anti-series connection model has been validated by SPECTRE RF simulation of the circuit in Figure 3.23. The input source is sinusoidal with a 2.025 GHz series resonance frequency and 4 V amplitude. The output magnitude is the source current.

For the series connection, both $C1$ capacitors have the characteristic:

$$c1 (3 out) cap1 c = 88.29e-15$$

$$model cap1 capacitor coeffs = [6e-5]$$

In case of anti-series connection, one of $C1$ capacitors had the same characteristic as the previous case, and the other one had a quadratic term with the opposite sign, namely:

$$c1 (3 out) cap1 c = 88.29e-15$$

$$model cap1 capacitor coeffs = [-6e-5].$$

The PSS analysis results are presented in Table 3.7. A significant second harmonic component reduction was obtained in the case of the anti-series connection, while the third harmonic had nearly the same amplitude.

The anti-parallel connection model was validated by SPECTRE RF simulation of the circuit in Figure 3.24.

The input source is sinusoidal with a 2.025 GHz frequency (the series resonance frequency) and 4 V amplitude. The output magnitude is the source current. The resonators models for the parallel connection are the same as

Table 3.7 PSS analysis results in the frequency domain for the anti-series connection

| BAW Filter Structure | $2f$ | $3f$ |
|------------------------|---------------|----------|
| Series connection | 10.58 μ A | 5.387 nA |
| Anti-series connection | 812.9 μ A | 5.392 nA |

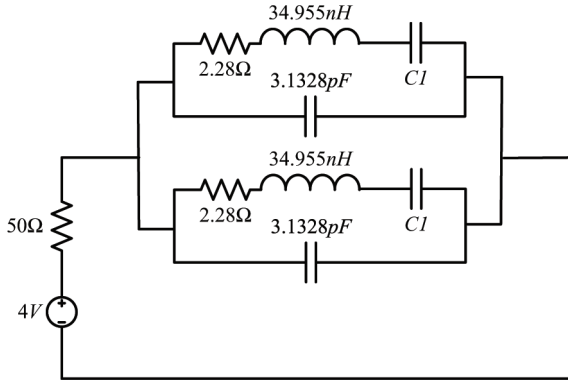


Figure 3.24 Circuit for the anti-parallel connection model validation.

Table 3.8 PSS analysis results in the frequency domain for the anti-parallel connection

| BAW Filter Structure | $2f$ | $3f$ |
|--------------------------|---------------|---------------|
| Parallel connection | 1.671 μ A | 427.7 μ A |
| Anti-parallel connection | 5.344 nA | 425.7 μ A |

the models for series. The quadratic coefficients of the anti-parallel resonator models connection have opposite signs.

The PSS analysis results in the frequency domain are presented in Table 3.8. A significant second harmonic component reduction is obtained in the case of the anti-parallel connection, while the third harmonic has nearly the same amplitude.

3.3.4 Example

The following example is a nonlinear amplifier with a filter using resonators with anti-series connection. In a class D power amplifier, the transistor has a switch behavior. The output of the amplifier is switched between the cut-off and saturation regions. The efficiency of this amplifier is close to 100% because the active operating region is swept only during the transitions between the cutoff and saturation regions.

The circuit simulated with PSS analysis from SPECTRE RF [20] consists in a class D amplifier together with a low-pass LC filter and a ladder band pass filter with 6 BAW resonators (Figure 3.25). The amplifier is driven with a sinusoidal signal of $f_1 = 2.025$ GHz frequency to “+” terminal of the comparator and a triangular signal of frequency $100f_1$ to “-” terminal. The $100f_1$ or greater frequency components are removed by the low-pass LC filter. Final filtering is performed by the BAW filter in which each resonator was replaced with the non-linear model presented in the preceding paragraph.

The frequency characteristic of this circuit for the input voltage in the range [1 mV, 5 V] is not altered significantly by the amplitude-frequency effect of the BAW filter.

To study the intermodulation effect, the second and the third harmonics have been computed for an input voltage of 1 V. Replacing the X2, X4 and X6 resonators with the anti-series connections of two resonators, we obtained a reduction in the second harmonic, while the third harmonic remained unchanged (Table 3.9).

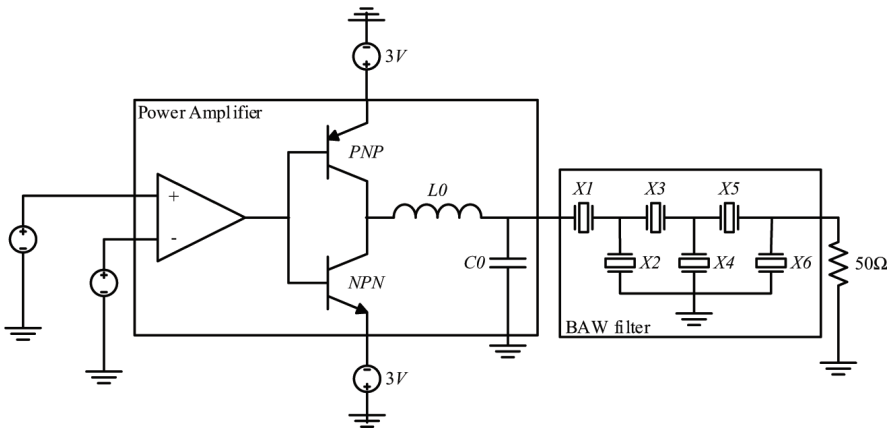


Figure 3.25 Class D amplifier with a power BAW filter.

Table 3.9 Results obtained for the class D amplifier with a power BAW filter

| Harmonic Component | f_1 | $2f_1$ | $3f_1$ |
|---|---------|---------------|---------------|
| Series connection | 3.822 V | 7.572 μ V | 2.321 μ V |
| X2, X4, and X6 replaced with anti-series resonators | 3.822 V | 1.541 μ V | 2.321 μ V |

3.4 Physical Model Using Transmission Lines

A BAW solidly mounted resonator (SMR) is a multi-layer structure including the piezoelectric layer, the electrodes, and other mechanical layers as the substrate and the reflector layers forming the Bragg mirror (Figure 3.26) [22].

This structure has a linear behavior and can be described using the Mason multi-layer model for each layer which takes into account the mechanical loads corresponding to the neighboring layers (Figure 3.27). This is a physical model including mechanical transmission lines having Z_a and Z_c impedances, an ideal transformer, and some capacitors. The parameters of this model depend on material parameters such as density, velocity of the mechanical waves, Young's modulus, the piezoelectric coefficient, electrical permittivity a.s.o., which makes it very useful in the physical design of BAW resonators and filters [21].

As the power level in the communication circuits increased, the nonlinear behavior of power BAW resonators came into attention of the researchers, even though it is known from the late 1980s [23]. This behavior consists mainly in the amplitude-frequency effect (the shift of the resonance frequencies as the incident power increases) and the intermodulation effect.

This nonlinear behavior is produced by some nonlinear constitutive equations of the material.

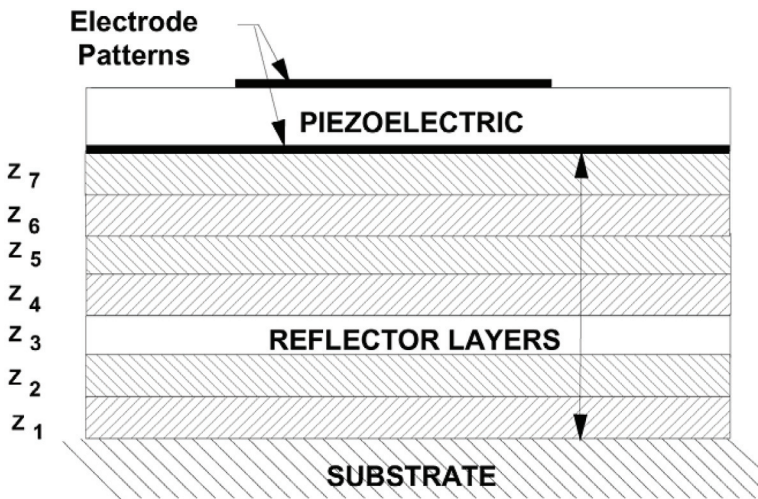


Figure 3.26 Structure of a solidly mounted BAW resonator [3].

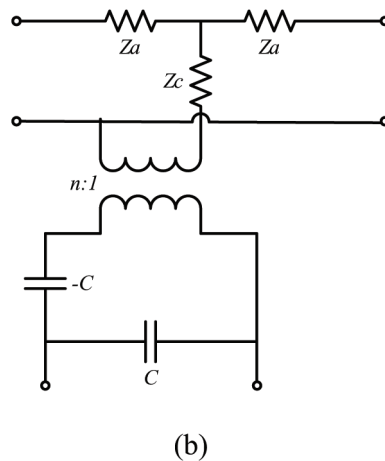
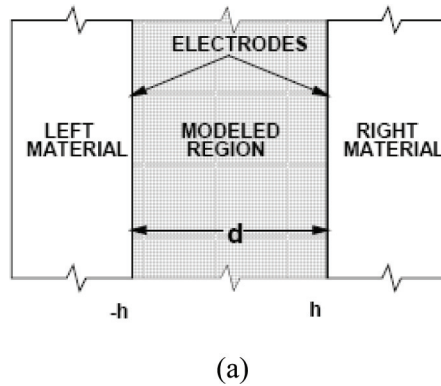


Figure 3.27 Mason multi-layer model [22]: (a) physical structure, (b) circuit model.

As the Mason multi-layer model cannot be extended for nonlinear materials, a useful design tool could be an electromechanical field solver, but there are some difficulties in solving these problems in materials with a nonlinear mechanical characteristic:

- Transient analysis of the electromechanical field in piezoelectric resonators gives a parasitic amplitude modulation, even though the materials are linear.
- Nonlinear mechanical characteristics of piezoelectric materials cannot be implemented in software packages like ANSYS and COMSOL.
- There is no harmonic balance algorithm implemented in ANSYS or COMSOL for the analysis of nonlinear piezoelectric materials.

On the other hand, some powerful harmonic balance algorithms are available in circuit simulation programs like ADS and CADENCE.

The linear artificial transmission line model of a piezoelectric transducer [24, 25] is a physical circuit model whose parameters depend on material characteristics and can be implemented in a circuit simulator. In the next paragraph is presented its extension for materials with mechanical nonlinearity [21]. The simulation results obtained using this new model are compared with the experimental data.

3.4.1 1D Linear Artificial Transmission Line Model

In the following paragraph is presented a slightly modified version of the 1D model given in [24]. This model takes into account only the propagation of the mechanical waves on the direction orthogonal to the electrodes [21].

Consider a part of length Δx of this model, shown in Figure 3.28, where T is stress, v is velocity, ξ is displacement, $S = \partial\xi/\partial x$ is strain, E is electric field, D is electric flux density, $h = e/\varepsilon$, ε is the dielectric constant, e is the piezoelectric coupling coefficient, and C_D is the Young modulus.

The piezoelectric effect equations are as follows:

$$T = C_D \cdot S - h \cdot D \quad (3.9)$$

$$E = -h \cdot S + \frac{D}{\varepsilon} \quad (3.10)$$

On the electrode surface $q(t) = D(t) \cdot A$, where A is the resonator area, and for any x we have the same current value, so that $I(t) = \frac{\partial q}{\partial t} = A \cdot \frac{\partial D}{\partial t}$. There is no volume charge density so that $\text{div}D = \frac{\partial D}{\partial x} = 0$. It follows:

$$\frac{\partial v}{\partial x} = \frac{1}{C_D} \cdot \frac{\partial T}{\partial t} + \frac{h}{A \cdot C_D} \cdot I(t) \quad (3.11)$$

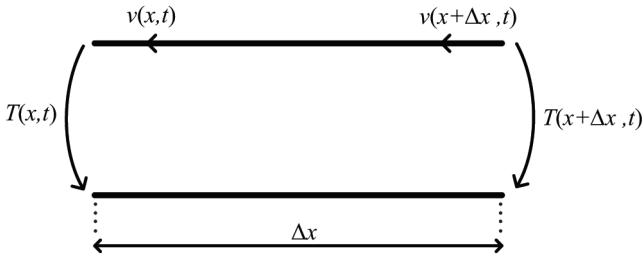


Figure 3.28 Part of length Δx of the linear 1D model.

From (3.10) it follows:

$$C_0 \cdot \frac{\partial V(x + \Delta x, t)}{\partial t} - C_0 \cdot \frac{\partial V(x, t)}{\partial t} = -h \cdot C_0 \cdot [v(x + \Delta x, t) - v(x, t)] + I(t) \tag{3.12}$$

where $C_0 = \frac{\varepsilon \cdot A}{\Delta x}$ and $v = \frac{\partial \xi}{\partial t}$. The second Newton's law leads to the following:

$$\frac{\partial T}{\partial x} = \rho \cdot \frac{\partial v(x, t)}{\partial t} \tag{3.13}$$

The mechanical equivalent circuit, where stress is a voltage-type variable and velocity is a current-type variable, can be built from (3.11) and (3.13) and is given in Figure 3.29. Here $L_e = \rho \Delta x$ is a "mechanical inductance", C_m is a "mechanical capacity", and I_s is the current through the electrical equivalent circuit.

The electrical equivalent circuit can be built from (3.12) and is given in Figure 3.30.

A 1D linear artificial transmission line model, which for simplicity has only three cells, is given in Figure 3.31. The parameters of this circuit are computed using the material parameters (e.g. those given in Table 3.11) in their expressions given above.

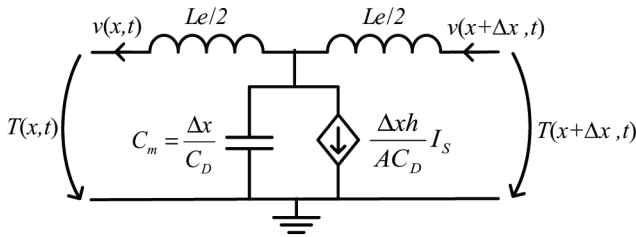


Figure 3.29 Linear mechanical equivalent circuit.

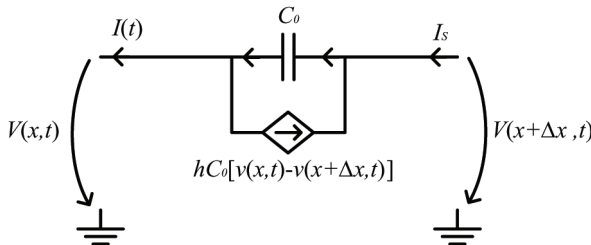


Figure 3.30 Linear electrical equivalent circuit.

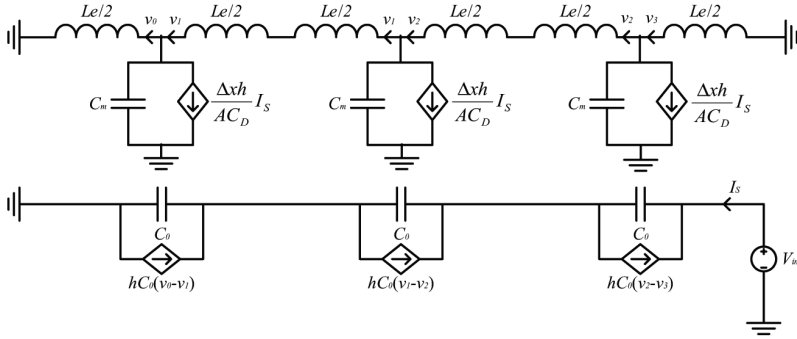


Figure 3.31 1D linear artificial transmission line model with 3 cells.

The mechanical boundary conditions are $T = 0$ at both edges and correspond to the short-circuits at both ends of the mechanical equivalent circuit. The electrical boundary conditions, resulting from the sinusoidal voltage applied to the resonator, are given by the sinusoidal voltage source V_{in} in the last cell of the electrical equivalent circuit and the short-circuit to ground in the first cell of the same equivalent circuit.

3.4.2 1D Artificial Transmission Line Model With Mechanical Nonlinearity

Various nonlinear mechanical characteristics are given in the literature as $S(T)$ or $T(S)$ polynomials [26–28]. Considering a polynomial nonlinearity $S(T)$, it follows [21]:

$$S = \frac{1}{C_D} \cdot T + \frac{k_2}{C_D} \cdot T^2 + \frac{k_3}{C_D} \cdot T^3 + \frac{h}{C_D} \cdot D \quad (3.14)$$

From (3.11) and (3.14), taking into account $\frac{\partial S}{\partial t} = \frac{\partial^2 \xi}{\partial t \partial x} = \frac{\partial v}{\partial x}$, it results:

$$\begin{aligned} \frac{\partial v}{\partial x} = & \frac{1}{C_D} \cdot \frac{\partial T(x, t)}{\partial t} + \frac{2 \cdot k_2}{C_D} \cdot T(x, t) \cdot \frac{\partial T(x, t)}{\partial t} + \\ & + \frac{3 \cdot k_3}{C_D} \cdot T^2 \cdot \frac{\partial T(x, t)}{\partial t} + \frac{h}{C_D \cdot A} \cdot I(t) \end{aligned}$$

The operating equation of the nonlinear capacitor in the mechanical equivalent circuit is as follows:

$$v(x, y) = \frac{1}{C_D} \cdot \left[1 + \frac{2 \cdot k_2}{C_D} \cdot T(x, t) + \frac{3 \cdot k_3}{C_D} \cdot T^2(x, t) \right] \cdot \frac{\partial T(x, t)}{\partial t}$$

or

$$v(x, y) = C_m \cdot [1 + K_2 \cdot T(x, t) + K_3 \cdot T^2(x, t)] \cdot \frac{\partial T(x, t)}{\partial t} \quad (3.15)$$

where K_2 and K_3 are the coefficients of the capacitor polynomial nonlinearity.

3.4.3 Example

The measured resonator has the layers structure described in Table 3.10, and the main parameters (density, velocity, Young's modulus, electrical permittivity, piezoelectric coupling coefficient) being given in Table 3.11.

Each layer is divided in 10 parts [21], except the piezoelectric one (AlN), which is divided into 21 parts. Each layer has an equivalent circuit similar to that in Figure 3.31, with the number of cells equal to the number of these parts.

Table 3.10 Layers structure of the measured resonator

| Material | Thickness (nm) |
|----------------------------------|----------------|
| Si (subs) | Semi-infinite |
| SiOC | 295 |
| SiN | 1160 |
| SiOC | 295 |
| SiN | 1160 |
| SiOC | 295 |
| Mo | 280 |
| AlN | 1170 |
| Mo | 240 |
| SiO2 | 140 |
| (only for loaded resonators) SiN | 200 |

Table 3.11 Material parameters

| Material | ρ (kg/m ³) | Velocity (m/s) | C_D (GPa) | ϵ (pF/m) | e (C/m ²) |
|----------|-----------------------------|----------------|-------------|-------------------|-------------------------|
| Mo | 10000 | 6600 | 435.6 | | |
| SiO2 | 2200 | 6000 | 79.2 | | |
| SiOC | 1500 | 2400 | 10.14 | | |
| SiN | 2700 | 9300 | 233.523 | | |
| Si | 2330 | 8400 | 164.4 | | |
| AlN | 3300 | 11000 | 399.3 | 82.6 | 1.5 |

All these equivalent circuits are connected in cascade and are linear, except the equivalent circuit of AlN that has nonlinear mechanical capacitors whose operating equations are defined by (3.15). The parameters of these circuits are computed using the values given in Tables 3.10 and 3.11.

The optimal values of the coefficients K_1 and K_2 are found in order to fit the simulation results to the experimental data. Considering $K_1 = 4e-10$ and $K_2 = 1.5e-19$, the amplitude-frequency effect presented in Figure 3.32 and Figure 3.33 and the second harmonic of the reflected power shown in Figure 3.34 are obtained.

The model simulation has been made with HB analysis of ADS having the following parameters: MaxOrder = 7, Order[1] = 7, KrylovSS.Tol = $1e-6$, KrylovMaxIters = 300, KrylovLooseIters = 150, oversample = 300, V_RelTol = $1e-5$, V_AbsTol = $1e-6$ V, I_RelTol = $1e-6$, I_AbsTol = $1e-10$ A.

The very good agreement between the simulated and measured data is obvious.

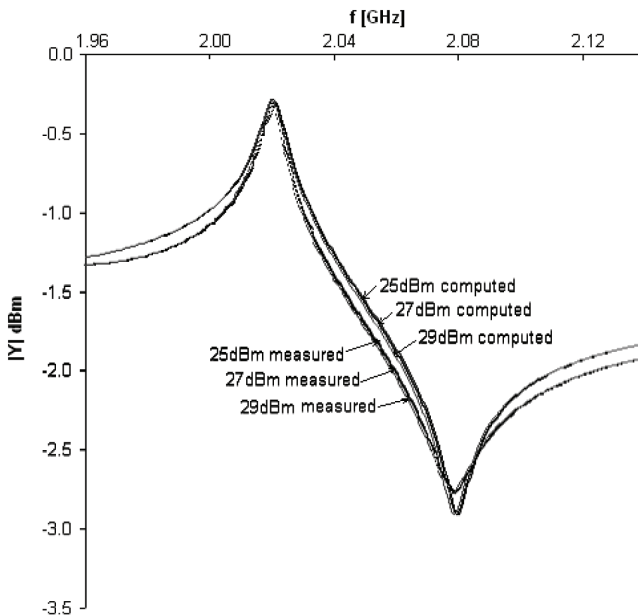


Figure 3.32 Amplitude-frequency effect.

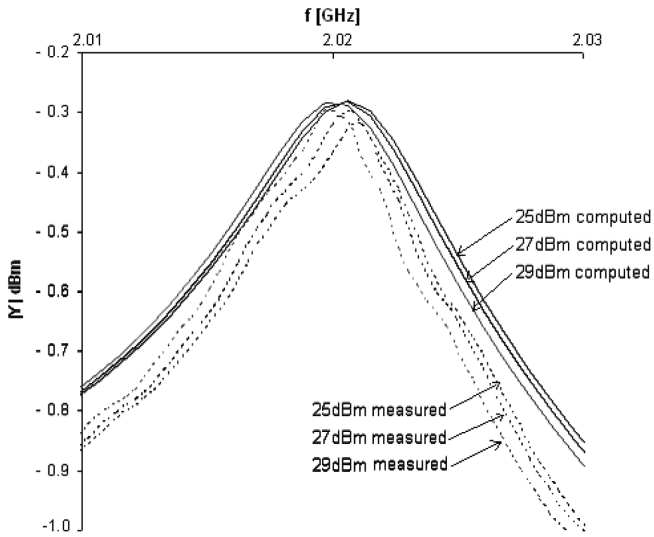


Figure 3.33 Amplitude-frequency effect (detail).

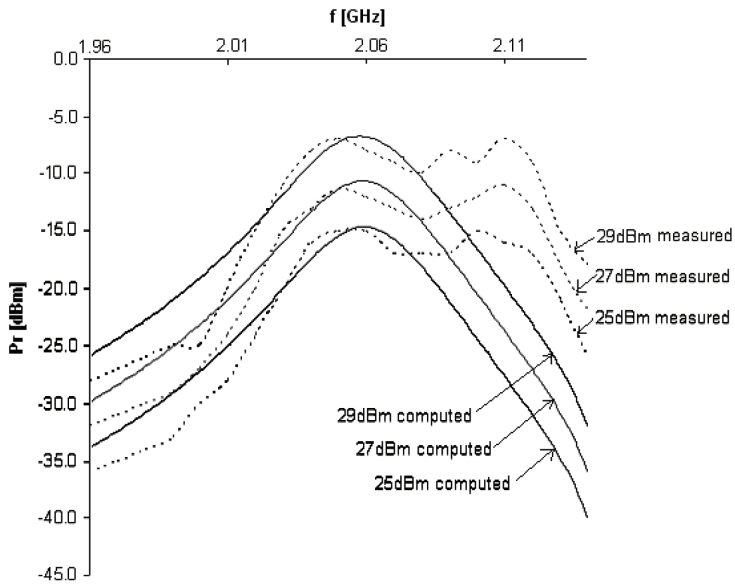


Figure 3.34 Second harmonic of the reflected power.

3.5 Behavioral Models for Frequency Domain Analysis of Power BAW Filters Driven by Multi-Tone Excitations

For a high input power, the bulk acoustic wave (BAW) resonators have a nonlinear behavior, consisting in the amplitude-frequency effect (dependence of the series and parallel resonance frequencies on the incident power) and the intermodulation effect [31, 32]. Some simple nonlinear circuits reproducing these effects for a one tone excitation are described in [33, 34]. The filters exhibiting these effects are called power BAW filters. A typical case of a power BAW filter is the duplexer filter in the mobile phone, which may operate at an incident power up to 5 W.

A new behavioral model, consisting in some files containing the measured frequency characteristics of the S-parameters as functions on the filter incident power, has been proposed in [32]. This model is valid for a one tone filter input signal, but can be easily extended for multi-tone excitations. Even though intricate circuits, as artificial transmission lines, are used as models for multi-tone excitation circuits [35], an accurate modeling of all intermodulation products remains an open problem.

The large-signal S-parameter model developed in [32] for a power BAW filter is based on the measurements performed using some wired connections of the filter input and output. If the model of the filter without connections is needed, for example, if this filter is used in an intricate SoC, the parameters of the behavioral model of the filter itself (without wired connections) must be developed. How this model is obtained is the subject of the next paragraph.

As the power at any input or output port can be computed via simulation, the compensation of the influence of the connection wires is treated firstly using a behavioral filter model built employing simple nonlinear circuits, which are the behavioral resonators models [29]. In the following is shown how the behavioral model of the filter without connections can be computed from the measurement data obtained using the equivalent circuits of the input and the output connections [30].

3.5.1 Compensation of Connection Wires Influence

A three resonator power BAW filter is shown in Figure 3.35, where $S1$ and $S2$ are identical series resonators and P is a parallel resonator [32]. The input wired connection is $W1$, while the output wired connection is $W2$.

The series resonators have an area of $32000 \mu\text{m}^2$ a series resonance frequency $f_s = 2.1344$ GHz and a parallel resonance frequency $f_p = 2.2035$ GHz and a quality factor around $f_s Q_s = 426.4$. The parallel resonator

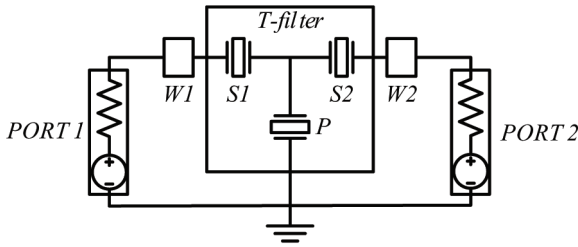


Figure 3.35 T filter with connection wires.

has an area of $44000 \mu\text{m}^2$, $f_s = 2.069 \text{ GHz}$, $f_p = 2.1344 \text{ GHz}$, and a quality factor $Q_s = 320$ around f_s .

The equivalent circuit of a wired connection is presented in Figure 3.36. The values of R , L , and C correspond to the wired input connection. For the output connection, these values are $R = 96.8 \text{ m}\Omega$, $L = 0.645 \text{ nH}$, and $C = 29.44 \text{ fF}$.

The behavioral model of a series resonator is given in Figure 3.37. The behavioral model of the parallel resonator is a similar circuit, having the same

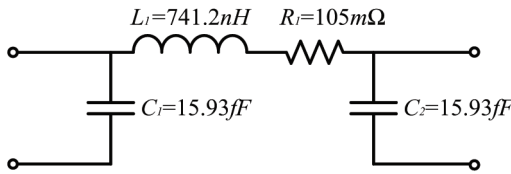


Figure 3.36 Equivalent circuit of a wired connection.

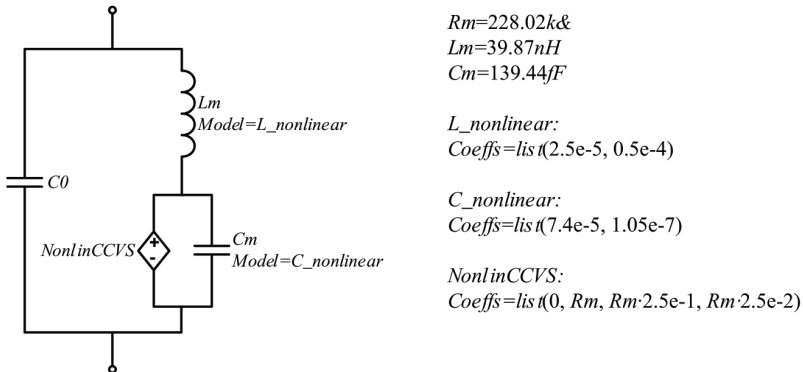


Figure 3.37 Behavioral model of S1 and S2.

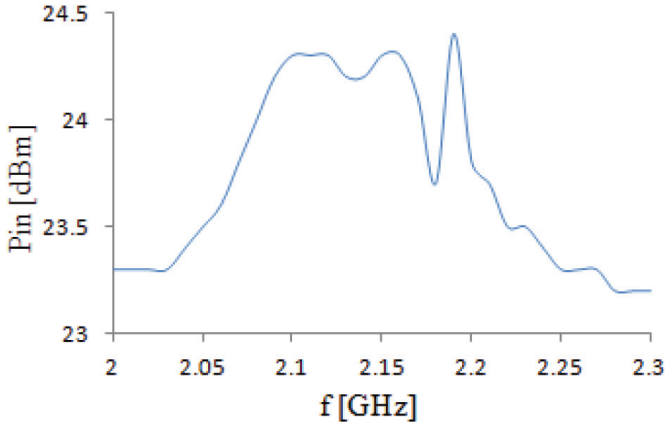


Figure 3.38 Power of the source in *PORT* 1 so that P_{in} in *T* filter is 24 dBm.

nonlinear coefficients lists, but other values for R_m , L_m , C_m , and C_0 , namely: $R_m = 168,845 \text{ k}\Omega$, $L_m = 31.43 \text{ nH}$, $C_m = 188.3 \text{ fF}$, $C_0 = 3.1 \text{ pF}$.

The connection of the two-ports *W1* and *T* filter, as well as the connection of the two-ports *T* filter and *W2* is a cascade one. In the case of two matched cascaded two-ports, any *S*-parameter is the product of the corresponding *S*-parameters of the two components [36]. As the impedances of the high *Q* series and parallel resonators have a significant dependence on frequency, unlike that of *W1*, the matching condition between *W1* and *T* filter is not fulfilled, and the parameter S_{21} of the *T* filter cannot be extracted using the above property.

The source connected at *PORT* 1 in Figure 3.35 gives a constant incident power for all frequencies. Its power can be modified for each frequency in order to obtain a constant incident power at the input of the *T* filter. These modifications can be made varying in small steps the power of the source connected to *PORT* 1. For example, in Figure 3.38 are shown the power values of the source in *PORT* 1 in order to obtain an incident power of 24 dBm at the *T* filter input.

The differences between the S_{21} frequency characteristics corresponding to various levels of the incident powers are negligible for this filter.

The frequency characteristic of the second harmonic of the reflected power at the filter output is used in order to validate this approach. To this end, we compare the reflected power on the second harmonic at the *T* filter output computed in the following two ways:

1. the reflected power at T filter output P_{2fr}^A computed as

$$P_{2fr}^A = \frac{P_{2fr}^{out}}{S_{21}^{W_2}} \tag{3.16}$$

where P_{2fr}^{out} is the reflected power on the second harmonic at $PORT2$ and $S_{21}^{W_2}$ is computed for the output connection W_2 on the second harmonic of the incident power with the frequency f , which is obtained using the simulation of the whole circuit driven by a power source whose parameter is chosen according to the data in Figure 3.38.

2. the reflected power at T filter output P_{2fr}^B computed using only the T filter behavioral model driven by a power source of 24 dBm.

The results are given in Figure 3.39, where P_{2fr}^A are the “extracted” data, while P_{2fr}^B are the “simulated” data.

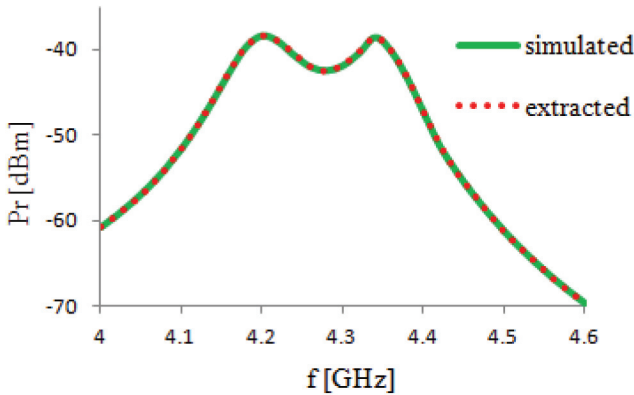


Figure 3.39 Comparison between the simulated and extracted data.

It can be observed that the “extracted” data are practically the same with the “simulated” data, which are the correct ones. By this way, the computation performed employing (3.16) is validated.

3.5.2 Example

Using a similar procedure to that described above, the input power at $PORT 1$ is “calibrated” in order to obtain an incident power of 28 dBm and 30 dBm at the T filter input. This “calibrated” source allows the computation of the characteristics of the T filter without connections.

The transfer characteristic $|S_{21}(f)|$ is given in Figure 3.40.

For this filter, it results that there is practically no influence of the connection wires on this characteristic. Moreover, the amplitude-frequency effect, which for other filters leads to slight variations in the pass-band filter depending on the incident power [37], is not observable at this scale of display.

The frequency characteristic of the $2f$ reflected power at the T filter output is given in Figure 3.41.

A slight influence of the connection wires on this characteristic can be observed.

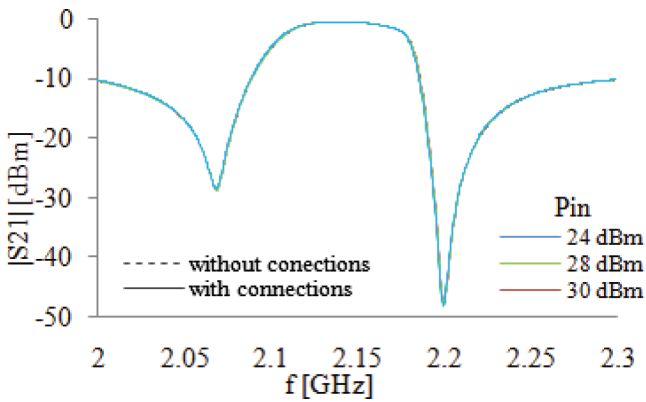


Figure 3.40 T filter transfer characteristic.

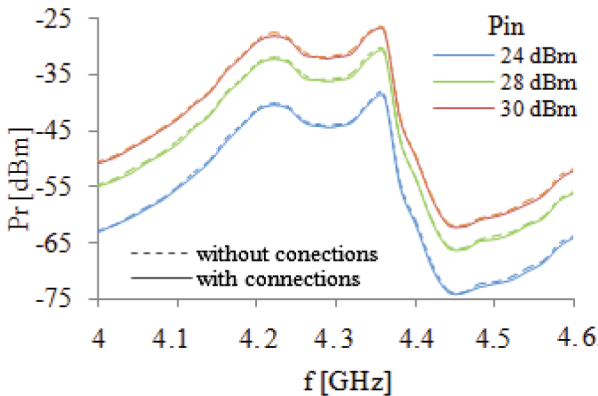


Figure 3.41 $2f$ reflected power at the T filter output.

3.6 Conclusions

Being proved the impossibility of direct measurement of the nonlinear constants in the constitutive equations describing the operation of a power BAW resonator from which some *physical circuit models* could be obtained, it follows that *behavioral circuit models* are desirable [9, 12]. They are derived from measurements data made under conditions similar to the actual operation. A first step in modeling the behavior of power BAW resonators has been the development of some *linear parametric circuits* that reproduce only the amplitude-frequency effect, in which the resistor and the capacitor in the mechanical branch are function of the r.m.s. value of the current from that branch.

In Section 3.2.2, a procedure for identifying the parameters for a linear parametric behavioral model of a power BAW resonator is presented. The model is an AC circuit with two elements that have a parametric dependence on the input current “energy”. This model follows naturally, as long as all resonator phenomena depend on the overall power. The behavioral nature of this model avoids the use of certain material parameters, for example “elastic constants” of 3rd or 4th order, which cannot be directly measured. Parameter identification procedure is simple and relies only on measured frequency characteristics. It was also found a way to minimize the influence of measurement errors.

Considering the future spread of power BAW resonators technology in the mobile phone design, the development of efficient models for time and frequency domain analysis is very useful. These new models should reproduce the resonator behavior driven by a real RF signal.

Contrary to some expectations, it is not possible to use r.m.s. values as parameters in user-defined models in a frequency domain analysis program as ADS, APLAC, or Serenade. These linear parametric models cannot be implemented in a time domain program like SPICE, also.

In Section 3.3.1, two new *nonlinear models* of power BAW resonators are presented. These models, unlike other up to date known models, highlight the amplitude-frequency and the intermodulation effects. Their APLAC implementation is made using non-linear controlled sources. For the first nonlinear model, the parameters were chosen to match the measured values taking into account only the amplitude-frequency effect. The second nonlinear circuit model allows adjustment of the second harmonic current amplitude without affecting the series resonance frequency dependence on the excitation amplitude. A methodology for the computation of the parameters of these behavioral

models, starting from the measured data, and including the estimation of the connection wires influence, is outlined in [29]. By simple AC impedance transformations, more complicated models, having more circuit elements which allow the fitting of various response characteristics to the measured data, can be generated.

In Section 3.3.3, two simple circuit models that reproduce the intermodulation effect of the anti-series and anti-parallel connections are presented. The model contains only one nonlinear element (the capacitor of the motional branch) described by a $q-u$ polynomial characteristic of the second degree. For the anti-series or the anti-parallel connection, the second degree coefficients have different signs to each resonator. These models have been validated by the SPECTRE RF simulation, resulting in an important reduction in the second harmonic. The proposed models were validated through a simulation of a nonlinear amplifier followed by a band pass filter. If some resonators in this filter are replaced by anti-series connections, there is a significant reduction in the second harmonic at the filter output; this filter structure corresponds to patented solutions used by the companies fabricating power BAW filters.

The linear artificial transmission line model of Morris and Hutchens is modified in the Section 3.4.1 for materials with mechanical nonlinearity. A very good agreement is observed between the simulated and experimental results concerning both the amplitude-frequency effect and the intermodulation effect. This fact suggests that the mechanical nonlinearity is a possible origin of the nonlinear resonator behavior. The undulations in the frequency characteristic of the second harmonic reflected power are produced by the reflections of the transversal waves at the resonator boundaries and cannot be reproduced by the 1D model. A 2D model, obtained in a similar manner, can explain these undulations. In order to avoid these effects of the transversal wave reflections, the electrode shape becomes a pentagon having no parallel edges (apodized resonator). For the simulation of the improvement produced by apodization, a 3D model, which can be an extension of that presented in this paper, may be useful.

Being very simple, the behavioral nonlinear circuit models [15, 29] are very efficient for simulation of circuits containing power BAW resonators, but their parameters are not directly related to the material parameters. The nonlinear artificial line models are physical models, their parameters having a known dependence on the material parameters. This feature makes them very useful in the physical design of the power BAW resonators. Moreover, these models can be implemented in circuit simulators avoiding the use of the commercial electromechanical field simulators that cannot handle mechanical

nonlinearities. Some material parameters cannot be measured directly in the operating conditions; some simulation errors can occur considering their values taken from the literature.

Section 3.5 presents a behavioral model for the frequency domain analysis, consisting in tables of S-parameters, whose values depend on frequency and incident power [32].

A procedure aimed to eliminate the influence of the connection wires is proposed in Section 3.5.1, knowing that the data on which the model proposed in [32] is based are measured using some wired connections to the test bench. This procedure is useful when the device is used in a more intricate circuit, and employs a behavioral circuit model of the filter, as well as the equivalent circuits of the connection wires.

This new kind of model is used for weakly nonlinear devices as power BAW resonators and filters built with AlN as the piezoelectric material. This model can reproduce the device behavior on the fundamental frequency f in the case of a one tone excitation, including the nonlinear amplitude-frequency effect as well as the frequency characteristics of the $2f$ reflected power at the device output, both being specified for a set of incident powers [32].

This kind of model seems to be superior to the behavioral model in the form of a simple circuit [33, 34], because it can reproduce exactly the measured values, while the simulation of the simple circuit can only approximate them. But the outstanding result of this approach can be obtained in the case of the multi-tone excitation for which no existing model is working well enough [35]. The large-signal S-parameter models for power BAW resonators and filters are used for the first time in [32] and in the present work, even though these magnitudes are mentioned in [38] and [39] for some nonlinear circuit models.

References

- [1] Campbell, C. K. (1998). *Surface Acoustic Wave Devices for Mobile and Wireless Communications*. Academic Press: Boston.
- [2] Vision 2020 – Nanoelectronics at the centre of change – A far-sighted strategy for Europe, Report of the High Level Group, June 2004.
- [3] Lakin, K. M. (2003). Thin film resonator technology. *IEEE Microwave Mag.* December, 61–67.
- [4] Hruska, C. K. (1996). Nonlinear constants of quartz-thirty years after the first nonlinear elastic tensor, *IEEE Int. Freq. Control Symp.* 179–182.

- [5] Nosek, J. Drive level dependence of the resonant frequency in BAW quartz resonator and his modeling. *IEEE Trans. Ultrasonics, Ferroel. Freq. Control*, 46, 823–829.
- [6] Albareda, A., Gonnard, P., Perrin, V., Briot, R., and Guyomar, D. (2000). Characterization of the mechanical nonlinear behavior of piezoelectric ceramics, *IEEE Trans. on UFFC* 47 (4), 844–853.
- [7] Nitescu, M., Constantinescu, F., and Gheorghe, A.-G. (2006). An AC linear parametric behavioral model of a nonlinear BAW resonator. *Proceedings of the 3rd IEEE International Conference on Circuits and Systems for Communications*, July 6–7, Bucharest, Romania, pp. 115–118.
- [8] Constantinescu, F., Marin, C. V., Nitescu, M., and Marin, D. (2003). Parameter identification using symbolic pole/zero expressions. *European Conference on Circuit Theory and Design, ECCTD'03*, Poland, September 1–4.
- [9] Constantinescu, F., Nitescu, M., and Gheorghe, A. G. (2006). Parameter Identification for a Behavioral Model of a Nonlinear BAW Resonator, NDES 2006 Symposium on Nonlinear Dynamic Electronic Systems, Dijon, June 2006.
- [10] Nitescu, M., Constantinescu, F., and Gheorghe, A. G. (2006). Fast solving of a linear parametric A.C. model using a symbolic admittance expression, SMACD: Proceedings of the Workshop on Symbolic Methods and Applications to Circuit Design, Firenze, Italia, October 12–13, 2006.
- [11] Fattinger, G. G., Kaitila, J., Aigner, R., and Nessler, W. (2004). Single-to-balanced Filters for Mobile Phones using Coupled Resonator BAW Technology. *IEEE International Ultrasonics, Ferroelectrics and Frequency Control Symposium*, 2004.
- [12] Nitescu, M., Constantinescu, F., Gheorghe, A. G. (2006). A.C. Analysis of Circuits with “Energetic” Parametric Models. *Proceedings of “Advanced Topics in Electrical Engineering”*, Politehnica University, Bucharest, Romania, November 24–25, 2006.
- [13] Nitescu, M., Constantinescu, F., Gheorghe, A. G. (2006). Fast Solving of a Linear Parametric A.C. Model Using a Symbolic Admittance Expression. *Proceedings of the Workshop on Symbolic Methods and Applications to Circuit Design (SMACD 2006)*, Florence, Italy, October 12–13, 2006.
- [14] Aigner, R., Huynh, N.-H., Handtmann, M., Markensteiner, S. (2004). Behavior of BAW devices at high power level. *Proceedings of 2004 IEEE MTT-S International Microwave Symposium*.

- [15] Constantinescu, F., Gheorghe, A. G., and Nitescu, M. (2008). “New Circuit Models of Power BAW Resonators”, *Revue Roumaine des Sciences Technique – Electrotechnique et Energetique*, 1, 2008.
- [16] Constantinescu, F., Nitescu, M., and Gheorghe, A. G. (2008). “New Nonlinear Circuit Models for Power BAW Resonators. *Proceedings of ICCSC 2008*, 26–28 Mai 2008, Shanghai, China.
- [17] Constantinescu, F., Nitescu, M., and Gheorghe, A. G. (2007). Simulation of nonlinear effects in power BAW resonators and filters, *SNET 2007*, Bucharest, October 12–14, 2007.
- [18] Constantinescu, F., Nitescu, M., and Gheorghe, A. G. (2007). Circuit Models for Power BAW Resonators—Set-up and Implementation. *Proceedings of IEEE AFRICON 2007*, September 26–28 Windhoek, Namibia ISBN 0-7803-8606-X
- [19] Aigner, R., and Handtmann, M. (2006). US Patent No. US 2006/0290446 A1, December 28.
- [20] Gheorghe, A. G., Nitescu, M., and Constantinescu, F. (2009). Circuit Models for Anti-Series and Anti-Parallel Connections of Power Bulk Acoustic Wave Resonators, *Electrotehnica, Electronica, Automatica*, 57 (3), 17–19.
- [21] Constantinescu, F., Gheorghe, Al. G., Florea, A., Nibescu, M., and Llopis, O. (2011). Artificial Transmission Line Model for Power BAW Resonators with Mechanical Nonlinearity. *Revue Roumaine des Sciences Techniques-Serie Electrotechnique et Energetique*, ISSN: 0035-4066, Nr.2, pp. 237–246.
- [22] Lakin, K. M. (1992). *Modeling of thin film resonators and filters. IEEE MTT-Symposium Digest*, pp. 149–152.
- [23] Ketcham, R. S., Kline, G. R., and Lakin, K. M. (1988) Performance of TFR filters under elevated power conditions. *42nd Annual Frequency Control Symposium*, pp. 106–111.
- [24] Morris, S. A. (1986). Equivalent circuit modeling for thin disk and bar type piezoelectric transducers, The University of Tulsa, USA.
- [25] Morris, S. A., and Hutchens, C. A. (1986). Implementation of Mason’s model on circuit analysis programs. *IEEE Trans. UFFC*, 33 (3), 295–298.
- [26] Simkovics, R., Landes, H., Kaltenbacher, M., and Lerch, R. (1999). Non-linear finite element analysis of piezoelectric structures. *1999 Ultrasonics Symposium*, pp. 1057–1061.
- [27] Kaltenbacher, B., Hofer, M., Kaltenbacher, M., Simkovics, R., and Lerch, R. (2003). Identification of Material Nonlinearities in Piezoelectric Ceramics, *2003 Ultrasonics Symposium*, pp. 360–361.

- [28] Xu, C.-G., Fiez, T. S., and Mayaram, K. (2003). Nonlinear Finite Element Analysis of a Thin Piezoelectric Laminate for Micro Power Generation. *IEEE J. Microelectromech. Syst.* 12 (5), pp. 649–655.
- [29] Constantinescu, F., Gheorghe, A. G., Nitescu, M., Florea, A., Llopis, O., and Taras, P. Parameter identification for nonlinear circuit models of power BAW resonators, *Advances in Electrical and Computer Engineering* (accepted for publication).
- [30] Taus, O. S., Constantinescu, F., and Gheorghe, A. G. (2015). Compensation of the Connection Wires Influence for a Behavioral Model of a Power BAW Filter. *2015 IEEE 21st International Symposium for Design and Technology in Electronic Packaging (SIITME)*, October 22nd–25th, 2015, Brasov, Romania.
- [31] Lakin, K. M. (2005). Thin film resonator technologies. *IEEE Trans. UFFC*, 52 (5) (May), pp. 707–716.
- [32] Constantinescu, F., Taus, O., and Gheorghe, A. G. (2015). A new behavioral model for frequency domain analysis of power BAW filters. *13th International Conference on Engineering of Modern Electric Systems (EMES)*, Oradea, Romania, 11–12 June 2015.
- [33] Constantinescu, F., Nitescu, M., Gheorghe, A. G., Florea, A., and Llopis, O. (2012). Behavioral circuit models of power BAW resonators and filters. *Analog Circuit Design Signal Process.* 73 (1), 57–64.
- [34] Popovici, D., Constantinescu, F., Maricar, M., Hantila, F. I., Nitescu, M., and Gheorghe, A. (2008). Modeling and simulation of piezoelectric devices. *Recent advances in modeling and simulation*, INTECH Open Access Publisher, Vienna.
- [35] Rocas, E., Collado, C., Orloff, N. D., Mateu, J., Padilla, A., O’Callaghan, J. M., and Booth, J. C. (2011). Passive intermodulation due to self-heating in printed transmission lines. *IEEE Trans. Microw. Theory Tech.* 59 (2), 311–322, Feb.
- [36] Niknejad, A. M. (2008). Introduction to Two-Port Parameters. *Two-Port Networks and Amplifiers*, University of California, Berkeley.
- [37] Stroe, G. (2012). Modeling of passive RF devices, Ph.D. Thesis, University Politehnica of Bucharest, Faculty of Electrical Engineering. Advisor: Prof. Florin Constantinescu.
- [38] Lee, V., Lee, S., Sys, S. A., Mortazawi, A. (2012). Large signal performance of ferroelectric FBARs. *Microwave Symp. Digest*, Montreal, QC, Canada, 17–22 June.
- [39] Lee, S., Lee, V., Sys, S. A., and Mortazawi, A. (2013). Linearity analysis of intrinsically switchable ferroelectric FBAR filters. *Microwave Symposium Digest*, Seattle, WA, 2–7 June.

Index

A

absolute
 error 18, 29, 51, 87, 95
 tolerances 22
admittance 106, 107, 144
admittance matrix 106, 107
affine function 97
amplifier 3, 42, 67, 94
amplitude-frequency
 effect 2, 138, 139, 177
analog 112, 135
analysis 3, 17, 29, 59, 68, 85
anti-parallel connection 157,
 159, 160, 176
anti-series connection 157, 159,
 160, 176
asymptotic 99
autonomous circuit 4, 8,
 54, 55
average
 step 41
 time step 29, 74
 value 98, 99, 104

B

backward Euler 17, 21, 62, 125
bandwidth 1, 124, 125, 127
basic 125, 126
BAW 2, 135, 139, 157, 170
Behavioral
 circuit model 177
 models 140, 147, 170, 175

nonlinear circuit

 models 176
 resonator model 156
bias-frequency effect 139, 157
branch
 current 142
 voltage 117, 120
brute force method 92, 98,
 99, 108
bulk acoustic wave resonator 45

C

CCVS 148, 152, 154, 156
circuit
 element 6, 21, 33, 154
 envelope method 123, 124,
 125, 130
 equations 21, 77, 92, 106
 model 3, 135, 140, 142
 coefficient 31, 137, 162, 167
 companion model 33, 35,
 54, 105
 comparator 161
 complex
 amplitude 106, 107, 108
 domain 142
 envelope 125
 magnitude 107
 time function 124
 voltage 118
 connected 8, 14, 106, 172
 constant 10, 22, 105, 125

controlled source 147, 148,
151, 175
converter 68, 71, 85, 86
corrector 64, 80
co-tree 10, 12
current
 controlled 7, 11, 14, 21, 30
 source 7, 14, 115, 151
curve 6, 144
customary behavior 4, 6, 57,
93, 98
cutoff 160

D

dBm 172, 173
DC analysis 17
decomposition 116
dependent source 117
determinant 33
device 1, 22, 137, 177
differential
 algebraic equation 102
 equation 100, 102,
112, 124
diode 25, 26, 81, 104, 120
discrete
 Fourier transform 106, 107,
111, 125
 spectral line 126, 128
dynamic
 circuit 9, 12, 13, 22
 element 7, 11, 14, 32, 54
 inductance 7, 12
 nonlinear circuit 6, 54, 170
 parameter 12

E

eigenvalue 17
electromagnetic 115, 137

energy
 balance error 30, 31, 32, 53
 error 20, 22, 29, 32
envelope following 59, 61,
63, 66
equation 11, 14, 61, 100
equivalent
 circuit 42, 45, 117, 165
 source 116, 117
Euler 17, 21, 62, 103, 125
excess state variables 10, 11, 12
existence and uniqueness 9, 11,
12, 13
exponential
 extrapolation 98, 99, 102,
103, 105
 stable 6, 9, 17, 98

F

filter 2, 46, 57, 99, 135
finite difference 18, 100, 103, 124
first order
 circuit 13, 15
 nonlinear circuit 108, 109
flux 12, 18, 21, 30, 164
flux controlled 12, 14, 21, 30
forward
 discrete Fourier
 transform 111, 125
 Euler 62
Fourier series 105, 107,
110, 118
frequency
 domain 105, 106, 108,
124, 175
 warping 54, 59
function 4, 12, 63, 91, 97
fundamental frequency 111, 124,
146, 177

- G**
 Gear 17, 57, 59
 global 31, 32, 54, 93
 GMRES 33, 34, 35, 36
- H**
 harmonic
 balance 105, 106, 108, 125
 component 6, 107, 108, 160
 hybrid representation 6
- I**
 impedance 116, 137,
 154, 176
 implicit 22, 63, 64
 independent
 source 4
 state variable 10, 12, 98
 inductance 7, 12, 137, 165
 inductor 3, 6, 10, 14, 15
 initial
 condition 17, 37, 64, 93
 estimation 22, 107
 state 4, 11, 43, 98, 99
 input signal 1, 67, 109, 170
 instantaneous 147
 integration
 algorithm 17, 21
 method 31, 54, 62, 64
 step 17, 22, 29, 33
 intermodulation
 distortion 157
 effect 139, 142, 170, 176
 product 2, 127, 149, 153
 iterative
 algorithm 22
 analysis 147
 method 33, 64
 procedure 107, 118, 119, 120
 process 116
- J**
 Jacobian 7, 22, 94, 108
 Jacobian matrix 22, 64
 jump 59, 62, 68, 71, 72
- K**
 Kirchhoff 11, 107
- L**
 ladder 161
 Laplace transform 6
 level 2, 37, 156, 162
 linear
 artificial transmission
 line 164, 165, 166, 176
 circuit model 3, 4, 142, 147
 extrapolation 97, 98, 99, 102
 parametric circuit model 140,
 141, 142, 147
 link 29
 Lipschitz 11, 12, 13, 116
 local
 minimum 156
 oscillator 1, 67, 72
 passive 6, 7, 8
 truncation error 17, 29,
 42, 156
 loop 7, 14, 85, 124
 low-pass 161
 LTE 17, 19, 22, 56
 LU factorization 36
- M**
 magnetic 4, 18
 magnitude 5, 33, 98, 159

matrix 7, 33, 64, 98, 106
 maximum 5, 17, 18, 33, 85
 mechanical
 boundary condition 166
 branch 151, 175
 characteristic 163, 166
 equivalent circuit 165, 166
 layers 162
 load 162
 motion 136
 resonance 136
 system 135
 transmission line 162
 vibration 136
 wave 137, 162, 164
 mesh 91, 103
 mixed frequency – time domain
 analysis 110, 130
 MNA 22
 model 3, 4, 33, 62, 144, 146
 modified nodal analysis 21, 22
 multiple 3, 9, 13, 100, 146
 multiplier 23, 67

N

natural
 frequencies 6, 98
 frequency 39, 57, 98
 Newton 22, 23, 64, 65
 Newton-Raphson method 61, 64,
 79, 102
 noise 1, 3, 127, 156
 non-autonomous circuit 4, 8,
 54, 62
 nonlinear
 amplifier 160, 176
 capacitive multiport 7
 capacitor 20, 94, 107, 166

circuit 6, 8, 11, 109, 135
 circuit model 135, 147,
 151, 157
 inductive multiport 7
 inductor 21
 resistor 13, 14, 15, 116, 119
 numerical 17, 19, 21, 65, 118

O

one-port 20, 117
 operating
 condition 86, 88, 177
 equation 10, 166, 168
 mode 8, 9, 67
 region 160
 output
 connection 170, 171, 173
 magnitude 159
 port 170
 signal 1, 67
 voltage 45, 51, 52, 84, 88

P

parallel
 connection 157, 159, 160, 176
 resonance frequency 170
 resonator 157, 160, 170, 172
 parametric
 circuit 140, 141, 142, 146, 175
 linear 142, 147
 model 147, 175
 parasitic 3, 163
 partial differentiation
 operators 100, 101
 passive 3, 6, 7, 8
 peak 31, 54
 periodic
 excitation 4, 6, 8, 62, 102

- response 5, 8, 9, 99, 102
- steady state 3, 9, 17, 92, 104
- periodicity error 92, 93, 96, 104
- phase 67, 68, 126, 127
- physical
 - circuit 164, 175
 - design 162, 176
 - model 3, 140, 162, 176
 - phenomena 135, 140
 - structure 163
- Picard-Banach 119
- piecewise linear 33, 81, 109, 114
- pole 144
- polynomial 6, 13, 33, 79, 156, 166
- port 6, 10, 107, 116, 117
- power 1, 9, 33, 35, 127
- predictor 64, 65, 79, 80

Q

- quality factor 33, 42, 56, 137, 145

R

- reciprocal 7
- reduced 54, 62, 68, 105, 154
- relative
 - energy error 32
 - error 18, 41, 49, 61, 104
 - tolerance 24
- representation 6, 90, 105, 107
- resistance 82, 84, 86, 89, 141
- resistive
 - circuit 13, 33, 54, 134
 - element 12, 13
 - multiport 6, 7, 10, 11, 14
- resonant
 - branch 39
 - frequency 137
- RF circuit 1, 3, 68, 92, 105

S

- saturation region 160
- scalar 21
- sensitivity 1, 78, 94
- series
 - connection 157, 159, 160, 176
 - resonance frequency 25, 45, 135, 175
- shooting
 - analysis 96
 - method 63, 72, 93, 97, 102
- short-circuit 166
- sinusoidal
 - excitation 9
- signal 1, 39, 45, 67, 81, 90
- small signal 2, 3, 8, 145
- sources iteration method 115, 130
- stable 6, 9, 17, 99
- state variable 10, 21, 79, 80, 85
- steady state 3, 17, 63, 96, 124
- stored energy 20, 21
- strictly
 - local passive 6, 7, 8
 - monotone 14
 - positive 6
- substitution theorem 10
- superposition theorem 11, 119
- symbolic 144, 147
- synthesis 137

T

- Taylor series 64, 140, 147
- terminal 107, 108, 138, 161
- time constant 5, 98, 99
- time domain analysis 17, 90, 105, 110
- time step 17, 20, 29, 32, 50
- time-domain 127

time-varying 125, 126, 128
trajectory 91, 92
transfer characteristic 174
transient analysis 17, 29, 58, 65,
74, 92
transistor 56, 96, 135, 160
transmission line 162, 166,
170, 176
trapezoidal 17, 39, 55, 62, 124
tree 10, 12
two time variables 59, 90, 92,
100, 105
two-port 116, 172

U

uncustomary behavior 3, 6, 8, 9
uniqueness 9, 11, 12, 13
unstable 17

V

variable 3, 10, 90, 100, 165
VCCS 148, 152, 154, 155, 156

vector 4, 94, 97, 107,
117, 124
voltage
gain 156
source 4, 12, 39,
120, 166
voltage controlled
capacitor 20, 106
current source 151
linear capacitor 30
nonlinear capacitive
multiport 7
nonlinear capacitor 7, 94
nonlinear resistor 94
resistor 14, 85, 106

W

waveform 21, 39, 87,
108, 128

Z

zero 5, 22, 124, 144

About the Authors

Alexandru Gabriel Gheorghe obtained the engineering degree in 2004 and the Ph.D. in 2009, both in Electrical Engineering, from the University Politehnica of Bucharest, Romania, where he is currently a lecturer in the Department of Electrical Engineering. His scientific area of interest includes transient analysis algorithms, envelope following algorithms, and modeling and simulation of power BAW resonators and filters. Dr. Gheorghe published two books, one book chapter, 12 papers in international and Romanian journals, and 56 papers in conference proceedings and was director of two research projects.

Florin Constantinescu obtained the engineering degree in Electronics and the Ph.D. in Electrical Engineering from the University Politehnica of Bucharest, Romania, where he is currently a professor of Electrical Engineering. His scientific areas of interest are in circuit theory (qualitative properties of nonlinear circuits, symbolic analysis of linear circuits, synthesis of nonlinear resistive circuits, fast computation of the periodic steady state in nonlinear circuits) and RF circuits design (transient analysis algorithms, envelope following algorithms, modeling and simulation of power BAW resonators and filters). Prof. Constantinescu published nine books, one book chapter, 56 papers in international and Romanian journals, and 122 papers in conference proceedings. He was director of 18 research projects financed by Romanian and European institutions. Prof. Florin Constantinescu is an IEEE Senior Member since 1980 and was organizer and chairman of the IEEE Romanian CAS Chapter.

New Topics in Simulation and Modeling of RF Circuits

Alexandru Gabriel Gheorghe and
Florin Constantinescu

New Topics in Simulation and Modeling of RF Circuits addresses two main topics: simulation of RF circuits and new models of nonlinear power BAW resonators and filters.

Since RF circuits have several unique features, and all analysis methods are based on the circuit essential properties, the book begins by describing the properties of RF circuits, characterization of circuits with customary and uncustomary behavior and some theorems of solutions existence and uniqueness for dynamic nonlinear circuits.

Thereafter, the main time domain and frequency domain analysis methods for RF circuits are presented. The advantages and disadvantages of each method have been highlighted, and an algorithm for the time step choice in transient analysis based on energy balance errors is also presented.

Lastly, the final part contains some nonlinear circuit models of power BAW resonators. The behavioral models for the time domain analysis are simple circuits containing weakly nonlinear elements. The behavioral models for frequency domain analysis are based on the measured values of the frequency dependent S parameters for a set of incident powers. S parameters corresponding to certain intermodulation products of practical interest are also considered. The physical models contain artificial transmission lines with nonlinear circuit elements corresponding to mechanical and electrical nonlinearities.

ISBN 978-87-93379-46-6



9 788793 379466



River Publishers